ORNL/TM-7486

ornl

OAK RIDGE NATIONAL LABORATORY

UNION CARBIDE

An Experimental Investigation of Solid Hydrogen Pellet Ablation in High-Temperature Plasmas Using Holographic Interferometry and Other Diagnostics

C. E. Thomas

OPERATED BY
UNION CARBIDE CORPORATION
FOR THE UNITED STATES
DEPARTMENT OF ENERGY

Printed in the United States of America. Available from
National Technical Information Service
U.S. Department of Commerce
5285 Port Royal Road, Springfield, Virginia 22161
NTIS price codes—Printed Copy: A11 Microfiche: A01

ORNL/TM-7486
Dist. Category UC-20 a,f

Contract No. W-7405-eng-26

FUSION ENERGY DIVISION

AN EXPERIMENTAL INVESTIGATION OF SOLID HYDROGEN PELLET ABLATION IN HIGH-TEMPERATURE PLASMAS USING HOLOGRAPHIC INTERFEROMETRY AND OTHER DIAGNOSTICS*

C. E. Thomas

Date Published: March 1981

*Doctoral dissertation: Massachusetts Institute of Technology.

Prepared by the
OAK RIDGE NATIONAL LABORATORY
Oak Ridge, Tennessee 37830
operated by
UNION CARBIDE CORPORATION
for the
DEPARTMENT OF ENERGY

Table of Contents

AN EXPERIMENTAL INVESTIGATION OF SOLID HYDROGEN PELLET ABLATION IN HIGH TEMPERATURE PLASMAS USING HOLOGRAPHIC INTERFEROMETRY AND OTHER DIAGNOSTICS

by

CLARENCE EARL THOMAS, JR.

Submitted to the Department of Nuclear Engineering on August 7, 1980, in partial fulfillment of the requirements of the degree of Doctor of Philosophy in Applied Plasma Physics

ABSTRACT

The technology currently most favored for the refueling of fusion reactors is the high-velocity injection of solid hydrogen pellets. Design details are presented for a holographic interferometer/shadowgraph used to study the microscopic characteristics of a solid hydrogen pellet ablating in a ∿1-keV plasma. Experimental data are presented for two sets of experiments in which the interferometer/shadowgraph was used to study ∿1-mm-diam solid hydrogen pellets injected into the Impurity Study Experiment (ISX-B) tokamak at Oak Ridge National Laboratory (ORNL) at velocities of 1000 m/s. In addition to the use of the holographic interferometer, the pellet ablation process is diagnosed by studying the emission of Balmer-alpha photons and by using the available tokamak diagnostics (Thomson scattering, microwave/far-infrared interferometer, pyroelectric radiometer, hard x-ray detector). Shielding of the pellet from high-energy plasma particles is determined to be greater than predicted by neutral shielding models. It is found that the material ablated from the pellet is significantly ionized even very close to the pellet (fractional ionization ∿20%) at high ablation rates; further, it is shown that the flow of ablated material is impeded perpendicular to the magnetic field. The conclusion is that the observed enhanced shielding is due to the interaction of the ablated material with the magnetic field. Finally, the work presented here, together with the theoretical work of others on transport processes, indicates that pellet velocities of the order of those already achieved (1-2 km/s) will be sufficient for fusion reactor refueling.

Thesis Supervisor: Professor P. A. Politzer

Title: Associate Professor of Nuclear Engineering

Acknowledgments

Many people have helped with the work presented in this thesis. I will try to say thanks to them all and hope that I do not neglect anyone.

My advisor, Professor Peter Politzer, has been a strong and steadying influence over the last five years. He has always been there when I needed help and has taught me more than half of the plasma physics I know.

Stan Milora and Chris Foster had the insight to support an experiment that many said would not work and built and operated the pellet injector used in these experiments.

My colleague at M.I.T., Mark McKinstry, first introduced me to holographic interferometry and suggested the basic principle of the velocimeter/timer, which was a critical part of the experiment.

Vern Lunsford, Terry Brooks, Jim Walters, and Jim Ping spent many long hours on the mechanical design of the stand and boom. It is a tribute to them that everything fit together, lined up, and operated as designed.

Sam DeCamp gave a great deal of good advice and supervision in getting the interferometer and electronics mounted on the tokamak.

Gene Purdy, Doc Turner, Cliff McCullough, Joe Campbell, T. D. Muhammad, T. C. Moore, Jim Webb, Jim Williams, Gary King, Max Holland, Jim Wilkerson, and Andy Anderson did excellent work assembling and maintaining the interferometer and pellet gun.

Lonzie Patterson, Jim Sexton, and Rick Rutter did a beautiful job of building the electronic systems.

J. J. Kluender, B. R. Kitts, and apprentices set the stand square and true.

A special thanks to Frank Bunner, who built a part of himself into the interferometer.

Jack Martin and Janice Cox performed hours of excruciating work digitizing the interferograms for computer analysis. It will be obvious from the figures that their work was excellent.

Pete Forman at Los Alamos Scientific Laboratory (LASL) provided invaluable advice on operating the interferometer, and he and B. Woodworth made available to me the LASL interferogram analysis software. Many thanks also to the LASL programmers who wrote the software.

John Wilgen, Don Hutchinson, Charlie Bush, Ed Lazarus, Phil King, Dave Swain, and Masanori Murakami all provided data from their diagnostics and consultation on the interpretation of the data.

Kathie Zell has done a consistently excellent job of preparing the typewritten version of the thesis and has always been cheerful and ready to help during the four years I have known her.

Teresa Yow edited the manuscript to make it consistent and readable. Gene Watkin, Susan Stockbridge, Cindy Johnson, Jane Martin, Judy Neeley, and Sandra Schwartz worked overtime producing the extra nice figures scattered throughout the text.

Last, and most of all, thanks to my Mother and Father.

List of Tables

List of Figures

Chapter 1

Introduction

The technology that is the leading candidate for the refueling of a fusion reactor is the high-velocity injection of solid hydrogen pellets. Until recently very little experimental data on pellet refueling existed. The first injection of solid hydrogen pellets into a plasma was performed on the Puffatron device at RISO in 1974.[1] Pellets ∿250 μm in diameter were injected at a velocity of 10 m/s into a rotating $\vec{E} \times \vec{B}$ plasma with an ion temperature of ∿400 eV. The $\vec{E} \times \vec{B}$ discharge lasted ∿5 μs. In 1975 and 1976 pellets 100 and 200 μm in diameter were injected at a velocity of 100 m/s into the Oak Ridge Tokamak (ORMAK) at Oak Ridge National Laboratory (ORNL).[2] The pellets barely penetrated the surface of the discharge, and no detectable fueling was achieved. In 1977 pellets were dropped into the Pulsator experiment at Garching,[3] and the discharge was initiated around the pellet. In 1978 the first detectable fueling of an established tokamak discharge was achieved at ORNL.[4] Pellets ∿600 μm in diameter were injected into an established discharge at a velocity of 350 m/s. A fueling effect of ∿30% was achieved with a stable discharge.

Experimental studies of pellet fueling are important to the fusion program. Before pellet fueling can be successfully used on a reactor or long-pulse experimental device, the physical processes involved must

be well understood. Theoretical scaling laws for the required fueling rate, pellet velocity, and fueling profile must be experimentally validated, or experimental scaling laws must be developed. The effects of pellet fueling on plasma confinement, transport, and profiles must be experimentally explored. Intertwined with the necessity of experimental understanding is the requirement of developing appropriate technology for the production of solid hydrogen pellets at the correct frequency, size, and velocity. The ranges of required injection frequency, pellet size, and pellet velocity must be known in order to determine whether refinements of existing technology are adequate or whether new technology must be developed. At the same time, suitable devices must be made available for experimental work.

The problem of reactor refueling with pellets can be divided into two parts, the ablation of the pellet by energetic plasma particles and the response of the plasma to the addition of cold fuel. The work to be reported here is a microscopic and macroscopic experimental study of the ablation (or evaporation) of the pellet. For these studies pellets $\sim$1 mm in diameter were injected into the Impurity Study Experiment (ISX-B) tokamak at a velocity of 1000 m/s. An examination of the plasma response was also made for this same set of experiments and is reported separately.[5] The microscopic part of the ablation studies consists of examining the pellet and its immediate environ while it is ablating using holographic interferometry and shadowgraphy. The

details of these techniques will be discussed in Chaps. 2 and 4, but basically they measure the electron density around the pellet and the remaining area of high-density neutral hydrogen. Holographic interferometry was first used to study plasma-pellet interaction by McKinstry,[6] who studied the ablation of polystyrene pellets in a z-pinch discharge.

No extensive review of previous experimental and theoretical work will be given. Other workers have recently done thorough reviews of pellet fueling.[7,8] The experimental apparatus used will be described in Chap. 2. The applicable aspects of theory will be discussed in Chap. 3. Chapter 4 presents the basic experimental results, and the data is analyzed in Chap. 5. Conclusions, a summary, and recommendations for further work will be given in Chap. 6.

References

1. L. W. Jorgensen, A. H. Sillesen, and F. Oster, Plasma Phys. 17, 453 (1975).

2. C. A. Foster, R. J. Colchin, S. L. Milora, K. Kim, and R. J. Turnbull, Nucl. Fusion 17, 1067 (1977).

3. W. Amenda, K. Buchl, R. Lang, L. L. Lengyel, and W. Reidmuller, p. 110, Proc. Fusion Fueling Workshop, NTIS USDC CONF-771129, Princeton, New Jersey (1977).

4. S. L. Milora, C. A. Foster, P. H. Edmonds, and G. L. Schmidt, Phys. Rev. Lett. 42, 97 (1979).

5. S. L. Milora et al., "Results of Hydrogen Pellet Injection into ISX-B," submitted to Nucl. Fusion.

6. M. L. McKinstry, An Experimental Simulation of Fusion Reactor Fuel Pellet Ablation, PFC/TR-79-4, Massachusetts Institute of Technology Plasma Fusion Center, Boston, Massachusetts (1979).

7. C. T. Chang, L. W. Jorgensen, P. Nielsen, and L. L. Lengyel, "The Feasibility of Pellet Refueling of a Fusion Reactor," to be published in Nucl. Fusion (1980).

8. S. L. Milora, "Review of Pellet Fueling," to be published in J. Fusion Energy (1980).

Chapter 2

Experimental Apparatus

2.1 The ISX-B Tokamak and Its Diagnostics

ISX-B is a very flexible and moderate-sized tokamak with moderate magnetic fields.[1] Its nominal major radius is 0.93 m, and the minor radius is 0.27 m. The maximum design toroidal magnetic field on axis is 1.8 T produced by 18 rectangular coils. The ohmic heating current of up to 200 kA is produced by an iron core transformer. The plasma position is feedback controlled both vertically and horizontally, and there is a shaping coil system to produce noncircular plasmas, but all experiments described here are with nearly circular cross section ($b/a \approx 1.2$). The nominal pulse length is 250 ms or less at high plasma currents. Plasma parameters for the experiment will be discussed in Chap. 4. Figure 2.1 is a schematic of the tokamak and its diagnostics.

ISX-B is equipped with standard tokamak diagnostics. A Rogowski coil measures plasma current, and a 2-mm horizontal and vertical microwave system measures line-integrated electron densities. A far-infrared (FIR) laser system was used during some of the pellet experiments to measure line-integrated electron density.[2] A four-pulse ruby laser Thomson scattering system gives time and space-resolved electron temperature and relative electron density. There is a pyroelectric radiometer system for measuring power loss from the plasma to the walls and

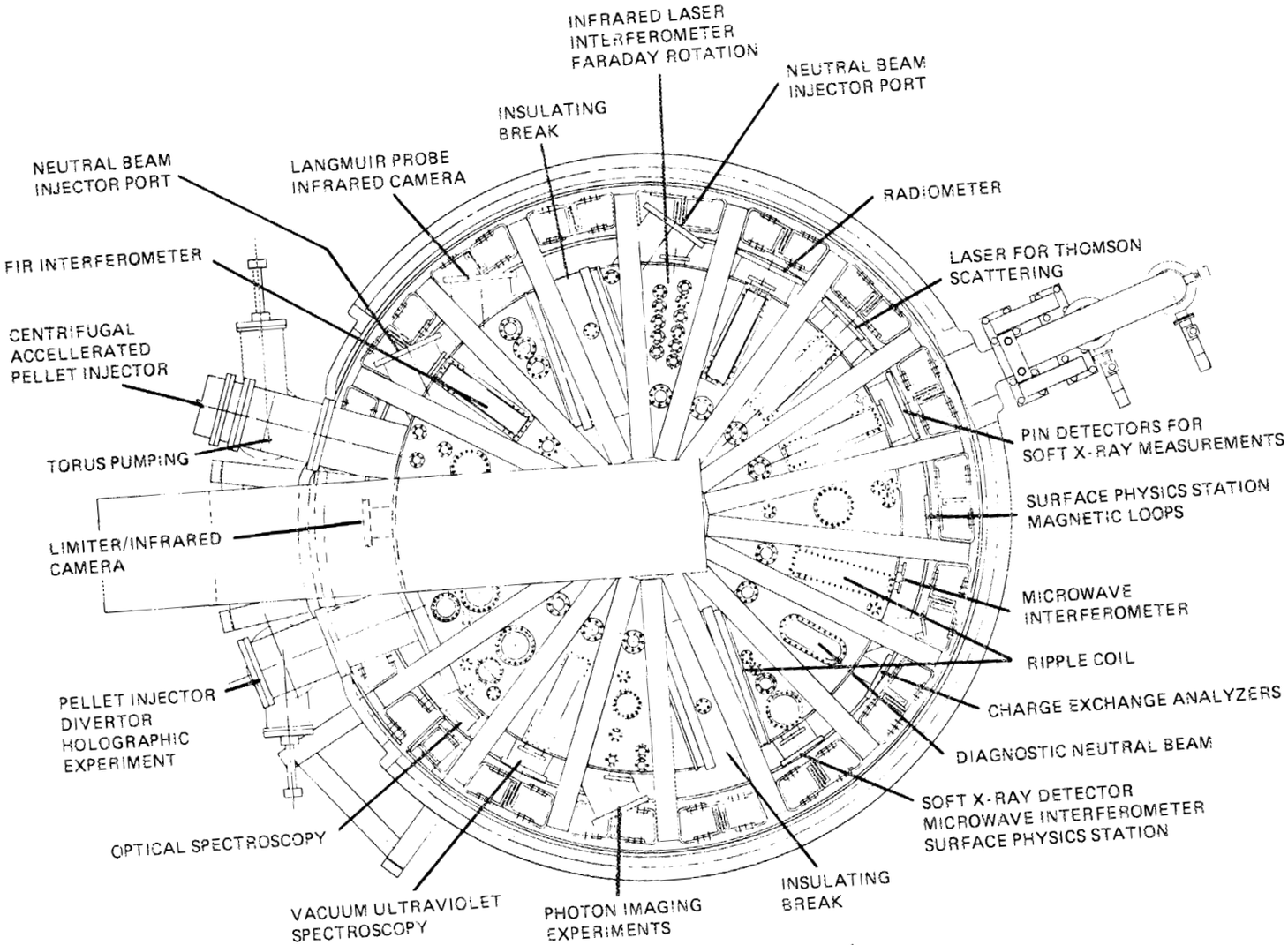

Fig. 2.1 ISX-B tokamak schematic.

an infrared camera for measuring energy to the limiters. A PIN diode soft x-ray detector measures the line integral of soft x-ray emission along a vertical central chord, and there are magnetic probes wound to detect variations in the poloidal magnetic field for MHD studies. A hard x-ray monitor looks at high-energy x rays caused by runaway electrons impacting the limiters or vacuum vessel. A charge exchange analyzer measures ion temperature.

In addition to the above, a pyroelectric radiometer was installed in the same sector as the pellet injector to study local power loss to the walls due to pellet injection.

2.2 The Pellet Injector

Reference 3 is a complete discussion of the pneumatic pellet injector used for these experiments on ISX-B. Only a brief description of the injector will be given here.

The injector produces nominal 1-mm-diam by 1.1-mm-long cylindrical hydrogen pellets. Liquid helium is used to freeze the solid hydrogen pellet in a hole in a rotating disk. The disk is then rotated in-line with a gun barrel, and a fast solenoid valve applies high-pressure helium gas to fire the pellet. When the apparatus is working well, the pellet velocity is 970 m/s with a standard deviation of 60 m/s at a helium gas pressure of $\sim$24 atm.

Between the pellet injector and the tokamak is a drift string consisting of two fast solenoid valves and a differentially pumped section. The fast valves are opened momentarily when the injector is fired. This drift line serves to isolate the tokamak from the helium gas propellant used to accelerate the pellet. Also located on the drift line are two lamp, lens, and photodiode assemblies used to detect the pellet in flight. When the pellet breaks the light beams to the photodiodes, voltage pulses are produced that trigger a digital velocimeter/diagnostic timer. The velocimeter/timer will be discussed later. Figure 2.2 is a schematic of the pellet injector and drift line on the tokamak.

2.3 The Holographic Interferometer

2.3.1 Brief review of holographic interferometry

Holography was invented in 1948 by Gabor.[4] With extraordinary insight Gabor realized that it was possible to record not only the amplitude but also the phase of a coherent wave (hence holography, for "the whole thing") by beating the wave of interest against a coherent reference wave and recording the resulting amplitude. Gabor also found that the original wavefront could be reconstructed. Holography languished after Gabor's initial work until the development of highly coherent light sources (lasers). In 1962 Leith and Upatnieks[5,6] developed a variant of Gabor's technique using laser beams. This method, known as

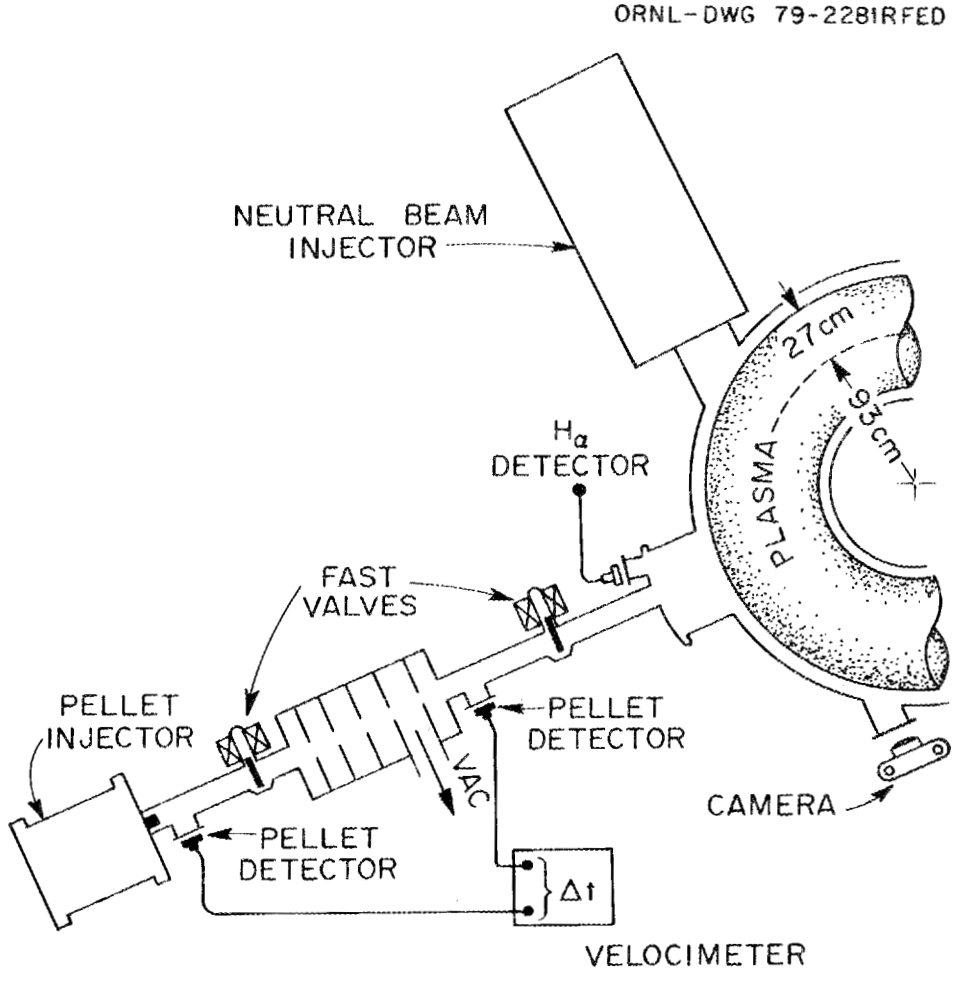

Fig. 2.2 Pellet injection line schematic.

"sideband" holography, is the basic technique used in constructing holographic interferograms. For an excellent (if highly mathematical) introduction to holography, see the works by Leith and Upatnieks referenced above and the book by Develis and Reynolds.[7]

Holographic interferometry was invented at TRW in 1965[8] and perfected as a plasma diagnostic at Los Alamos Scientific Laboratory (LASL).[9] Figure 2.3 is a schematic of a simple holographic system. To form the holographic interferogram the photographic plate is exposed twice (two holograms are formed on the same photographic plate). The first hologram is formed with no object present. Then the second hologram is formed by exposing the photographic plate again with an object in the object beam path. The mirror is tilted slightly between the two exposures. When the hologram is replayed, both object waves are recreated. The object wave from the first hologram will be a plane wave, but the object wave from the second hologram will differ from the first by the optical path length of whatever object was inserted. The two waves will thus interfere with each other, and their interference fringes will represent the optical path length of the object. Tilting the mirror between exposures produces linear background fringes, which make it possible to measure fractional fringe shifts. For a thorough introduction to holographic interferometry, see the works by Heflinger, Wuerker, and Brooks,[8] Jahoda et al.,[9,10] and Vest.[11]

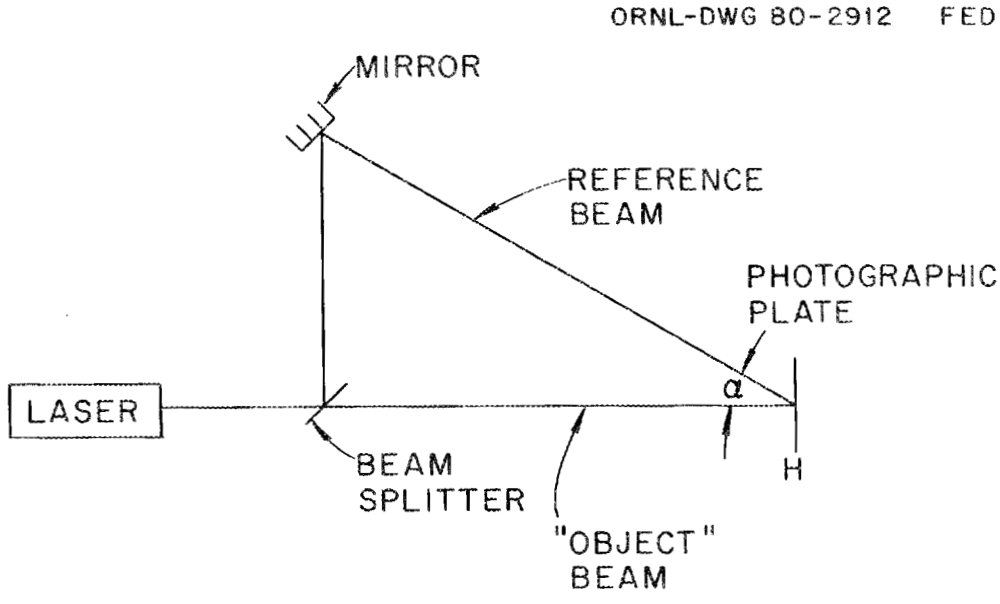

Fig. 2.3 Simple holographic system.

2.3.2 Design considerations for holographic interferometry

As discussed by Jahoda and Siemon,[10] the most important element in producing high-quality interferograms is the laser. The laser should have both high spatial and high temporal coherence. If the laser beam is not spatially and temporally coherent to a great degree, then it will interfere with itself in an unpredictable manner, resulting in poor quality (or even undecipherable) interferograms. The laser used will be described later.

The temporal and spatial resolutions of the system are important. The time resolution is limited by the pulse width of the laser, which should be much shorter than the time scale of the event being studied. Spatial resolution is affected by four factors:

1) film resolution,

2) diffraction limitation,

3) lens aberrations, and

4) object velocity.

Develis and Reynolds[7] show that the film resolution limits the object resolution to

$$RL_{obj} = 1.64(\ell_1 - \frac{\alpha_o}{\lambda}) \text{ lines/m}, \qquad (2.1)$$

where

$\ell_1 \equiv$ resolution limit of film (lines/m),

$\alpha_o \equiv$ angle of incidence of reference beam (radians), and

$\lambda \equiv$ wavelength of laser used to form hologram (m).

For Agfa Gaevert 10E75 plates that resolve $\sim 3 \times 10^6$ lines/m, Eq. (2.1) has the implication that the hologram is $\sim$2 m in extent. For holograms smaller than this, the diffraction spot size gives the ultimate theoretical limit on the object resolution:[7]

$$RL_{obj} \sim \frac{d}{(1.64)\lambda z} \text{ (lines/m)}, \tag{2.2}$$

where λ is as above,

$z \equiv$ distance from object plane or imaging lens to hologram plane, and

$d \equiv$ smaller of diameter of imaging lens system or hologram.

For $z = 3$ m, $d = 0.08$ m, and $\lambda = 0.7 \times 10^{-6}$ m (parameters typical of this experiment), the diffraction-limited object resolution is $\sim 7 \times 10^4$ lines/m or $\sim$15 μm. In practice the interferometer resolution will almost always be limited by either lens aberrations or object velocity. The object velocity is important because if the optical path length through any portion of the object changes more than $\lambda/8$ during the exposure, the interferogram will be washed out in this area.[10] For an object traveling at 1 km/s perpendicular to the interferometer and a 50-ns laser pulse, this implies that the gradient of the optical path length must be less than $\sim$600 m/m.

Vibration must be considered when desiguing the interferometer for the same reason that object motion must be considered. If any optical component moves more than $\lambda/8$ during the laser pulse, the hologram will be washed out. When using a short-pulse (50-ns) laser, this is not important. The author clamped a vacuum pump to his optical bench, with an unbalanced weight attached to the pump pulley. This caused the optical components to have a vibration amplitude of $\sim$2 mm at 400 Hz, which had no effect on the quality of the holograms produced. For an object to move $\lambda/8$ in 50 ns ($\lambda = 0.7 \times 10^{-6}$ m), it must have a velocity of $\sim$2 m/s. For a vibration amplitude of 2 mm this would imply a frequency of 1 kHz. If the system is designed with any mass at all, it is very difficult to spoil the hologram.

Refraction of the laser beam by the object is of concern. The object fringes can be displaced from their true position by object refraction. This can be corrected by imaging the object on the hologram plane with a lens.[10] If the lens is perfectly focussed, then refraction error is zero. In the experiments under discussion, it would be impossible to achieve perfect focussing with a fixed lens. This is because there was some jitter in the pellet trajectory ($\ell_o \pm \sim$1.3 cm) and because with a plasma present the pellet's trajectory curved downward (more of this later). In any event, refractive errors can still be corrected. Because the hologram recreates the original object wave, it is possible to refocus the object wave when replaying the hologram, thereby eliminating

refractive errors. This is a tremendous advantage of the holographic interferogram over other forms of interferometry.

2.3.3 Laser system design

Because there are a number of manufacturers of ruby laser systems and ruby laser components, design consisted of assembling a set of components capable of producing the desired system performance. What performance was desired? As previously discussed, high spatial and temporal coherence is necessary. In this case, "high" means that the laser beam should have only TEM_{oo} transverse mode structure and that it should have a line width of less than 0.05 Å (which corresponds to a coherence length of $L_c = \lambda^2/\Delta\lambda = 0.10$ m). It was necessary that the laser pulse timing have a jitter $\leq$1 μs to provide temporal resolution and that the pulse length be $\leq$50 ns to eliminate the effects of object velocity and system vibration. Further, the laser had to produce a minimum energy of ∿50 mJ to expose the photographic plate and had to be capable of two pulses in six minutes. Figure 2.4 is a schematic of the laser system.

The laser system operation will be briefly described. All that is necessary to make a simple ruby laser is a ruby rod, flashlamp, 100% rear reflector, and partially reflecting output reflector. The flashlamp pumps the chromium atoms in the ruby crystal to the $^4F_1$ and $^4F_2$ levels. These then decay to the laser level, which decays to the ^2E

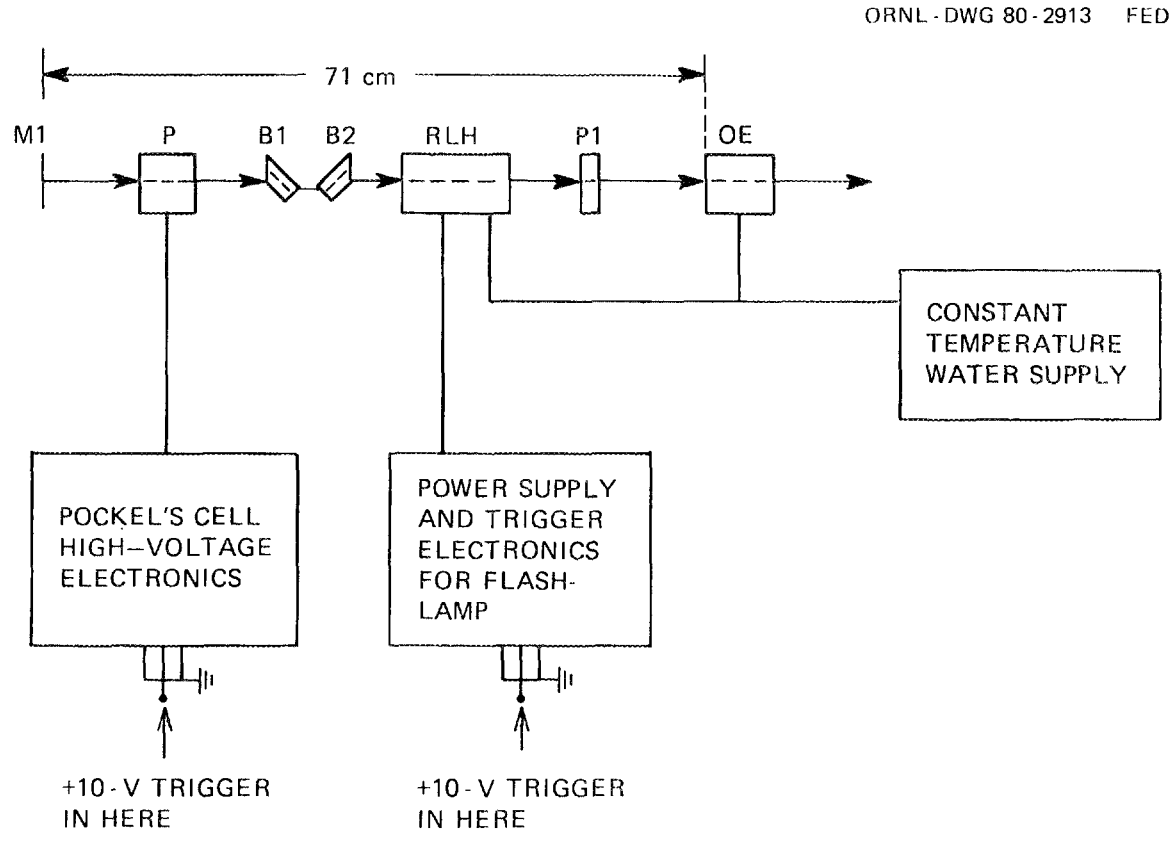

M1 – LASER CAVITY 100% REAR REFLECTOR
P – POCKEL'S CELL Q-SWITCH
B1, B2 – BREWSTER STACKS
RLH – RUBY LASER HEAD, CONTAINS HELICAL FLASHLAMP AND 4" x 3/8" HOLOGRAPHIC RUBY LASER ROD
P1 – 1.7-mm-DIAM PINHOLE
OE – FOUR-PLATE TEMPERATURE TUNED SAPPHIRE OUTPUT ETALON (LASER CAVITY OUTPUT REFLECTOR)

Fig. 2.4 Schematic of holographic ruby laser system.

level.[12] This is the laser transition. If the mirrors are aligned parallel to the ruby rod and the flashlamp is pumped hard enough to achieve population inversion in the ruby rod, then the laser oscillates. Because the gain coefficient for a ruby crystal is much higher along one axis than along the other, the output of a ruby laser is naturally polarized. This natural polarization allows the laser output to be a single giant pulse. To achieve this an optically active crystal and polarization elements are inserted into the laser cavity. When high voltage is applied to the optically active crystal (Pockel's cell), it rotates the plane of polarization of light passing through it. The Brewster angle stacks are aligned to pass the high-gain polarization of the ruby rod, but the return radiation from the rear cavity reflector has had its plane of polarization rotated by the Pockel's cell. The Brewster angle stacks then reflect this radiation. The gain of the cavity is very low. In analogy to electronics one says that it has low Q. If the voltage on the Pockel's cell is now rapidly brought to zero, the return radiation from the rear cavity reflector has its original polarization and is not reflected by the Brewster stacks. The cavity is suddenly a high-gain cavity (high Q). If sufficient population inversion has been achieved before the Q-switch, the laser oscillation will build up very rapidly, and the laser energy will be released as a single giant (Q-switched) pulse. This is known as pulse-off Q-switching because the high voltage is suddenly brought to ground. For a better discussion of lasers, ruby lasers, and Q-switching, see Yariv.[12]

The laser system components will now be described (see Fig. 2.4). The rail for mounting the laser optical components was an aluminum I-beam supplied by Korad. The mount for the rear reflector itself was also supplied by Korad, and the rear reflector was supplied by CVI Laser Corporation. The Pockel's cell and Brewster stacks were from Apollo Lasers, and the laser head and ruby rod were supplied by Korad. The ruby rod was a special select holographic quality rod, 4-in. long by 3/8-in. diameter. The 1.7-mm internal cavity pinhole, purchased from Korad, was a movable aperture (micrometer adjustment) to limit the transverse mode content of the laser cavity and to select the best portion of the rod (best being the portion giving the most uniform transverse mode structure). The temperature-tuned four-plate sapphire output etalon, supplied by Korad, was used to give the laser good temporal coherence (long coherence length). The cavity length of the etalon (and therefore the allowed longitudinal laser mode) was varied by changing the temperature of the cooling water that flowed through the etalon. An Apollo power supply and Q-switching electronics (formerly used for Thomson scattering) were used to drive the Pockel's cell and laser head xenon flashlamp. The water circulator/temperature regulator was supplied by Korad. It cooled the laser head between pulses and regulated the temperature of the output etalon. Water temperature was maintained within $\pm 0.5°C$.

The laser system performed reliably. With the internal 1.7-mm pinhole, four-plate sapphire output etalon, and flashlamp power supply

100 V above threshold for laser operation, a 50-ns full width at half maximum (FWHM) Q-switch laser pulse was produced with a nominal energy of 40 mJ. The scatter in the energy was ±10% (any given day). The pulse width was measured using a United Detector Technology PIN-6LC photodiode and the circuit of Fig. 2.5. The laser energy was measured with a Control Data Corporation thermopile and a Hewlett-Packard microvoltmeter.

The coherence length of the laser was experimentally found to be >70 cm because clear bright interferograms were made with path differences greater than this.

Figure 2.6 is an example of the typical far-field pattern of the laser. Clearly it is not a simple TEM_{oo} mode pattern. In spite of this, bright clear interferograms were achieved with no broken, split, or wavy fringes.

2.3.4 Optical system design

Figure 2.7 is a schematic of the optical system for the interferometer. Listed below are the component symbols and a description of each:

He-Ne = 2-mW polarized helium neon laser used for alignment (Oriel Corporation),

RLS = ruby laser system as previously discussed,

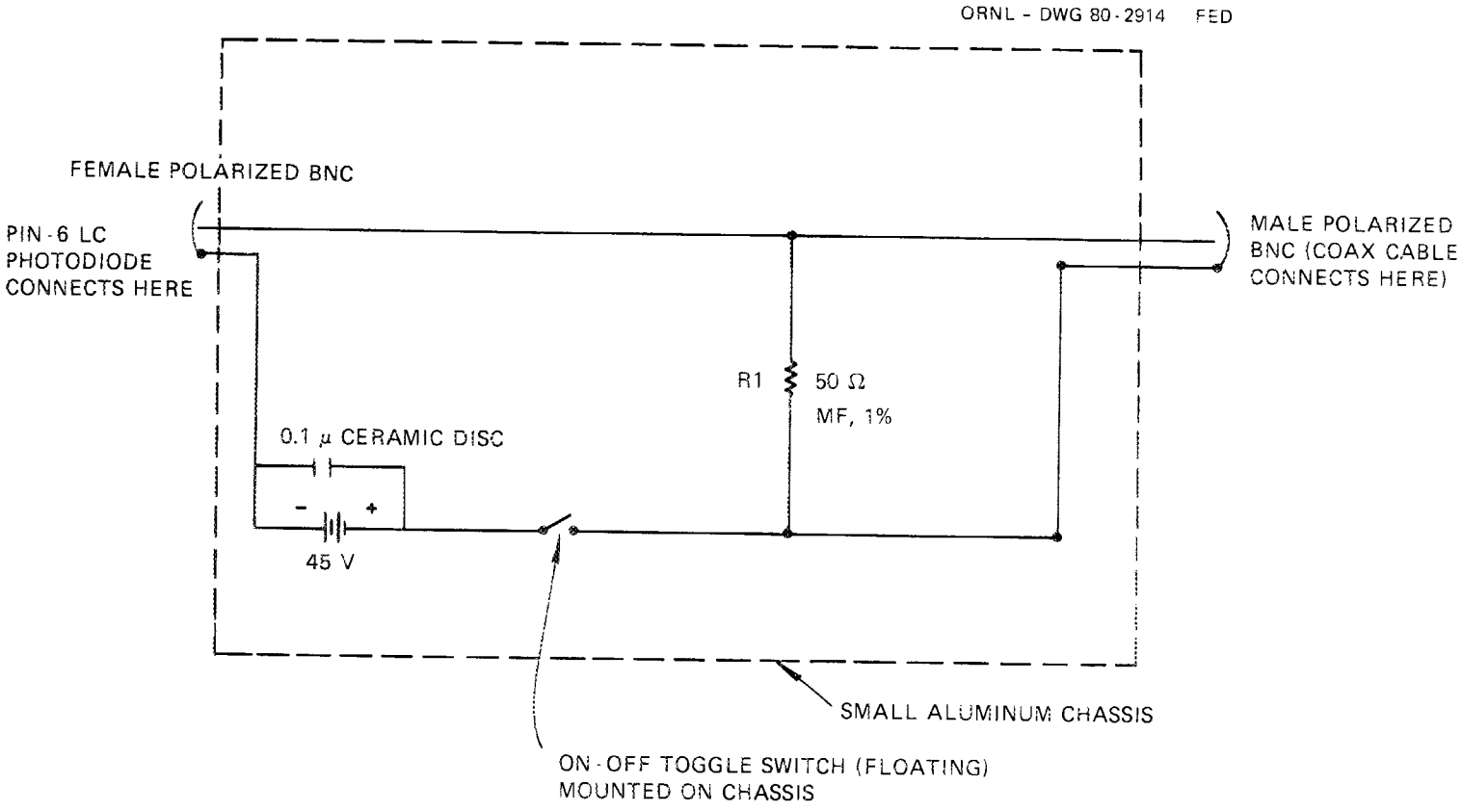

Fig. 2.5 Laser pulse detector circuit schematic.

Fig. 2.6 Far-field pattern of ruby laser.

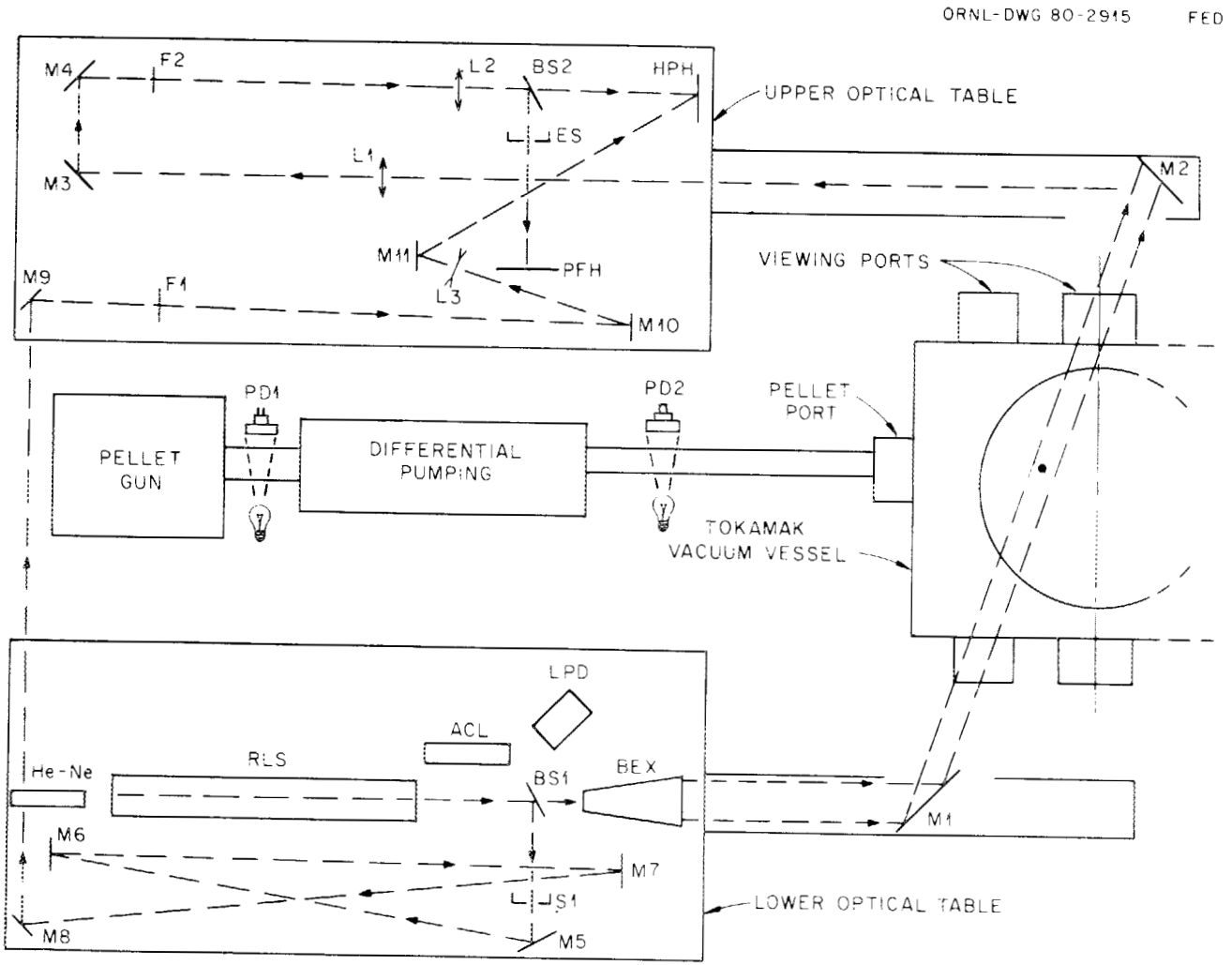

Fig. 2.7 Holographic interferometer optical schematic.

ACL ≡ autocollimator on kinematic rotating mount for laser alignment (Newport Research Corporation),

LPD ≡ laser pulse detector previously discussed,

BS1 ≡ 50/50 dielectric beam splitter (CVI Laser Corporation),

BEX ≡ 50-to-1 beam expander (Melles Griot),

M1 ≡ 4-in. by 5-in. aluminum first-surface mirror with corners chopped and mounted on sliding mount (mirror from Edmunds),

M2 ≡ same as M1,

L1 ≡ achromatic doublet lens with 1185-mm focal length (Melles Griot),

L2 ≡ 165-mm focal length lens (Edmunds),

M3, M4 ≡ 99% reflectivity dielectric mirrors (Newport Research),

F2 ≡ 100 Å FWHM ruby laser line filter (Melles Griot),

BS2 ≡ 50/50 dielectric beam splitter (CVI Laser Corporation),

HPH ≡ holographic plate holder (Linhoff),

S1 ≡ 2-mm slit (Oriel),

M5-M11 ≡ 99.8% reflectivity dielectric mirrors (Newport Research),

F1 ≡ neutral density filter (Kodak wratten gelatin),

L3 ≡ -70-mm focal length lens (Edmunds),

ES ≡ electronic shutter (Uniblitz),

PFH ≡ polaroid film holder, and

PD1, PD2 ≡ photodiodes for detecting the hydrogen pellet in flight (UDT PIN-10).

The function of the optical system will be discussed briefly. The He-Ne laser was used to align the entire optical system. It was mounted on a two-ring holder on a vertical and transverse translator. The ruby laser was mounted on a three-point mount on vertical and transverse translators. After the optical system was aligned on the He-Ne laser, the ruby laser was aligned with the He-Ne laser. Final adjustment for parallelism of all optical surfaces in the ruby laser cavity was made with a kinematically mounted autocollimator that could be swung in-line with the ruby laser. The beam splitter following the autocollimator split the laser beam into a "scene" and "reference" beam. The scene beam was immediately expanded to approximately 75 mm. The reference beam was kept unexpanded until just before recombining it with the scene beam. Mirrors M1 and M2 were mounted on sliding mounts in booms extended below and above the tokamak. The sliding mounts were adjustable so that it was possible to view all of the plasma from minor radius r = 22 cm to r = -7.5 cm. Lenses L1 and L2 imaged the centerline of the plasma on the holographic plate and polaroid film. The focal lengths of the lenses and their separation were chosen so that an image magnification of one was maintained. With the system set up as shown the distance from the plasma centerline to L1 was 3.556 m with an estimated maximum error of $\leq \pm 25$ mm. The distance from L2 to L1 was 2.025 m with an estimated maximum error of $\leq \pm 2$ mm. The distance from L2 to the holographic

plate was 0.495 m with an estimated maximum error of $\leq \pm 1$ mm. Whenever the viewing path of the interferometer was changed the positions of lens L1 and mirrors M3 and M4 were adjusted to keep all path lengths as described above. Filter L2 kept stray plasma light from exposing the holographic plate. Beam splitter BS2 split off a portion of the scene beam to form a shadowgraph of the pellet on polaroid film. The electronic shutter was closed during the reference shot for the interferogram so that the polaroid film for the shadowgraph would not be exposed. Mirrors M5, M6, M7, M8, M9, M10, and M11 were used for translating the reference beam and path length equalization. The reference and scene beam path lengths were equalized with an estimated maximum error of ≤ 25 mm. Lens L3 expanded the reference beam to approximately the same size as the scene beam. Filter F1 was used to adjust the intensity of the reference beam so that it was approximately equal to the scene beam intensity.

Light-tight covers were designed for the upper and lower optical tables, and light-tight shrouds extended from the booms to the tokamak. These light-tight covers prevented injury to innocent bystanders from the ruby laser pulse and also prevented the holographic plate and polaroid film from being exposed by room light. All removable covers were double electrically interlocked with the ruby laser power supply to prevent the laser from being fired with a cover removed.

The mount for mirror M11 was specially modified to allow tilting between the reference and object shots for the interferogram (to provide background fringes). An electrically heated wire, as described by Jahoda and Siemon,[10] was used to tilt the mirror. Figures 2.8 and 2.9 are photographs of the lower and upper optical table.

2.3.5 Stand and boom design

Figure 2.10 is a picture of the completely assembled interferometer sitting in the high-bay area outside the ISX-B experiment. A temporary box has been extended from the lower to the upper boom to protect passers-by from the laser. The pellet gun, which rides on the two rails between the upper and lower optical tables, had not yet been installed when this picture was taken. Figure 2.11 is a photograph of the complete interferometer/pellet gun system installed on ISX-B.

In designing the stand and booms three objectives were kept in mind.

1) The system should not vibrate excessively.
2) The system must contain the pellet injector and interfero meter and fit in the space provided.
3) The system should not move under the influence of rapidly varying magnetic fields.

To prevent excessive vibration the stand was designed to have mass and to be rigid. The optical tables were 1-in.-thick aluminum sheets,

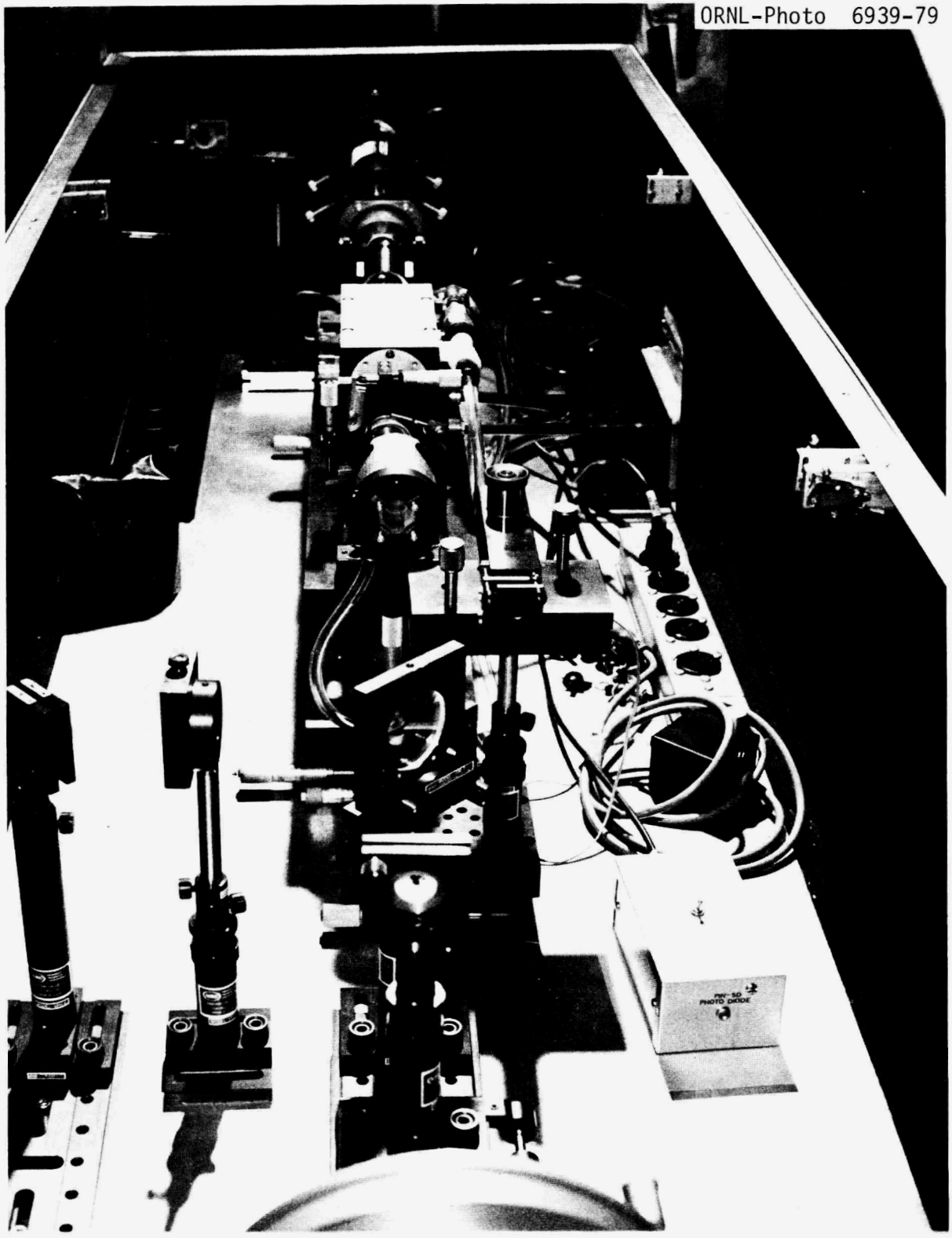

Fig. 2.8 Photograph of lower optical table looking at output etalon of ruby laser.

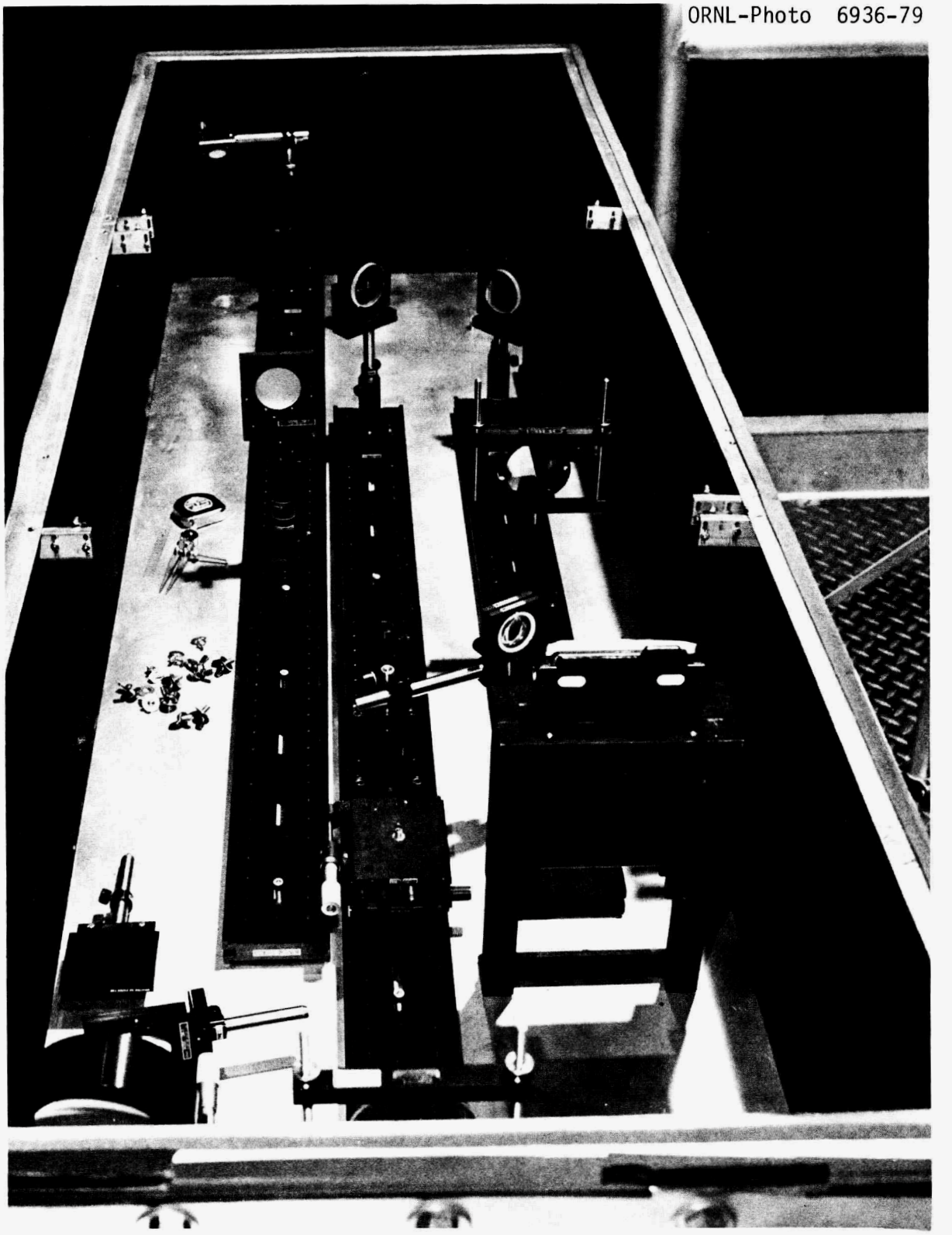

Fig. 2.9 Photograph of upper optical table (some components not installed) looking from back of photographic plate holder.

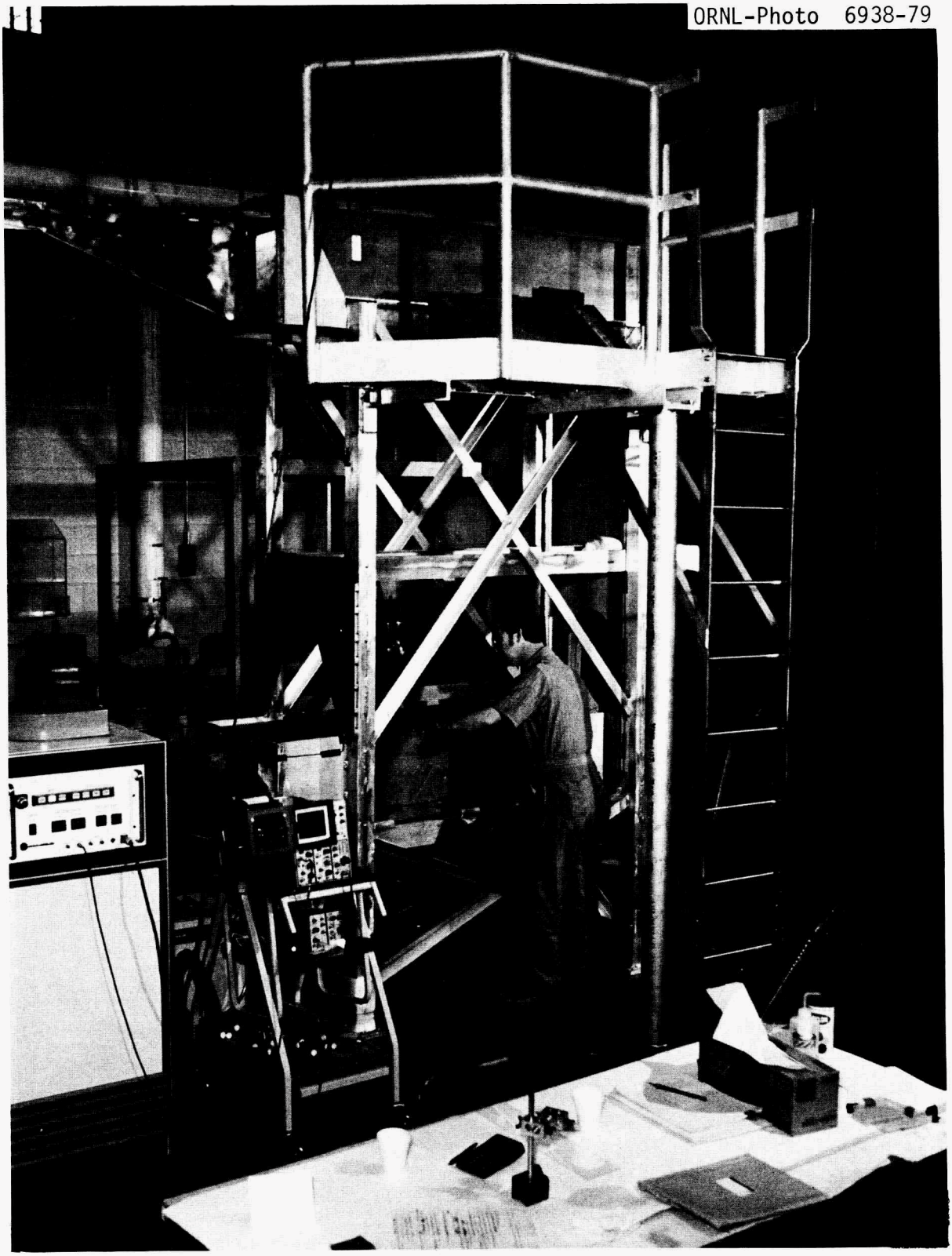

Fig. 2.10 Photograph of holographic interferometer assembled but not installed on ISX-B.

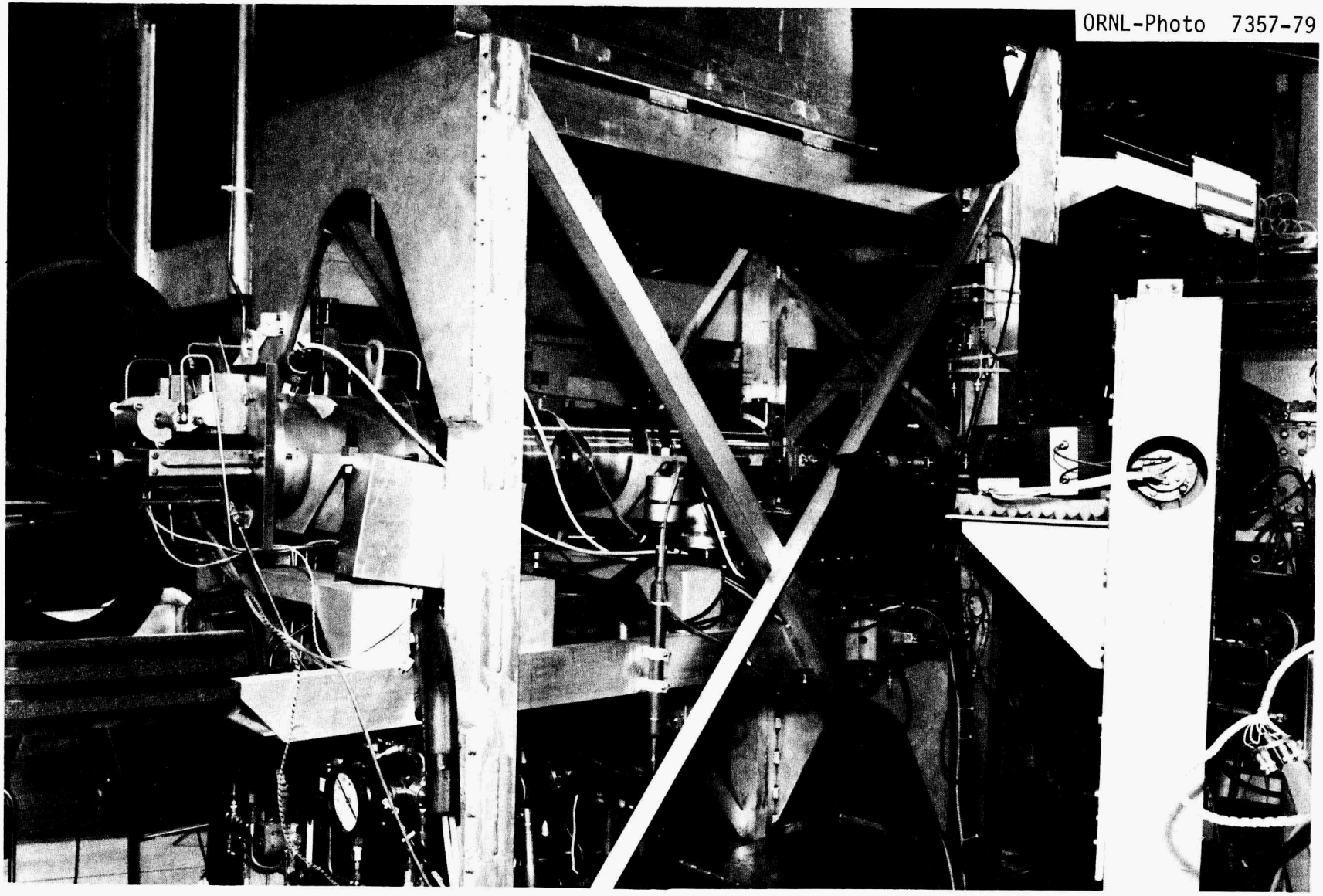

Fig. 2.11 Photograph of interferometer and pellet gun installed on ISX-B.

and the legs and braces were constructed from 4-in. aluminum channel. The structure was cross-braced in all directions, and a 0.5-in.-thick aluminum plate was welded on each end to add rigidity in the transverse direction.

The main concern with the booms was that they might react to the rapidly varying magnetic fields. A test boom 5 ft long was constructed of 4-in.-diam stainless pipe with a 1/16-in.-thick wall. The boom was rigidly mounted at one end with the other end over the tokamak viewing ports to be used for the experiment. A mirror was mounted on the end of the boom. A He-Ne laser beam was bounced off a mirror on the end of the boom onto a target mounted on the wall. The position of the laser beam on the target was observed during several tokamak shots. There was no observable motion. The booms were therefore constructed from 1/16-in.-thick 316 stainless steel sheet spot-welded together. This provided adequate rigidity and high enough resistivity so that the time-varying magnetic fields caused no motion of the booms. So that motion of the tokamak would not move the booms, the light shrouds extending from the tokamak to the booms were designed so as not to actually touch the boom.

Great care was taken in designing the stand and booms so that everything would fit together in the allotted space. More than 30 engineering drawings were produced. Fabrication of the stand, booms, and light shrouds was done in the shops of the Y-12 plant of Union Carbide Nuclear Division in Oak Ridge.

2.3.6 Hologram replay system

Figure 2.12 is a schematic of the hologram replay system. Figure 2.13 is a photograph of the author replaying a hologram. The hologram replay system was very simple. A He-Ne laser was used as a source of coherent light. Immediately after the beam left the laser, a 35-mm lens expanded the beam into a spherically diverging wave. A mirror was used to deflect the laser beam onto the developed hologram (the holograms were developed and bleached as described by Jahoda and Siemon[10]). The hologram then diffracted the incident light into converging and diverging reconstructions, as indicated. The author found that using the converging wave for replay provided superior reconstructions. The reason for this is trivial — because the wave converges it is possible to get more of the diffracted beam into the microscope input optics. The microscope used for focussing the reconstructed image onto the polaroid camera was supplied by Wilde-Heerbrugg. It was equipped with a five-axis mount that allowed x-y-z translation and rotation about a vertical and horizontal axis. This facilitated aligning the microscope with the reconstructed wavefront.

Whenever a hologram was reconstructed, the microscope was carefully focussed to eliminate all diffraction lines around the reconstructed image. It was usually quite clear when the best focus was achieved because obvious diffraction rings would be present on a poorly focussed

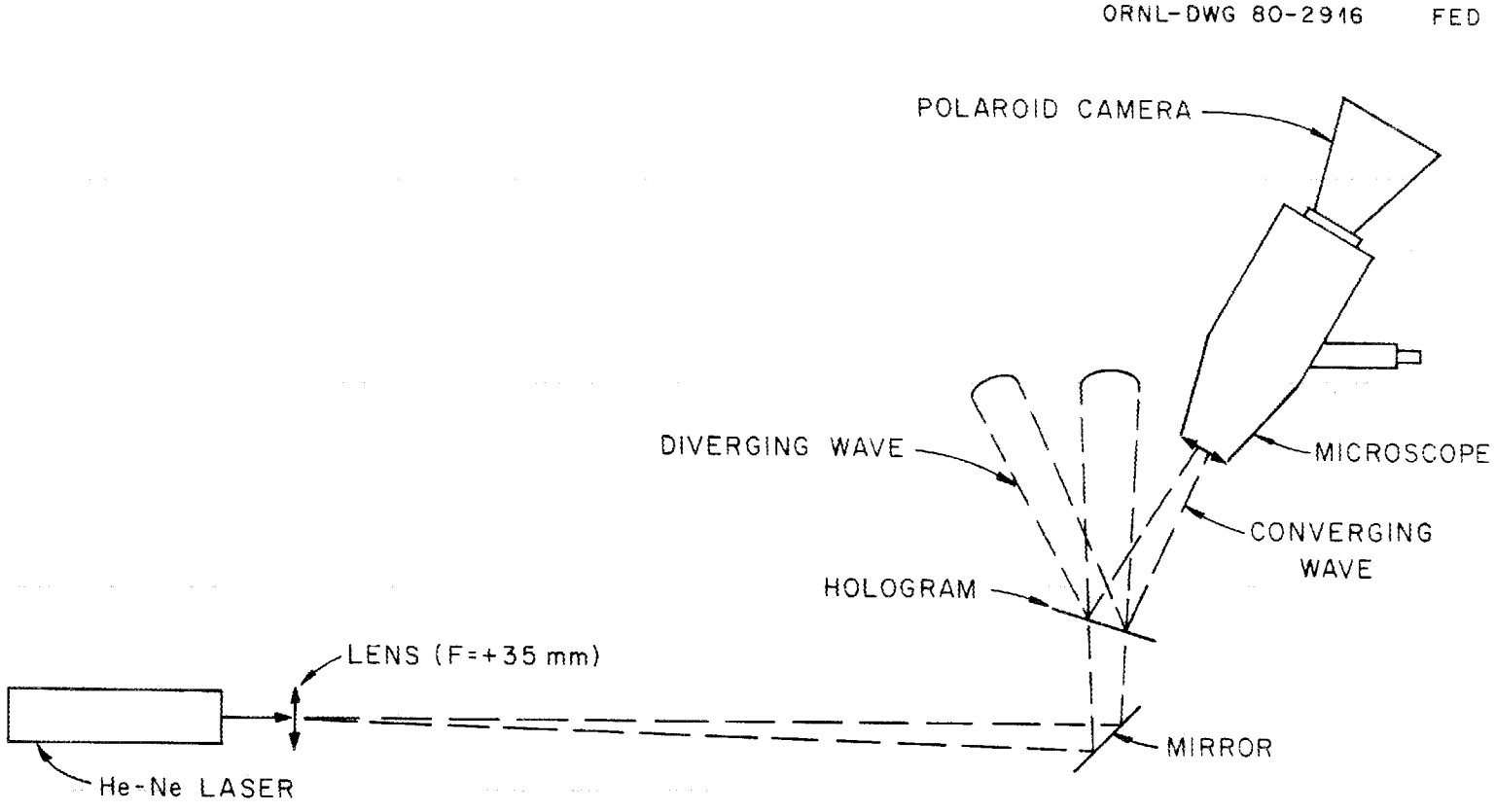

Fig. 2.12 Schematic of hologram replay system.

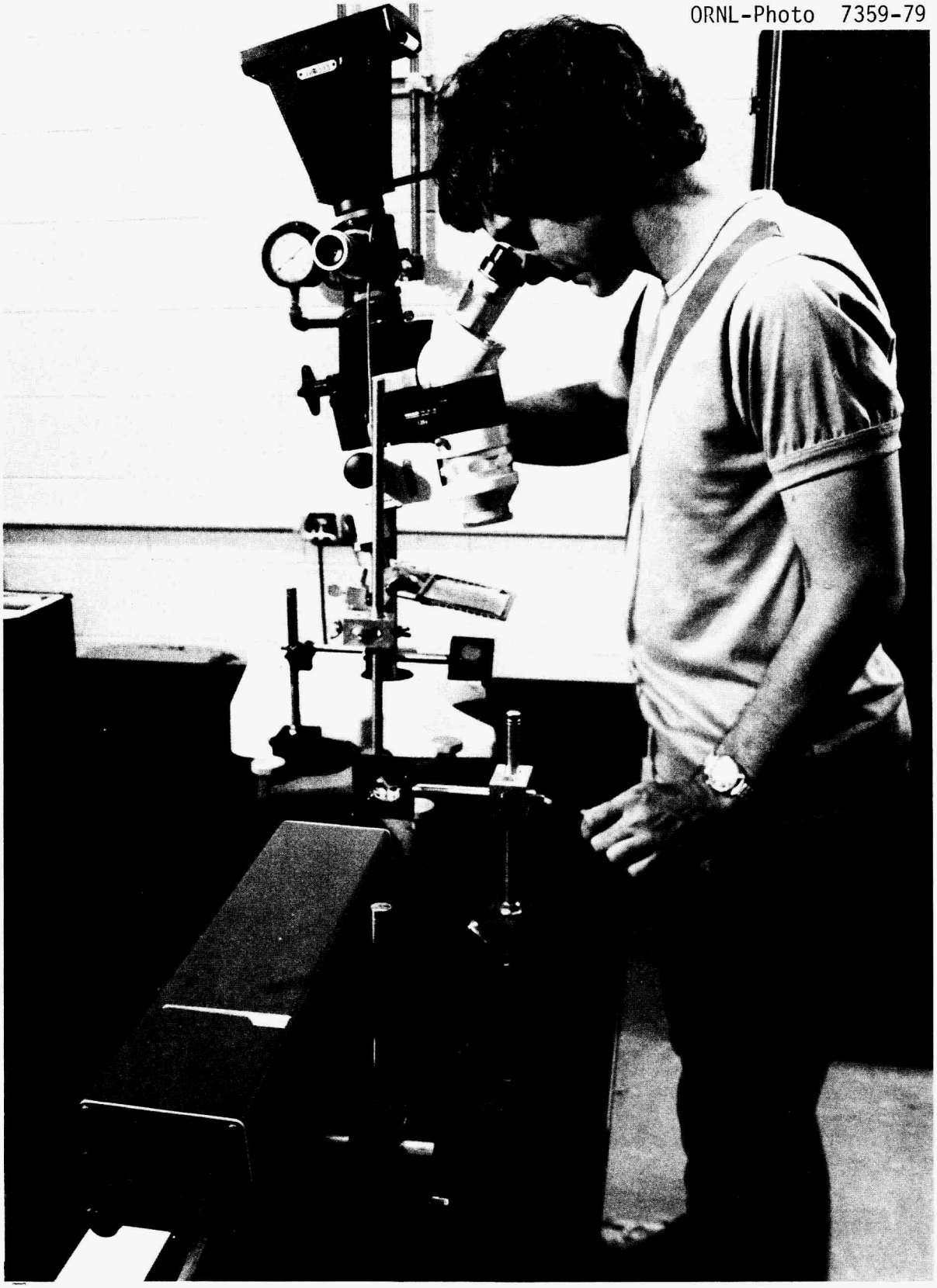

Fig. 2.13 Photograph of author replaying hologram.

interferogram of a pellet. After the best focus was found the distance from the microscope input lens to the holographic (photographic) plate was carefully measured to the nearest millimeter. This measurement allowed the error in focussing and magnification (due to the downward curvature of the pellet's trajectory) to be calculated. If the pellet had been in the same horizontal plane on every shot, then the focal distance from the microscope to the holographic plate would have been the same for every shot. Polaroid pictures of the reconstructed image were made at three different microscope magnifications (7.5 X, 15 X, or 31.2 X) and at multiple exposure lengths to achieve the most accurate replay of each interferogram. Replay normally took about one hour per interferogram.

2.3.7 Calculation of errors in interferogram magnification

Errors in magnification of the reconstructed interferogram are introduced in two ways. The first source of error is the change in the ratio of object-to-lens and lens-to-image distances due to imperfect focussing of the object on the photographic plate. The second source of error is due to replaying the hologram with a spherically diverging wave and using a spherical wave for the reference beam in forming the hologram. The error in magnification due to all of these sources goes to zero if the object is perfectly focussed on the holographic plate (the image plane of the lens corresponds to the plane of the photographic plate).

The first source of error examined will be that due to the change in ratio of image-to-lens and object-to-lens distances.

Consider Figure 2.14. There is a lens system consisting of two lenses that images an object (arrow at the object plane) onto an image plane. There is more than one way to analyze this lens system, but one simple way is to consider it as a relay lens system. Lens L1 with focal length f1 images the object at distance R1 onto an image plane at distance R4. Then lens L2 images the image at distance (R2 - R4) onto the image plane at R3. The equations describing the system are

$$\frac{1}{R1} + \frac{1}{R4} = \frac{1}{f1} , \tag{2.3}$$

$$\frac{1}{(R2 - R4)} + \frac{1}{R3} = \frac{1}{f2} , \tag{2.4}$$

$$M_1 = \frac{R4}{R1} , \text{ and} \tag{2.5}$$

$$M_2 = \frac{R3}{(R2 - R4)} . \tag{2.6}$$

Equations (2.3) and (2.4) are the conditions necessary for focussing the object on the image plane, and Eqs. (2.6) and (2.7) give the magnification of lens L1 and lens L2. The magnification of the total lens system is

$$M = (M_1 \cdot M_2). \tag{2.7}$$

Now suppose that the object was not exactly distance R1 from lens L1 but was at distance (R1 + ΔR1) from lens L1. This would cause an error ΔR4 in the location of the image plane of lens L1 and an error ΔR3 in the

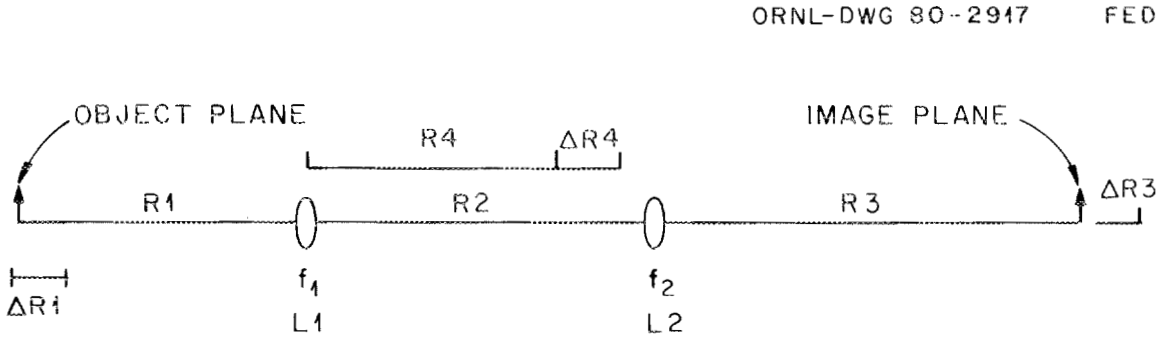

Fig. 2.14 Schematic for analysis of magnification error due to focussing errors.

location of the image plane of lens L2. The equations that describe the lens system now are

$$\frac{1}{(R1 + \Delta R1)} + \frac{1}{(R4 + \Delta R4)} = \frac{1}{f1}\ , \tag{2.8}$$

$$\frac{1}{R2 - (R4 + \Delta R4)} + \frac{1}{(R3 + \Delta R3)} = \frac{1}{f2}\ , \tag{2.9}$$

$$M_1' = \frac{R4 + \Delta R4}{R1 + \Delta R1}\ , \tag{2.10}$$

$$M_2' = \frac{R3 + \Delta R3}{R2 - (R4 + \Delta R4)}\ , \text{ and} \tag{2.11}$$

$$M' = (M_1' \cdot M_2'). \tag{2.12}$$

M_1 and M_2 are the new magnifications of lens L1 and L2, and M' is now the total magnification of the system. The above lens system is exactly like the focussing optics for the holographic interferometer (Fig. 2.7). The interferometer optics focus the midplane of the tokamak on the holographic plate. If the pellet is above or below the midplane, there is a focussing error $\Delta R1$, leading to an error $\Delta R3$ in the focussing of the interferogram on the photographic plate. As discussed above, $\Delta R3$ is measured when the hologram is replayed. Because $\Delta R3$ is a known quantity, Eqs. (2.8)-(2.11) are a system of four equations in four unknowns, $\Delta R1$, $\Delta R4$, M_1', M_2'. Solving for the unknowns,

$$\Delta R4 = \frac{-1}{1/f2 - 1/(R3 + \Delta R3)} + \frac{R3}{M_2}\ , \tag{2.13}$$

$$\Delta R1 = \frac{1}{1/f1 - 1/(L1 \cdot M_1 + \Delta R4)} - R1, \tag{2.14}$$

$$M_2' = (1 + \Delta R3/R3)/(1/M_2 - \Delta R4/\Delta R3), \text{ and} \tag{2.15}$$

$$M_1' = (M_1 + \Delta R4/R1)/(1 + \Delta R1/R1). \tag{2.16}$$

Note that $\Delta R3$, $\Delta R4$, and $\Delta R1$ are signed quantities and that $\Delta R3 > 0$ implies $\Delta R4 > 0$ implies $\Delta R1 < 0$.

The second source of error in interferogram magnification will now be analyzed. Consider Fig. 2.15. DeVelis and Reynolds[7] show that using spherical waves and reconstructing the hologram with a different wavelength than it was formed with changes the focussing condition and magnification. If $\Delta R3$ is the distance from the image plane to the photographic plate while forming the hologram, R0 is the radius of curvature of the reference wave as it strikes the photographic plate, R5 is the radius of curvature of the replay wave as it strikes the developed hologram, Z3 is the distance from the hologram to the reconstructed image plane, and $\lambda 1$ and $\lambda 2$ are the wavelengths used for hologram formation and hologram replay, then the focussing condition for the convergent reconstructed wave is

$$-\frac{1}{\lambda 1 \cdot \Delta R3} + \frac{1}{\lambda 1 \cdot \Delta R0} + \frac{1}{\lambda 2 \cdot Z3} + \frac{1}{\lambda 2 \cdot R5} = 0 \tag{2.17}$$

and the magnification of the system is

$$M_3 = [1 - \Delta R3/R0 - \lambda 1 \cdot \Delta R3/(\lambda 2 \cdot R5)]^{-1}. \tag{2.18}$$

Solving Eq. (2.17) for $\Delta R3$ gives

$$\Delta R3 = \frac{1}{\lambda 1/(\lambda 2 \cdot Z3) + 1/R0 + \lambda 1/(\lambda 2 \cdot R5)}. \tag{2.19}$$

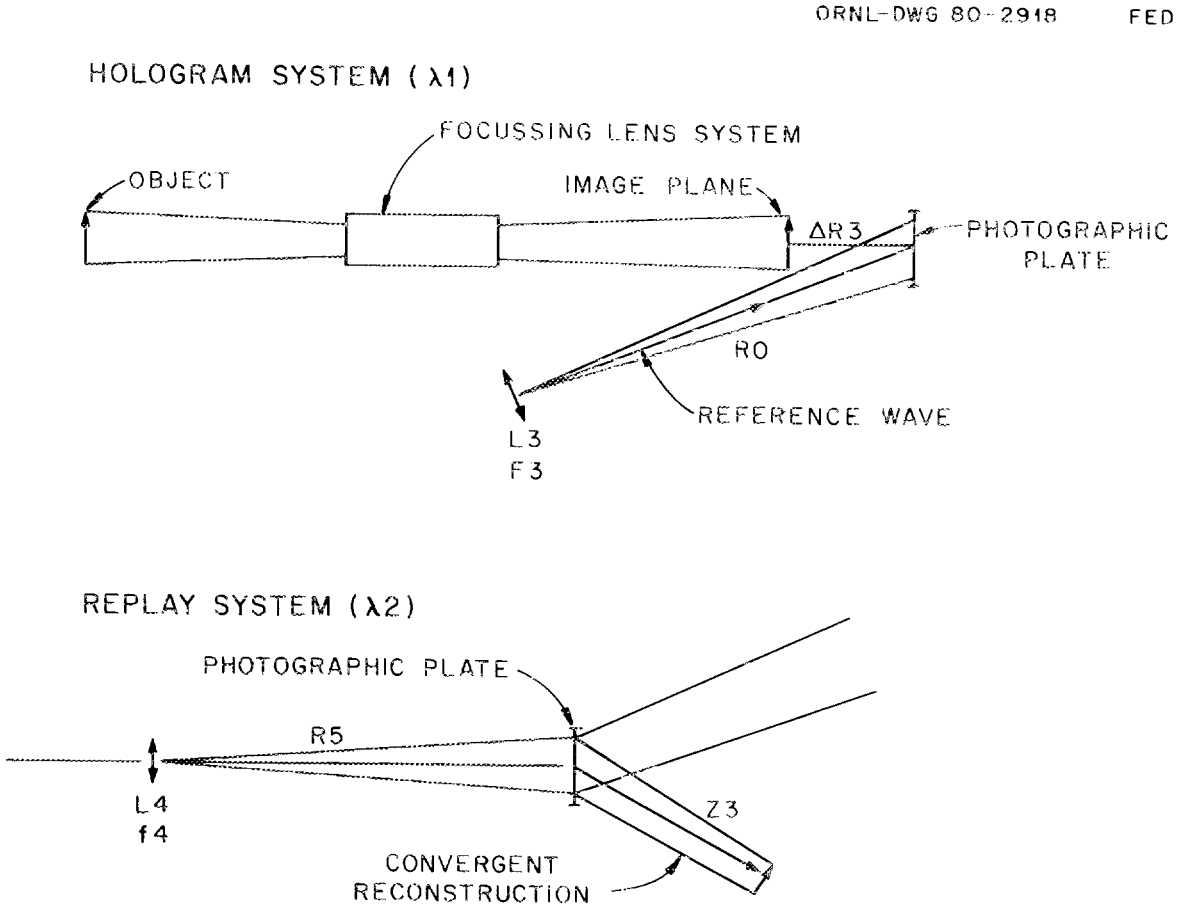

Fig. 2.15 Schematic for analysis of magnification errors due to replay with spherical waves at a different wavelength.

Equations (2.13)-(2.16), (2.18), and (2.19) are a complete description of the known magnification and focussing errors. Note that if the error in focussing goes to zero, the system magnification returns to its design value. The experimentally measurable quantity in the above equations is Z3, the distance from the hologram to the image plane when reconstructing the hologram. Given Z3, Eqs. (2.18) and (2.19) can be solved for $\Delta R3$ and M_3. Given $\Delta R3$, Eqs. (2.13)-(2.10) are solved, and the final system magnification is

$$M_{sys} = M_3 \cdot M_2' \cdot M_1'. \tag{2.20}$$

An example typical of the parameters of the interferometer system will now be calculated. If Z3 is measured as 0.08 m and if

$\lambda 1 = 6943$ Å, $\lambda 2 = 6328$ Å,

R0 = 0.876 m, R5 = 1.245 m,

R1 = 3.556 m, R2 = 2.0252 m,

R3 = 0.4953 m,

$M_1 = 0.5$, $M_2 = 2$, and

f1 = 1.185 m, f2 = 0.165 m,

then using Eqs. (2.18) and (2.19) gives

$\Delta R3 = 0.0635$ m,

$M_3 = 1.144$.

Using the above result for $\Delta R3$ in Eqs. (2.13)-(2.16) and (2.20) gives

$\Delta R4 = 0.0135$ m,

$\Delta R1 = -0.056$ m,

$M_1' = 0.5118$,

$M_2' = 2.3865$, and

$M_{sys} = 1.397$.

A measured distance of 8 cm from the hologram to its image plane indicates that the image is 1.397 times larger than the design magnification and that the pellet was 5.6 cm above the lens focus (plasma midplane).

2.3.8 Timing and firing — digital velocimeter and velocity-dependent diagnostic timer

Timing was critical in this experiment. The laser had to be fired when the pellet was in the field of view of the interferometer. However, not only was it necessary to have the pellet in the field of view; it was also necessary to have the pellet at a selected place in the field of view within ± 5 mm. This would allow interferograms to be conveniently made of the pellet at different spatial locations. The interferometer field of view was approximately 75 mm; therefore, the above condition was much more restrictive than just requiring the pellet to be in the field of view. Because the jitter in the pellet velocity could be as much as 300 m/s (although on a good day the standard deviation for the velocity was 60 m/s), a velocity-dependent diagnostic timer was designed and built.

The principle of the diagnostic timer is quite simple. Consider Fig. 2.16. Suppose that a digital up/down counter starts counting up from zero when the pellet passes photodiode PD1 and counts up at frequency F_1. When the pellet passes photodiode PD2, the counter starts counting down at frequency F_2. The distance D2 that the pellet will be from photodiode PD2 when the counter again reaches zero is given by

$$D2 = D1 \cdot F_1/F_2, \tag{2.21}$$

where D1 is the distance between photodiodes PD1 and PD2. In words, the ratio of the distances D2/D1 is equal to the ratio of the frequencies F_1/F_2. If F_2 is a fixed frequency and F_1 is continuously variable, then the distance D2 can be continuously varied by varying the frequency F_1. Further, because F_2 is a fixed frequency any desired diagnostic can be pretriggered by comparing a desired time to the time in the counter. When the counter time is less than or equal to the preset time the comparator provides a trigger to the diagnostic. The comparator must be inhibited from operation until after the signal from photodiode PD2 is received.

Figure (2.17) is a block diagram of the electronics for the velocimeter/diagnostic timer. PD1 and PD2 are the photodiodes that produce a signal when the pellet interrupts their light source. A voltage comparator/pulse generator follows the photodiodes. The signal from the photodiodes is typically 30-300 mV and must be cleaned up and amplified to be compatible with the rest of the velocimeter, which is all transis-

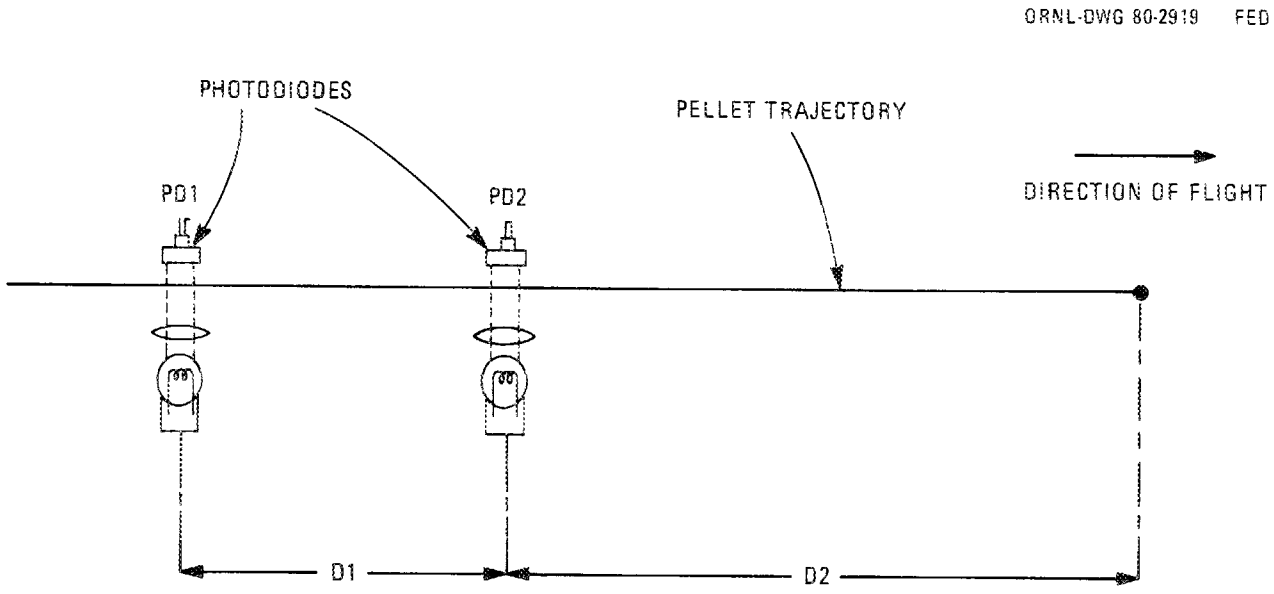

Fig. 2.16 Schematic to illustrate principle of velocity-dependent digital diagnostic timer.

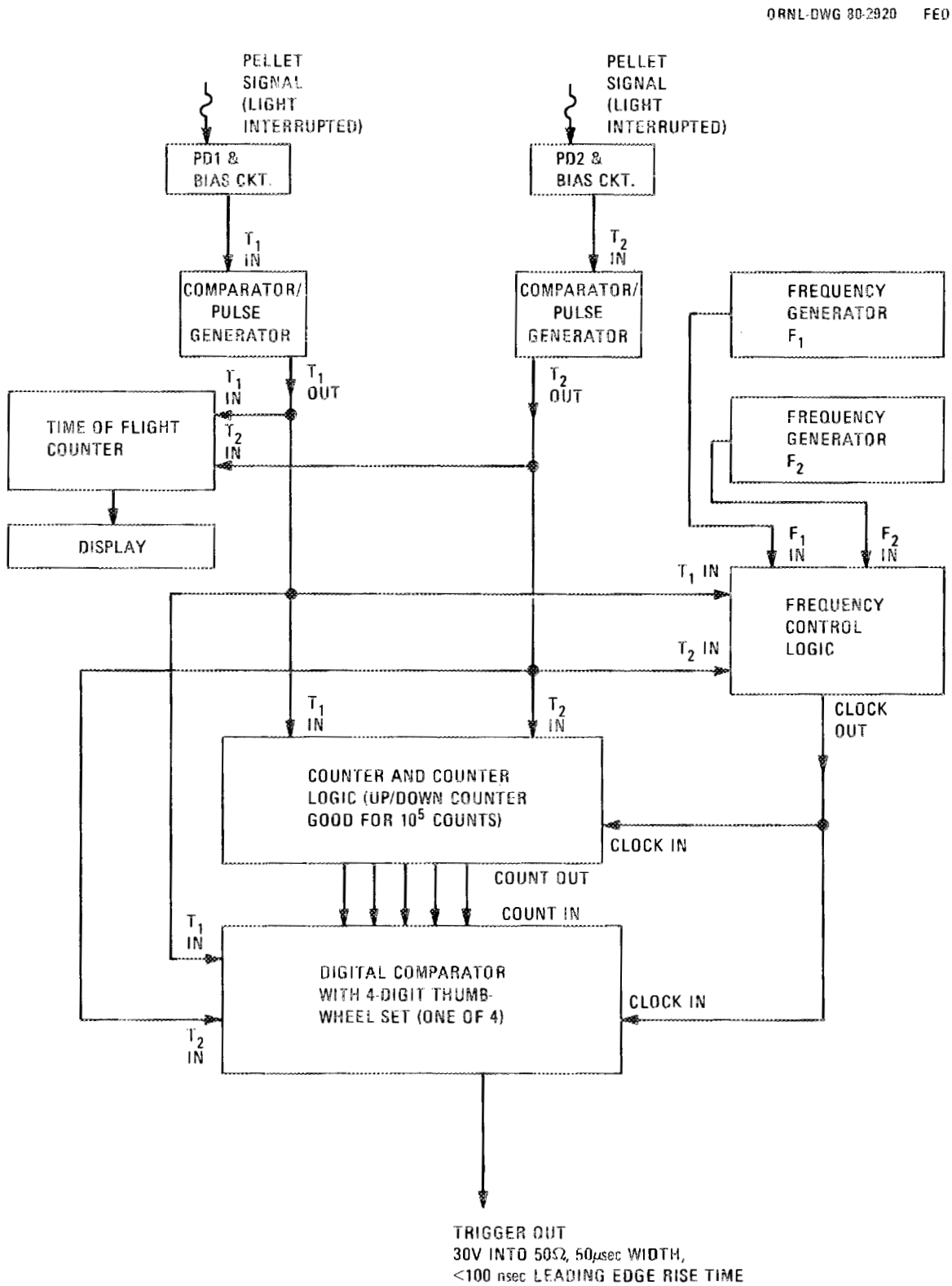

Fig. 2.17 Block diagram of velocimeter/velocity-dependent digital diagnostic timer.

tor-transistor logic (TTL). The comparator/pulse generator is designed to put out a TTL-compatible 5-V, 20-ms pulse when it receives a signal voltage above its comparator threshold. The comparator threshold is adjustable from 10-500 mV. The frequency generators F_1 and F_2 feed into the frequency control logic. When a T_1 pulse is received (from PD1) the frequency control logic uses F_1 for the clock pulse until a T_2 pulse is received (from PD2). After T_2 is received the frequency control logic uses F_2 for the clock pulse. The digital counter starts counting clock pulses when signal T_1 is received. When T_2 is received the counter reverses mode and starts counting down every time a clock pulse is received. The counter changes state on the leading edge of each clock pulse. On the trailing edge of each clock pulse the digital comparator compares the number in its storage register (four-digit thumbwheel set) with the number in the counter. If the number in the counter is less than or equal to the number in the comparator and if both pulses T_1 and T_2 have been received, then the comparator fires its trigger pulse to whatever diagnostic is desired. There are four comparator boards and therefore four possible triggers.

Pulses T_1 and T_2 are also used to start and stop a time-of-flight counter, which uses a 1-MHz crystal oscillator to count the time of flight, in μs, between T_1 and T_2. This provides a measurement of the pellet velocity on each shot.

For the experiment on ISX-B the distance between PD1 and PD2 was 1.138 m $\pm$ 1 mm and the distance from PD2 to the centerline of the torus (nominal plasma center) was 2.425 m $\pm$ 5 mm.

The velocimeter performed quite well during the experiments. Frequency F_2 was set at 5 MHz, and frequency F_1 was varied around 10 MHz to achieve the desired timing. The measured maximum jitter in the pellet position was 15 mm, and the standard deviation of the jitter was 6 mm for 20 vacuum shots (pellet fired into the torus with no plasma), corresponding to a jitter in timing of $\sim$6 μs. The jitter inherent in the system is one clock pulse or 0.2 μs. The difference between the inherent jitter in the system and the observed jitter is attributed to the nonuniform illumination of the photodiodes and the finite slit width of the photodiodes, resulting in a jitter in T_1 and T_2 of 2-3 μs each.

The author would like to acknowledge the contribution to this design of Dr. M. L. McKinstry, who suggested the basic principle for the velocimeter/timer and helped with several of the circuits. Dr. McKinstry was a graduate student with the author at M.I.T. at the time of the velocimeter construction and now does research at the National Bureau of Standards in Washington, D.C.

2.3.9 Experimental performance of the interferometer

Figure 2.18 shows a vacuum (no pellet or plasma in the torus) interferogram replayed at three magnifications. As previously discussed, the background fringes are produced by tilting a mirror between the two laser pulses that form the interferogram. The point of this

ORNL-DWG 80-2921 FED

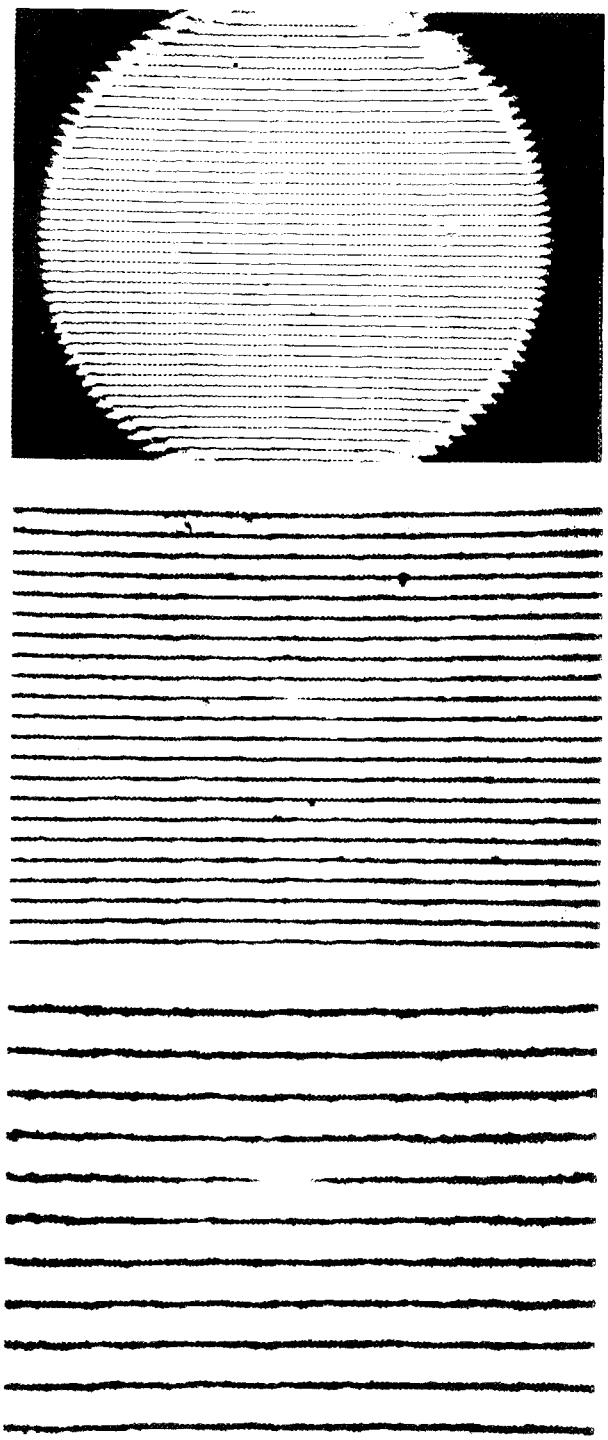

Fig. 2.18 Vacuum holographic interferogram replayed at three different microscope magnifications.

figure is that the fringes are clear and bright and that there are no broken, split, or irregular fringes. Noise is present on the fringes at about the 0.1-fringe level. The alert reader will notice a small systematic curvature of the fringes at the top of each photo. This is not part of the interferogram but is attributed to the lens of the polaroid camera affixed to the microscope used for replay. This curvature is present on all of the interferograms presented in this work and contributes a systematic error of $\sim$0.1 fringe at the upper portion of the interferogram.

Although not shown, replay of the outer 5 mm of any interferogram would reveal a large irregularity and curvature of the fringes due to lens error and diffraction. This portion of any interferogram was unusable. The circular aperturing on the 7.5-X photograph is produced by the microscope input optics and is not caused by the edge of the hologram.

Figure 2.19 is an interferogram of a metal target suspended on a fine wire and inserted into the field of view of the interferometer in the torus. The target was on the order of 1 mm by 1 mm and the wire was approximately 75 μm thick. The fact that the wire is visible places an upper limit of $\sim$70 μm on the experimental resolution of the interferometer. As will be seen in viewing the pellet interferograms, the experimental resolution is probably closer to 30 μm. The diffraction-limited resolution of the interferometer previously discussed would be $\sim$15 μm.

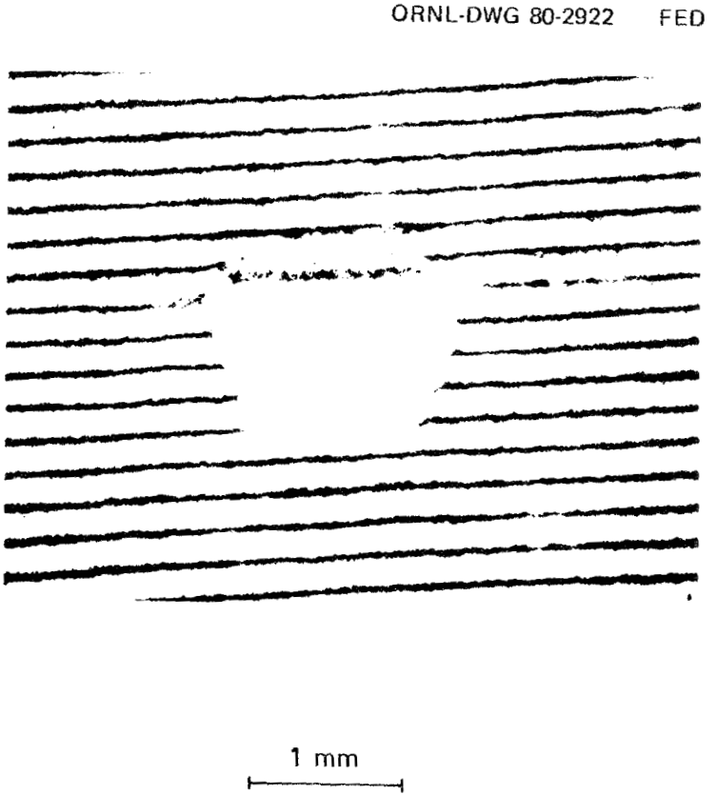

Fig. 2.19 Interferogram of 1-mm by 1-mm metal target in vacuum chamber of tokamak.

2.4 Summary of Chapter 2

In Sect. 2.1 the ISX-B tokamak and its diagnostics were described. Section 2.2 discussed the pneumatic hydrogen pellet injector.

Section 2.3 went over briefly the theory of holographic interferometry and detailed the design and construction of the interferometer systems. In particular, Sect. 2.3.7 calculated the magnification errors inherent in the system if the pellet is not at the focus of the interferometer. It was shown that a 5.6-cm difference in the pellet position and the interferometer focus could lead to a magnification error of $M \sim 1.4$ in replaying the hologram. Also, Sect. 2.3.8 described the timing and firing systems and presented the experimental result of a 6-μs jitter in the time of triggering the interferometer laser. Section 2.3.9 discussed the experimental performance of the interferometer as a whole and gave experimental evidence for a lower limit of ∿70 μm on the interferometer resolution but indicated that the interferograms to be presented later will show that the experimental resolution is ∿30 μm compared with a diffraction-limited resolution of 15 μm.

References

1. D. W. Swain, T. E. Smith, D. J. Sigmar, and M. Murakami, Proposal for a Major Modification to the ISX Tokamak to Study Equilibrium And Stability of Externally Heated High-Beta Plasmas in Noncircular Geometry, ORNL/TM-5985, Oak Ridge National Laboratory, Oak Ridge, Tennessee (1977).

2. D. P. Hutchinson, P. A. Staats, K. L. VanderSluis, and J. B. Wilgen, A Multichannel Submillimeter Interferometer for Tokamak Density Measurements, ORNL/TM-7015, Oak Ridge National Laboratory, Oak Ridge, Tennessee (1979).

3. S. L. Milora and C. A. Foster, Rev. Sci. Instrum. 50, 482 (1979).

4. D. Gabor, Proc. Roy. Soc. London Ser. A A197, 459 (1949).

5. E. Leith and J. Upatnieks, J. Opt. Soc. Am. 52, 1123 (1962).

6. E. Leith and J. Upatnieks, J. Opt. Soc. Am. 53, 1377 (1963).

7. J. B. DeVelis and G. O. Reynolds, Theory and Application of Holography, Addison-Wesley, Reading, Massachusetts, 1967.

8. L. O. Heflinger, R. F. Wuerker, and R. E. Brooks, J. Appl. Phys. 37, 642 (1966).

9. F. C. Jahoda, R. A. Jeffries, and G. A. Sawyer, Appl. Opt. 6, 1407 (1967).

10. F. C. Jahoda and R. E. Siemon, Holographic Interferometry Cookbook, LA-5058-MS Informal Report UC-37, Los Alamos Scientific Laboratory, Los Alamos, New Mexico (1972).

11. C. M. Vest, Holographic Interferometry, John Wiley and Sons, New York, 1979.

12. A. Yariv, Introduction to Optical Electronics, Holt, Rinehart, and Winston, New York, 1971.

Chapter 3

Theory

3.1 A Brief Review of the Existing Theoretical Work on Hydrogen Pellet Ablation in High-Temperature Plasmas

The refueling of fusion reactors by the injection of liquid or solid hydrogen was first proposed by Spitzer et al.,[1] and they also made theoretical estimates of the pellet ablation rate. In making their estimate, they considered many of the processes that are fundamental to more recent theories. In particular, they mention shielding of the pellet from the incident plasma energy flux by the ablated neutral molecules and ions, possible negative charging (electrostatic shielding) of the ablatant and pellet, and retardation of the ionized ablatant flow across the magnetic field. The following quote from this work is particularly pertinent:

> The direct conclusion is that a cloud of cool gas due to vaporization would form immediately and act as a shield for the enclosed globule. This neutral molecular gas cloud would then suffer ionization and dissociation, thereby attenuating the energy of the impinging plasma particles, and creating a local ionized cloud developing out of the neutral one.

In 1968 an additional shielding mechanism was proposed by Rose,[2] who assumed that the ablated material from the pellet would form a dense, highly ionized blanket around the pellet and that this dense, highly ionized plasma would exclude the magnetic field. Because incident-particle trajectories would now be directed around the pellet,

ablation would be due to heat conduction to the pellet through the ablation cloud from the background plasma.

Chang[3] modified Rose's zero-dimensional (0-D) model by making it 1-D and assuming that the magnetic field would partially penetrate the ablated pellet material. Other magnetic shielding models were proposed by Politzer and Thomas[4] and by Lengyel.[5]

Gralnick[6] assumed that the material ablated from the pellet would be fully ionized, neglected magnetic field effects, and considered shielding of the pellet by the slowing down of the incident hot plasma particles on the cold, dense, ablated plasma surrounding the pellet.

The shielding theories that have most successfully described experimental results to date are the neutral shielding models. Vaslow[7] and Parks, Turnbull, and Foster[8] independently developed scaling laws that are almost identical. These models assume that the material ablated from the pellet comes off as neutral gas and that the incident hot plasma particles lose most of their energy through inelastic and elastic collisions with the neutral gas.

The neutral shielding model was modified by Parks and Turnbull[9] and independently by Milora and Foster[10] to account for the effects of supersonic flow as the ablated material streamed away from the pellet. The scaling laws developed are very similar. The scaling law given by Parks and Turnbull for plasma temperatures in the range 1-30 keV is

$$G = 4\pi r_p^2 n_s \dot{r}_p \text{ (atoms/s)},$$

$$\dot{r}_p = 8.94 \times 10^{14} r_p^{-2/3} n_{eo}^{1/3} T_{eo}^{1.64} n_s^{-1} \text{ (cm/s)}, \qquad (3.1)$$

where

$G \equiv$ ablation rate (atoms/s),

$n_s \equiv$ density of solid hydrogen (atoms/cc) $\simeq 5.2 \times 10^{22}$,

$r_p \equiv$ pellet radius (cm),

$n_{eo} \equiv$ background plasma density (cm^{-3}), and

$T_{eo} \equiv$ background plasma temperature (eV).

The results of Milora and Foster are essentially the same.

The neutral shielding model was extended by Felber et al.[11] to include the effects of ionization, dissociation, and radiation. They calculated that additional energy absorbed by these processes extended pellet lifetimes by 10-20%.

Parks[12] and Gilliard and Kim[13] extended the neutral shielding model to include the effects of decrease of incident plasma power due to the exclusion of the magnetic field by the ablatant flow. Their calculations show these effects to be modest, increasing pellet lifetimes only fractionally.

Milora et al.[14] have recently developed a "self-limiting" ablation model that accounts for the perturbative effects of massive pellet injection on the background plasma. This model assumes that the material ablated from the pellet cools the background plasma.

3.2 Discussion of Existing Theories in the Light of Experimental Work

The earlier theories of pellet ablation were plasma physics models. They assumed that the fuel pellet was immediately immersed in a fusion plasma and that the ablatant was completely ionized as it left the pellet and therefore predicted ablation rates much smaller than seen experimentally in any plasma to date. These models were developed for high-T_e cases for which the assumption of ionization is likely to be correct.

The neutral shielding models go to the other extreme; they assume that the ablatant does not become ionized until it is so far from the pellet surface that it no longer matters, which is probably true for low T_e.

The work of Felber et al., Parks, and Gilliard and Kim, makes an excellent attempt at marrying the atomic physics and plasma physics aspects of the problem. However, the recent experimental data from ISX-B, to be presented in Chaps. 4 and 5, show that there is a difficulty with their models. They assume that the ionization fraction of the ablated material can be calculated from the Saha equilibrium equation using a single-temperature model. These calculations based on Saha equilibrium show that the ionization fraction close to the pellet surface is negligibly small. In Chap. 5 it will be shown from experimental data that the average ionization fraction of the ablatant near the

pellet surface is ∿20%. It seems that there is trouble with the way the ionization fraction is being calculated. The models should probably be extended to allow for a separate electron temperature, or else the ionization fraction should be calculated by equating the rates of ionization and recombination at a given radius.

The significance of the high ionization fraction is in the exclusion of the magnetic field and also in the retardation of the ablatant flow across the magnetic field. If the ablatant is forced to stream away in one or one and one-half dimensions, rather than three, there will be more ablated material shielding the pellet from the hot background plasma. Exclusion of magnetic flux will force some of the incident hot plasma particles to stream around rather than through the ablated material.

References

1. L. Spitzer, D. J. Grove, W. E. Johnson, L. Tonks, and W. E. Westendorp, Problems of the Stellerator as a Useful Power Source, USAEC Report NYO-6047, Princeton University, Princeton, New Jersey (1954).
2. D. J. Rose, On the Fusion Injection Problem, Culham Laboratory Technology Division Memorandum No. 82 (1968), unpublished.
3. C. T. Chang, Nucl. Fusion 15, 595 (1975).
4. P. A. Politzer and C. E. Thomas, Jr., p. 94, Proc. Fusion Fueling Workshop, NTIS USDC CONF-771129, Princeton, New Jersey (1978).
5. L. L. Lengyel, Phys. Fluids 21 1945 (1978).
6. S. L. Gralnick, Nucl. Fusion 13, 703 (1973).
7. D. F. Vaslow, IEEE Trans. On Plasma Science PS-5, 12 (1977).
8. P. B. Parks, R. J. Turnbull, and C. A. Foster, Nucl. Fusion 17, 539 (1977).
9. P. B. Parks and R. J. Turnbull, Phys. Fluids 21, 1735 (1978).
10. S. L. Milora and C. A. Foster, IEEE Trans. on Plasma Science PS-6, 578 (1978).
11. F. S. Felber, P. H. Miller, P. B. Parks, R. Prater, D. F. Vaslow, Nucl. Fusion 19, 1061 (1979).
12. P. B. Parks, Magnetic Field Effects on Plasma-Pellet Ablation Rates, General Atomic Report GA-A15042, General Atomic Project 2101, General Atomic Corporation, San Diego, California (1978).

13. R. P. Gilliard and K. Kim, The Significance of Magnetic Shielding in the Ablation of a Solid Hydrogen Pellet in a Plasma, preprint of work to be published, Fusion Technology Laboratory, Department of Electrical Engineering, University of Illinois, Urbana, Illinois (1979).

14. S. L. Milora et al., Results of Hydrogen Pellet Injection into ISX-B, submitted to Nucl. Fusion.

Chapter 4

Experimental Results

4.1 Introduction

The purpose of this chapter is to present the general conditions of the experiment and the experimental results. The data are presented with as little manipulation as is reasonable. Analysis of the data will be presented in the next chapter.

The interferometer and pellet gun were first operated together on ISX-B on May 16, 1979, and experiments continued until November 11, 1979. During this period the interferometer and pellet gun were operated ten days when the tokamak was running. On several of those days only a few shots were taken with pellets/interferometry, and on several others the Thomson scattering laser was inoperative. On three days (September 5, 6, and 11) the pellet gun, interferometer, tokamak, and Thomson scattering laser were all operative so that a well-characterized and diagnosed experiment was performed. Unfortunately, the interferograms from September 5 did not come out because of misalignment of the reference beam. The data presented will be from September 6 and 11, 1979.

Fifteen interferograms and associated data will be presented from the September 6 experiment. Two of these are actually taken from a very similar experiment on August 2, when the interferometer was in a different spatial location. The September 6 sequence was at relatively low

electron density and high electron temperature, $\bar{n}_e = 0.8 \times 10^{19}$ m^{-3} and $T_e(r = 0) = 1500$ eV. On this date runaway electrons were present in the discharge on most of the shots. The pellets were generally stopped well short of the magnetic center of the plasma, and a stable high-density plasma was achieved after pellet injection.

The September 11 run was made at a higher electron density and lower electron temperature, $\bar{n}_e = 3.2 \times 10^{19}$ m^{-3} and $T_e(r = 0) = 1$ keV. Eighteen interferograms and associated data will be presented from this sequence. In general, the pellet went all the way past the center of the plasma and was stopped on the far side. Large density increases were seen, but the plasma always exhibited large-scale MHD oscillations (minor disruptions) within 10 ms after pellet injection. Whether the MHD oscillations were due to injection of the pellet or were simply the result of exceeding the stable operating parameters of the machine is unknown.

4.2 Data from September 6, 1979 (Low $\bar{n}_e$, High T_e)

4.2.1 Thomson scattering data from September 6

As discussed previously, the Thomson scattering system on ISX-B has a four-pulse ruby laser. This means that on any single tokamak shot it is possible to get data from one spatial location at four different times during the discharge. The entire laser system can be moved between discharges to look at different spatial locations. A trigger was

provided to the Thomson scattering laser from the velocimeter/timer so that the timing of the Thomson scattering laser system with respect to the arrival of the pellet in the plasma was repeatable within ∿5 μs.

Figure 4.1 shows electron density and temperature profiles made 1 ms prior to pellet injection for the September 6, 1979, sequence. The nominal pellet injection timing was at 96 ms into the discharge. The discharge current was 113 kA, the magnetic field on axis was 1.5 T, the line-averaged electron density was 0.8×10^{19} m^{-3}, and the safety factor q at the limiter was 5.1. The plasma Z_{eff} inferred from Thomson scattering was 7.1 (high Z_{eff} due to vacuum opening immediately before). All of the Thomson scattering data are presented courtesy of E. A. Lazarus, P. H. King, and M. Murakami of ORNL.

Figure 4.2 shows the electron density and temperature 1 ms after pellet injection for the September 5 and 6, 1979, sequence. These sequences were almost exactly alike. Because the pellets were stopped short of the center, the density profile is hollow. Later in time it will fill in the center. Similarly, the electron temperature is peaked at the center. Because the pellet did not reach the center, the center was not cooled as much as the outer regions of the plasma. The data from the September 5 sequence are included because it has a central data point whereas the September 6 sequence does not. The error bars shown on the Thomson scattering data are from photon-counting statistics.

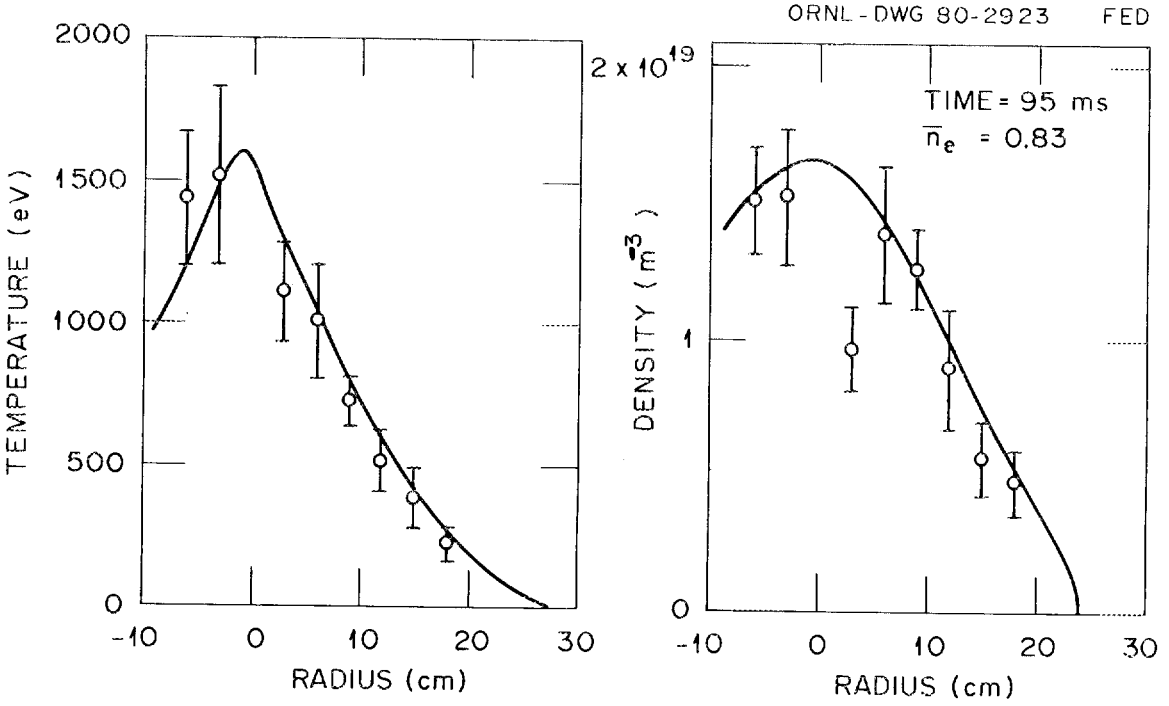

Fig. 4.1 Thomson scattering electron density and temperature 1 ms before pellet injection, sequence of September 6, 1979.

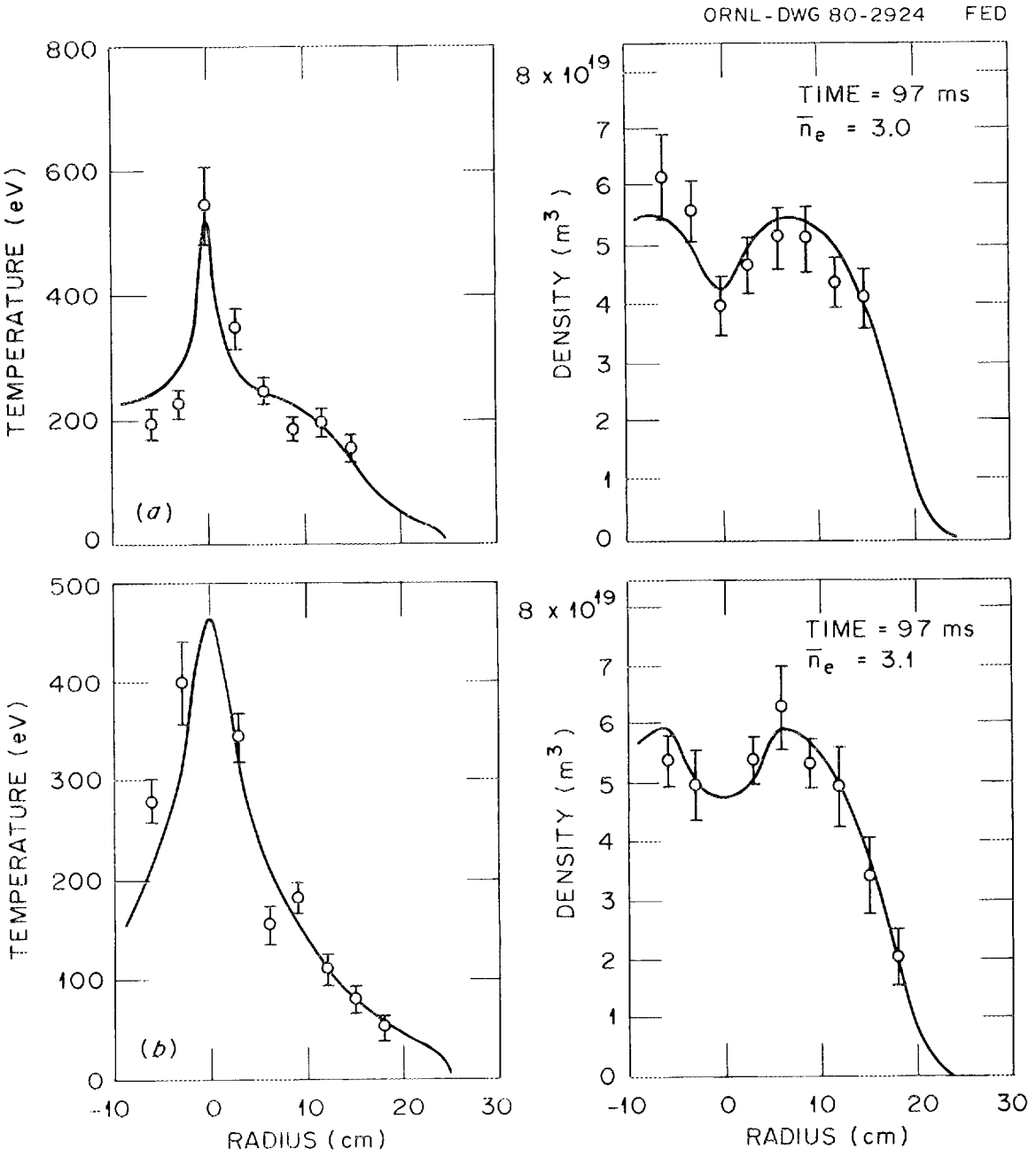

Fig. 4.2 Thomson scattering electron density and temperature 1 ms after pellet injection, sequence of September 5 and 6, 1979.

4.2.2 Line-averaged density data from September 6

During the experiments three interferometers were operative on the tokamak. There were microwave interferometers with vertical and horizontal paths through the plasma and a FIR interferometer with a vertical path through the plasma. The two microwave interferometers operated at a wavelength of 2 mm, and the FIR interferometer operated at a wavelength of ∿400 μm. The cutoff density was $\sim 2.8 \times 10^{20}$ m^{-3} for the microwave interferometers and $\sim 7 \times 10^{21}$ m^{-3} for the FIR interferometer. The horizontal microwave interferometer could respond to a maximum density rate of change of $\bar{n}_e = 1.0 \times 10^{23}$ m^{-3} s^{-1}, the vertical microwave interferometer could respond to a maximum density rate of change of $\bar{n}_e = 2.0 \times 10^{24}$ m^{-3} s^{-1}, and the FIR interferometer could respond to a maximum density rate of change of $\bar{n}_e = 1.0 \times 10^{24}$ m^{-3} s^{-1}.

Typical density changes for September 6, 1979, were $\Delta\bar{n}_e = 2.4 \times 10^{19}$ m^{-3} in 200 μs. This means that the horizontal interferometer normally could not follow the density change. As previously discussed, the configuration of the poloidal field system used in this experiment produces slightly elongated plasmas. The ratio of the fringe shifts from the vertical microwave interferometer to the horizontal interferometer just before pellet injection gives the elongation. For September 6 and 11, 1979, the elongation was 1.2. Because of this elongation a 64.8-cm path length is assumed for the vertical interferometer.

Figure 4.3 shows three typical plots of density versus time for pellet injection on September 6, 1979. All interferometer data are courtesy of J. Wilgen and D. Hutchinson of ORNL.

The upper and middle plots of Fig. 4.3 are vertical 2-mm microwave data, and the bottom plot is FIR data. The "noise" on the FIR data is the result of mechanical vibration. On shots where the pellet penetrated deep into the plasma center, only the FIR interferometer could follow the density change. The 2-mm systems lost signal due to refraction and reflection.

Figure 4.4 is a typical 2-mm density trace from September 6 without pellet injection. The point of interest on the density data is the maximum $\bar{n}_e$ immediately following pellet injection. In the next chapter the measured $\bar{n}_e$ from the interferometer will be compared with the $\bar{n}_e$ calculated by inferring a pellet ablation rate from Balmer-alpha (H_α) light emitted by the pellet as it ablated.

Table 4.1 lists shot numbers and maximum $\bar{n}_e$ seen by the FIR or microwave interferometer immediately after pellet injection.

4.2.3 Local energy loss during pellet injection

A pyroelectric radiometer was located underneath the same sector where the pellet injector was installed on ISX-B. A pyroelectric detector is sensitive to incident power; therefore, the pyroelectric radiometer measured all local power loss, both radiation and charge

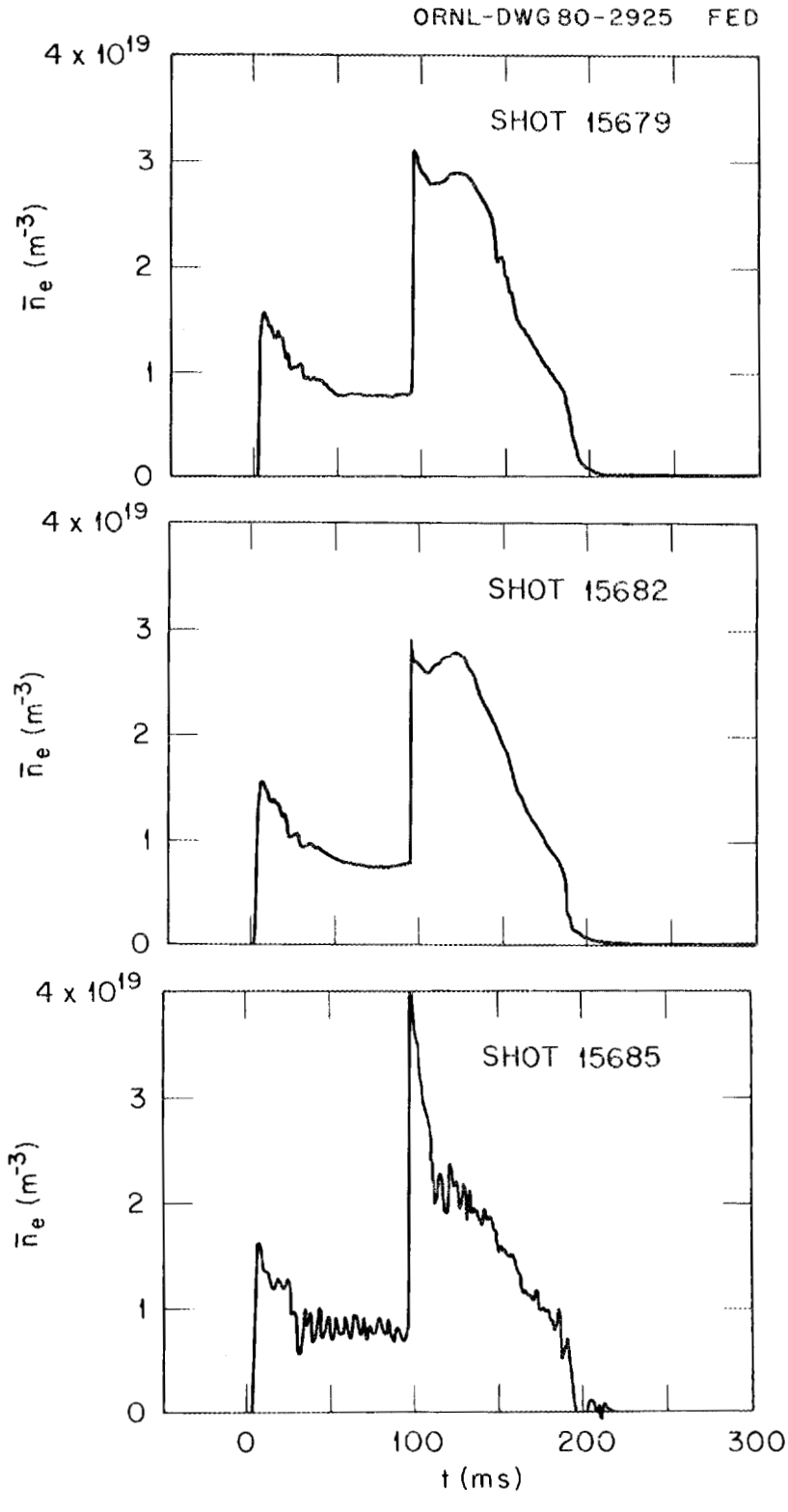

Fig. 4.3 Line-averaged density vs time for three shots from September 6, 1979, with pellet injection.

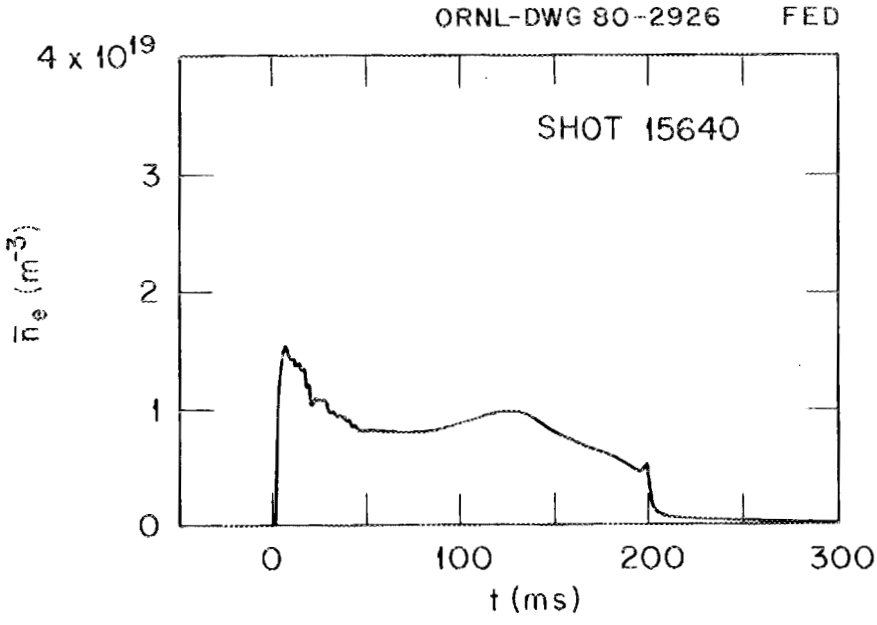

Fig. 4.4 Typical $\bar{n}_e$ density plot vs time without pellet injection from September 6, 1979.

Table 4.1. Line-averaged density immediately before and after pellet injection, sequence of September 6, 1979

Shot number[a]	$\bar{n}_e$ (prepellet) ($\times 10^{19}$ m^{-3})	$\bar{n}_e$ (postpellet) ($\times 10^{19}$ m^{-3})	$\Delta\bar{n}_e$ ($\times 10^{19}$ m^{-3})
15633*	0.9	3.3	2.4
15638*	0.8	3.9	3.1
15639*	0.8	3.3	2.5
15641*	0.9	2.9	2.0
15642	0.8	4.3	3.5
15643	0.9	4.2	3.3
15644*	0.8	2.9	2.1
15646	0.8	2.9	2.1
15647	0.9	3.5	2.6
15649*	0.8	3.3	2.5
15651*	0.9	3.3	2.4
15656*	0.9	3.3	2.4
15657	0.8	4.2	3.5
15661	0.9	2.4	1.5
15664*	0.8	2.5	1.7
15665*	0.8	2.8	2.0
15667	0.9	3.8	2.9
15668*	0.9	2.8	1.9
15669	0.8	3.9	3.1
15672*	0.9	3.0	2.0
15678	0.8	3.0	2.0
15679	0.8	3.1	2.3
15681*	0.8	2.9	2.1
15682*	0.8	2.9	2.1
15683*	0.9	3.3	2.4
15685	0.8	4.0	3.2
15686*	0.8	3.1	2.3
15687	0.9	2.5	1.6
15690	0.8	2.2	1.4
15697	0.8	3.1	2.3

$(\bar{n}_e)\text{AVG} = (3.2 \pm 0.6) \times 10^{19}$ m^{-3}

$(\bar{n}_e)^*\text{AVG} = (3.1 \pm 0.3) \times 10^{19}$ m^{-3}

$(\Delta\bar{n}_e)\text{AVG} = (2.4 \pm 0.6) \times 10^{19}$ m^{-3}

} (Postpellet averages)

[a] * indicates Thomson scattering data taken this shot.

exchange neutrals, during pellet injection.[1] The pyroelectric diagnostic was built and operated by C. E. Bush of ORNL, and all radiometer data are courtesy of him. Figure 4.5 illustrates the geometry of the pyroelectric detector, which was centered underneath the vacuum vessel with a vertical distance to the vacuum vessel centerline of 56 cm and a horizontal distance to the limiter of 27 cm.

A transient-event recorder was not available to record and digitize the data for analysis, so the data are presented and analyzed from oscilloscope traces. Figures 4.6 and 4.7 give six oscilloscope traces showing power emitted by the pellet as it traversed the plasma. The total power emitted by the pellet at time t is

$$P = \frac{dE}{dt} = \frac{4\pi r^2}{A'} \frac{S(t)}{C} , \qquad (4.1)$$

where

r ≡ distance from pellet to detector,

S(t) ≡ radiometer voltage at time t,

C ≡ calibration factor for radiometer = 11.07 V/W,

A′ ≡ effective detector area = A cos (θ), and

A ≡ detector area = 7.07×10^{-6} m^2.

The power scale on the figures is found by assuming r = constant = $[(12)^2 + (56)^2]^{1/2}$ = 57.3 cm and θ = $\tan^{-1}$ (12/56) = 0.211 radians. The lower trace on the figures is from a photodiode detecting the H_α light emitted by the pellet as it traversed the plasma (discussed below).

It can be shown that the error factor in assuming a constant radius is

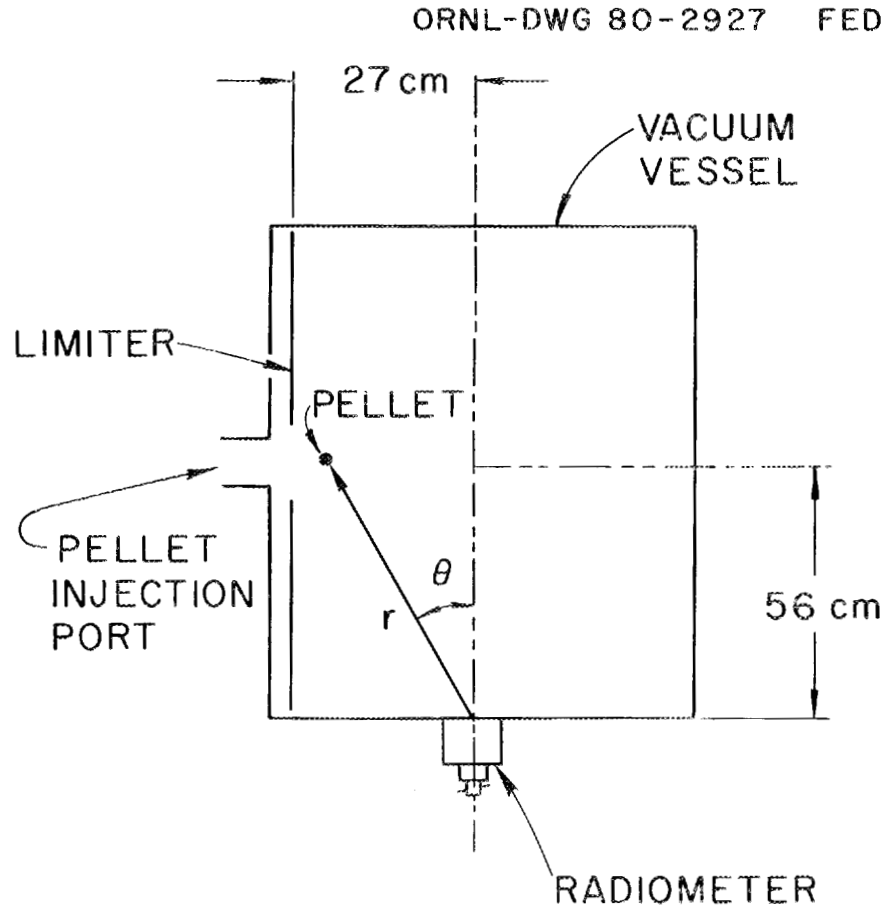

Fig. 4.5 Illustration of pyroelectric detector geometry.

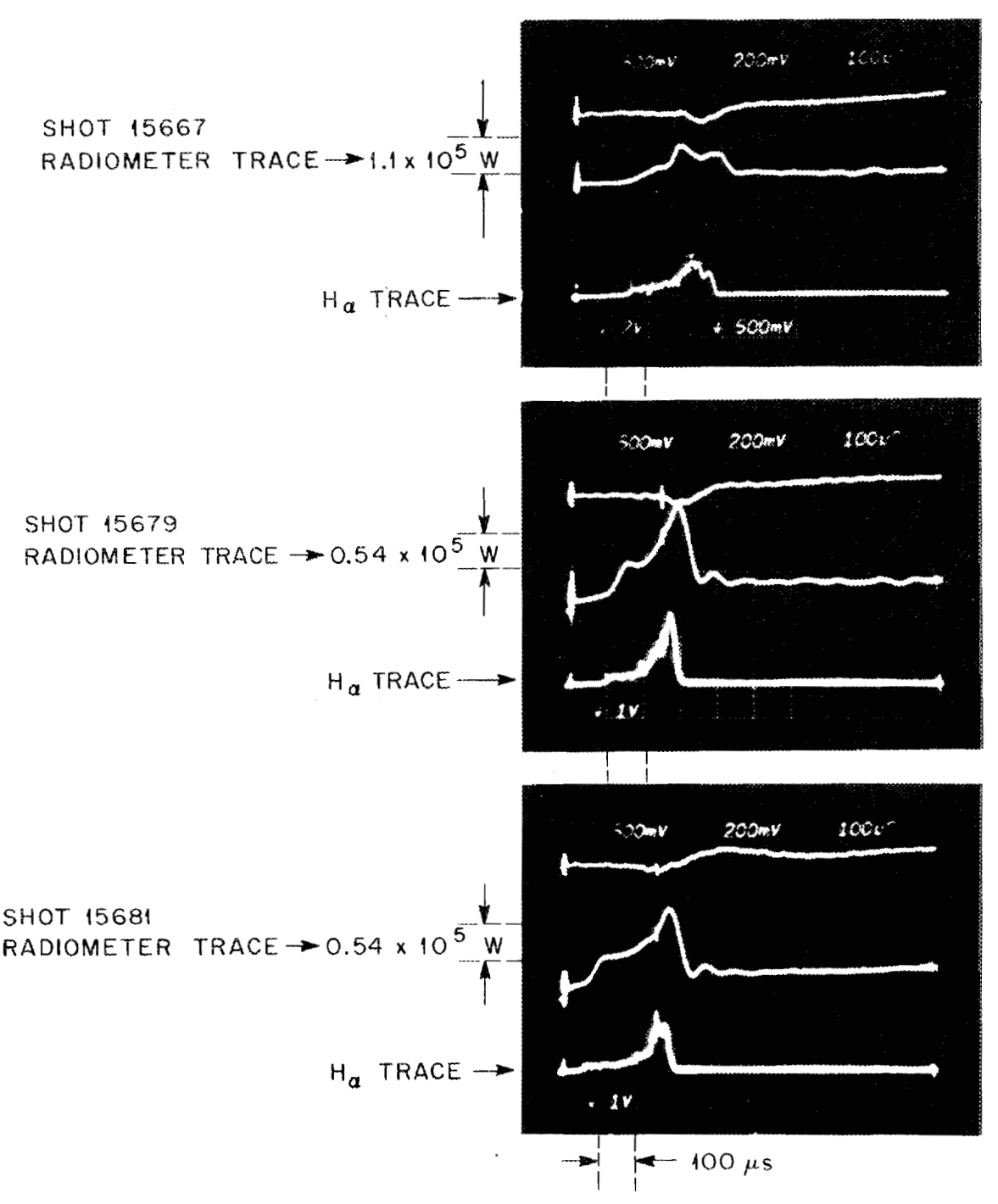

Fig. 4.6 Pellet radiometer data from shots 15667, 15679, and 15681.

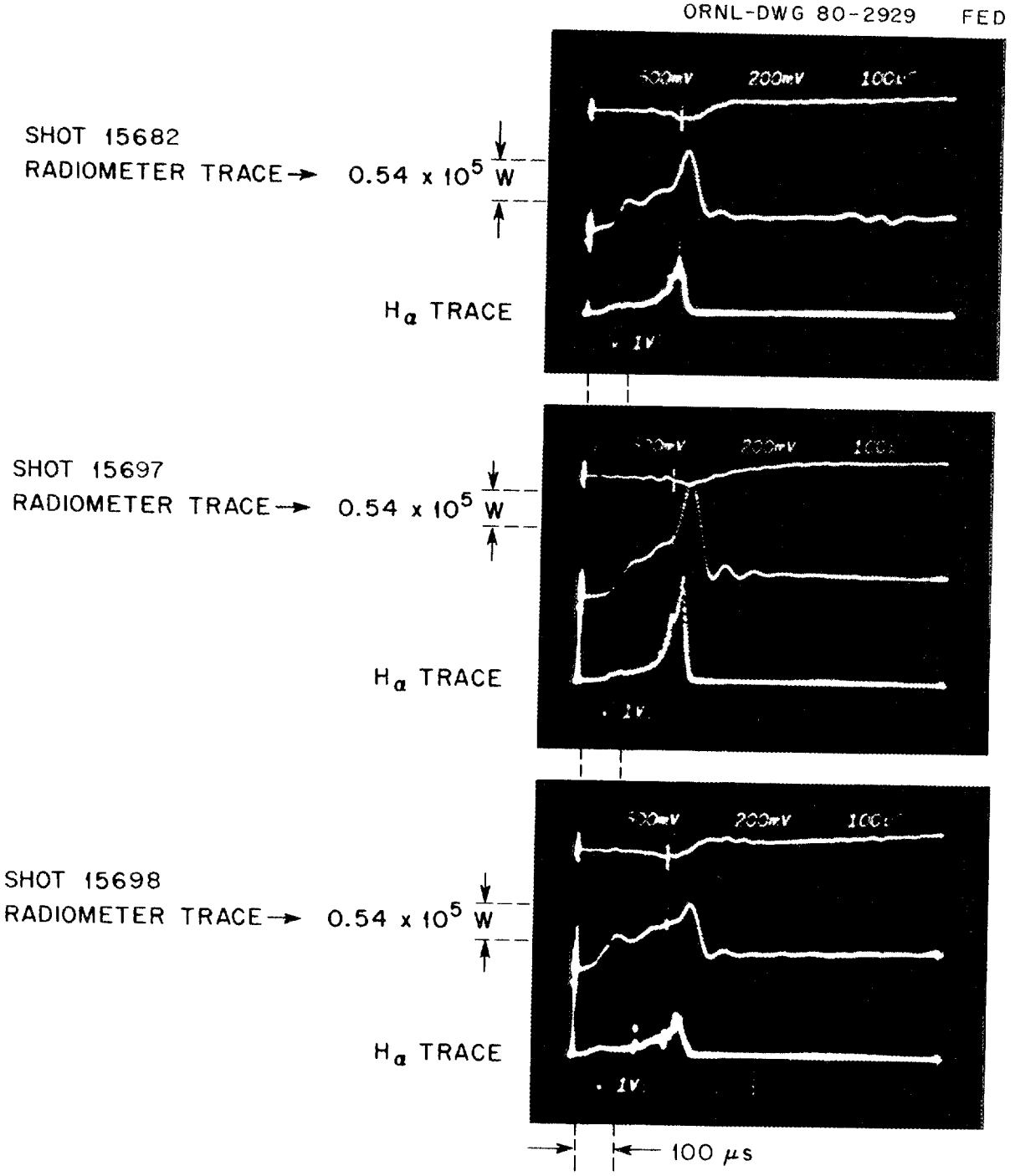

Fig. 4.7 Pellet radiometer data from shots 15682, 15697, and 15698.

$$\Delta \equiv \frac{\text{True power}}{\text{Calculated power } (r = \text{const})} = \frac{\cos^3(\theta')}{d\theta'} \frac{d\theta}{\cos^3(\theta)} , \quad (4.2)$$

where θ is the actual angle to the radiometer and θ' is the angle at $r = r' = \text{constant}$ ($\theta' = 0.211$ radians). The error in the above assumption ranges from $\Delta = 1.28$ at minor radius $a = 27$ cm to $\Delta = 0.93$ at minor radius $a = 0$. The error factor at $a = 12$ cm is $\Delta = 1.00$ (no error).

Table 4.2 gives the local energy radiated during pellet ablation found by integrating the power from Figs. 4.6 and 4.7. The error factor in calculating the energy this way is found by multiplying Eq. (4.2) by the signal strength and integrating

$$\int \Delta = \cos^3(\theta') \int \frac{s(\theta)\, d\theta}{\cos^3\theta} \cdot \left[\int s(\theta)\, d\theta\right]^{-1} . \quad (4.3)$$

If $S(\theta)$ were a constant, the maximum error factor would be (pellet stopped at $a = 7$ cm)

$$\int \Delta = 1.09.$$

Because $S(\theta)$ is peaked near $a = 12$ cm, the actual error in finding the energy this way is less than 10%.

4.2.4 Evidence for runaway electrons in plasma during sequence of September 6, 1979

In order to diagnose the presence of runaway electrons a hard x-ray detector is located on the wall of the ISX-B enclosure. The detector is a scintillation detector and looks at total photon output (it is not a

Table 4.2. Total local radiated energy during pellet injection, September 6, 1979

Shot number	Total local radiated energy (J)
15667	17
15679	18
15681	17
15682	15
15697	21
15698	17

E_{AVG} = (18 +/-2) J

pulse-height analysis or energy spectroscopy system). When runaway electrons impact the limiters of the tokamak, hard x rays are emitted with energy proportional to the runaway electron energy. The ISX-B detector is sensitive to x rays in the 0.5-3 MeV range, and the signal from the detector is proportional to the total number of x rays in this energy range and to their energy spectrum. Hard x-ray data are courtesy of D. W. Swain of ORNL.

Figure 4.8 shows hard x-ray data for five shots from the September 6 sequence when pellets were not injected into the machine. Note the large positive spike at the end of the shot (around t = 180 ms) on three of the traces and a small positive spike on the other two traces.

Figure 4.9 shows hard x-ray data from five shots on September 6 when pellets were injected. Note that there is no hard x-ray spike at the end of the shot nor any associated with the pellet injection at t = 96 ms.

Twenty-two out of thirty shots without pellet injection on September 6 exhibited a hard x-ray spike at the end of the shot. None of the 45 shots with pellet injection on September 6 exhibited a hard x-ray spike at the end of the shot. The inferred result is that pellet injection, like gas puffing, removes runaway electrons from the discharge.

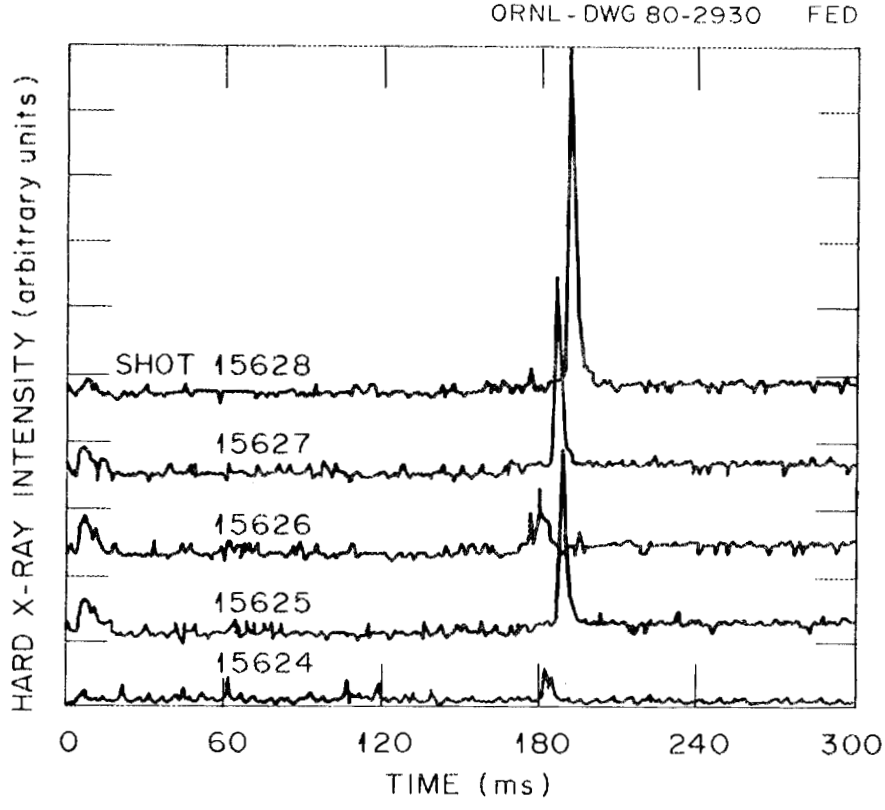

Fig. 4.8 Hard x-ray data for five shots from sequence of September 6 without pellet injection.

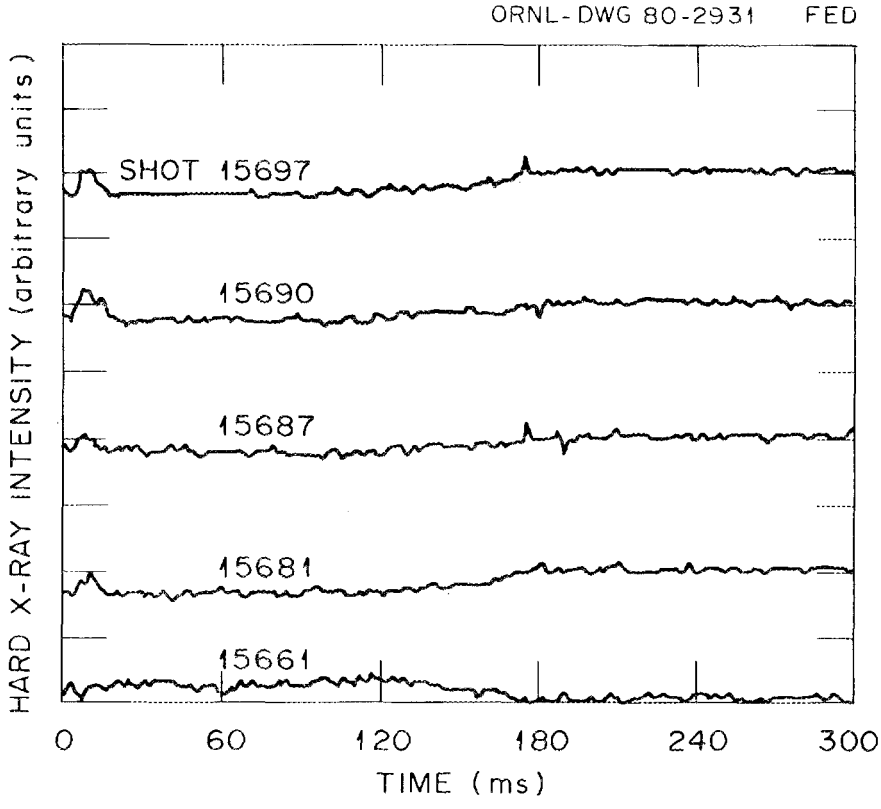

Fig. 4.9 Hard x-ray data for five shots from sequence of September 6 with pellet injection.

4.2.5 Pellet ablation rate inferred from H_α line radiation

Foster et al.[2] first suggested using hydrogen line radiation as a means of inferring pellet ablation rates. The rationale is that the ratios of the cross sections for photon emission and ionizing events are approximately constant over the electron energy ranges of interest.[3,4] To date, this linear relationship has been experimentally found to be correct,[3,4] although it may not continue to be valid as energy densities incident on the pellet rise. The coefficient found by Milora et al.[4] is $\sim$0.02 H_α photons radiated per atom ablated from the pellet.

Figure 4.10 is a schematic of the H_α detector position on ISX-B and its construction. The optics for the detector were designed by the author, and the wideband transimpedance amplifier was designed by J. W. Pearce and S. L. Milora of ORNL.

The output of the H_α detector was recorded with a transient-event recorder at a digitization rate of one data point per microsecond.

Figures 4.11-4.17 show H_α traces from September 6, 1979, for which interferograms were made. The original data have been transformed according to Eq. (4.4) to give ablation rate rather than volts:

$$\frac{dN_H}{dt} = S(t) \frac{(4\pi r^2)}{AC_1} C_2 C_3, \qquad (4.4)$$

where

$N_H \equiv$ atoms of hydrogen in pellet,

$S(t) \equiv H_\alpha$ detector voltage at time t,

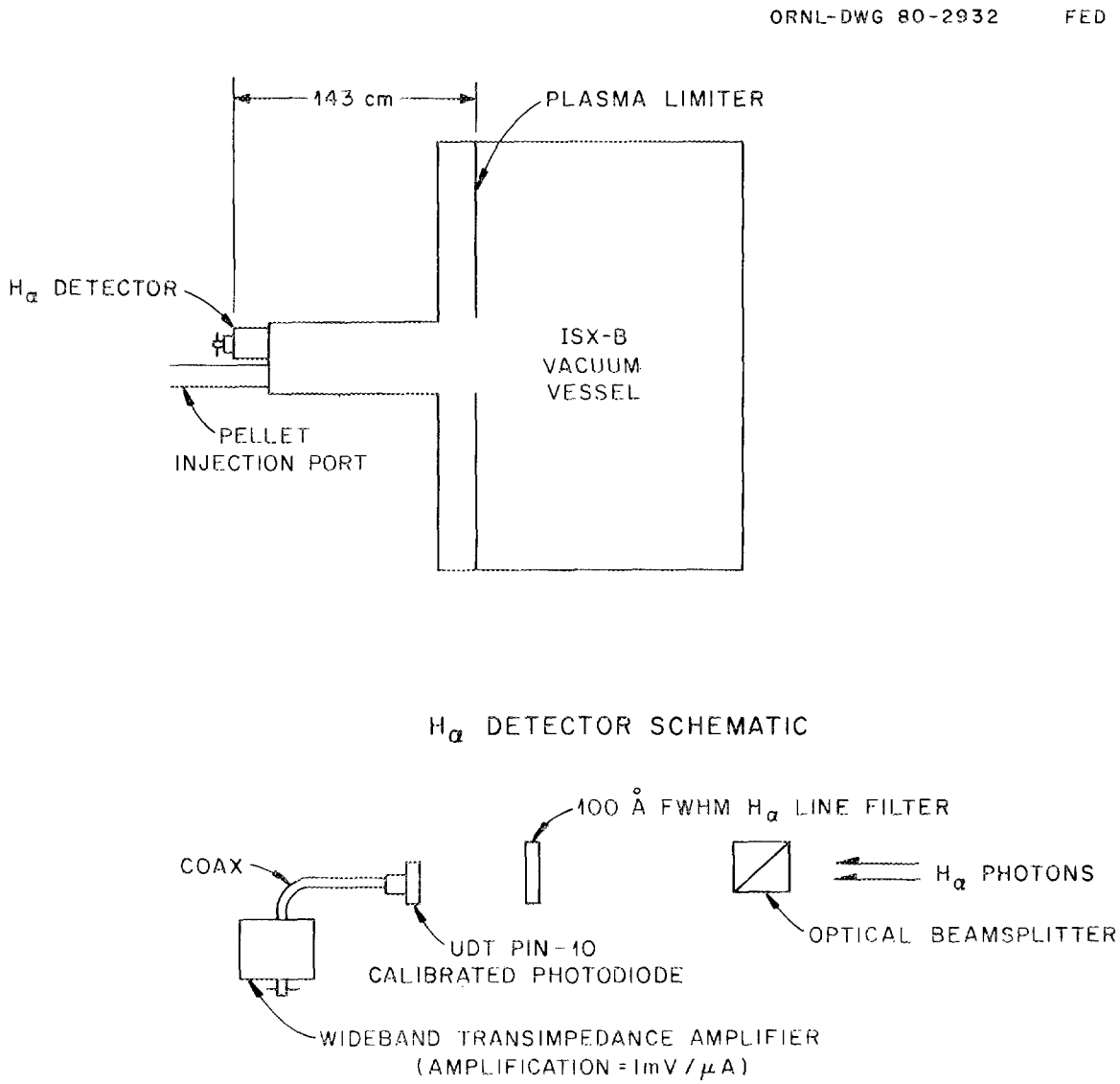

Fig. 4.10 Schematic of H_α detector.

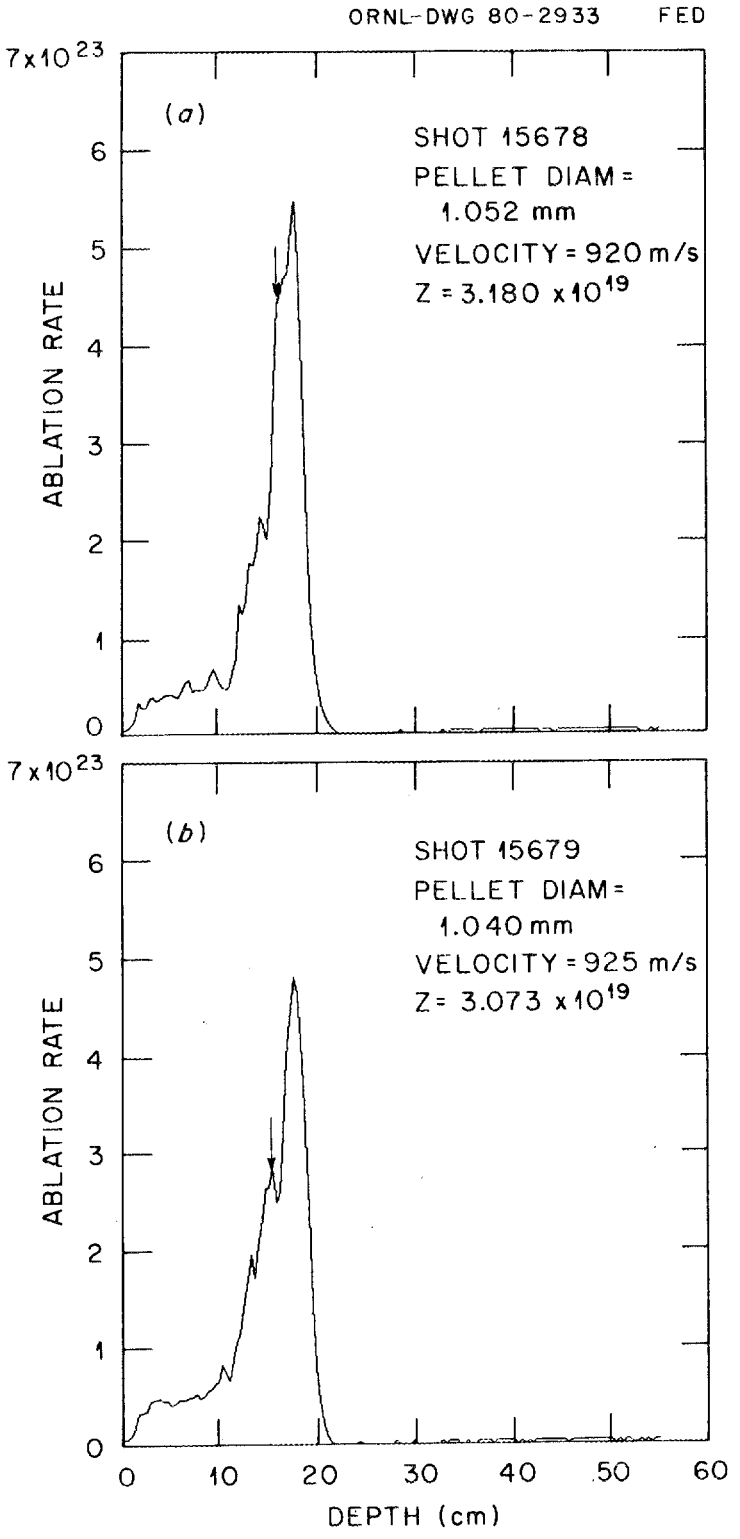

Fig. 4.11 Ablation rate (atoms/s) for shots 15678 and 15679.

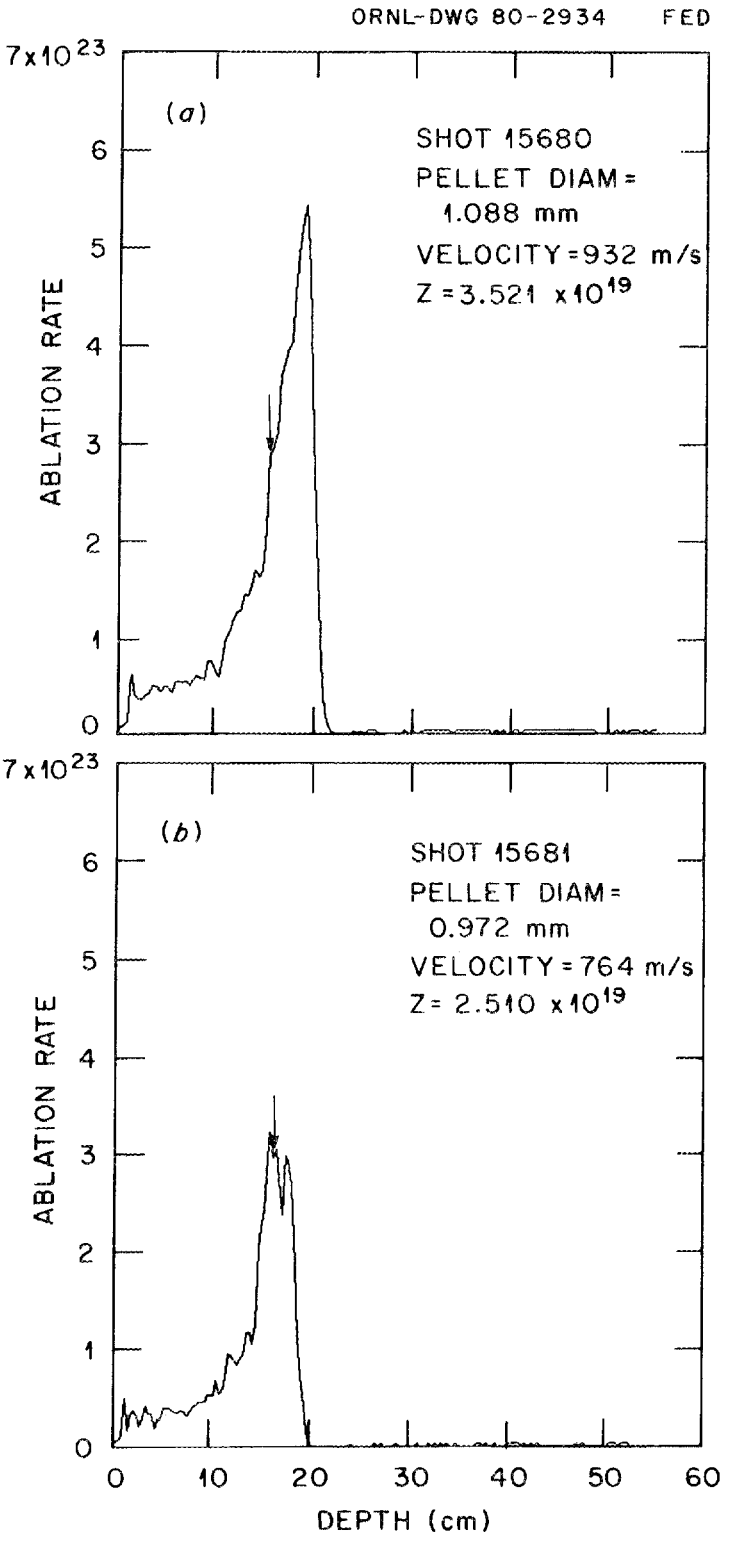

Fig. 4.12 Ablation rate (atoms/s) for shots 15680 and 15681.

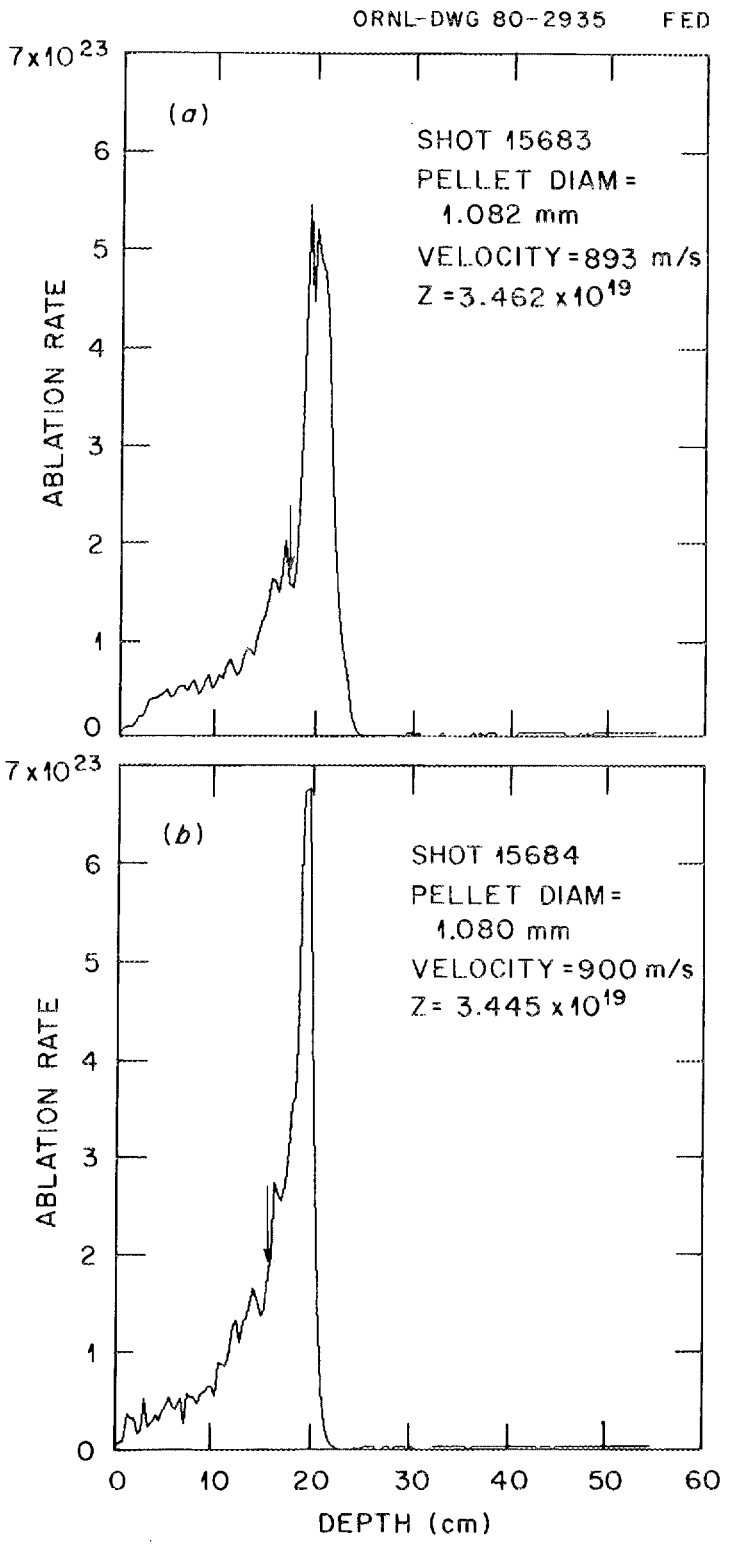

Fig. 4.13 Ablation rate (atoms/s) for shots 15683 and 15684.

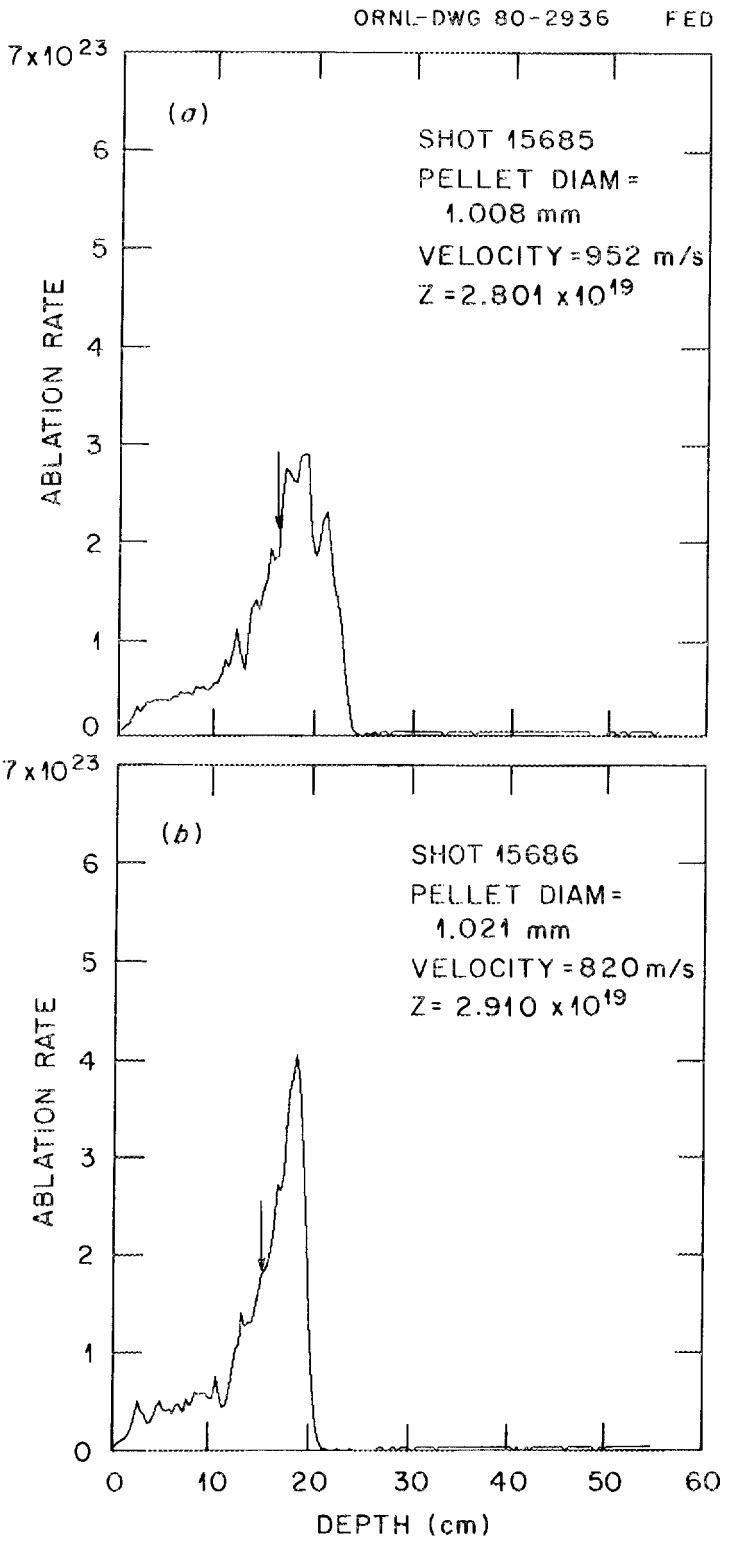

Fig. 4.14 Ablation rate (atoms/s) for shots 15685 and 15686.

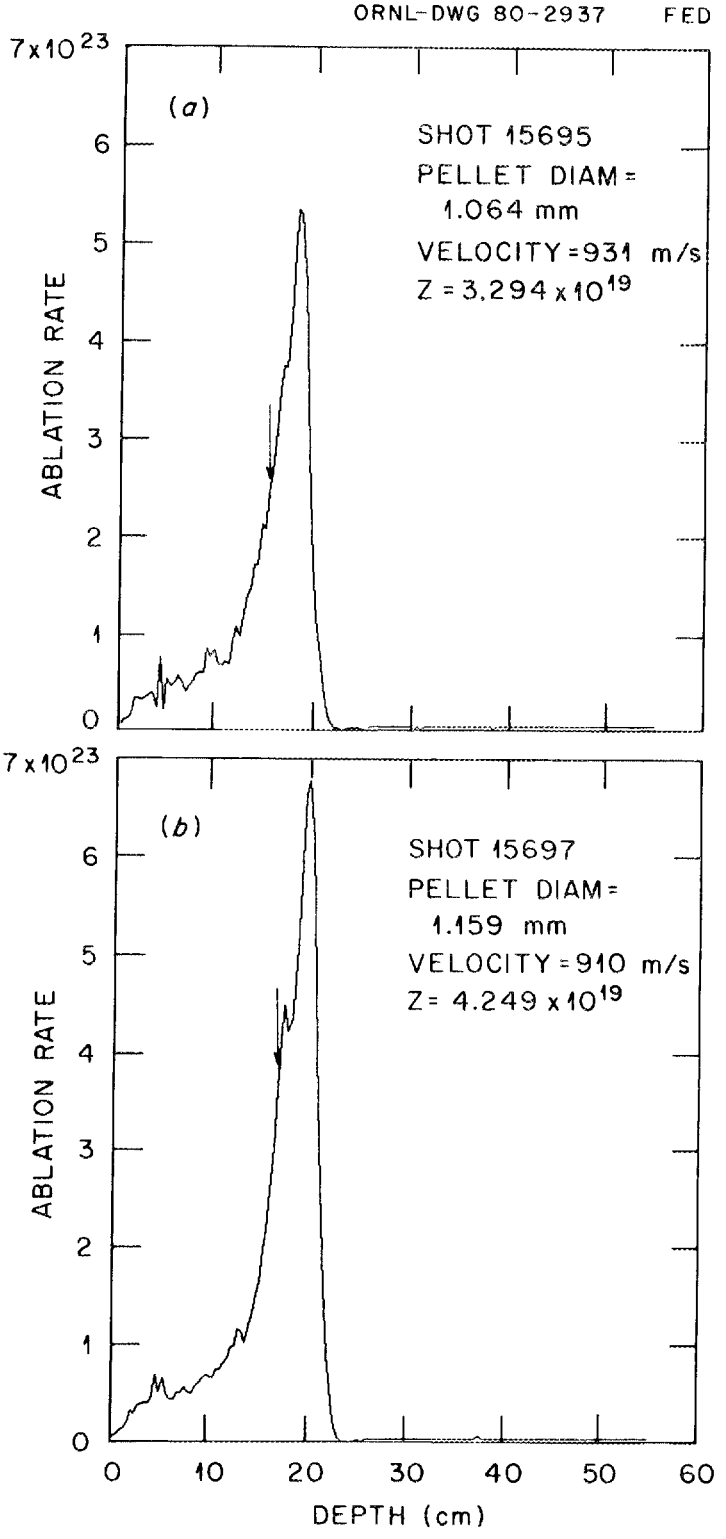

Fig. 4.15 Ablation rate (atoms/s) for shots 15695 and 15697.

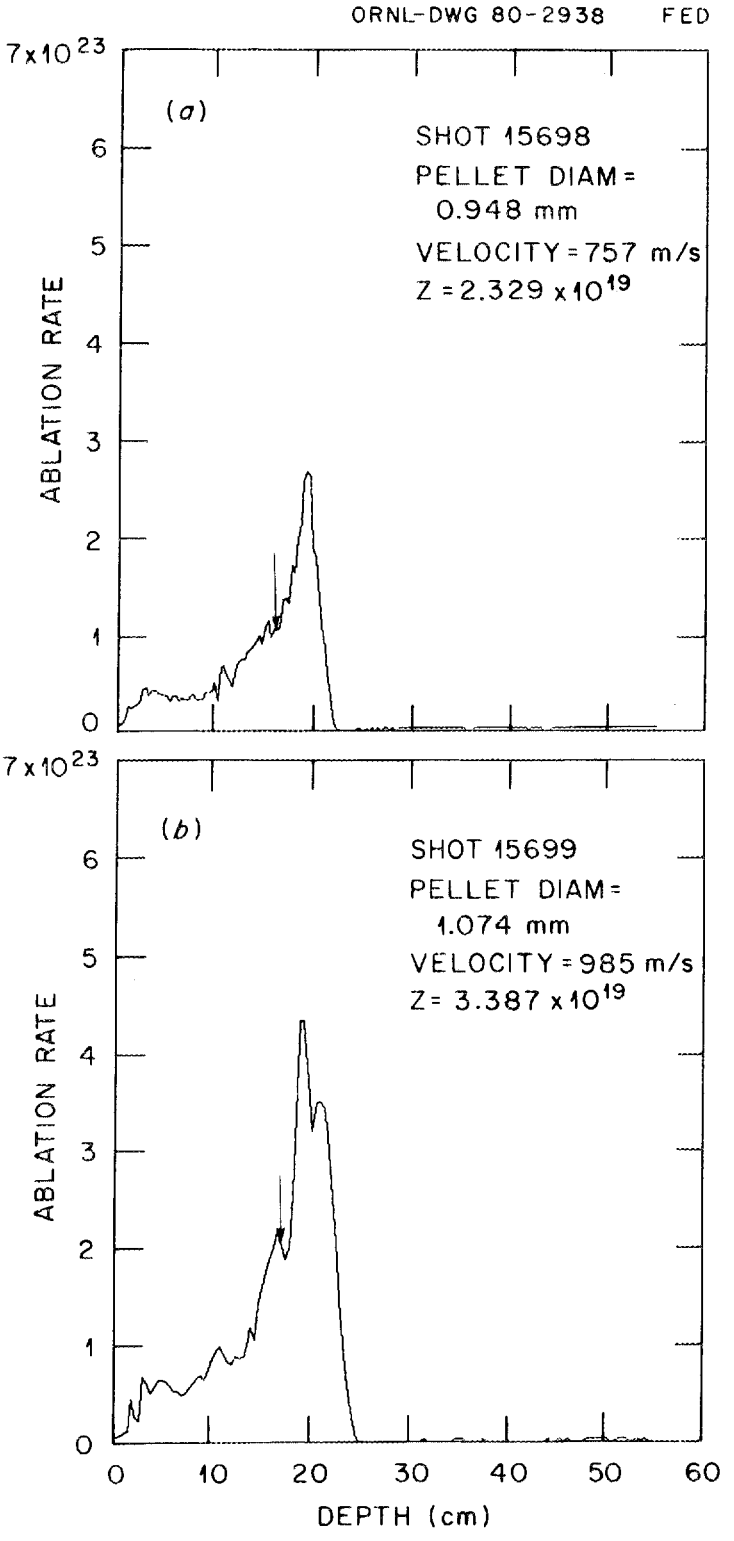

Fig. 4.16 Ablation rate (atoms/s) for shots 15698 and 15699.

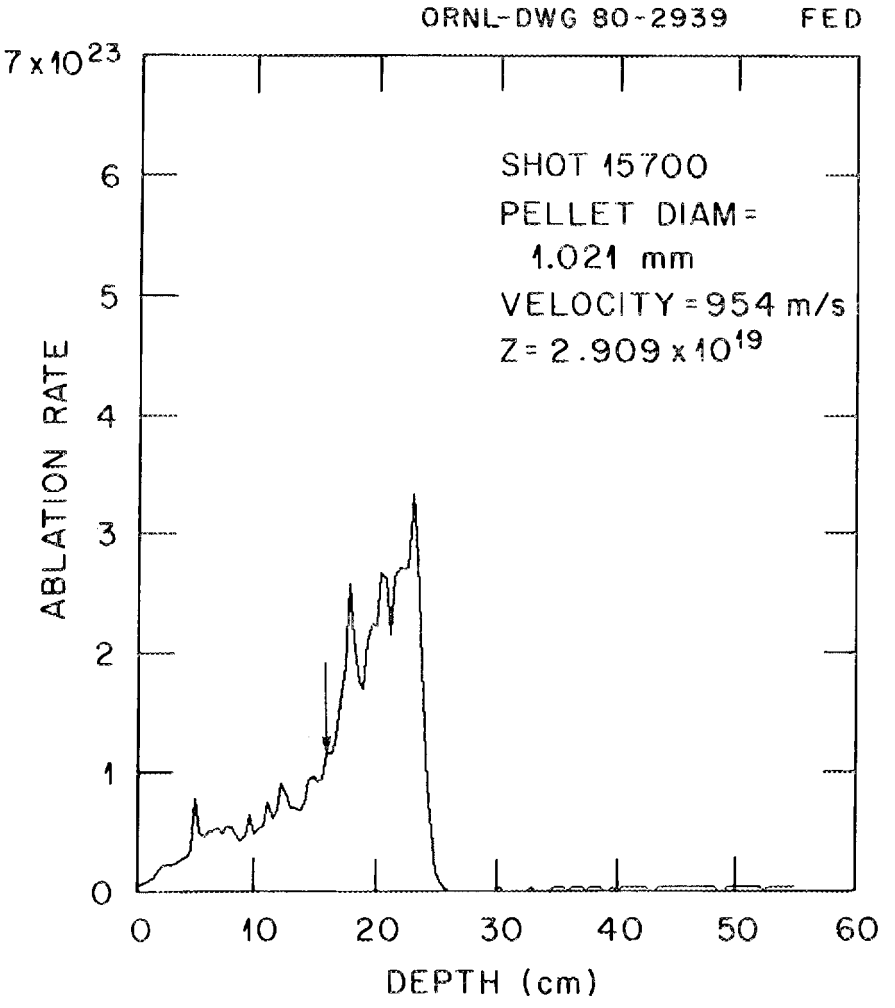

Fig. 4.17 Ablation rate (atoms/s) for shot 15700.

$r \equiv$ distance from detector to pellet at time t,

$C_3 \equiv$ (energy of one H_α photon)$^{-1} = (3.02 \times 10^{-19}\ J)^{-1}$,

$C_1 \equiv$ constant accounting for detector quantum efficiency, line filter efficiency, beam splitter efficiency, vacuum window reflection, and amplification = 38 (V/W),

$A \equiv$ active area of photodiode = $1 \times 10^{-4}\ m^2$, and

$C_2 \equiv$ atoms ablated per H_α photon emitted = 46.

The distance scale shown is the nominal distance of the pellet from the limiter calculated by taking the time recorded by the transient-event recorder and multiplying by the pellet velocity. It does not account for any curvature of the pellet's trajectory.

The arrow on the H_α traces indicates the point in the pellet's ablation at which the holographic interferogram was made.

On each of the computer-analyzed traces is also recorded the initial pellet "Z" (total hydrogen atom content), initial pellet diameter, and pellet velocity. The Z of the pellet is inferred from integrating the H_α trace. The pellet diameter is an equivalent spherical diameter assuming solid density at 4.2 K, inferred from Z. The velocity is that measured by the velocimeter/timer discussed in Chap. 2.

Figure 4.18 shows two H_α oscilloscope traces from the data of August 2, 1979. The spike on the upper trace is a signal from the holographic laser indicating when it was fired. These traces are for the other two interferograms that will be presented as typical of the data of September 6, 1979.

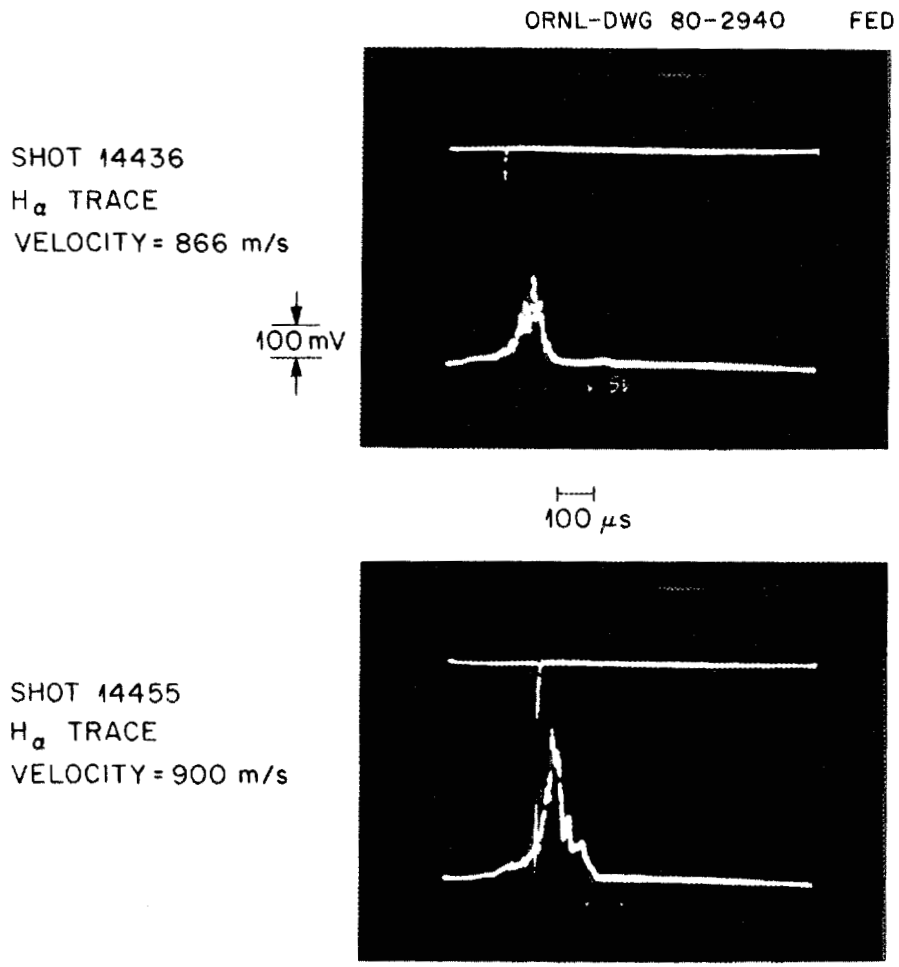

Fig. 4.18 H_α oscilloscope traces for shots 14436 and 14455.

Figure 4.19 is the average ablation rate curve inferred from all of the shots where pellets were injected on September 6. The solid curve is the average. The dashed curves are the average +/- the standard deviation.

4.2.6 Interferograms and shadowgraphs

The formation of shadowgraphs was not discussed in Chap. 2 because the modification to the interferometer to form a shadowgraph and interferogram simultaneously is almost trivial. The modification is shown, however, on Fig. 2.7. A beam splitter (BS2), an electronic shutter (ES), and a polaroid film holder (PFH) are indicated on the figure. The beam splitter splits off a portion of the object beam after the last lens and directs it through the shutter onto the polaroid film holder, which is placed the same optical distance from the last lens as the holographic plate holder so that objects in the field of view at the midplane of the tokamak will be in focus on the polaroid film. Polaroid Type 57 3000-speed 4-in. by 5-in. sheet film was used in the polaroid film holder. Solid hydrogen or very high density plasma will refract the laser light out of the system so that an image of the pellet made from the interferometer object beam will be dark in these areas (therefore "shadowgraph"). The polaroid shadowgraph provides instant verification of whether the pellet was in the field of view of the interferometer and also provides qualitative information about the interaction of the

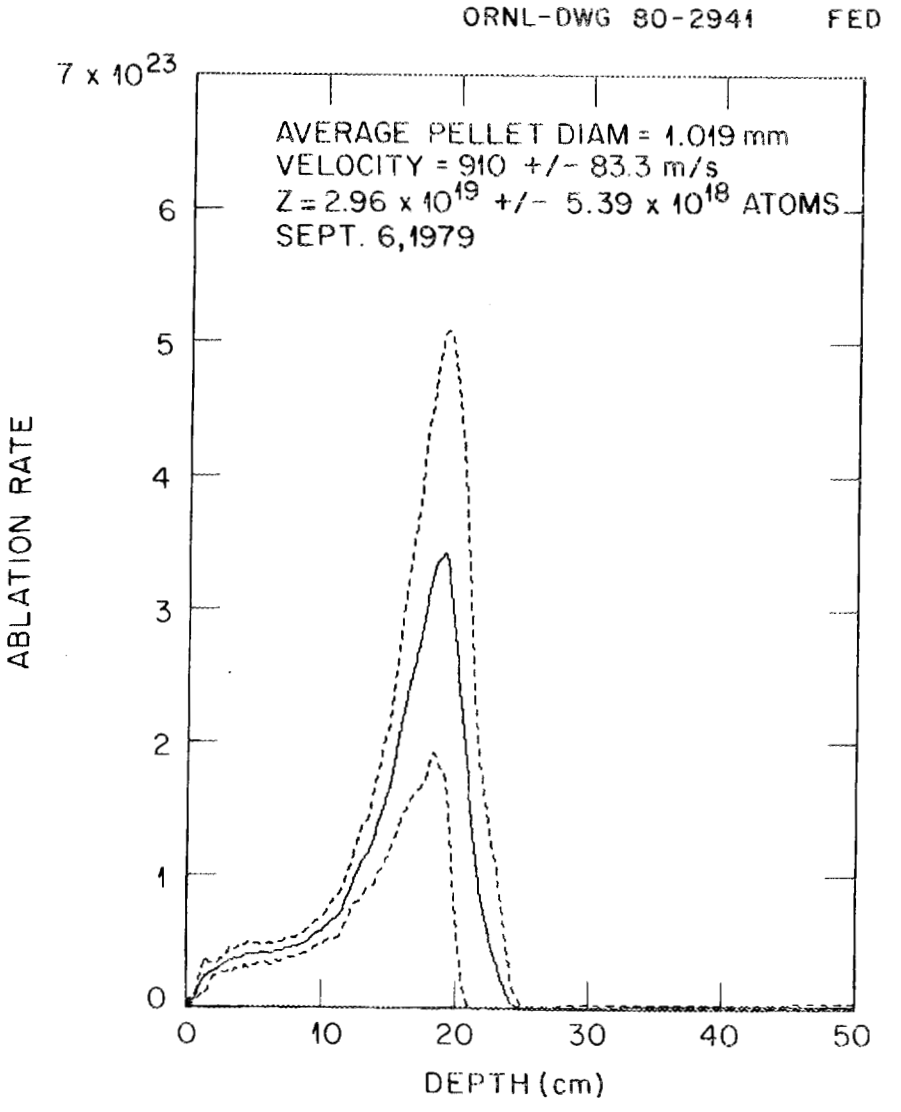

Fig. 4.19 Average ablation rate (atoms/s) for September 6, 1979.

laser beam with the ablated material and pellet. The electronic shutter is closed during formation of the first hologram and open during formation of the second so that the polaroid film is exposed only when the pellet is in the interferometer field of view.

The interaction of laser light with neutral hydrogen and electrons is discussed in the Appendix. For electrons, a shift of one fringe (phase shift of 2π) is produced by an electron density times path length of $(n_e \times \ell) = 3.2 \times 10^{21}\ m^{-2}$ (at $\lambda = 6943\ \mathring{A}$), and a shift of one fringe is produced by a molecular hydrogen density times path length of

$$(n_{H_2} \times \ell) = 1.35 \times 10^{23}\ m^{-2}\ (\lambda = 6943\ \mathring{A}).$$

It should also be kept in mind that electrons produce a negative phase shift and neutral molecules a positive phase shift.

Figures 4.20-4.27 are interferograms and shadowgraphs made on September 6, 1979. Shadowgraphs are not included for shots where the pellet was more than 1 cm from the focus of the interferometer (horizontal midplane of the vacuum vessel). The shadowgraphs included are for qualitative rather than quantitative information. Some features show up more clearly on the shadowgraphs than on the interferograms. Discontinuities in refractive index (shocks?), for instance, are much clearer on the shadowgraphs than on the interferograms, although once located on the shadowgraphs, they are clearly visible on the interferograms.

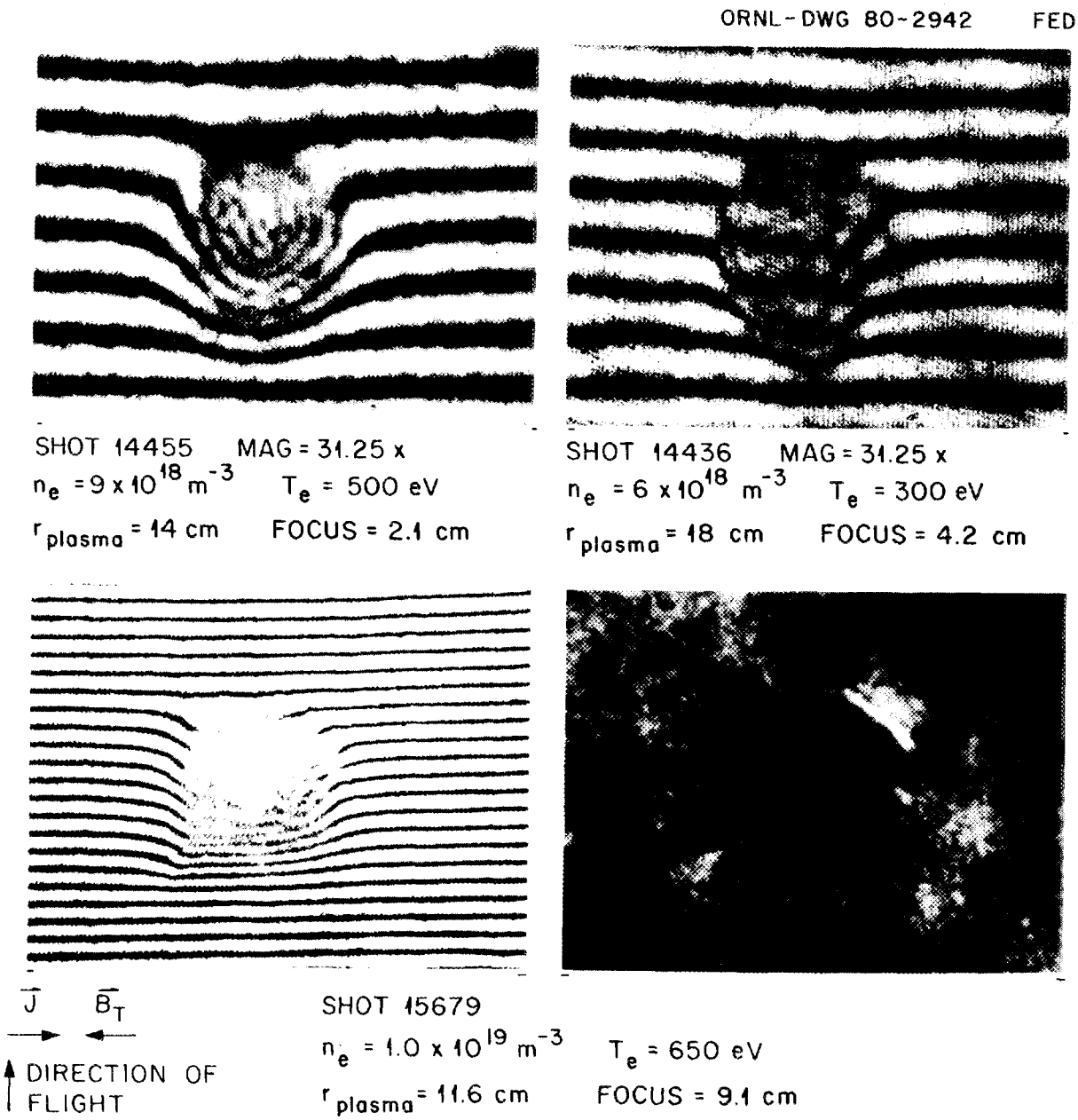

Fig. 4.20 Interferograms for shots 14436, 14455, and 15679; shadowgraph for shot 15679.

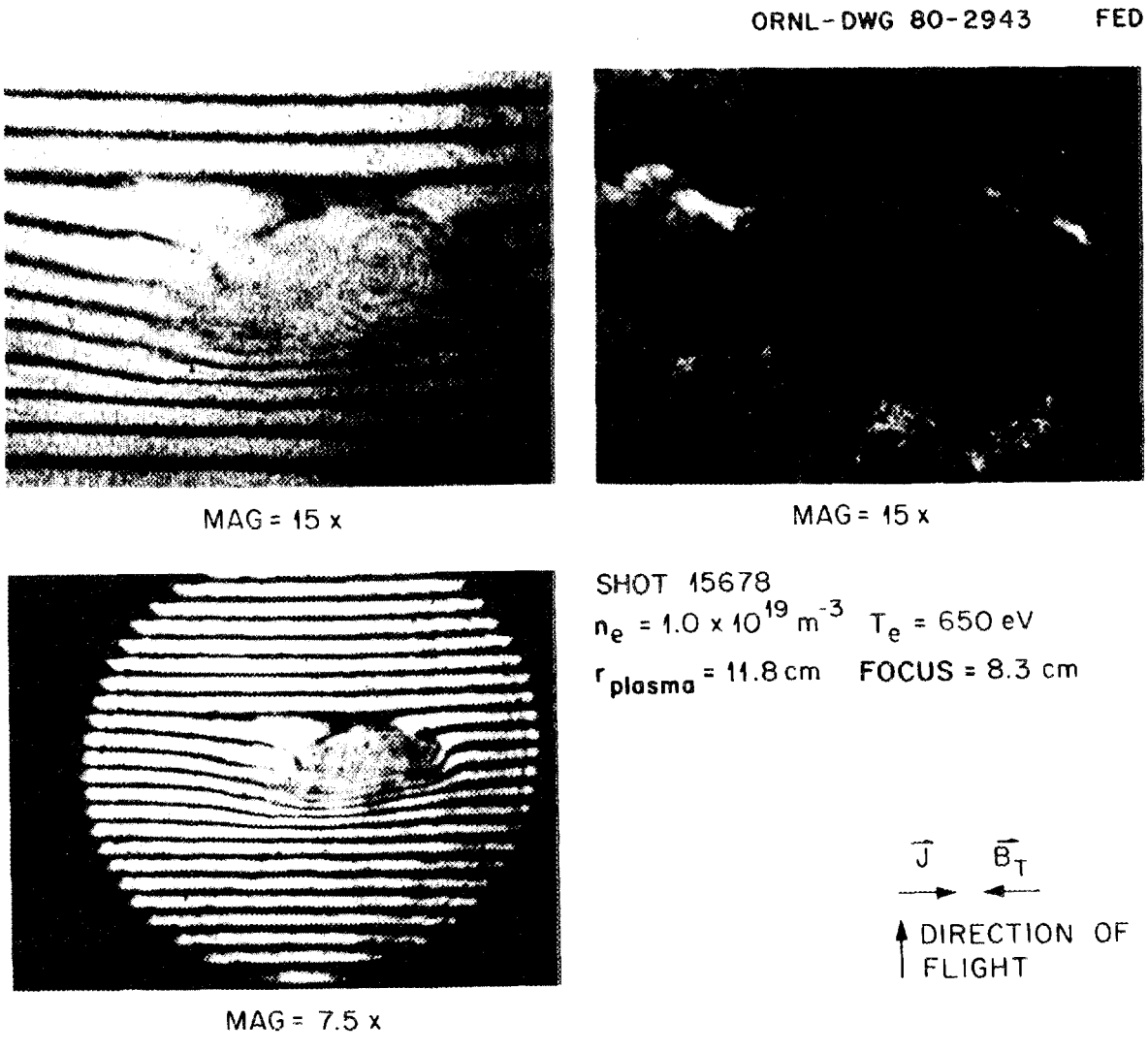

Fig. 4.21 Interferograms and shadowgraph for shot 15678.

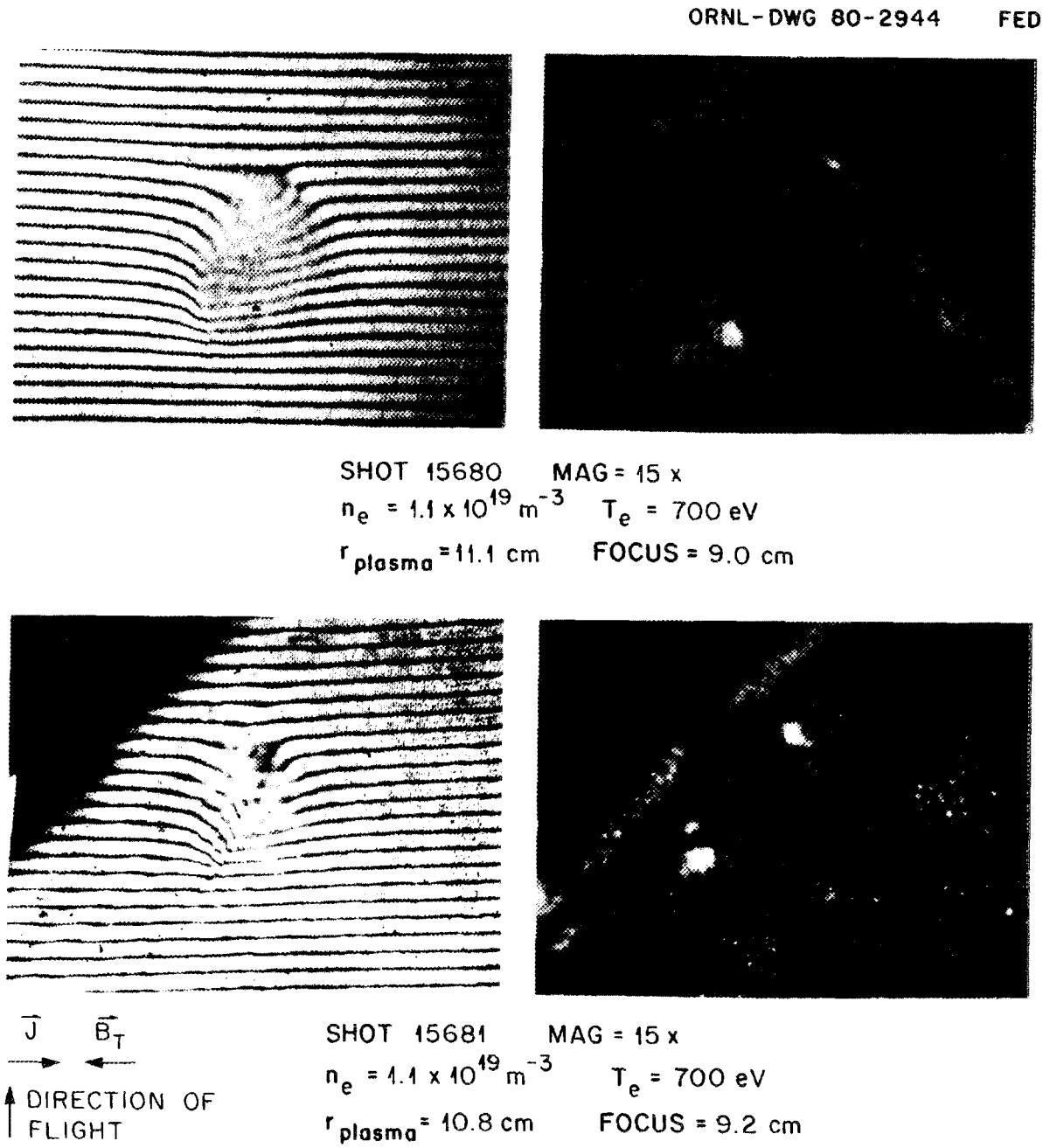

Fig. 4.22. Interferogram and shadowgraph for shots 15680 and 15681.

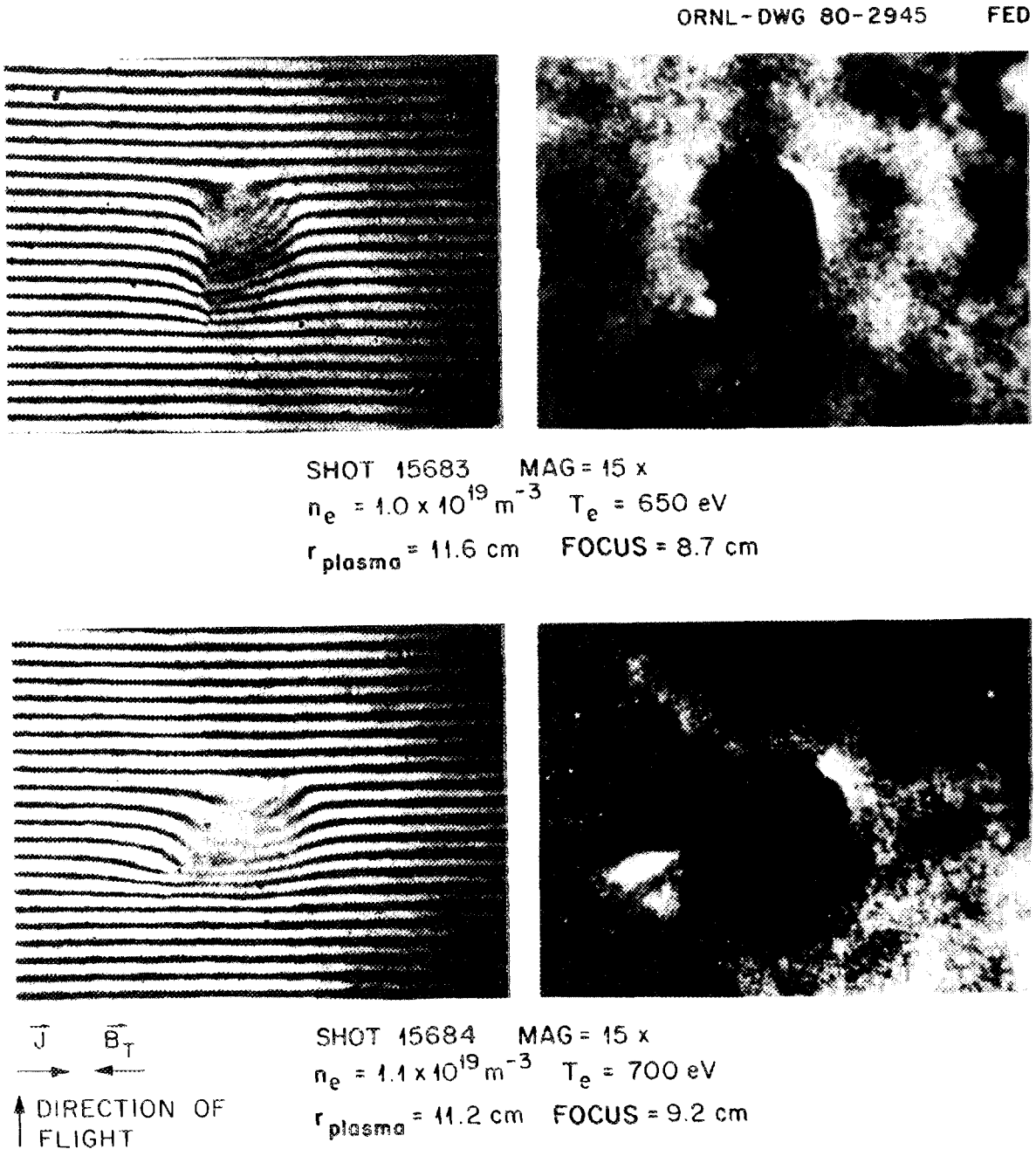

Fig. 4.23. Interferogram and shadowgraph for shots 15683 and 15684.

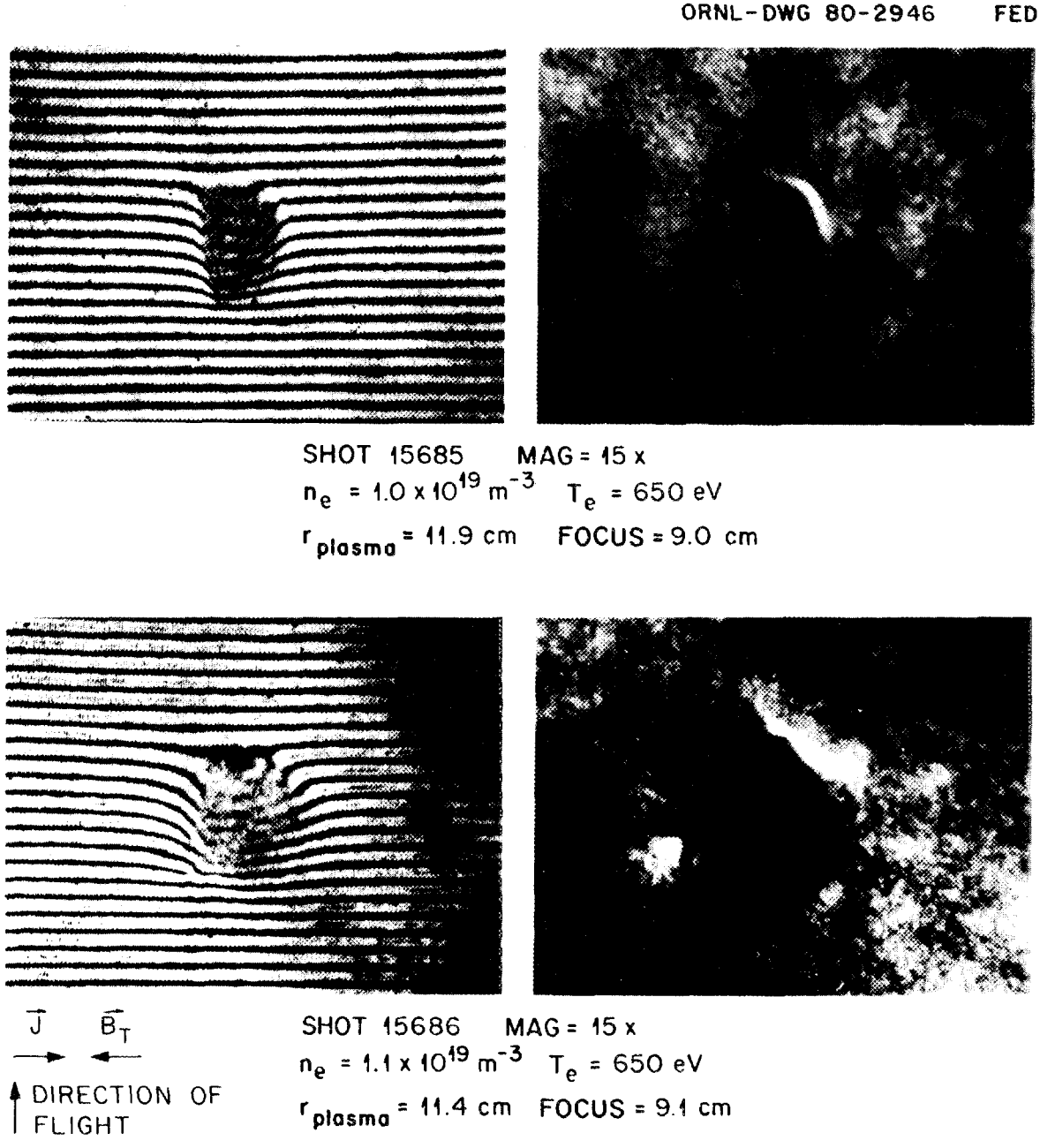

Fig. 4.24 Interferogram and shadowgraph for shots 15685 and 15686.

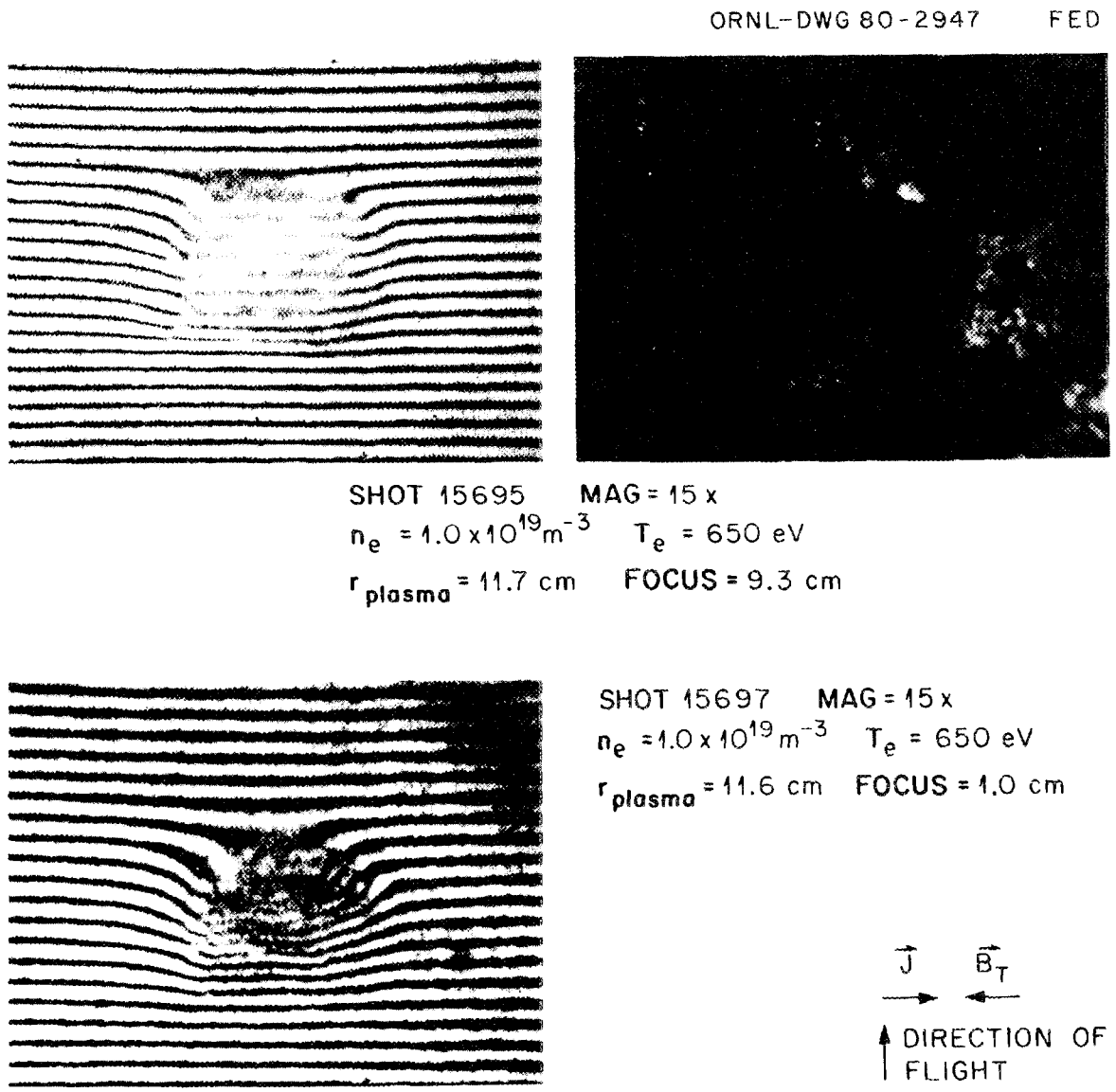

Fig. 4.25 Interferogram and shadowgraph for shots 15695 and 15697.

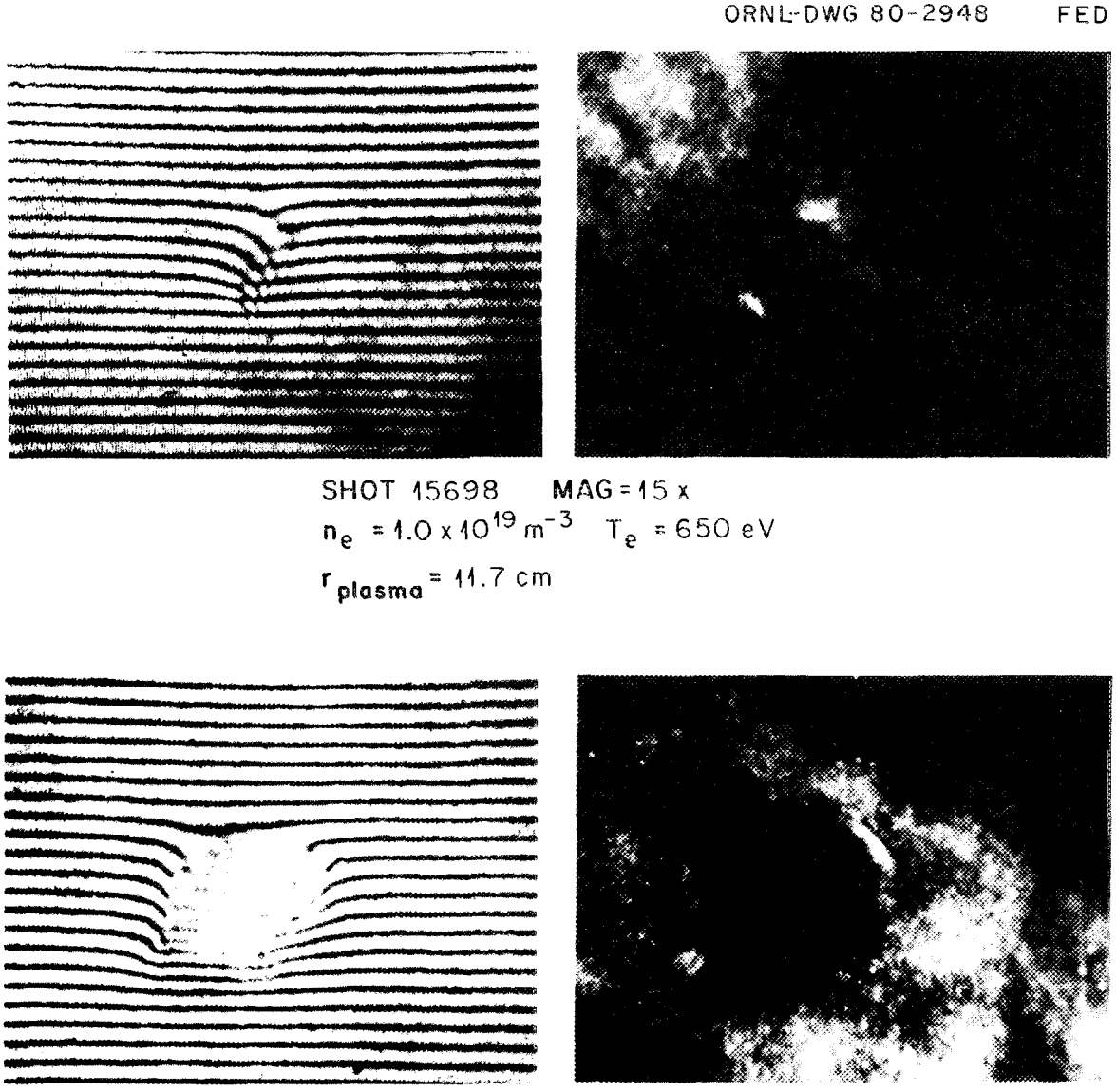

Fig. 4.26 Interferogram and shadowgraph for shots 15698 and 15699.

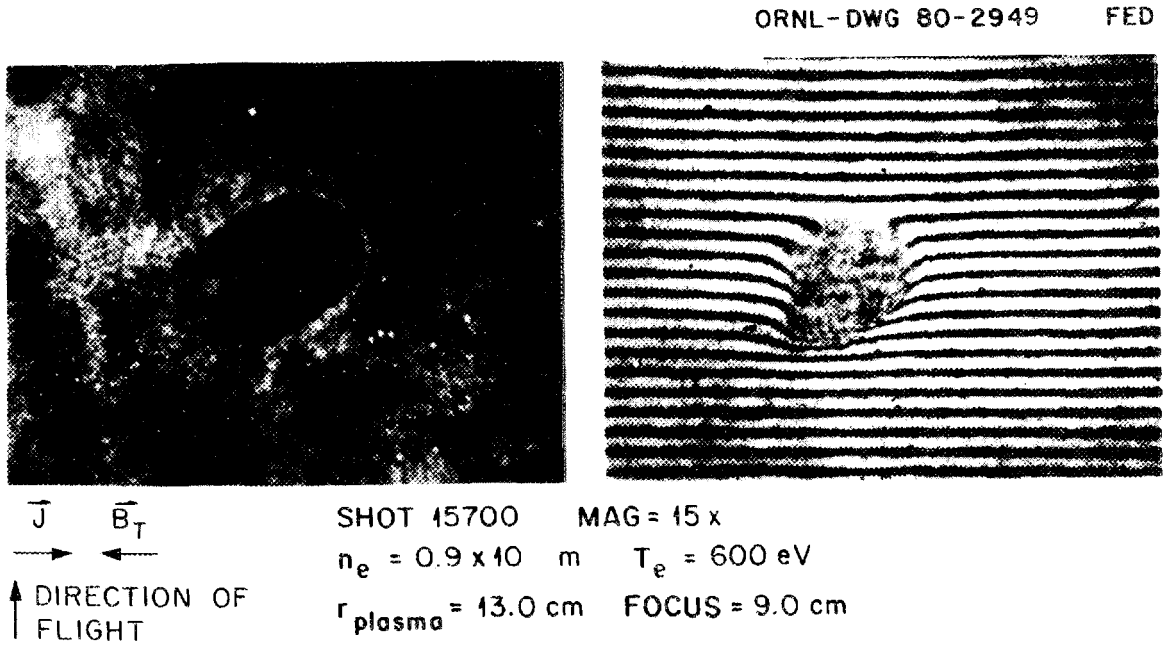

Fig. 4.27 Interferogram and shadowgraph for shot 15700.

There is noise present on the shadowgraphs and the interferograms. On the shadowgraphs the noise is in the form of variations in intensity of the laser beam and small white specks visible on some of the shadowgraphs. The intensity variations on the laser beam appear after it passes through the vacuum windows of the tokamak and are presumably due to imperfections in the vacuum windows.

Noise on the interferograms is in the form of diffraction rings from small particles of dust on the replay optics and from very small imperfections in the emulsion on the photographic plate. Because in general these dust particles and imperfections are not in focus, they produce a series of diffraction rings on the photograph of the replayed interferogram when the hologram is replayed in coherent light. Noise is also present on the interferogram for shot 15861 because the pellet was very close to the edge of the lens, causing some waviness of the background fringes.

Noted with each interferogram/shadowgraph is the shot number, magnification, distance from the microscope focussing lens when in focus, plasma minor radius where the interferogram was made, and plasma electron density and temperature, inferred from Thomson scattering, at that minor radius.

The interferograms are oriented on the page so that a downward fringe shift indicates a negative phase shift due to electron density.

The direction of increasing/decreasing phase on the interferogram is controlled by the direction of the mirror tilt between the formation of the two holograms for the interferogram. The interferograms/shadowgraphs are presented in order of shot number unless it was necessary to present them out of order to minimize the number of figures.

Figure 4.28 is a scale reference for the interferograms/shadowgraphs. The same microscope used to replay the holograms and blow up the shadowgraphs was used to make photographs of a machinist's metric scale. The scale for the interferograms/shadowgraphs can be found by choosing the correct magnification of the machinist's scale. (The discussion of the magnification of the interferograms in Chap. 2 should be kept in mind.) The true scale for the shadowgraphs can be found by comparing with the correct magnification of the machinist's scale because the shadowgraphs presented were at the approximate focus of the interferometer; the magnification is therefore true.

The focus of the microscope was 9.2 cm from the input lens. The focus listed under each interferogram is the actual distance from the hologram film plane to the microscope when the interferogram was in focus. As discussed in Chap. 2, the difference between these two numbers is proportional to the distance the pellet was from the midplane of the tokamak when the interferogram was made.

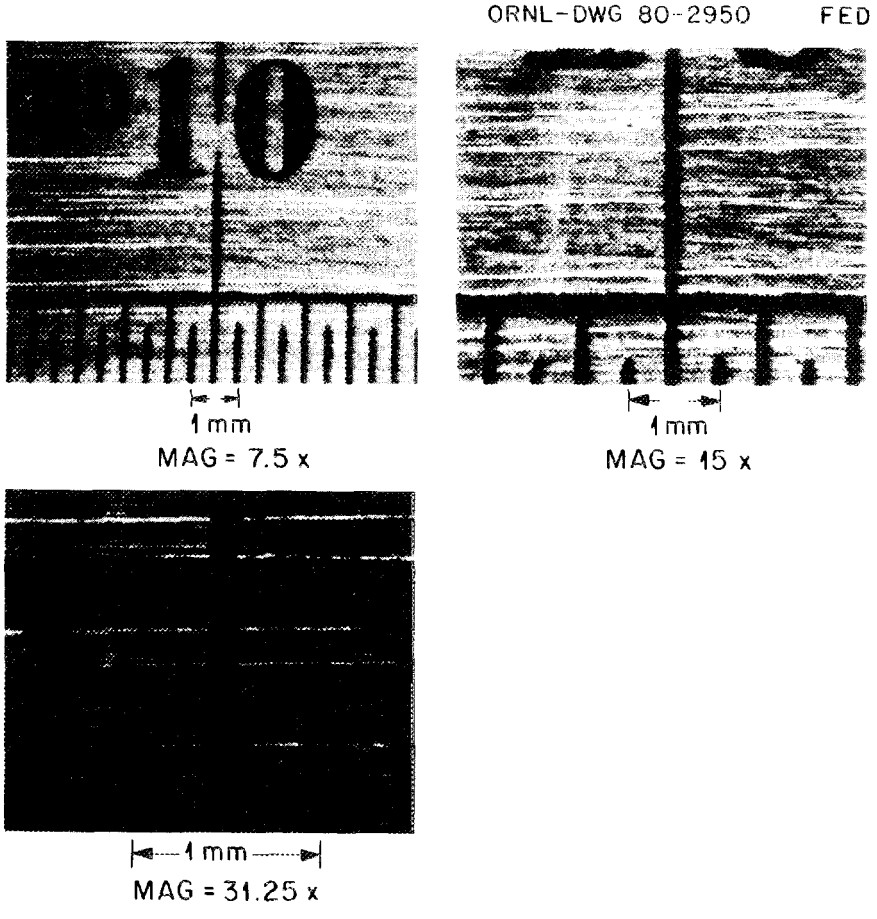

Fig. 4.28 Magnifications of metric machinist's scale.

It may be noticed that portions of the shadowgraph that appear very dark have clear fringes on the interferogram. The explanation is that the interferogram was pre-exposed (by formation of the first hologram) and was therefore much more sensitive to low light levels than the shadowgraph.

4.3 Data from September 11, 1979 (High n_e, Low T_e)

4.3.1 Thomson scattering data from September 11

Figure 4.29 shows electron temperature and density profiles made 1 ms prior to pellet injection for the September 11, 1979, sequence. The nominal pellet injection timing was at 100 ms into the discharge. The discharge current was 150 kA, the toroidal magnetic field on axis was 1.5 T, the line-averaged electron density was 3.2×10^{19} m^{-3}, and the safety factor q at the limiter was 4.0. The plasma Z_{eff} inferred from Thomson scattering was 5.3.

Figure 4.30 shows the electron density and temperature 1 ms after pellet injection for the September 11 sequence. The pellets penetrated all the way past the center of the plasma and were stopped at r = -13 cm. The discharge evolved for a few milliseconds after pellet injection and then, as previously discussed, experienced large-scale MHD activity and rapid loss of confinement. It is not known whether this was triggered by pellet injection or by exceeding the operating parameters for which the machine was stable on that day.

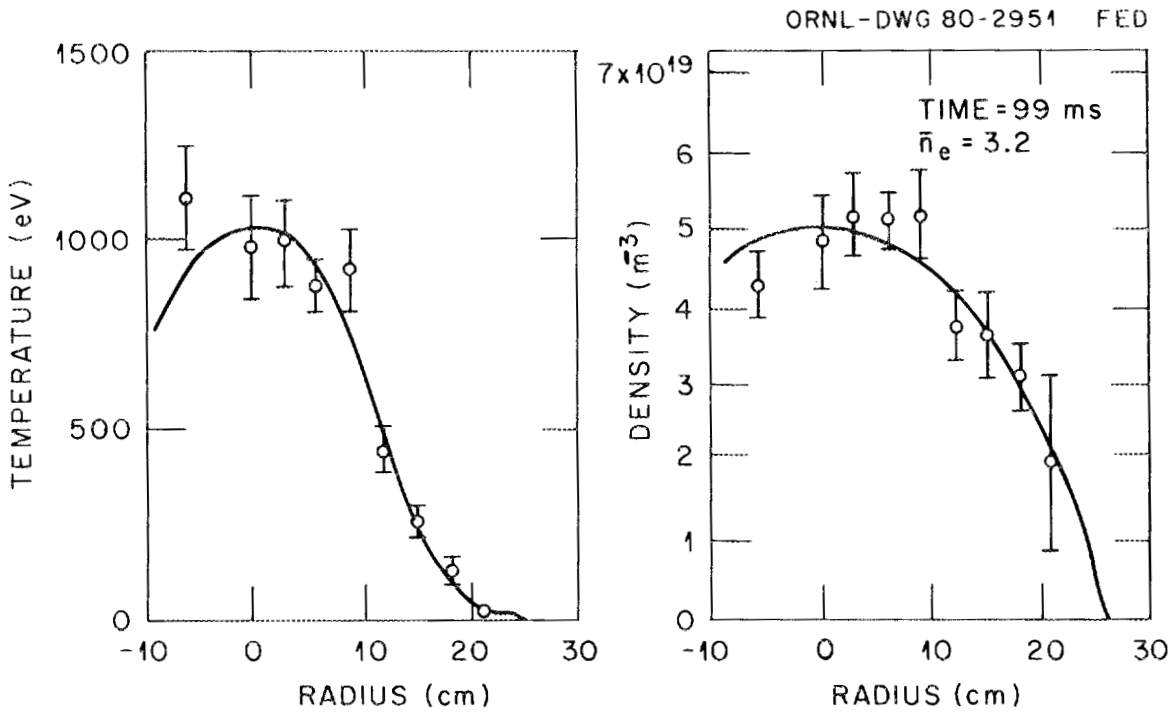

Fig. 4.29 Thomson scattering electron density and temperature 1 ms before pellet injection, sequence of September 11, 1979.

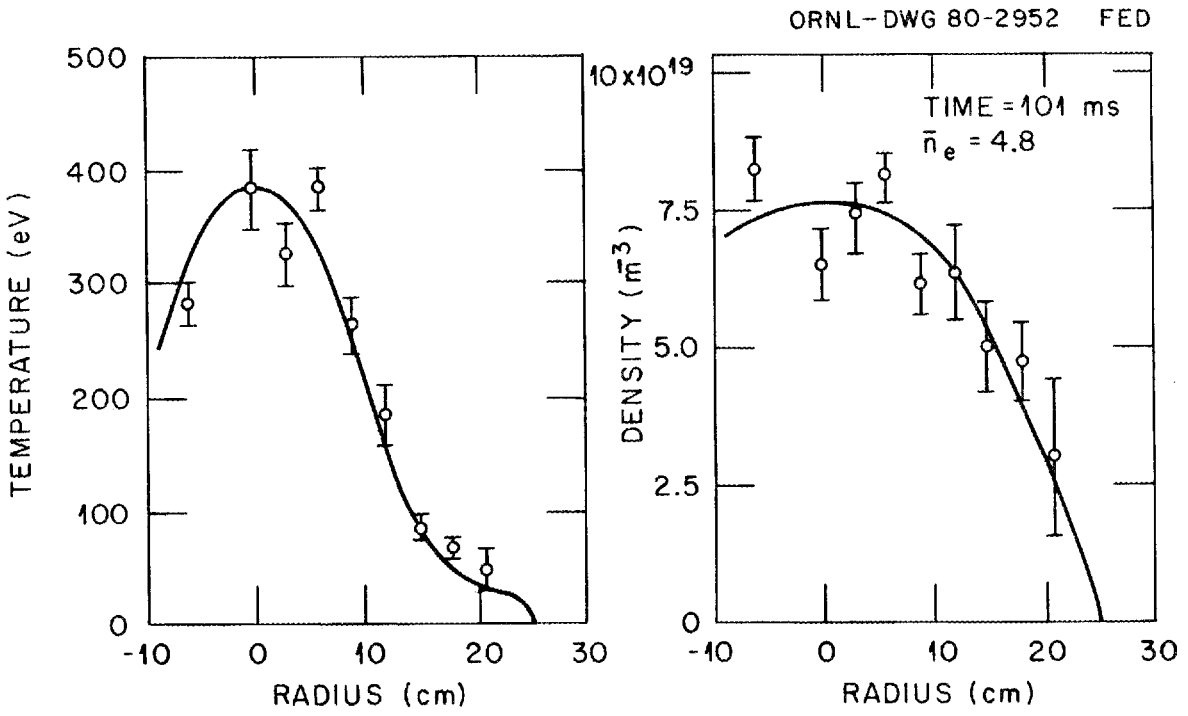

Fig. 4.30 Thomson scattering electron density and temperature 1 ms after pellet injection, sequence of September 11, 1979.

4.3.2 Line-averaged density data from September 11

On September 11 neither of the microwave interferometers could follow the density change due to the pellet. The densities achieved probably did not reach the cutoff densities for the 2-mm microwave interferometers but came close enough so that reflection and refraction caused severe loss of signal.

The FIR interferometer was operative; however, there were some noise problems due to vibration, and the FIR data are presented with the following disclaimer from the responsible physicists: "Data is not entirely believable! Reconstruction is largely a good guess and fringes may have been missed or added in the wrong place." With the above kept in mind, the data will be presented and used.

Figure 4.31 shows three density traces from September 11 shots with pellet injection. Table 4.3 lists maximum line-averaged density immediately after pellet injection for a number of shots. A path length of 65 cm is assumed for both Fig. 4.31 and Table 4.3 in calculating $\bar{n}_e$.

4.3.3 Local energy loss during pellet injection on September 11

Figures 4.32 and 4.33 are pyroelectric radiometer traces from September 11, 1979. The comments made concerning the September 6 data are again applicable here. Table 4.4 gives integrated power (energy) for the shots shown in Figures 4.32 and 4.33. An average minor radius of 12 cm is again assumed in making the power and energy calculations, as discussed with the September 6 data.

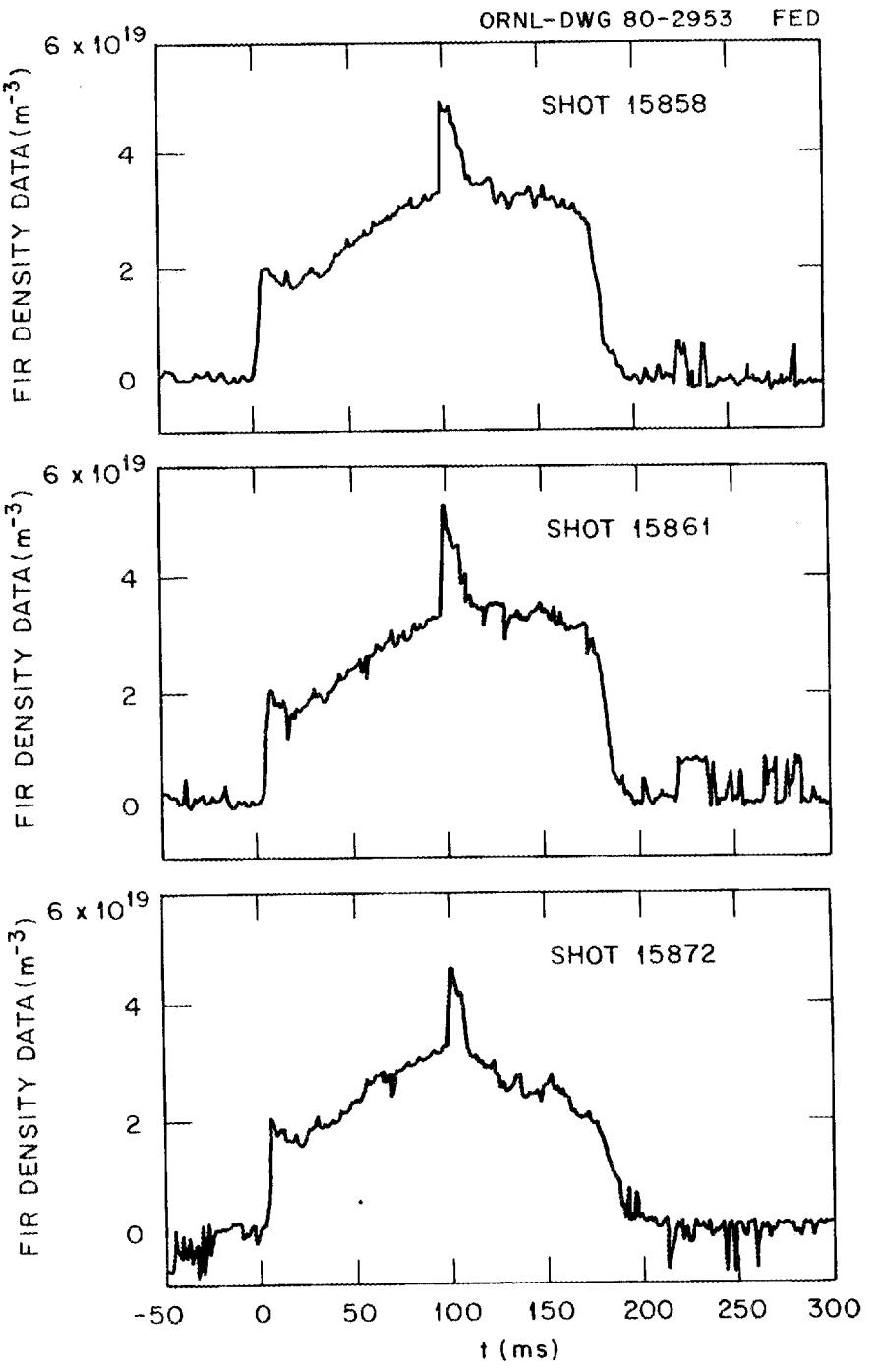

Fig. 4.31 FIR laser line-averaged density data from shots 15858, 15861, and 15872.

Table 4.3. Line-averaged density immediately before and after pellet injection, sequence of September 6, 1979 (assumes 65-cm path length)

Shot number[a]	$\bar{n}_e$ (prepellet) ($\times 10^{19}$ m^{-3})	$\bar{n}_e$ (postpellet) ($\times 10^{19}$ m^{-3})	$\Delta\bar{n}_e$ ($\times 10^{19}$ m^{-3})
15858*	3.3	4.8	1.5
15860*	3.4	4.8	1.4
15861*	3.5	5.2	1.7
15869*	3.1	4.9	1.8
15872*	3.2	4.9	1.7
15873	3.0	4.4	1.4
15874*	3.0	4.3	1.3
15875	3.0	5.2	2.2
15877*	2.9	4.8	1.9
15885*	3.1	4.6	2.5
15888*	3.1	5.5	2.4
15889*	3.0	4.2	1.2

Postpellet averages

$$(\bar{n}_e)\text{AVG} = (4.8 \pm 0.4) \times 10^{19}\ m^{-3}$$

$$(\bar{n}_e^*)\text{AVG} = (4.8 \pm 0.4) \times 10^{19}\ m^{-3}$$

$$(\Delta\bar{n}_e)\text{AVG} = (1.8 \pm 0.4) \times 10^{19}\ m^{-3}$$

[a] * indicates shot where Thomson scattering data were taken.

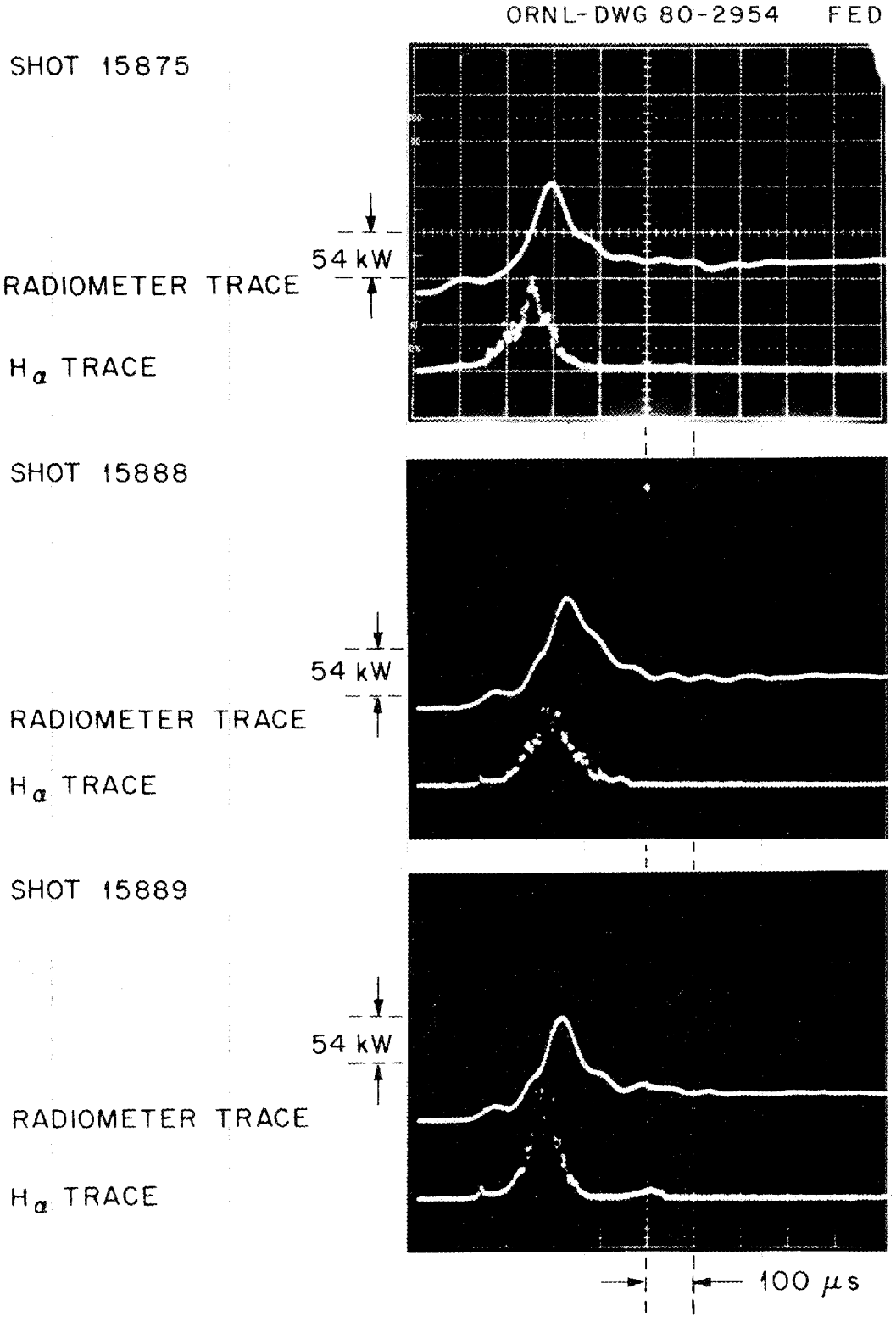

Fig. 4.32 Pellet radiometer data from shots 15875, 15888, and 15889.

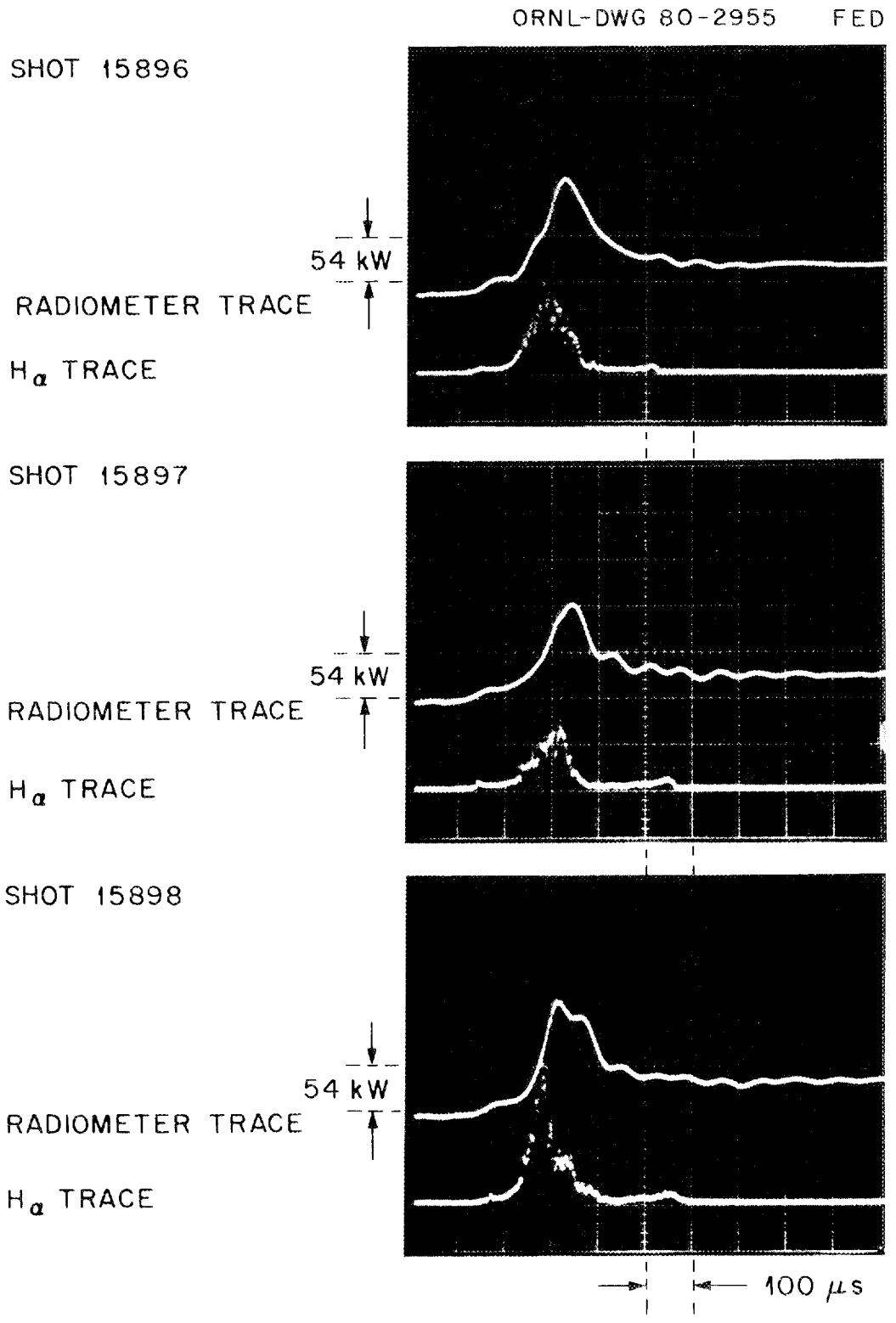

Fig. 4.33 Pellet radiometer data from shots 15896, 15897, and 15898.

Table 4.4. Total local radiated energy during pellet injection, September 11, 1979

Shot number	Total local radiated energy (J)
15875	18
15888	20
15889	18
15890	23
15897	16
15898	21

E_{AVG} = (19 +/-3) J

4.3.4 Pellet ablation rate inferred from H_α line radiation on September 11

Inferring pellet ablation rates from H_α data was discussed with the September 6 data.

Figures 4.34-4.41 are plots of the pellet ablation rates inferred from H_α radiation for the shots where interferograms were made on September 11. The arrow on the plot indicates the point at which the interferogram was made. The nominal center of the plasma would be at 27 cm on the plots. However, the pellet may not have gone through the plasma center. The feedback controls were set to hold the plasma at a nominal position of 2 cm below the horizontal midplane of the vacuum vessel, and the nominal trajectory of the pellet was 4-6 cm above the midplane, in vacuum. However, as previously discussed, the pellet trajectory curves down when ablating in a plasma. The pellet trajectory will be discussed further in the next chapter.

The relationship of pellet injection to MHD activity (minor disruptions) has been discussed by Milora et al.[4] In cold plasmas it is possible for relatively massive pellets to trigger disruptions. This is probably not important for a reactor.

Figure 4.42 is the average ablation rate from all of the pellet shots on September 11 where the plasma was not immediately disruptive on pellet injection and the pellet did not penetrate the entire plasma

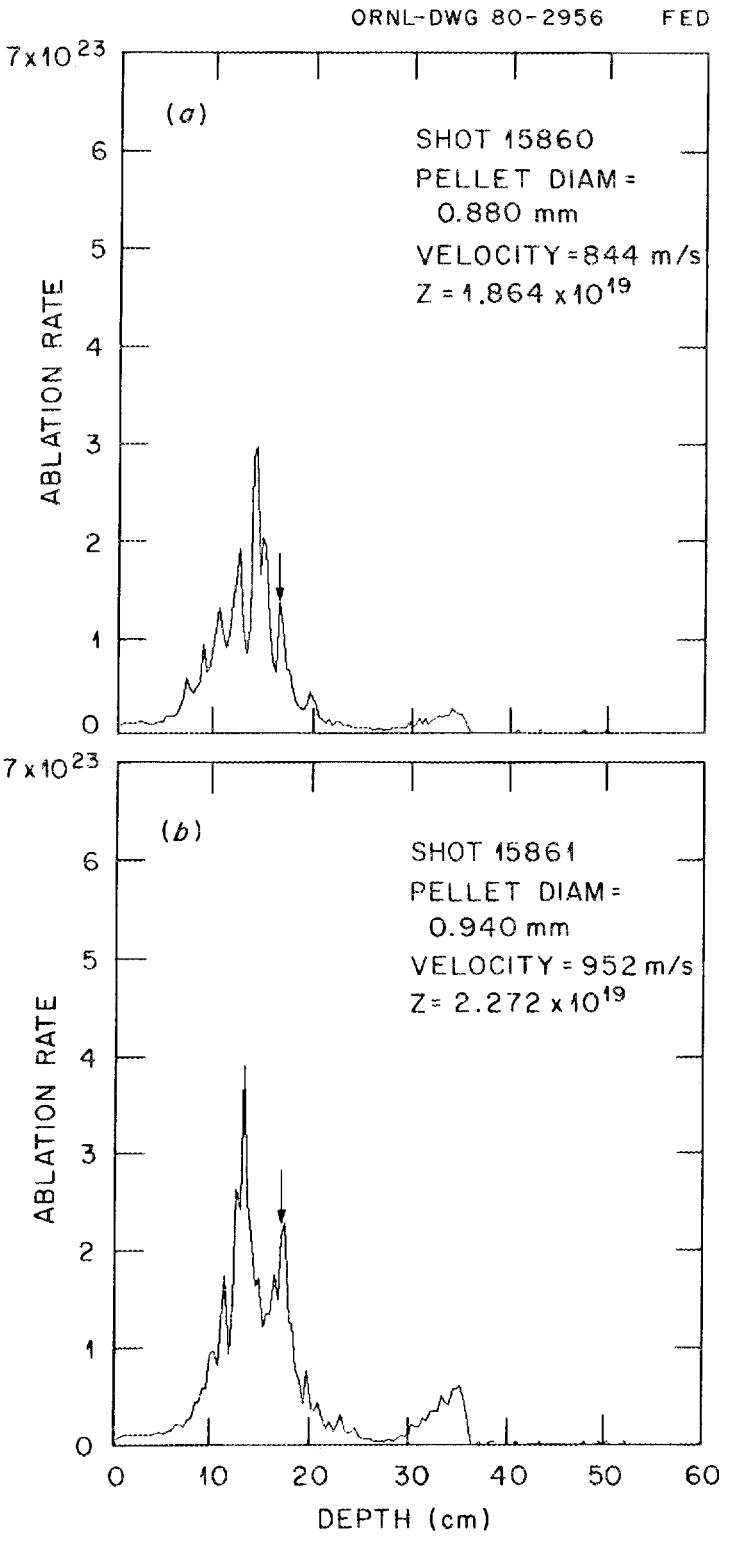

Fig. 4.34 Ablation rate (atoms/s) for shots 15860 and 15861.

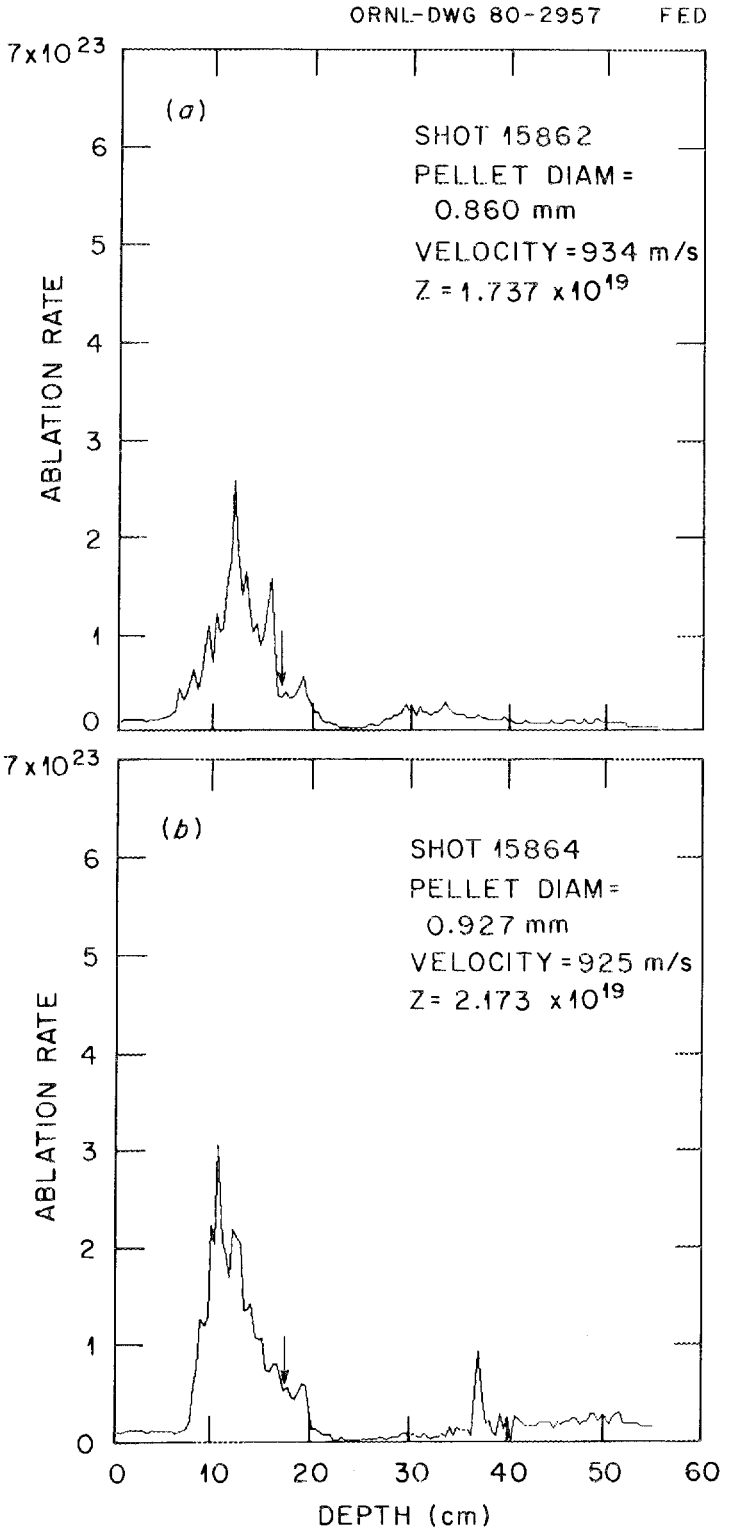

Fig. 4.35 Ablation rate (atoms/s) for shots 15862 and 15864.

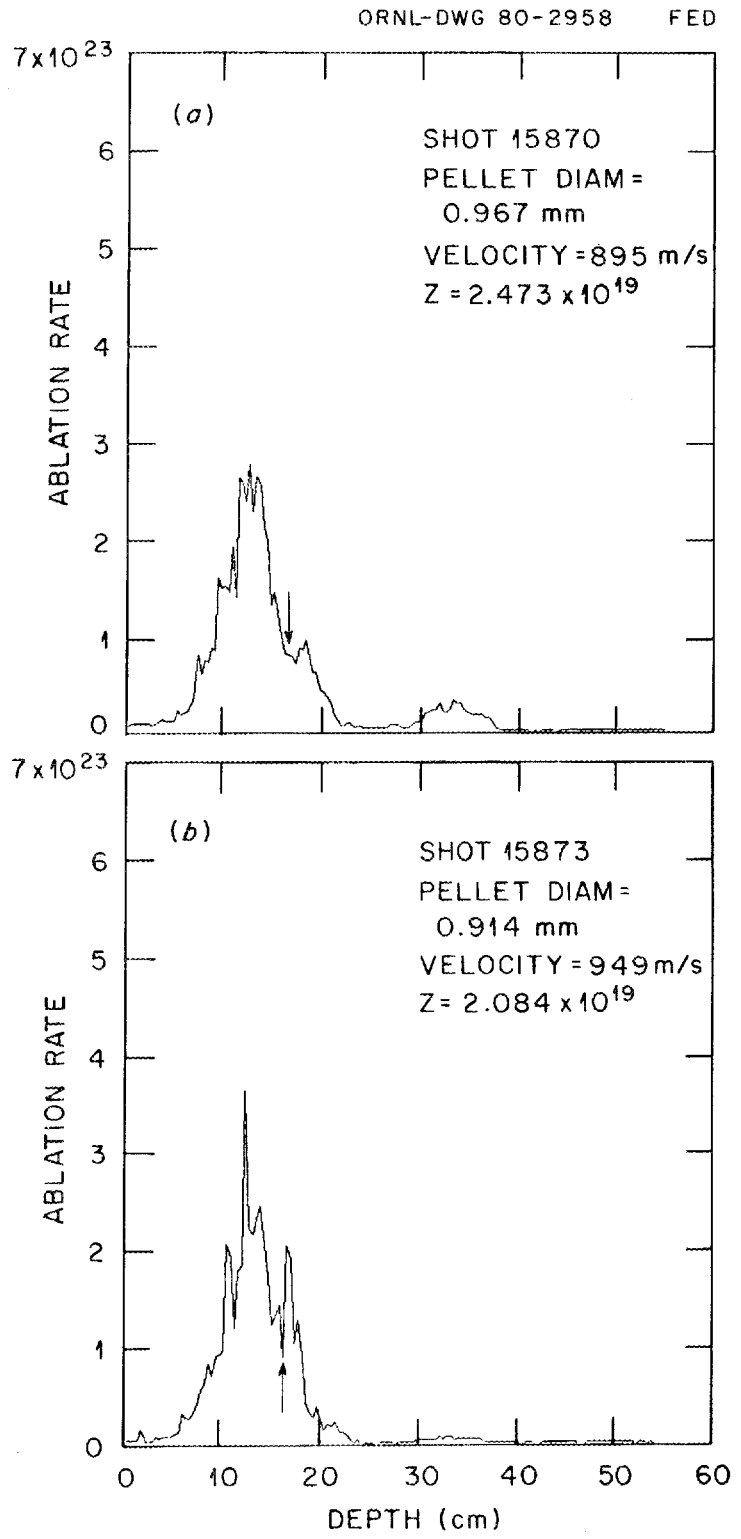

Fig. 4.36 Ablation rate (atoms/s) for shots 15870 and 15873.

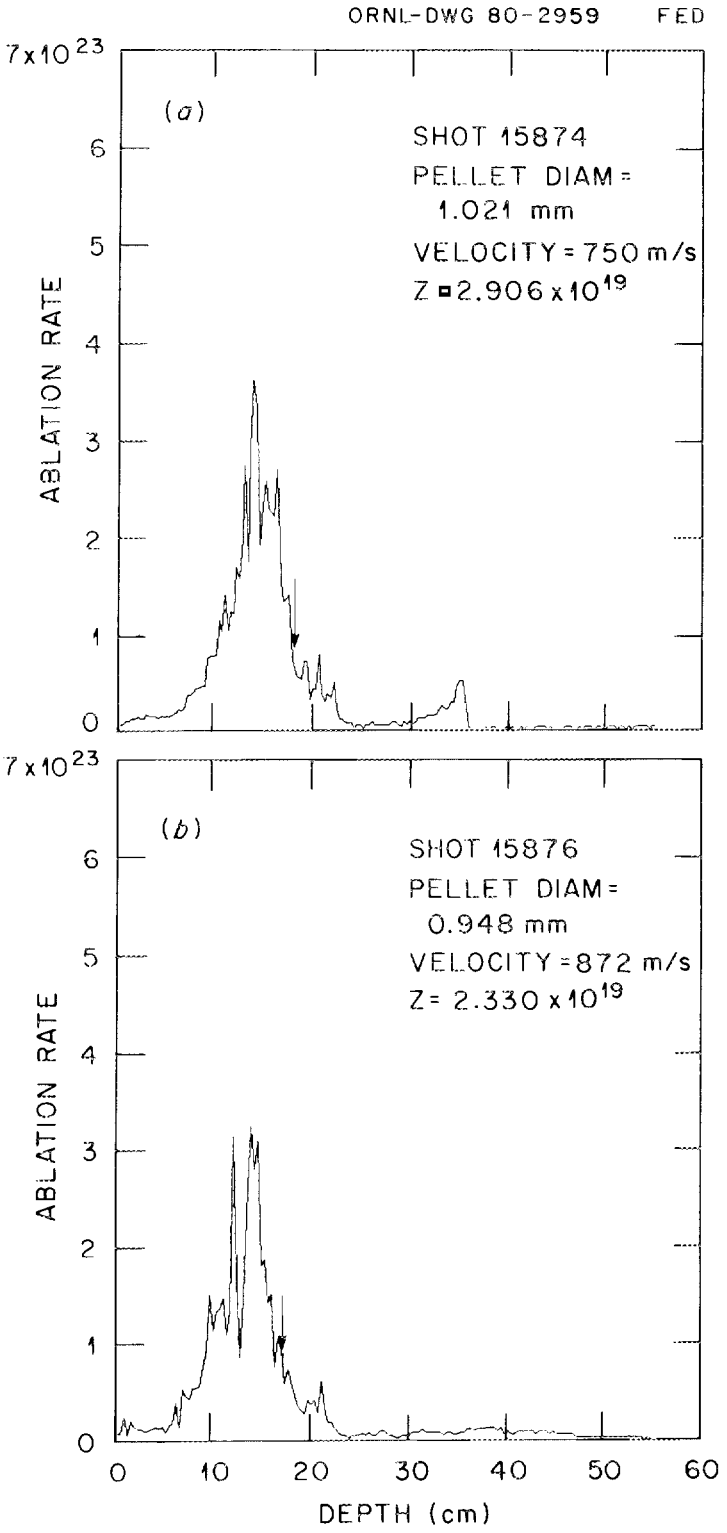

Fig. 4.37 Ablation rate (atoms/s) for shots 15874 and 15876.

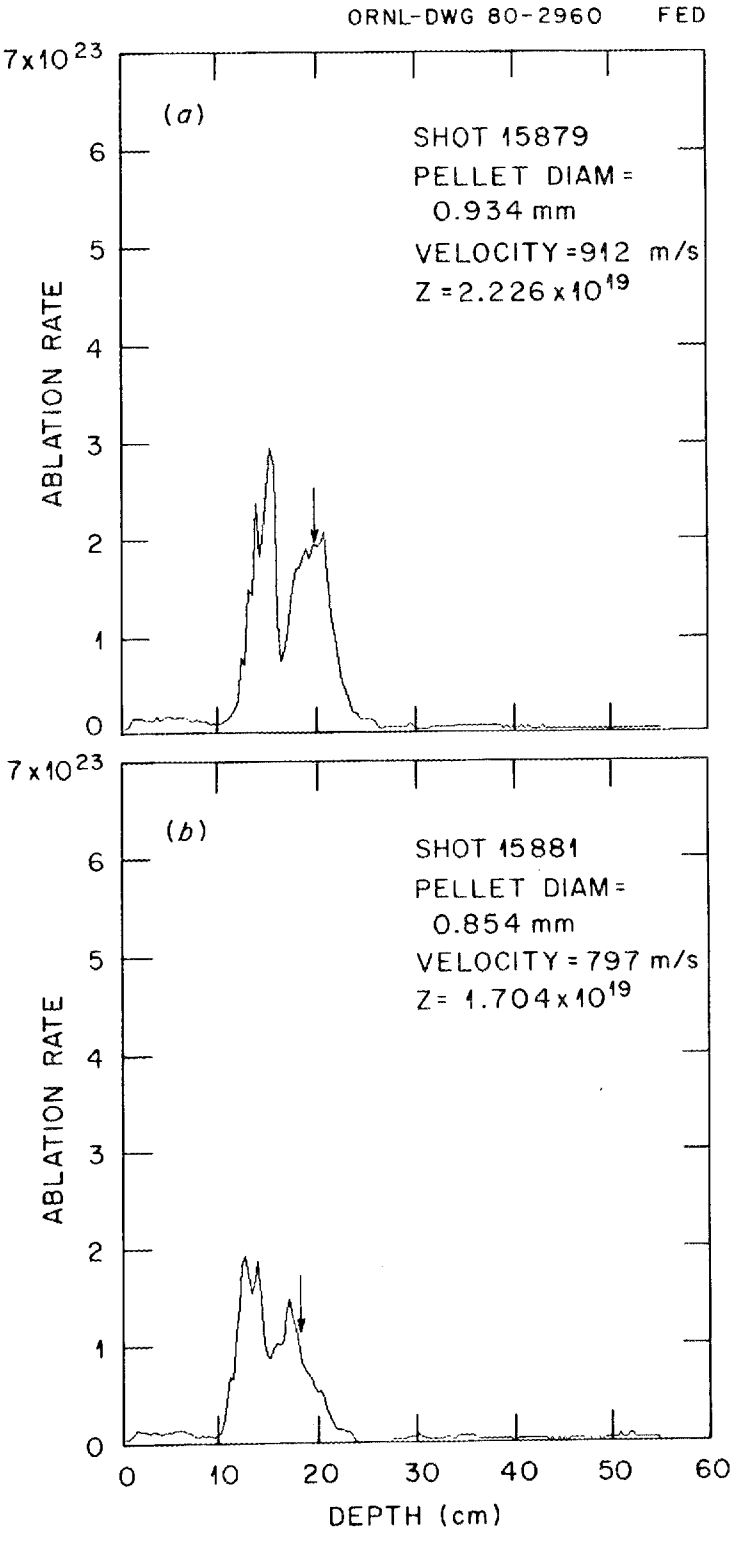

Fig. 4.38 Ablation rate (atoms/s) for shots 15879 and 15881.

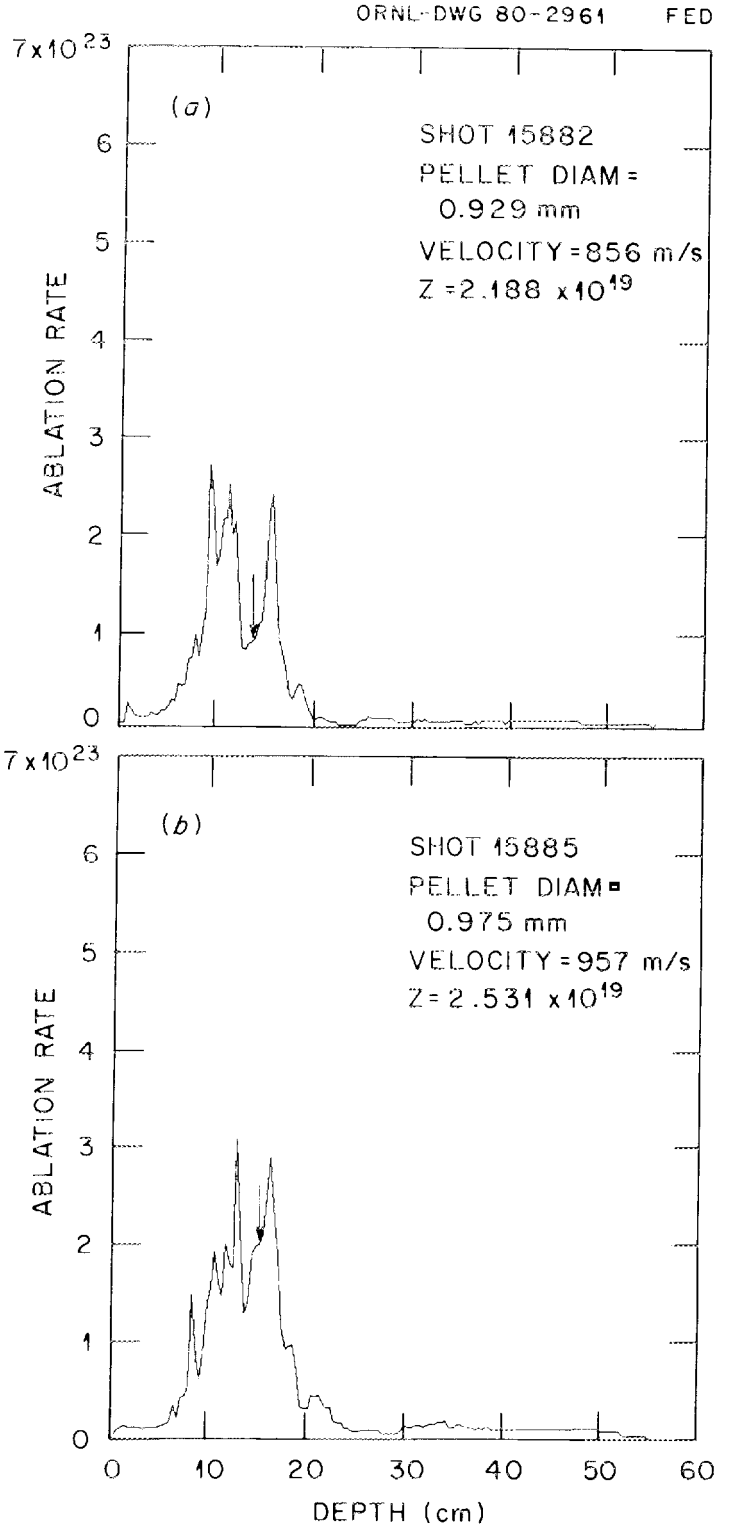

Fig. 4.39 Ablation rate (atoms/s) for shots 15882 and 15885.

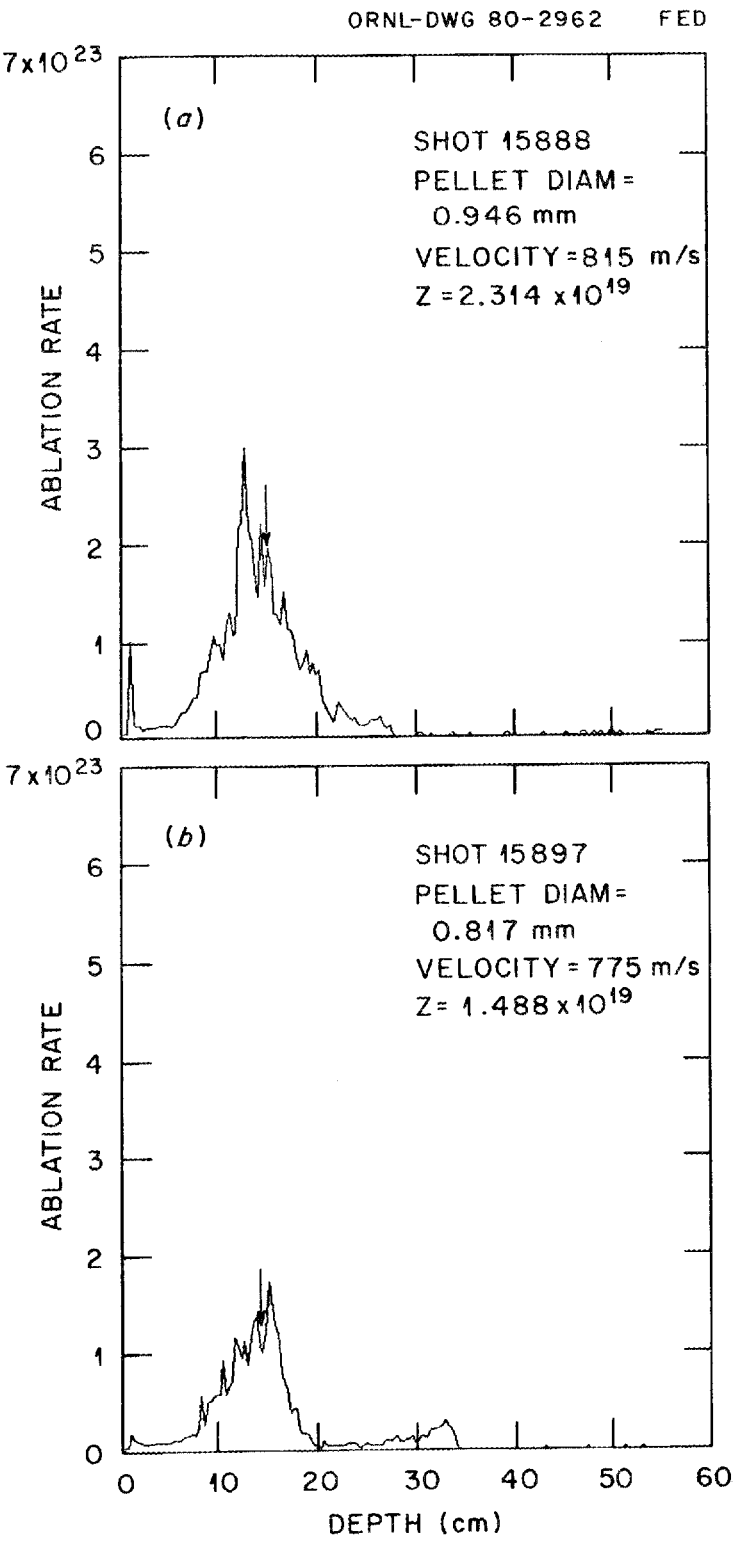

Fig. 4.40 Ablation rate (atoms/s) for shots 15888 and 15897.

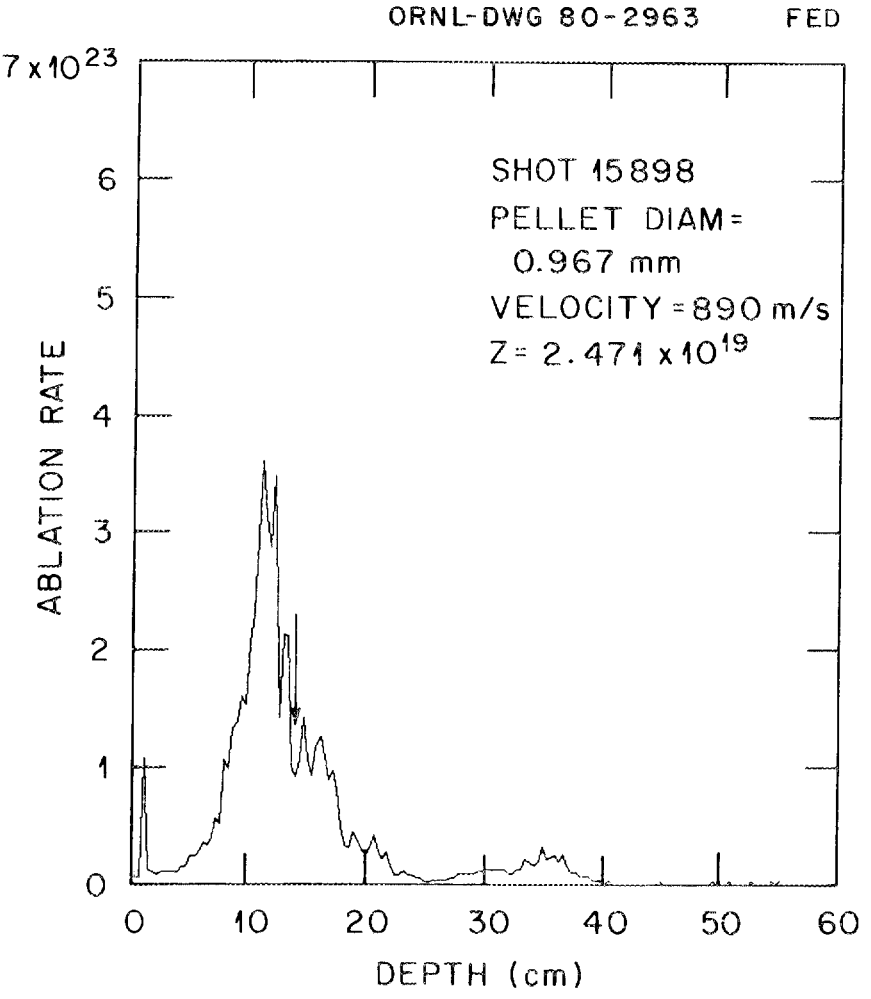

Fig. 4.41 Ablation rate (atoms/s) for shot 15898.

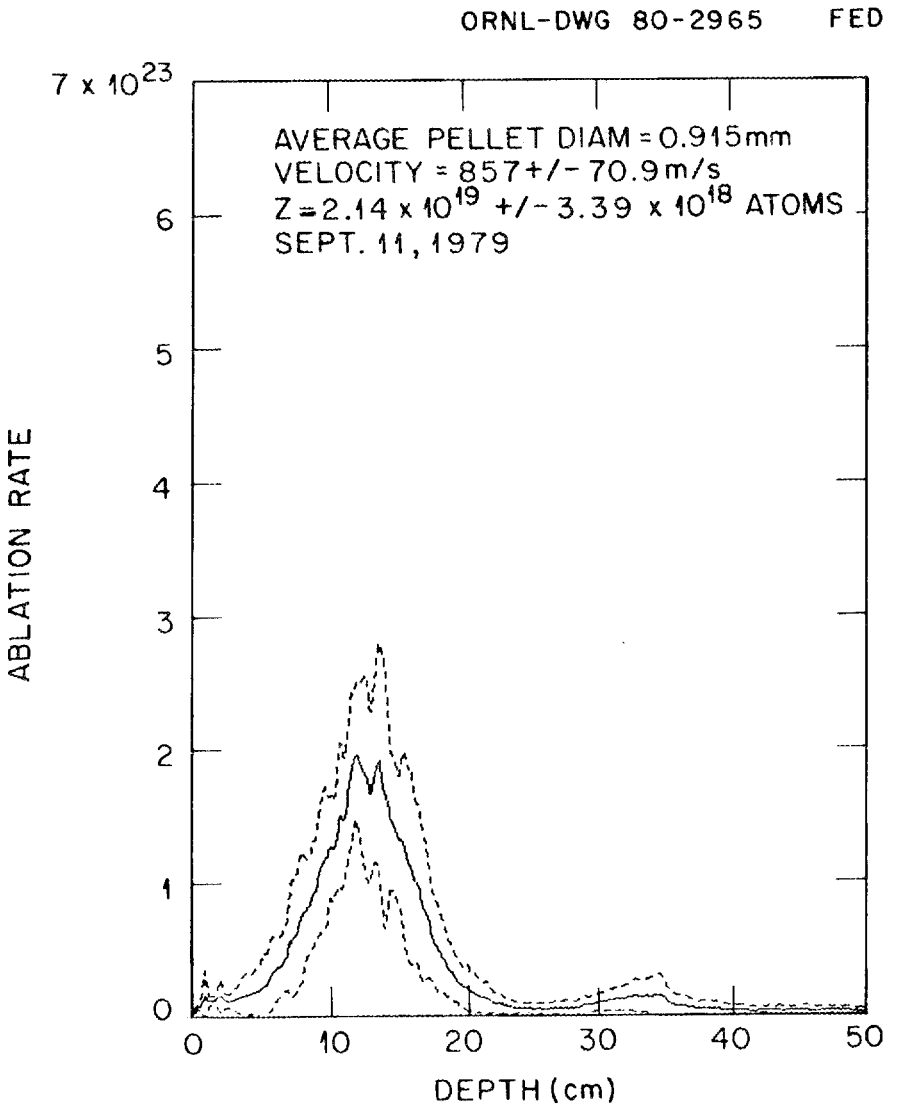

Fig. 4.42 Average ablation rate (atoms/s) inferred from H_α signals for September 11, 1979.

column and strike the wall of the vacuum vessel. The dashed lines indicate the average +/- the standard deviation.

As before, measured pellet velocity and pellet Z and diameter (calculated from integrating the ablation rate) are presented on each plot.

The computer-stored data were not available for shots 15863, 15872, and 15887, and the oscilloscope traces are presented instead (Fig. 4.43) to indicate the timing of the interferogram.

The signal present on the H_α plots for $r \geq 54$ cm is indicative of the pellet having passed all the way through the plasma and striking the vacuum vessel on the far side.

Because of the low level of the signal as the pellet entered the plasma on September 11, there is approximately a 2-cm jitter in determining where the H_α trace starts (and thus the position of the plasma edge). It should also be noted from examining Figure 4.43 that the placement of the arrow indicating where the interferogram was made on Figs. 4.34-4.41 has some uncertainty in it and that there will therefore be some uncertainty in the exact ablation rate at the time the interferogram was made.

4.3.5 Interferograms and shadowgraphs from September 11, 1979

Figures 4.44-4.50 are the interferograms and shadowgraphs made on September 11, 1979. Again shadowgraphs are not presented if the pellet

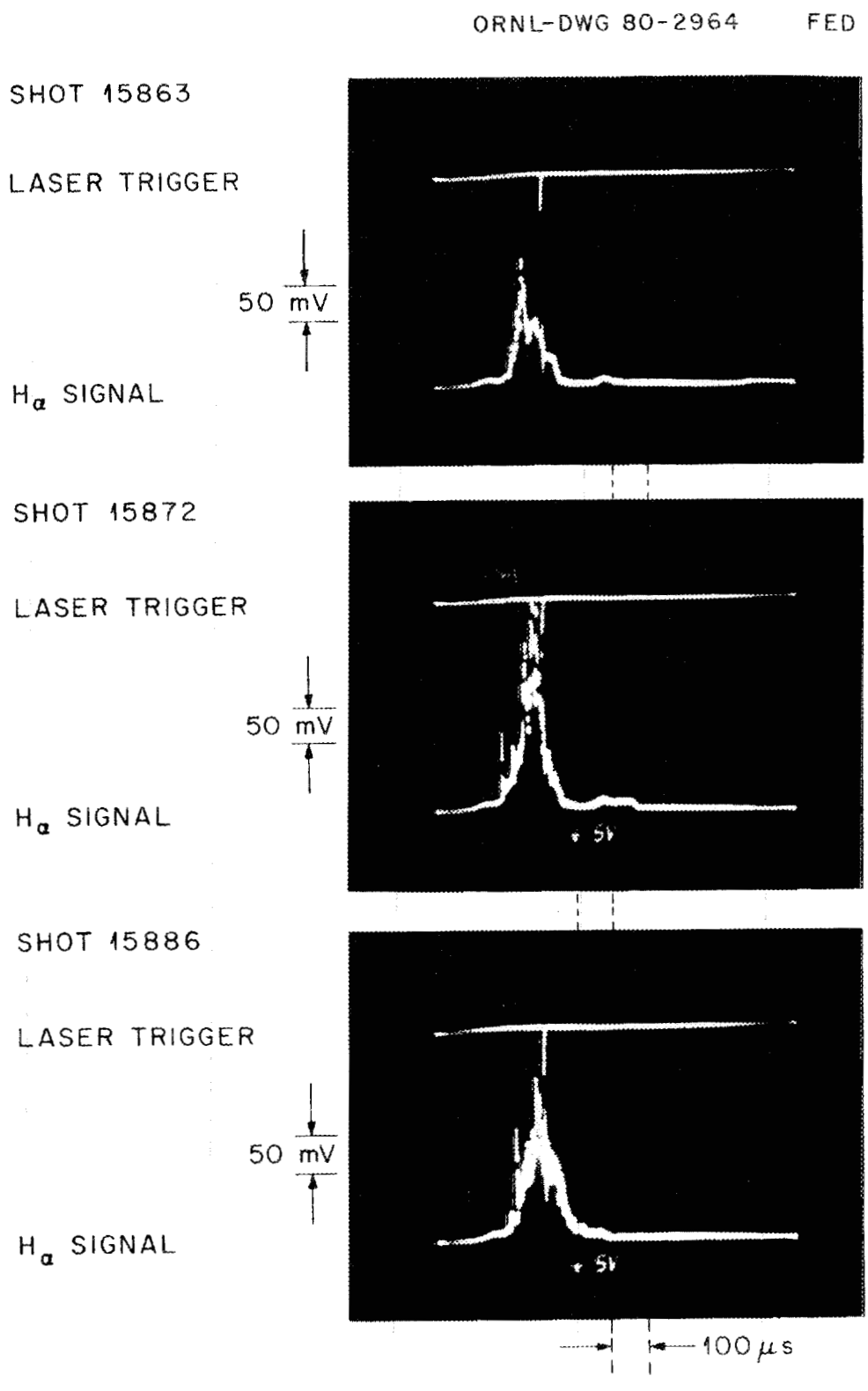

Fig. 4.43 H_α oscilloscope traces for shots 15863, 15872, and 15886.

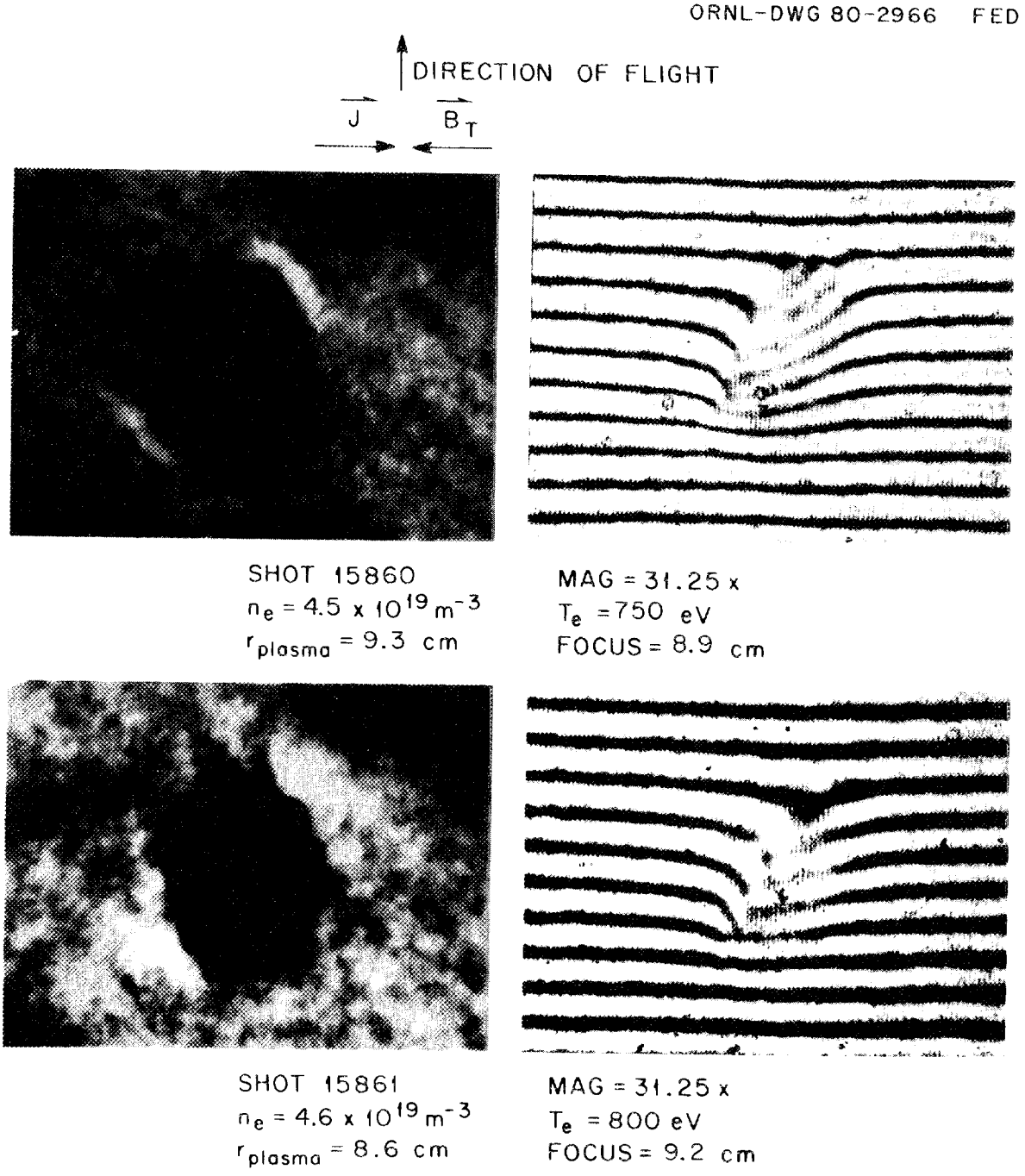

Fig. 4.44 Interferograms and shadowgraphs for shots 15860 and 15861.

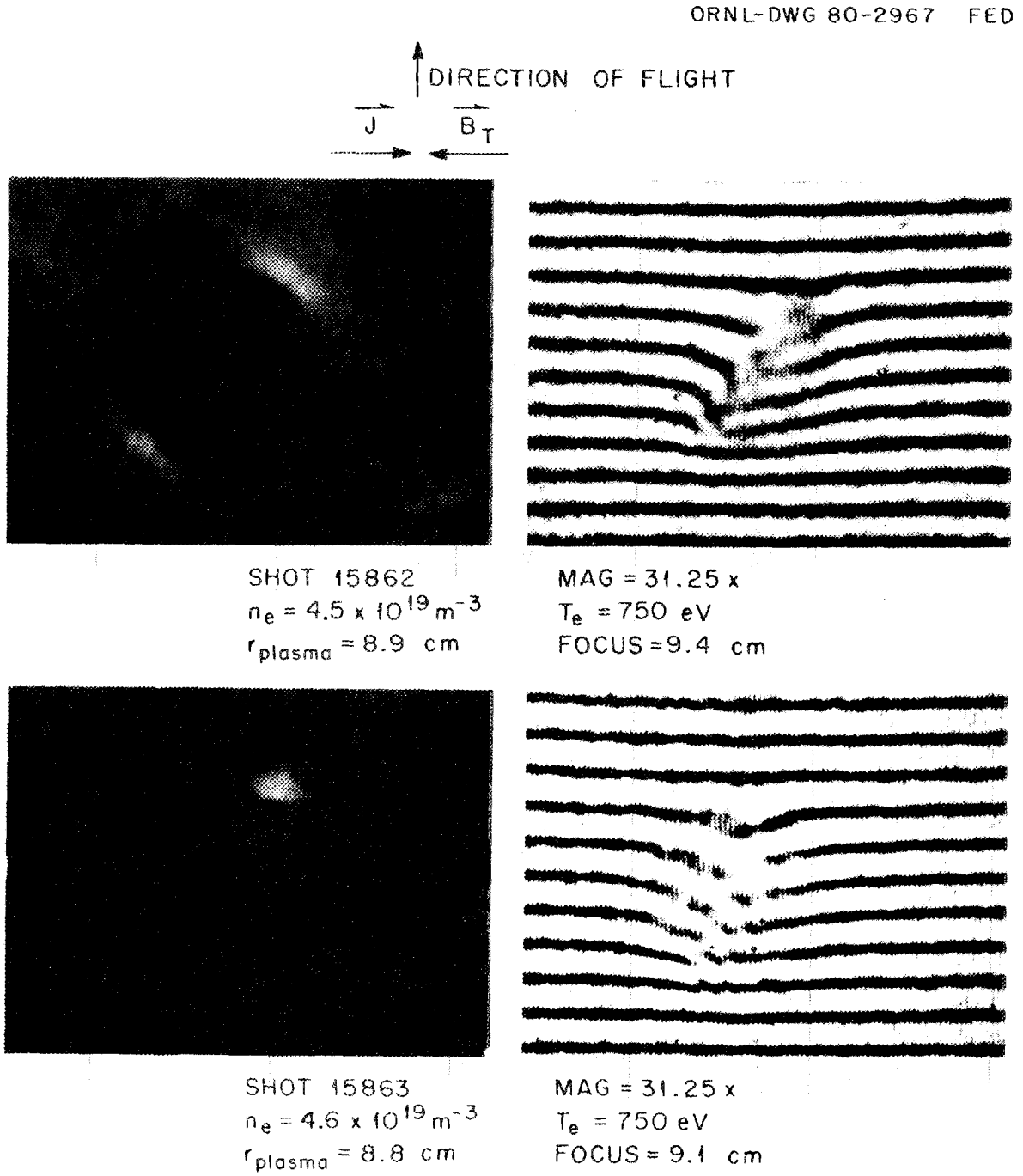

Fig. 4.45 Interferograms and shadowgraphs for shots 15862 and 15863.

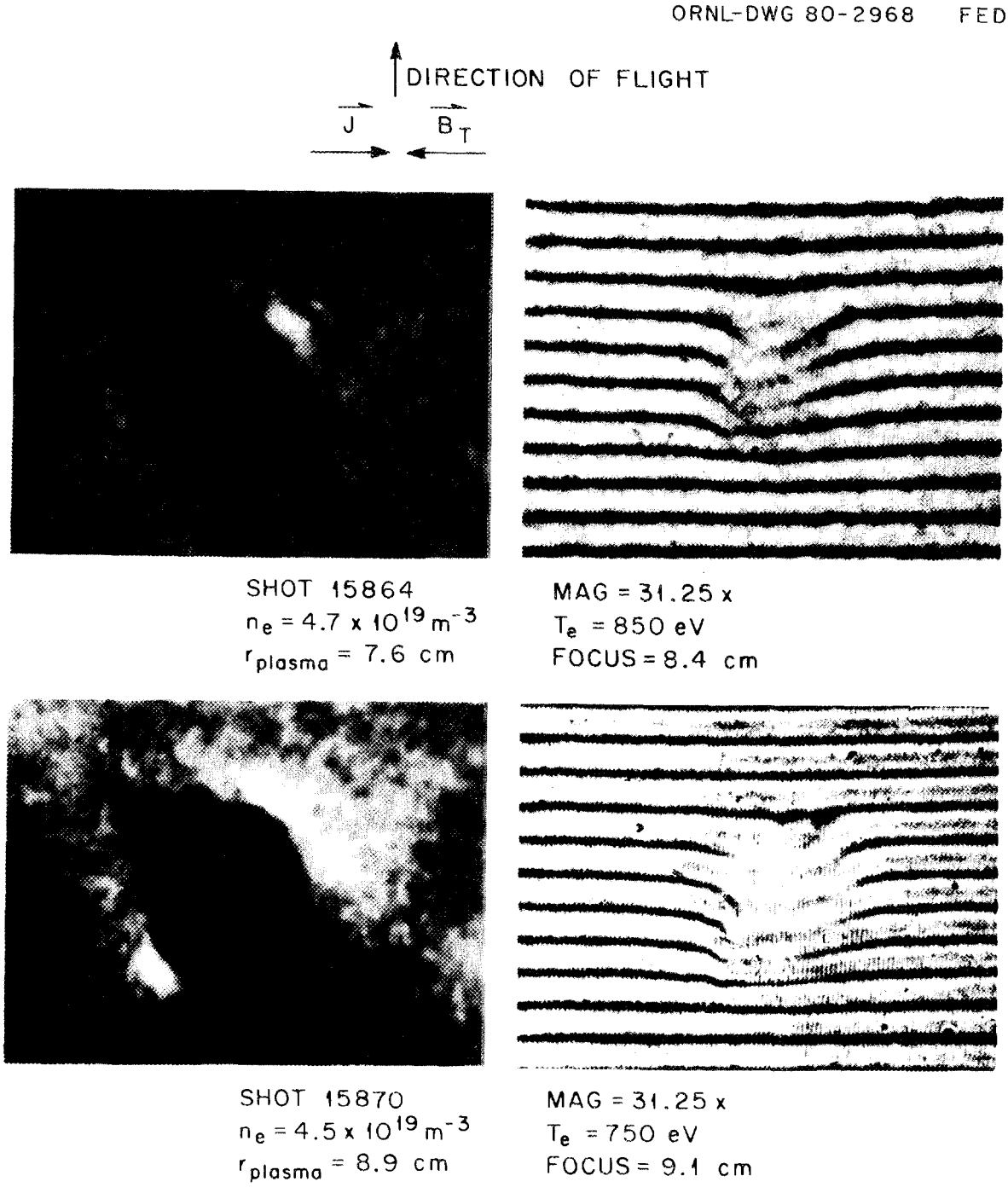

Fig. 4.46 Interferograms and shadowgraphs for shots 15864 and 15870.

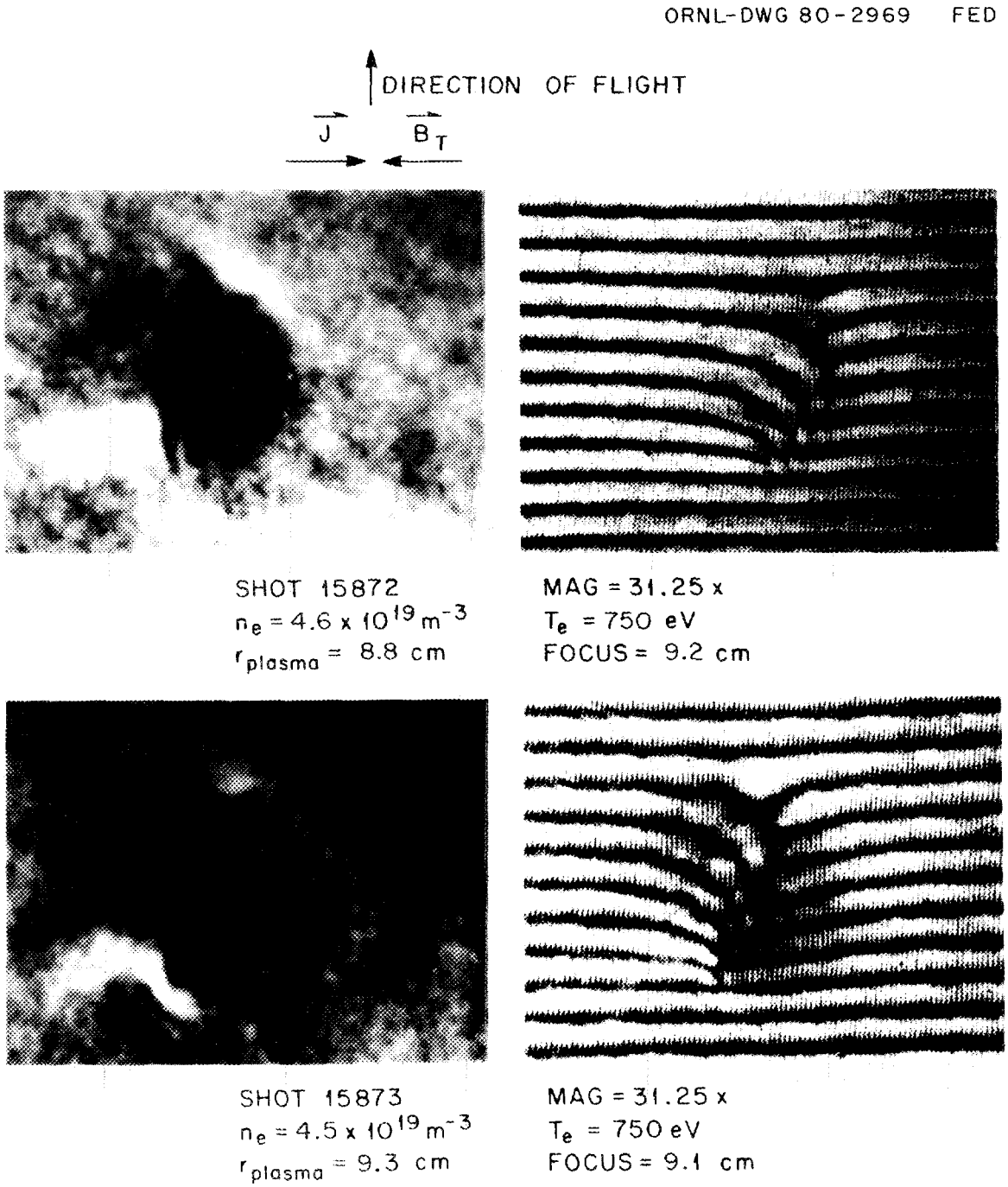

Fig. 4.47 Interferograms and shadowgraphs for shots 15872 and 15873.

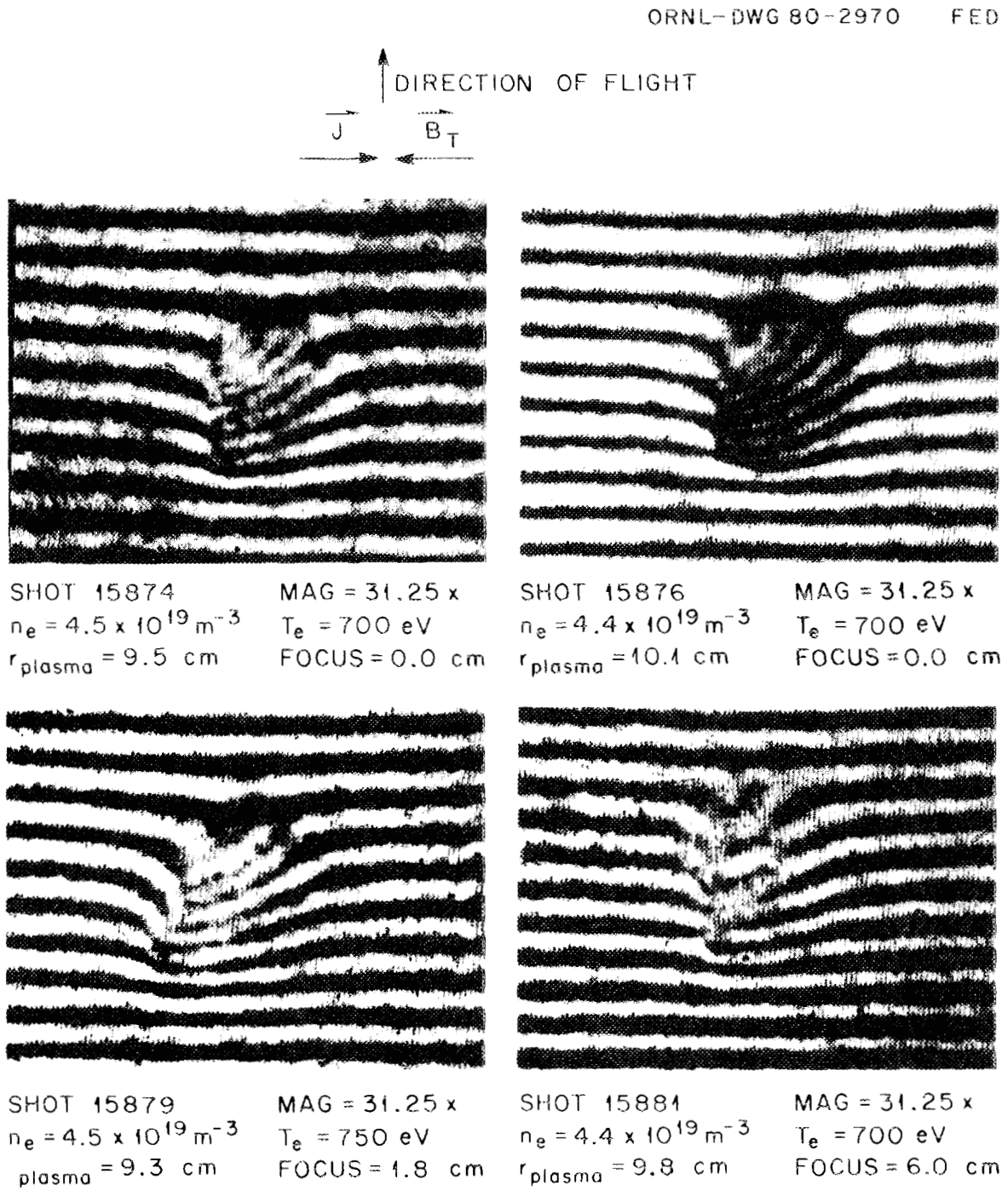

Fig. 4.48 Interferograms for shots 15874, 15876, 15879, and 15881.

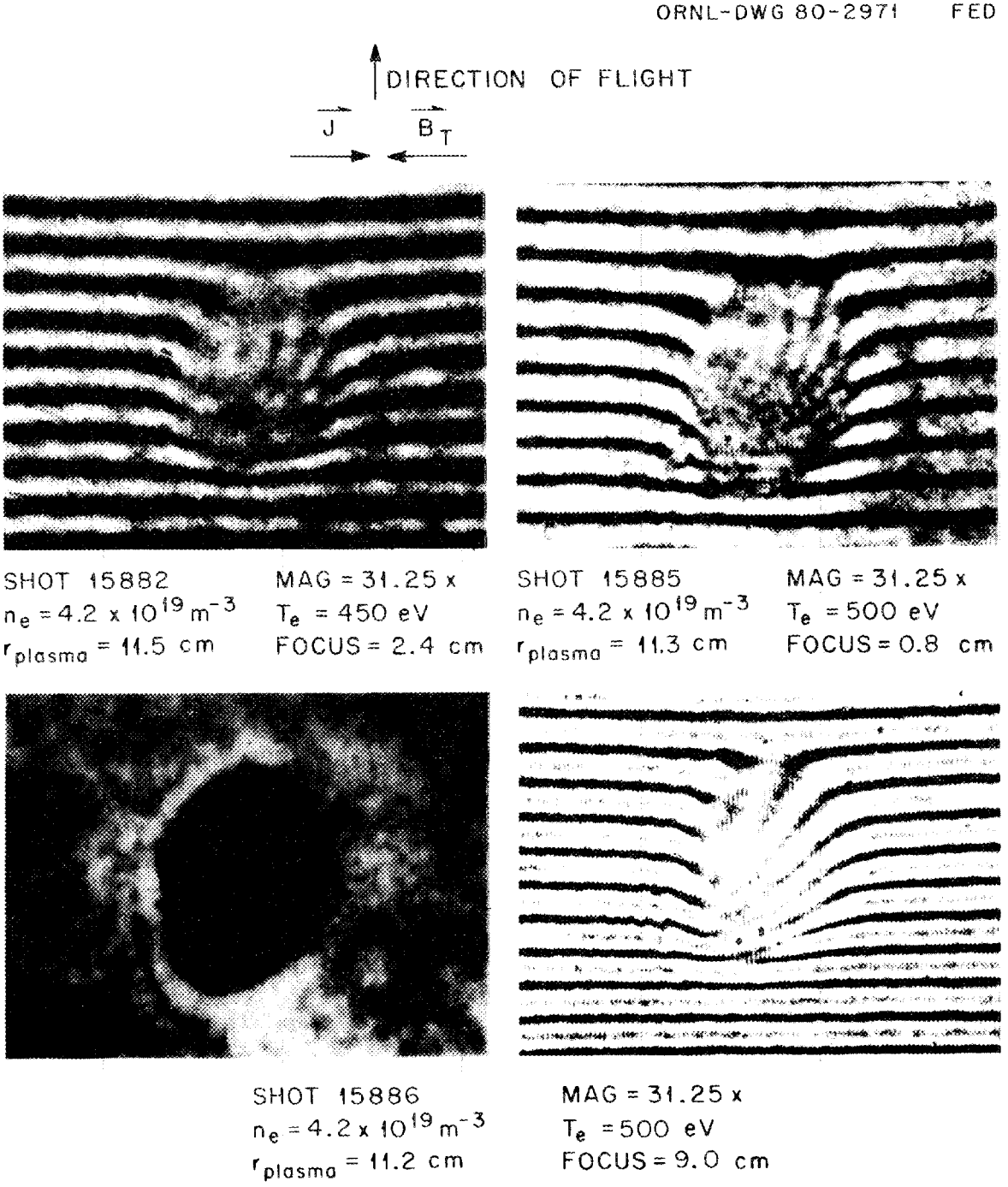

Fig. 4.49. Interferograms for shots 15882, 15885, and 15886; shadowgraph for shot 15886.

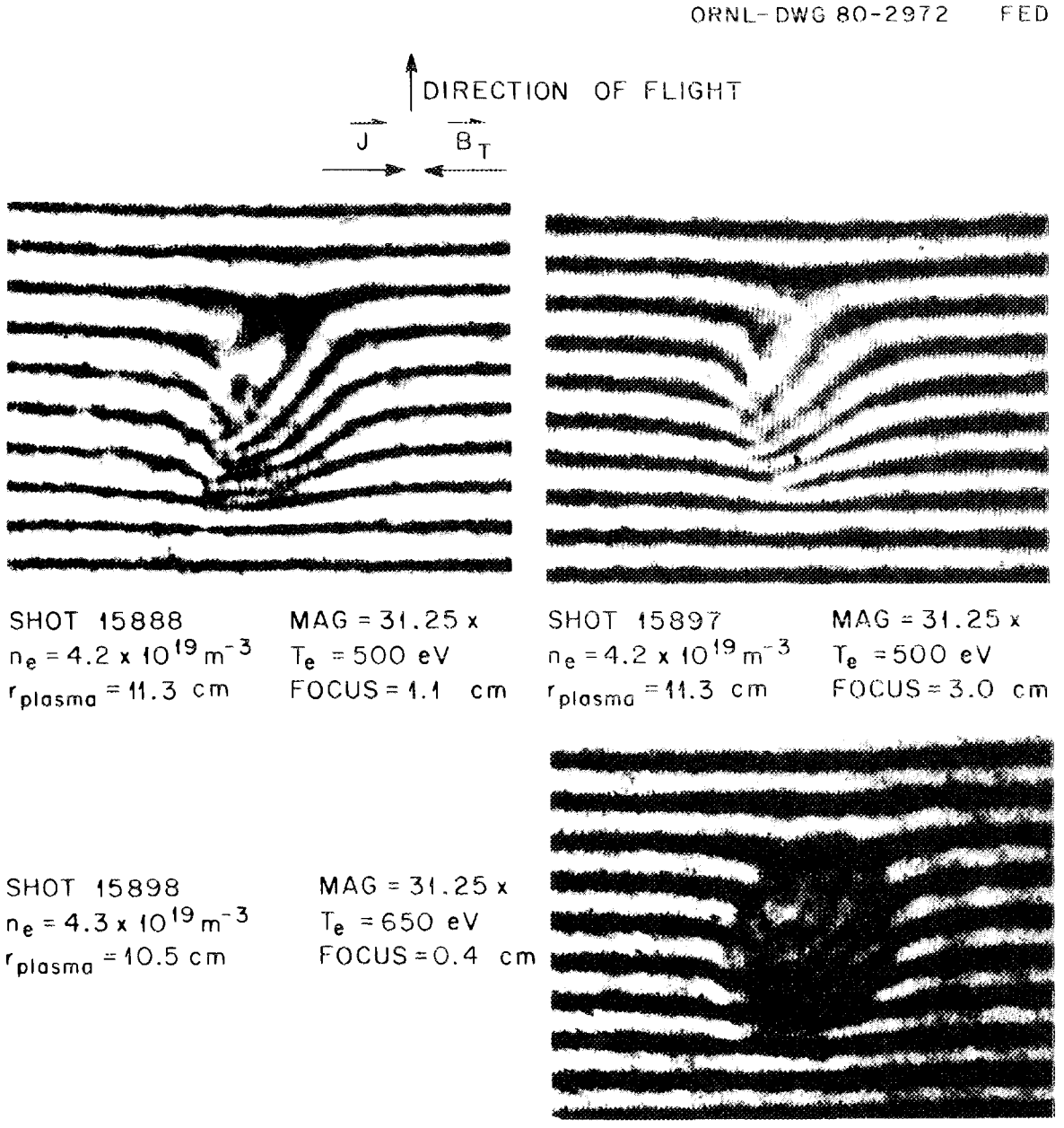

Fig. 4.50 Interferograms for shots 15888, 15897, and 15898.

was more than 1 cm from the interferometer focus. The general comments made in discussing the September 6 data as to orientation, scale factors, noise, etc., are still applicable.

4.4 Time-Exposure Photographs of Pellet Ablation

Figure 4.51 is a shadowgraph of a pellet superimposed on a time-exposure photograph of the light emitted by the neutrals in the vicinity of the pellet. This photograph was made by removing the ruby laser line filter from the interferometer optics. Thus, the shadowgraph became a time exposure of the light emitted by the neutrals ablated from the pellet, and the shadow of the pellet is also visible from firing the ruby laser.

The H_α trace from the shot is shown above the shadowgraph along with the trigger pulse that fired the ruby laser.

It can be seen that pellet end-of-life occurred in the field of view of the shadowgraph. The point of interest is the very short scale length for transport across magnetic field lines as compared to along them. The timing on the H_α trace indicates that the pellet vanished at a minor radius of 8 cm (approximately 10 μs after the shadowgraph was made). The film appears to be relatively unexposed for minor radius $r \leq$ 8 cm, indicating that the ablation products are rapidly ionized to H^+ and H_2^+ and contained on magnetic field lines. ASA 400-speed color film was used for this photo.

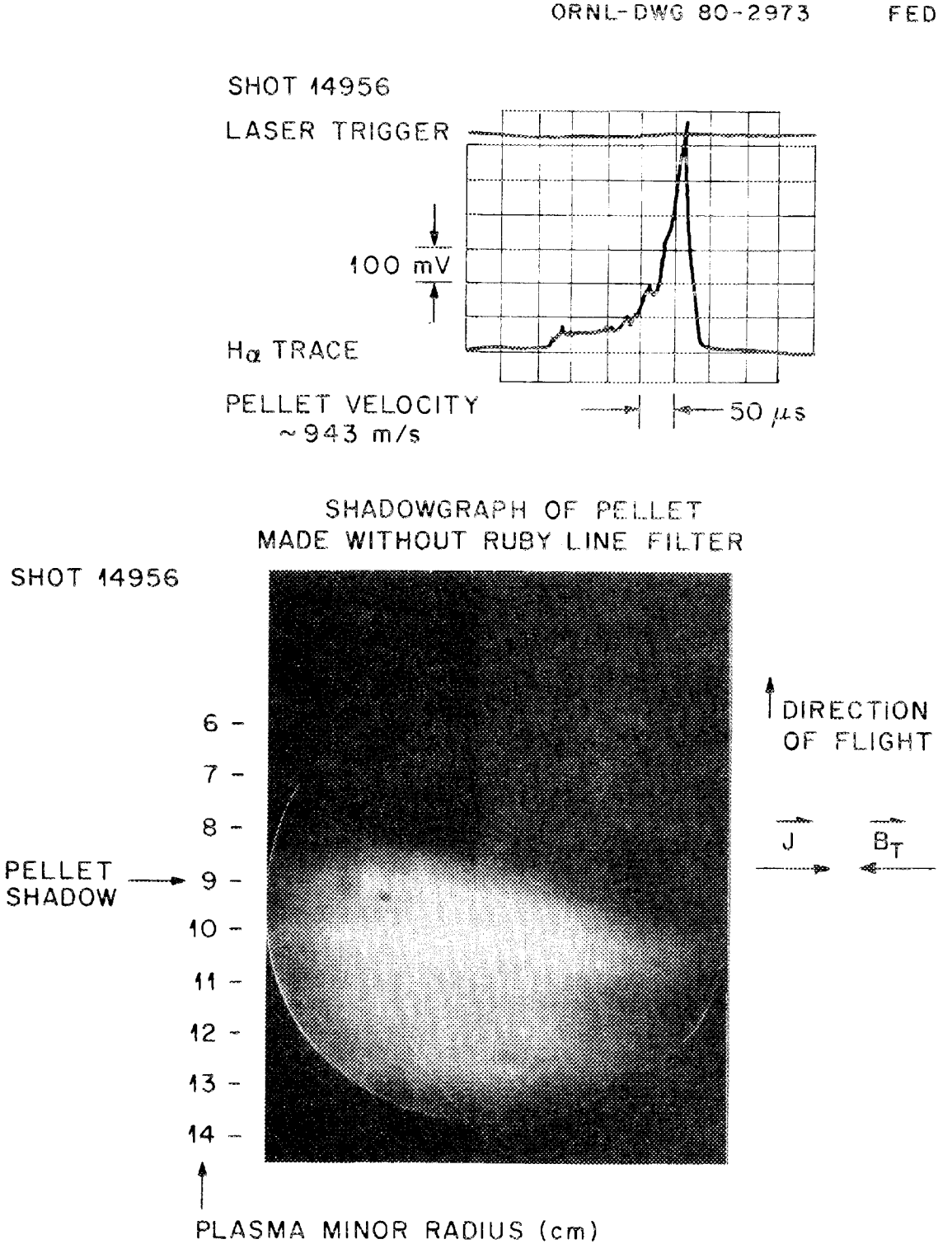

Fig. 4.51 Shadowgraph and time exposure of pellet for shot 14956.

Figure 4.52 is a time exposure of the light from a pellet. The ruby laser was not fired for this photo; otherwise it is the same as Figure 4.51. The H_α trace for shot 14590 is not available, but the traces for the shots immediately before and after are shown above. Again the streaks in the light along the magnetic field lines corresponding to the spikes on the H_α traces indicate that ablation products travel away from the pellet along magnetic field lines. ASA 3000-speed black and white polaroid film was used for this photo.

4.5 Summary of Chapter 4

Chapter 4 presents the experimental data with minimal analysis and comment. Data analysis will be done in Chap. 5.

Section 4.2 gives the data from September 6, 1979, and Sect. 4.3 gives the data from September 11, 1979. The data consist of Thomson scattering profiles of the electron density and temperature 1 ms before and 1 ms after pellet injection, instantaneous pellet ablation rates inferred from H_α photon emission, line-averaged density before and after injection, local power and energy loss during injection, hard x-ray data showing the presence or absence of runaway electrons, and interferograms and shadowgraphs of pellets taken at various minor radii and ablation rates.

Section 4.4 discusses time-exposure photographs of the pellet ablation made using the shadowgraph optics with the ruby laser line filter

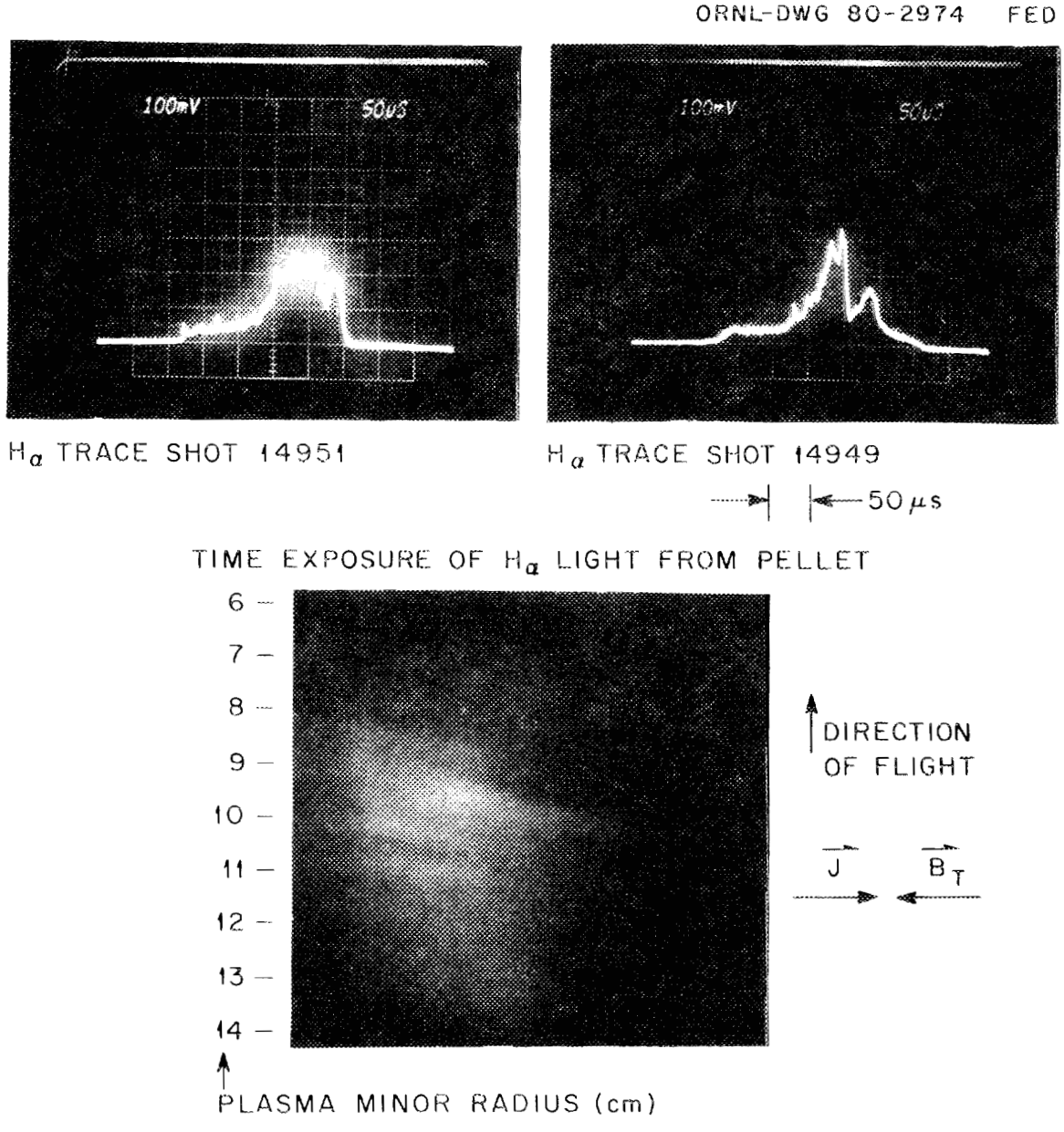

Fig. 4.52 Time exposure of H_α light from pellet made with shadowgraph optics for shot 14950.

removed from the system. The point of interest is the apparent rapid confinement of ablation products on magnetic field lines.

References

1. J. Cooper, J. Sci. Instrum. 39, 467 (1962).

2. C. A. Foster, R. J. Colchin, S. L. Milora, K. Kim, and R. J. Turnbull, Nucl. Fusion 17, 1067 (1977).

3. S. L. Milora, C. A. Foster, P. H. Edmonds, and G. L. Schmidt, Phys. Rev. Lett. 42, 97 (1979).

4. S. L. Milora et al., "Results of Hydrogen Pellet Injection into ISX-B," submitted to Nucl. Fusion.

Chapter 5

Analysis of Data

Data analysis will begin with a discussion of the downward curvature of the pellet trajectory in Section 5.1. The effect of superthermal electrons on the pellet ablation rate will be analyzed in Sect. 5.2. Section 5.3 will show that charge exchange losses due to pellet injection are small. Pellet ablation rates inferred from emission of H_α photons will be compared with data from other diagnostics in the first parts of Sect. 5.4, and will be compared with the predictions of neutral shielding theory in the last parts of Sect. 5.4. Results of computer analysis of the interferograms will be discussed in Sect. 5.5, along with the presence of discontinuities on the shadowgraphs and interferograms. Finally, an energy loss equation and $n_e \times \ell$ data from the interferograms will be used to calculate the ionization fraction of the ablated pellet material.

5.1 Pellet Trajectories

As mentioned in Chap. 4, the pellet trajectories were observed to curve downward and parallel to the magnetic field in the direction of the electron drift velocity. The curvature parallel to the magnetic field has been previously observed and explained in terms of differential ablation pressure.[1] Figure 5.1 is a tangential photograph of the H_α light emitted as the pellet traversed the plasma. The downward curvature is observable.

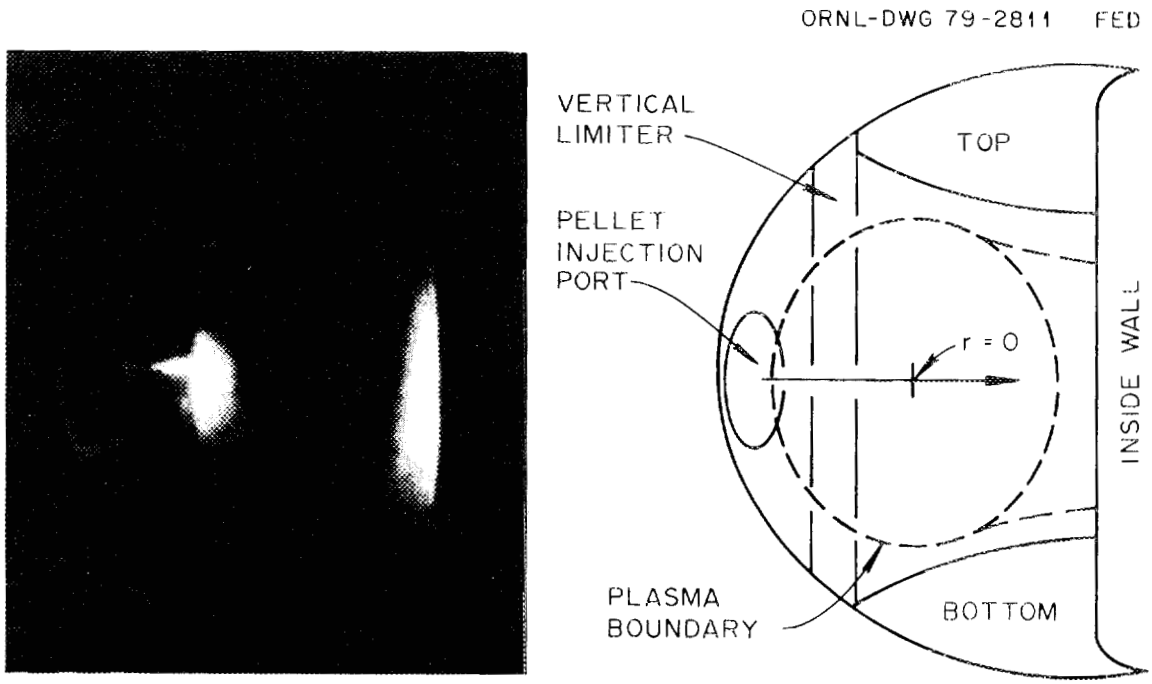

Fig. 5.1 Photograph of pellet trajectory.

As previously discussed, the vertical distance of the pellet from the horizontal midplane of the tokamak can be calculated from the focal point of the holographic interferogram of the pellet. Tables 5.1 and 5.2 list the experimentally observed or inferred quantities at the time of the hologram formation. The column labeled r_v is the vertical distance of the pellet from the tokamak horizontal midplane at the time of hologram formation. The nominal injection trajectory in vacuum was $\sim$5 cm above the tokamak midplane with a standard deviation of 1 cm. It can be seen from the data that the pellet trajectory curved sharply downward as the pellet penetrated the plasma. There were no observations of the pellet actually dropping below the tokamak horizontal midplane. The downward drop correlates with the decrease in pellet radius r_p. The pellet radius listed is found by integrating the ablation rate inferred from the H_α signal. The pellet trajectory is observed to drop 4-5 cm in a horizontal distance of $\sim$5 cm as the pellet nears the center of the plasma (r = 8-13 cm).

The curvature of the pellet trajectory made little difference in the effect of the pellet on the plasma. On September 6 the pellet was completely ablated at an average distance of $\sim$5 cm from the plasma center; therefore, it did not matter if the pellet trajectory missed the plasma center by 4 cm. On September 11, as has been shown in Chap. 4, the pellet ablation rate was small to zero as it passed through the central portion of the plasma; thus, missing the plasma center would have very little effect on the experimentally observable quantities.

Table 5.1. Experimentally observed or inferred quantities at time of interferogram for September 6, 1979

Minor radius (cm)	Shot number	$n_e(r)$ ($\times 10^{19}$ m^{-3})	$T_e(r)$ (eV)	r_p (mm)	G (atoms/s $\times$ 10^{23})	r_v (cm)	ℓ_p (mm)
10.8	15681	1.1	700	0.34	3.0	0.5	1.6
11.0	15699	1.1	700	0.45	2.0	0.5	1.5
11.1	15680	1.1	700	0.43	3.0	0.6	2.0
11.2	15684	1.1	700	0.47	2.0	0.0	1.5
11.4	15686	1.1	650	0.42	2.0	0.5	1.5
11.6	15679	1.0	650	0.42	2.8	0.5	2.0
11.6	15683	1.0	650	0.47	1.5	0.8	1.7
11.6	15697	1.0	650	0.51	4.0	5.7	1.4
11.7	15698	1.0	650	0.38	0.5	0.0	1.2
11.7	15695	1.0	650	0.43	2.0	0.3	1.7
11.8	15678	1.0	650	0.43	4.5	0.0	2.0
11.9	15685	1.0	650	0.43	2.0	0.6	1.5
13.0	15700	0.9	600	0.46	1.0	0.6	1.4
13.7	14455	0.9	500	0.50	0.5	5.2	0.88
17.5	14436	0.6	300	0.53	0.2	4.0	0.96

Table 5.2. Experimentally observed or inferred quantities at time of interferogram for September 11, 1979

Minor Radius (cm)	Shot number	$n_e(r)$ $\times 10^{19}$ m^{-3}	$T_e(r)$ (eV)	r_p (mm)	G ($\times 10^{23}$ atoms/s)	r_v (cm)	ℓ_p (mm)
7.6	15864	4.7	850	0.26	0.4	1.1	0.83
8.6	15861	4.6	800	0.28	2.0	0.0	1.0
8.8	15872	4.6	750	0.18	2.0	0.0	1.0
8.8	15863	4.6	750	0.27[a]	1.0	0.5	1.1
8.9	15862	4.5	750	0.24	0.3	0.2	0.97
8.9	15870	4.5	750	0.26	0.9	0.5	1.0
9.3	15873	4.5	750	0.20	1.5	0.5	1.2
9.3	15860	4.5	750	0.22	1.0	0.7	0.97
9.3	15879	4.5	750	0.35	2.0	5.3	0.73
9.5	15874	4.5	700	0.29	1.0	6.1	0.68
9.8	15881	4.4	700	0.26	1.5	2.9	0.86
10.1	15876	4.4	700	0.26	1.0	6.1	0.68
10.5	15898	4.3	650	0.25	1.2	5.9	0.83
11.2	15886	4.2	500	0.17	1.3	0.6	1.3
11.3	15897	4.2	500	0.24	1.2	4.7	0.94
11.3	15882	4.2	450	0.26	0.9	5.0	0.90
11.3	15888	4.2	500	0.30	2.0	5.6	0.93
11.3	15885	4.2	500	0.35	2.0	5.8	0.99

[a]Estimated.

The force necessary to cause the downward curvature can be estimated. If one assumes a typical average mass (where the curvature is important) of 0.75×10^{19} protons, a distance of 5 cm, and a time of 50 μs, then the necessary average force at constant acceleration is ∿0.3 N. Over an area of ∿1 mm^2, this is a pressure of ∿3×10^5 Pa, or ∿3 atm. This is very difficult to explain in terms of differential ablation pressure, not only because of the magnitude of the force, but also because of the direction. The force from differential ablation would be along the helical magnetic field lines, and any force along the field lines sufficient to move the pellet down 5 cm would also have swept it out of the 7.5-cm field of view of the interferometer.

One might speculate that a current from front to back of the pellet causes the downward force. Using $\bar{F} = \bar{I}\ell \times \bar{B}$, the necessary current (for B = 1.5 T) is I = 200 A. For an area of 1 mm^2 this implies a current density of 2×10^8 $A \cdot m^{-2}$. If the ablated hydrogen was 20% ionized, its conductivity would be[2]

$$\sigma \approx \frac{n_e q^2}{m_e(\nu_{ei}/2 + \nu_{eo})}$$

$$= \frac{f_i}{[2.38 \times 10^{-6} T^{1/2}(1 - f_i) + 5.18 \times 10^{-5} f_i T^{-3/2}\ \ell n\Lambda]}\ , \qquad (5.1)$$

where the resistivities due to $e^- - H_2$ and $e^- - H^+$ collisions have been added and

$f_i \equiv n_e/(n_e + n_o) \equiv$ ionization fraction,

$\nu_{ei} = 2.91 \times 10^{-12}\ T_e^{-3/2} n_e\ \ell n\Lambda \equiv$ electron-ion collision time, and

$\nu_{eo} = n_o \sigma_{eo} V_e \equiv$ electron-H_2 collision frequency.

For 1-eV electrons and $\sigma_{eo} \tilde{=} 10^{-19}\ m^2$, then[3] (with $\ell n\Lambda = 3$)

$$\sigma \tilde{=} 6.4 \times 10^3\ (\Omega\text{-m})^{-1}.$$

This implies an electric field

$$E = J/\sigma \tilde{=} 3 \times 10^4\ V/m$$

or a potential difference

$$V = E\ell \tilde{=} 30\ V.$$

This kind of front-to-back potential difference and driven current seems plausible and is one possible explanation for the downward curvature of the pellet trajectory. This potential difference is the same order of magnitude as the thermal gradient.

5.2 Effects of Nonthermal Electrons

It was shown in Chap. 4 that superthermal electrons were present in the discharge on September 6. Over the course of the experiments the presence of runaway electrons was correlated with a dramatic growth in the effective area of the pellet as the pellet penetrated the plasma; the pellet area is inferred from the dark area on the shadowgraphs and the area of disturbed fringes on the interferogram. The column labeled

ℓ_p in Table 5.1 is the effective length of the pellet perpendicular to the magnetic field found by measuring the length of the area of indistinct fringes on the interferogram perpendicular to the magnetic field and correcting for magnification. The data show that over a distance of $\sim$5 cm the effective perpendicular length of the pellet increases from $\sim$1 mm to $\sim$2 mm while the actual mass of the pellet decreases about a factor of 2. The column labeled r_p shows what the spherical radius of the pellet would be if it had solid hydrogen density. This is found by subtracting the integral of the pellet ablation rate from the original pellet mass, which is assumed to be the total integral of the ablation rate. Because the pellet radius increased $\sim$0.5 mm in $\sim$50 μs, the velocity of expansion is $\sim$10 m/s. This velocity will be used in later calculations.

From the empirical formulas presented by Evans[4] it can be calculated that electrons with energy less than $\sim$100 keV can be stopped by 1-mm of solid hydrogen. This is subject to large statistical fluctuations, however, due to the occurrence of electron-electron collisions in which large energy losses can be experienced.

The energy necessary to cause the pellet expansion can be estimated. Because the neutral hydrogen has expanded about a factor of 20 in volume over its solid density, assume that it is a fluid near the thermodynamic critical point (where the compressibility is high). The enthalpy at the critical point is[5] 77.6 J/mole, and for solid hydrogen at 13 K, $h \tilde{=} -740.2$ J/mole or

$$\Delta h \overset{\sim}{=} 800 \text{ J/mole.}$$

There are $\sim 3 \times 10^{-5}$ moles of hydrogen remaining so that

$$\Delta E \sim 2.5 \times 10^{-2} \text{ J.}$$

Assuming 500-keV runaways depositing all their energy (for instance), this corresponds to 3.13×10^{11} runaway electrons compared to a total plasma electron number of $\sim 10^{19}$. Alternatively, it corresponds to a runaway electron current of

$$I = \frac{dq}{dt} = \frac{NqV}{2\pi R} \overset{\sim}{=} 2 \text{ A}$$

compared to a total plasma current of 110 kA. Clearly it does not take many runaway electrons depositing energy deep in the pellet to cause it to expand at a high rate.

This process is important because the plasma power incident on the pellet increases as the square of the pellet radius. Neutral shielding theory predicts that the total ablation rate G increases as the 4/3 power of the pellet radius. However, at some point as the pellet increases in radius, the pellet becomes unshielded because there is no longer enough material to maintain a shielding cloud. At this point the pellet's life comes to a catastropic end. This description bears a striking resemblance to the September 6, 1979, ablation data.

5.3 Charge Exchange Losses

An estimate of local charge exchange losses due to pellet injection will be made by comparing the estimated power lost in radiation to the measured local energy loss.

It was shown in Chap. 4 that the local energy loss during pellet injection was about 18 J. The ratio of the cross section for the production of Lyman-alpha radiation to that for the production of Balmer-alpha radiation by dissociative excitation is about a factor of 15 for electron energies from 100 eV-1 keV.[3] Assuming 0.02 H_α photons per atom ablated (experimental data), this implies 0.3 Lyman-alpha photons per particle ablated. Using an average of 3×10^{19} atoms per pellet and a photon energy of 10.2 eV, this implies a radiated power of $\sim$15 J and a local charge exchange loss during pellet injection of $\sim$3 J (18 J minus 15 J). Assuming an average energy of 1 keV per charge exchange loss, this corresponds to a loss of 2×10^{16} particles to charge exchange during pellet injection compared with $\sim 10^{19}$ particles in the plasma.

Note that the above calculation is rather crude and that the charge exchange losses could be much smaller than the above figure. In any event, the loss of energy and particles due to charge exchange during pellet injection is small (too small to measure within the accuracy of the available diagnostics).

5.4 Analysis of H_α Data

It was shown in Chap. 4 how pellet ablation rates were derived from the emission of H_α photons during pellet injection. The first two parts of Sect. 5.4 will compare quantities inferred from H_α ablation rate data with other experimentally observable quantities. The remainder of Sect. 5.4 will discuss the experimentally observed ablation rates and compare them with theory.

5.4.1 Comparison of measured line-averaged density rise with that inferred from H_α data

Tables 5.3 and 5.4 give a shot-by-shot comparison of the line-averaged density rise measured by the microwave/FIR interferometer and $\Delta\bar{n}_e$ calculated from the H_α data. The calculated line-averaged density increase was found numerically by multiplying the ablation rate by the time to cross a differential volume in the tokamak and by assuming that the Δn_e thus derived was added to n_e in the differential volume.

The agreement between the measured line-averaged density rise and that calculated from the H_α data is good (as seen in the small difference (Δ)AVG in the tables). The error bars on the measured line-averaged density rise are on the order of 0.5×10^{19} m^{-3}. Given this error bar the agreement between the two measurements is very good.

Table 5.3. Comparison of $\Delta\bar{n}_e$ measured by microwave/FIR interferometer with that inferred from H_α data for September 6, 1979

Shot number	$\Delta\bar{n}_e$ (from interferometer) ($\times 10^{19}$ m^{-3})	$\Delta\bar{n}_e$ (from H_α data) ($\times 10^{19}$ m^{-3})	(Δ) ($\times 10^{19}$ m^{-3})
15633	2.4	3.7	1.3
15638	3.1	3.6	0.5
15639	2.5	3.9	1.3
15641	2.0	2.4	0.4
15642	3.5	3.7	0.2
15643	3.3	3.5	0.2
15644	2.1	3.0	0.9
15646	2.1	3.2	1.1
15647	2.6	3.0	0.4
15649	2.5	2.8	0.3
15651	2.4	2.4	0.0
15656	2.4	2.6	0.2
15657	3.5	3.9	0.4
15661	1.5	1.9	0.4
15667	2.9	2.6	-0.3
15668	1.9	1.9	0.0
15669	3.1	3.2	0.1
15678	2.0	2.6	0.6
15679	2.3	2.7	0.4
15681	2.1	2.1	0.0
15682	2.1	1.9	-0.2
15683	2.4	4.1	1.7
15685	3.2	3.0	-0.2
15686	2.3	2.4	0.1
15687	1.6	1.3	-0.3
15690	1.4	1.1	-0.3
15697	2.3	3.0	0.7

Table 5.3. — cont'd.

$(\Delta\bar{n}_e)$AVG Interf = $(2.43 \pm 0.57) \times 10^{19}$ m^{-3}

$(\Delta\bar{n}_e)$AVG H_α = $(2.80 \pm 0.79) \times 10^{19}$ m^{-3}

$(|\Delta|)$AVG = $(0.48 \pm 0.44) \times 10^{19}$ m^{-3}

(Δ)AVG = $(0.37 \pm 0.52) \times 10^{19}$ m^{-3}

Table 5.4. Comparison of $\Delta\bar{n}_e$ measured with FIR interferometer with that inferred from H_α data for September 11, 1979 (RCA = 6 cm)

Shot number	$\Delta\bar{n}_e$(FIR) ($\times 10^{19}$ m^{-3})	$\Delta\bar{n}_e(H_\alpha)$ ($\times 10^{19}$ m^{-3})	Δ ($\times 10^{19}$ m^{-3})
15858	1.5	1.1	-0.4
15860	1.4	1.0	-0.4
15861	1.7	1.5	-0.2
15869	1.8	1.2	-0.6
15872	1.7	1.2	-0.5
15873	1.4	1.6	0.2
15874	1.3	2.4	1.1
15875	2.2	1.4	0.8
15877	1.9	2.1	0.2
15885	2.5	1.9	-0.6
15888	2.4	1.9	-0.5
15889	1.2	1.8	0.6

$(\Delta\bar{n}_e)$AVG FIR = $(1.75 \pm 0.43) \times 10^{19}$ m^{-3}

$(\Delta\bar{n}_e)$AVG H_α = $(1.59 \pm 0.44) \times 10^{19}$ m^{-3}

$(|\Delta|)$AVG = $(0.51 \pm 0.26) \times 10^{19}$ m^{-3}

(Δ)AVG = $(-0.03 \pm 0.59) \times 10^{19}$ m^{-3}

It should be mentioned that the calculated $\overline{\Delta n}_e$ for September 11, 1979, was found by assuming that the pellet missed the center of the plasma by 6 cm (RCA = 6 cm). This calculation was repeated assuming the pellet went through the center of the plasma and the change in $(|\Delta|)$AVG was less than 10%.

5.4.2 Comparison of postpellet Thomson scattering density and temperature profiles with those inferred from H_α data

Figure 5.2 shows average postpellet n_e and T_e profiles calculated from H_α pellet ablation rate data for the September 6, 1979, sequence. The calculation of n_e from the data was described above, and T_e was found by assuming that the product $(n_e \cdot T_e)$ on any flux surface was constant (local conservation of energy). This figure should be compared with the n_e and T_e profiles found from Thomson scattering 1 ms after pellet injection (Fig. 4.2 of Chap. 4).

Figure 5.3 shows average postpellet n_e and T_e profiles calculated from ablation rate data from September 11, 1979. The upper plot assumes that the pellet trajectory was through the center of the plasma. The lower plot assumes that the pellet trajectory missed the center of the plasma by 6 cm. These plots should be compared with the postpellet Thomson scattering data in Fig. 4.30 of Chap. 4.

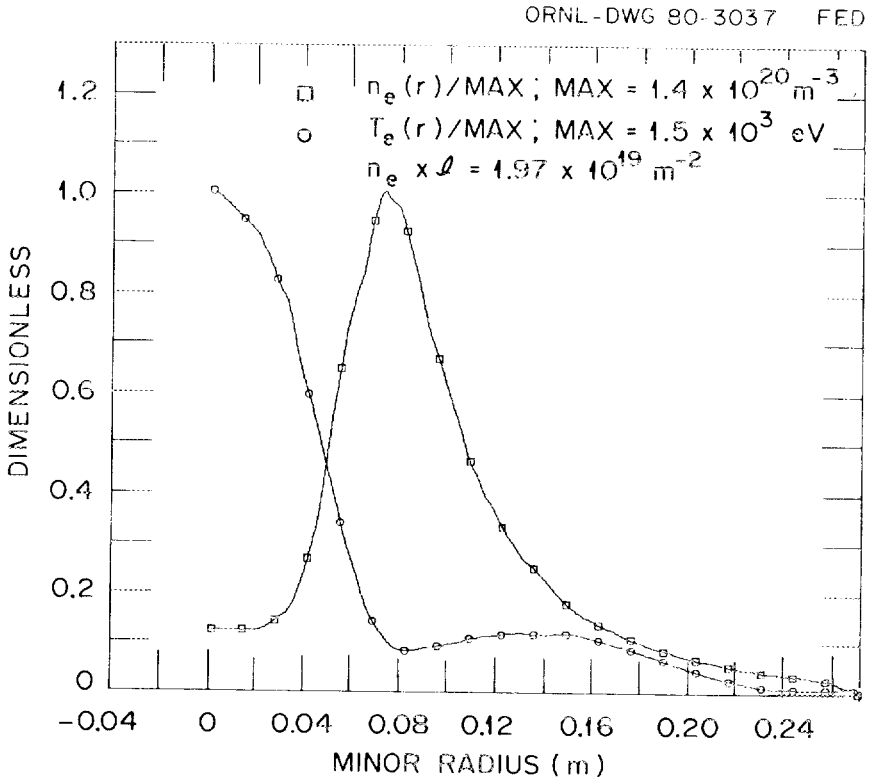

Fig. 5.2 Average postpellet n_e and T_e calculated from pellet ablation rate data from September 6, 1979.

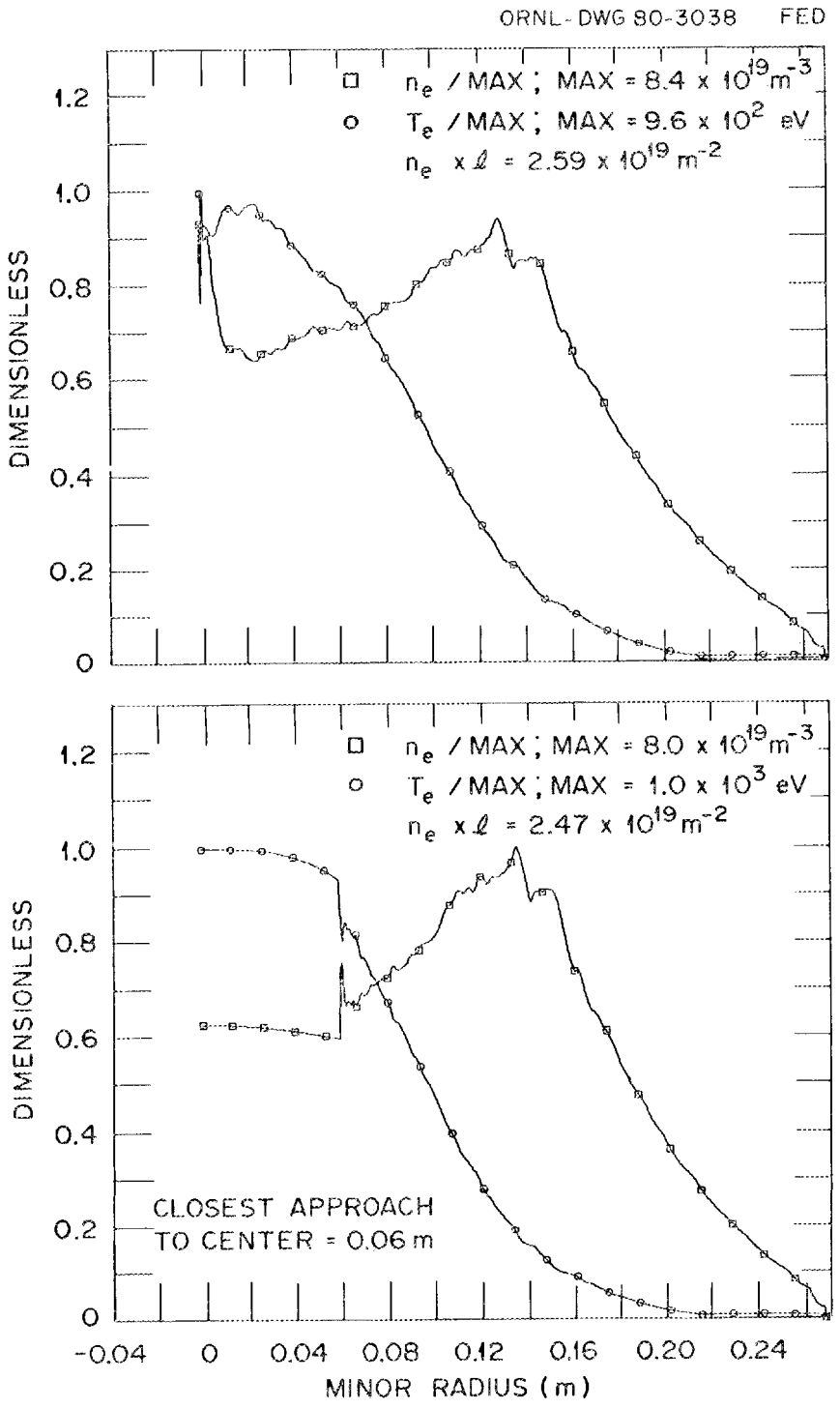

Fig. 5.3 Average postpellet n_e and T_e calculated from pellet ablation rate data from September 11, 1979.

The Thomson scattering and calculated profiles are qualitatively quite similar, although the Thomson scattering profiles are markedly relaxed from the calculated profiles. This is not surprising. Given the steep gradients shown 1 ms is a significant period of time to allow for relaxation.

The average total number of electrons in the plasma calculated from the H_α data on September 6 was 3.8×10^{19}, and that calculated from Thomson scattering was 3.6×10^{19}. The average total number of electrons in the plasma calculated from H_α data from September 11 was 6.0×10^{19}, and that calculated from Thomson scattering was 5.9×10^{19}.

Within the error bars of the experiment the agreement between the Thomson scattering data and the H_α ablation rate data is very good.

5.4.3 Comparison of average ablation rate inferred from H_α signal with neutral shielding theory

Figure 5.4 shows the theoretical pellet ablation rate calculated using the non-self-limiting neutral shielding model of Milora and Foster.[6] The plasma density and temperature profiles used were taken from curves fitted to the September 6 Thomson scattering data, and the pellet size and velocity used are the average pellet size and velocity from the September 6 data. The calculation for the upper plot assumes that the pellet density remains that of solid hydrogen. The calculation for the lower plot assumes that the pellet radius blows up at the rate of 10 m/s for penetration depths greater than 13 cm.

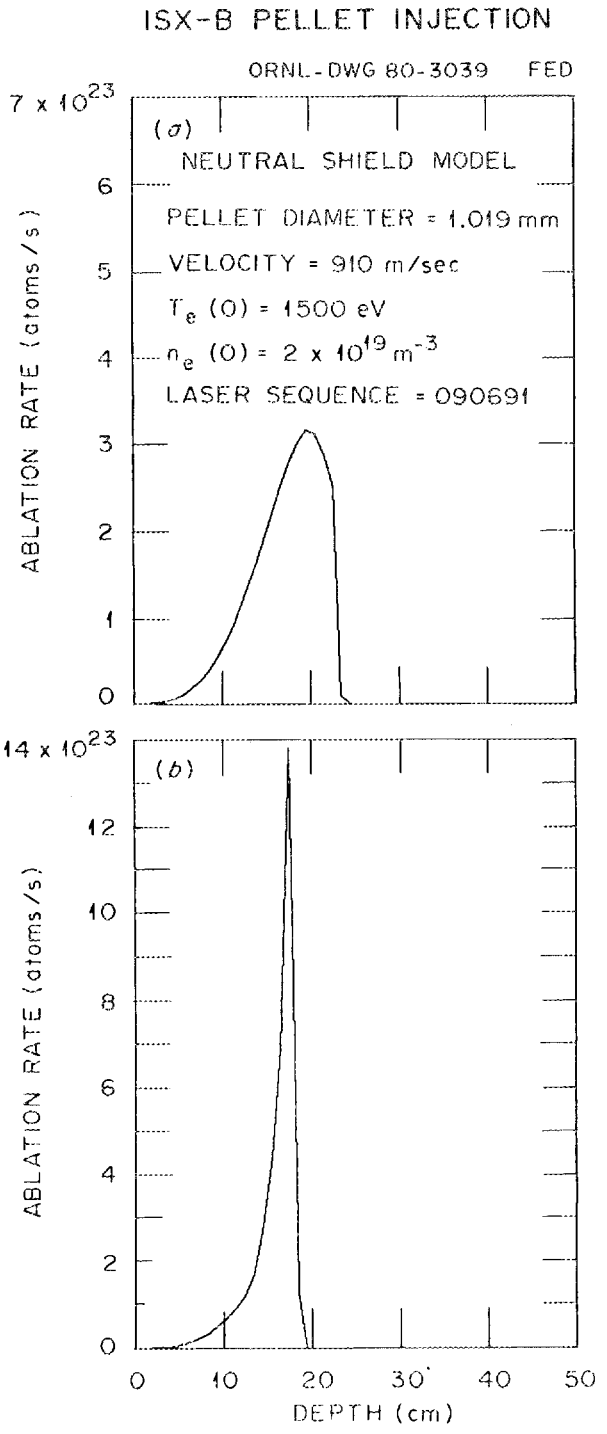

Fig. 5.4 Theoretical calculation of pellet ablation rate for plasma profiles of September 6, 1979, using the non-self-limiting neutral shielding model of Milora and Foster. Pellet radius is assumed to be expanding for lower plot.

Figure 5.5 shows the theoretical pellet ablation rate for September 6 using the self-limiting neutral shielding model of Milora et al.[7] Again the upper plot assumes the pellet remains solid, and the lower plot assumes the pellet radius increases at 10 m/s for depths greater than 13 cm.

If one reviews the ablation data from September 6, 1979, Figs. 4.11-4.19, the self-limiting ablation model in which the pellet radius is allowed to blow up seems to most closely resemble the data. One infers from the hard x-ray data in Chap. 4 that some shots had more runaway electrons than others. This could explain the large shot-to-shot difference in peak ablation rates for the September 6, 1979, sequence.

Figure 5.6 shows the theoretical pellet ablation rate for the September 11, 1979, sequence. The upper plot uses the non-self-limiting neutral shielding model, and the lower plot uses the self-limiting model. The unablated pellet material is assumed to remain solid.

The September 11, 1979, experimental ablation data, Figs. 4.34-4.43, are different from both models. The ablation rate is less than predicted by the theoretical models.

5.4.4 Discussion of spikiness of H_α data

In examining the ablation rate data (H_α data) it can be seen that there are large oscillations (spikes) on the ablation rate. The oscillations have about a 3-μs period. The cause of the oscillations is

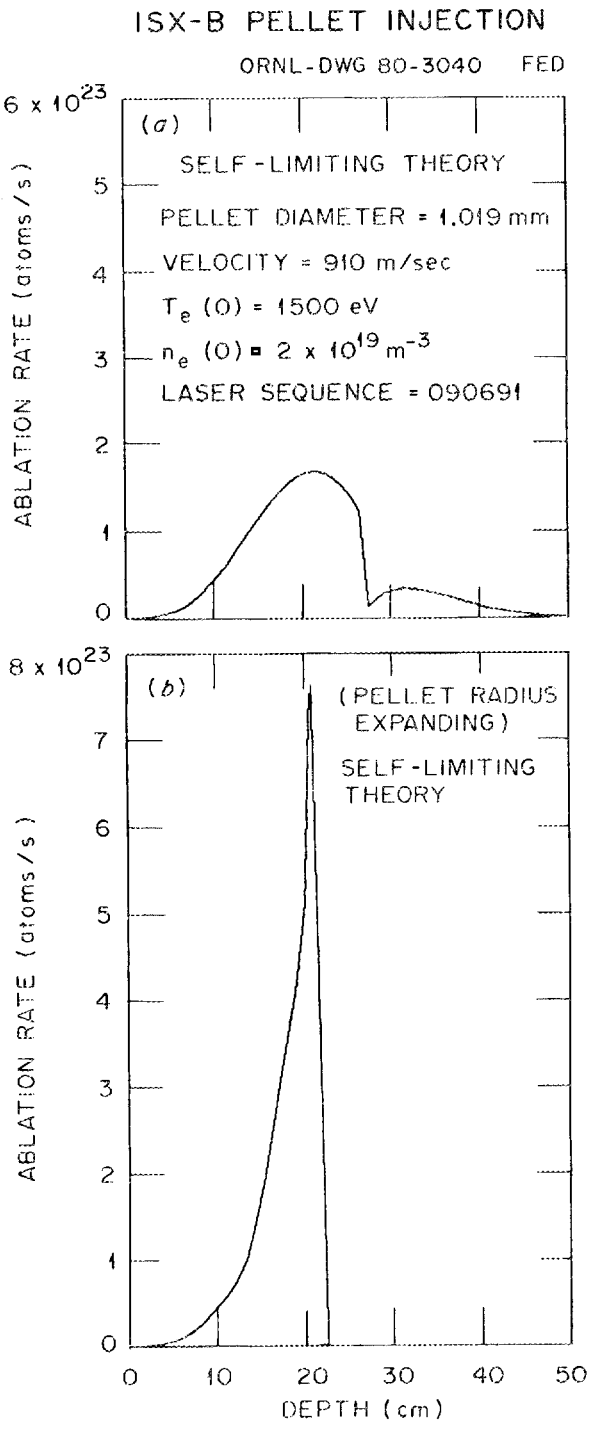

Fig. 5.5 Theoretical calculation of pellet ablation rate for plasma profiles of September 6, 1979, using the self-limiting neutral shielding model of Milora et al.

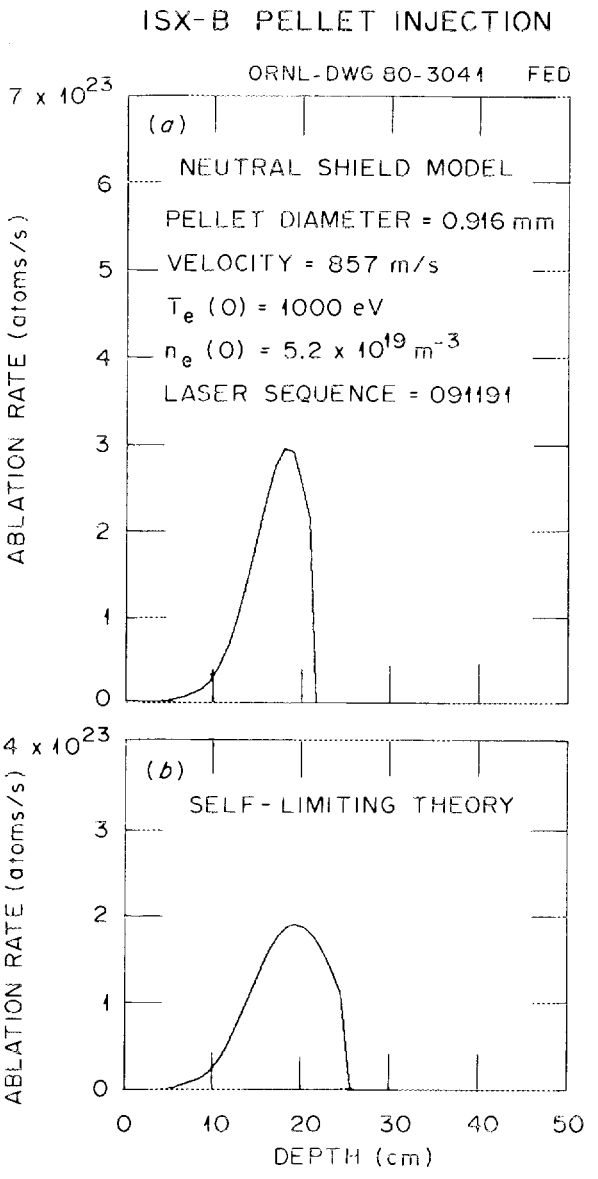

Fig. 5.6 Theoretical calculation of pellet ablation rate for plasma profiles of September 11, 1979, using both non-self-limiting and self-limiting neutral shielding models.

unknown, but one can speculate on two possible causes. The first is a granularity of the plasma profile (perhaps due to magnetic islands?) with a scale length of about 3 mm. The second possible cause is an oscillation in the protective ablatant layer around the pellet. The transit time for ablated material through the ablatant layer is on the order of 3 μs (say ∿1.5 mm at ∿500 m/s), consistent with the oscillation period.

There is not enough available information to validate or contra-indicate either of these possibilities.

5.4.5 Comparison of shielding factor inferred from H_α data with theoretical shielding factor

An instantaneous shielding factor for an ablating pellet may be defined as

$$\varepsilon \equiv \frac{P(r)}{G(r)} \text{ (eV/atom)}, \tag{5.2}$$

where

$P(r) \equiv$ power incident on the pellet at plasma minor radius r in eV/s,

$G(r) \equiv$ ablation rate of the pellet at plasma minor radius r in atoms/s.

Figure 5.7 shows the calculated average experimental shielding factor for the September 6, 1979, data, where

$$P(r) = \frac{n_e \bar{V}_e}{4} [2T_e(r)](2\pi r_p^2) \text{ (eV/s)}; \tag{5.3}$$

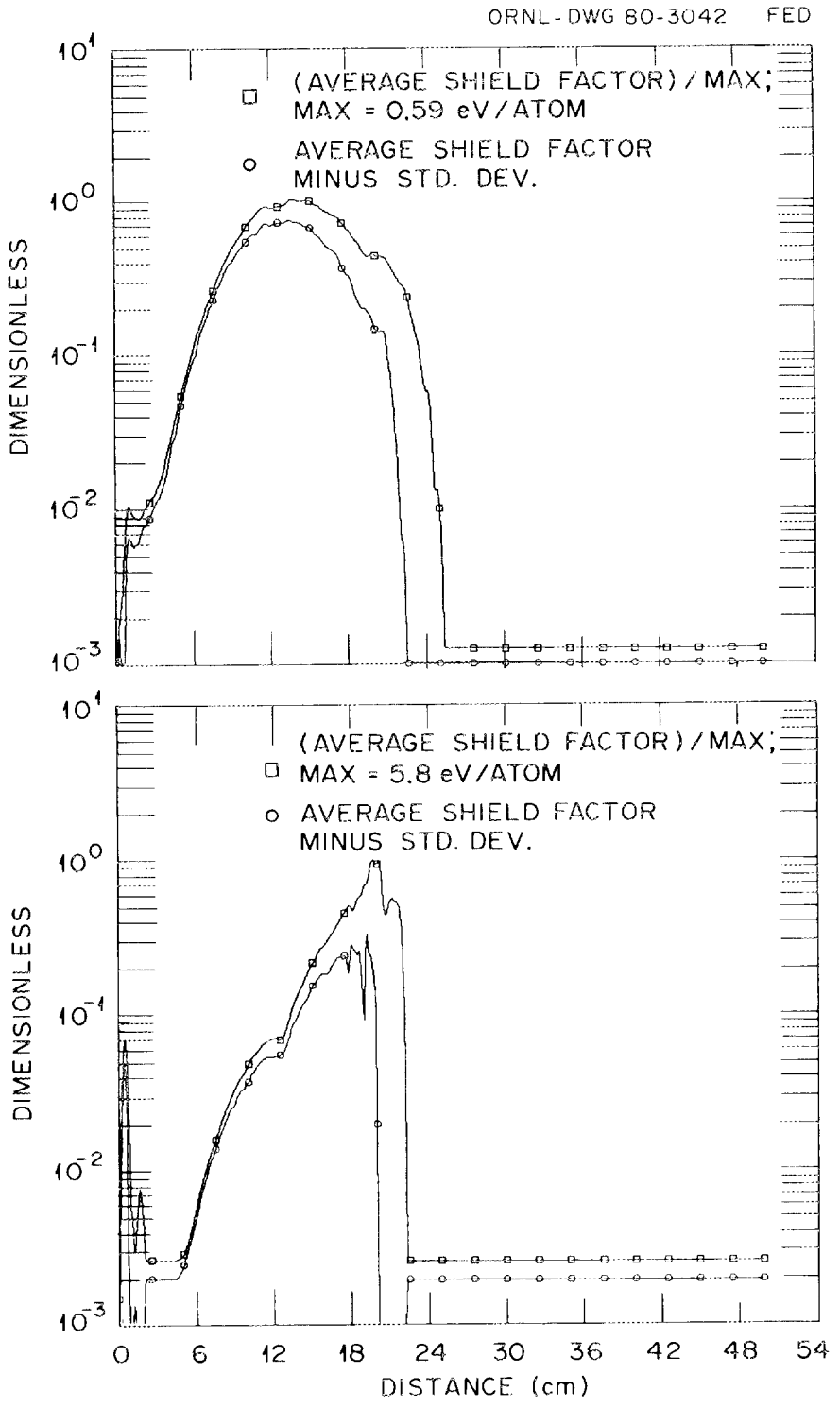

Fig. 5.7 Experimental shield factor plot for data of September 6, 1979. Upper plot assumes solid pellet density; lower plot assumes expanding pellet radius.

n_e and T_e are taken from the Thomson scattering data, G(r) is taken from the H_α ablation rate data, and r_p is the pellet radius. For the upper plot r_p was calculated from the ablation rate data assuming the pellet remained solid. For the lower plot the pellet radius was allowed to expand at the rate of 10 m/s for penetration depths greater than 13 cm into the plasma.

With the pellet radius expanding, the shielding factor is seen to increase approximately exponentially as the pellet penetrates the plasma until just before the pellet disappears (i.e., a straight line is a reasonable approximation to the shielding factor curve on this log-linear plot).

It is also possible to calculate a theoretical shielding factor. Figure 5.8 is the ratio of the average experimental shielding factor to the theoretical shielding factor for the experiment of September 6, 1979. The theoretical model used is the non-self-limiting model of Milora and Foster. In calculating the theoretical shielding factor, the pellet radius and plasma profiles used are the same as those used in calculating the experimental shielding factor for the lower plot of Fig. 5.7. The only difference between the two calculations is that the theoretical rather than the experimental ablation rate is used. This means that Fig. 5.8 can also be directly interpreted as the ratio of the theoretical to the experimental ablation rate. The calculation was cut

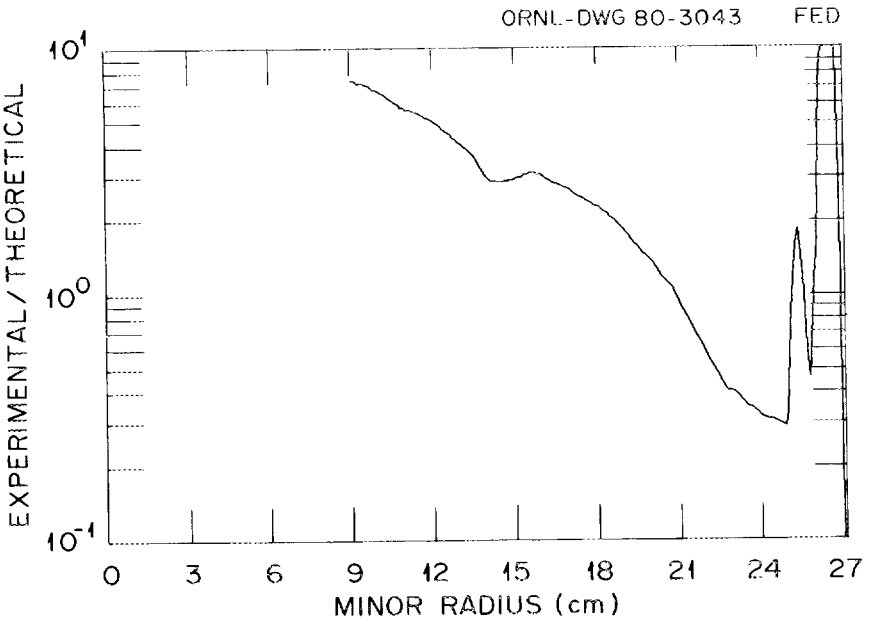

Fig. 5.8 Ratio of experimental to theoretical shield factor for data of September 6. The pellet radius is assumed to be expanding.

off at a minor radius of 9 cm because beyond this point the error bars on the average experimental shielding factor make the calculation meaningless.

The upper plot of Fig. 5.9 is the experimental shielding factor for the experiment of September 11, 1979. The lower plot of Fig. 5.9 is the ratio of the experimental to the theoretical shielding factor for this experiment. Again the error bars on the average experimental shielding factor are very large for plasma minor radii less than 9 cm. For this calculation the pellet was assumed to remain at solid density, and as in Fig 5.8 the ratio can also be interpreted directly as the ratio of theoretical to experimental ablation rates.

5.5 Analysis of Interferograms/Shadowgraphs

The interferograms made on September 6 and 11, 1979, were digitized and analyzed with the computer. Digitization was accomplished with a Gerber Scientific x-y digitizer. The x-y coordinates of each fringe were digitized at enough points for the computer to make a reasonable reconstruction of the interferogram. From the digitized interferograms, $n_e \times \ell$ (electron density times path length) was calculated for a matrix of 100-by-100 points covering the interferogram. The first two parts of Sect. 5.5 will discuss computer reduction of the interferograms to contours of constant $n_e \times \ell$ and inference of electron densities by curve fitting. The remaining parts of Sect. 5.5 will discuss interpretation

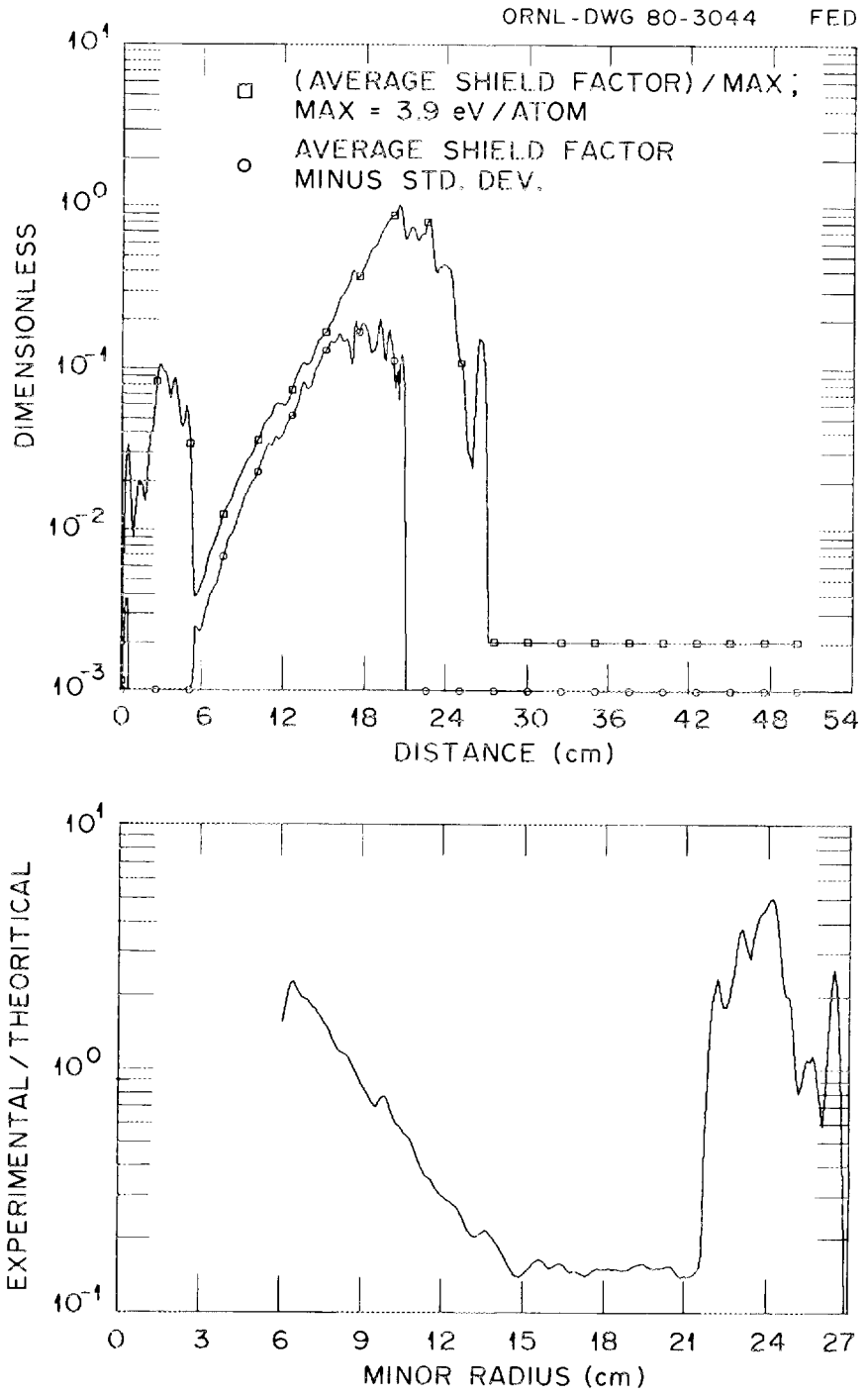

Fig. 5.9 Average experimental shield factor plot (upper) and ratio of experimental to theoretical shield factor for data of September 11, 1979. Note that upper x-scale is distance from limiter and lower is distance from plasma center. Calculation for lower plot is cut off at r = 6 cm.

of the computer-reduced interferograms and general characteristics of the original interferograms.

5.5.1 Reduction of interferograms to $n_e \times \ell$ plots

Once the interferograms were digitized, they were converted to plots of $n_e \times \ell$ (electron density times path length). The relationship between the observed fringe shift at any point and $n_e \times \ell$ is linear ($\lambda = 6943$ Å):

$$n_e \times \ell = (\text{shift in fringes}) \cdot (3.2 \times 10^{21})\ m^{-2}. \qquad (5.4)$$

Thus, given the x-y coordinates and fringe number of a fringe on the interferogram, $n_e \times \ell$ can be calculated by subtracting the fringe number of the fringe from the number of the unshifted background fringe and using Eq. (5.4). It should be noted that Eq. (5.4) assumes that the index of refraction is dominated by the electron density. If the electron density is less than ∿20% of the neutral density, then the correction to the refractive index due to the neutrals is greater than 10% and should be taken into account. The changes in refractive index due to electrons and neutrals are exactly equal and opposite in sign (at $\lambda = 6943$ Å) when the electron density is ∿2.39% of the neutral density.

Figures 5.10-5.20 are the computer reconstructions of the interferograms and the plots of contours of constant $n_e \times \ell$. Because real data points were available only where fringes existed on the interferogram, the value of $n_e \times \ell$ between fringes was found by solving

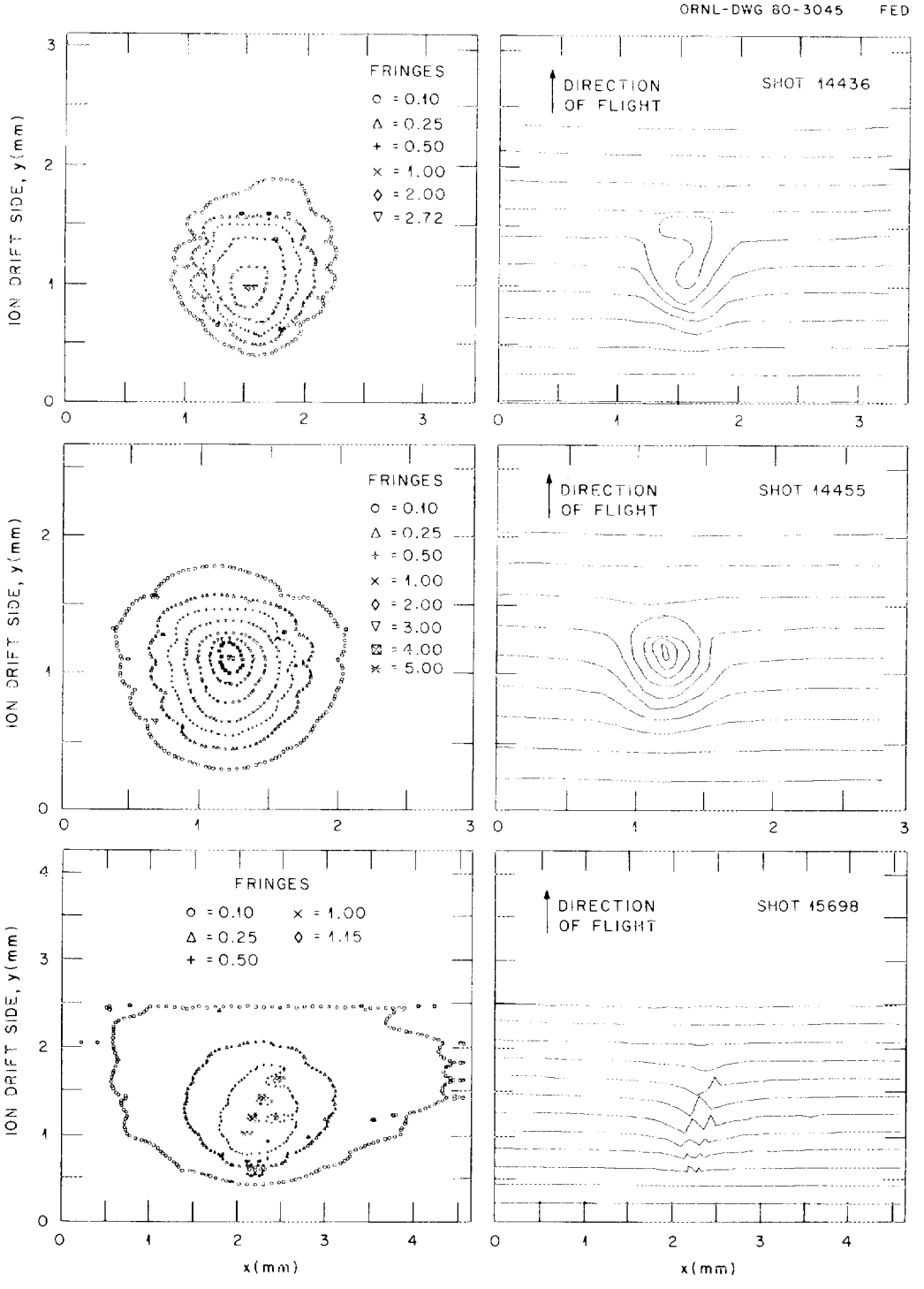

Fig. 5.10 Computer reconstruction of interferograms and plots of contours of constant $n_e \times \ell$ for shots 14436, 14455, and 15698.

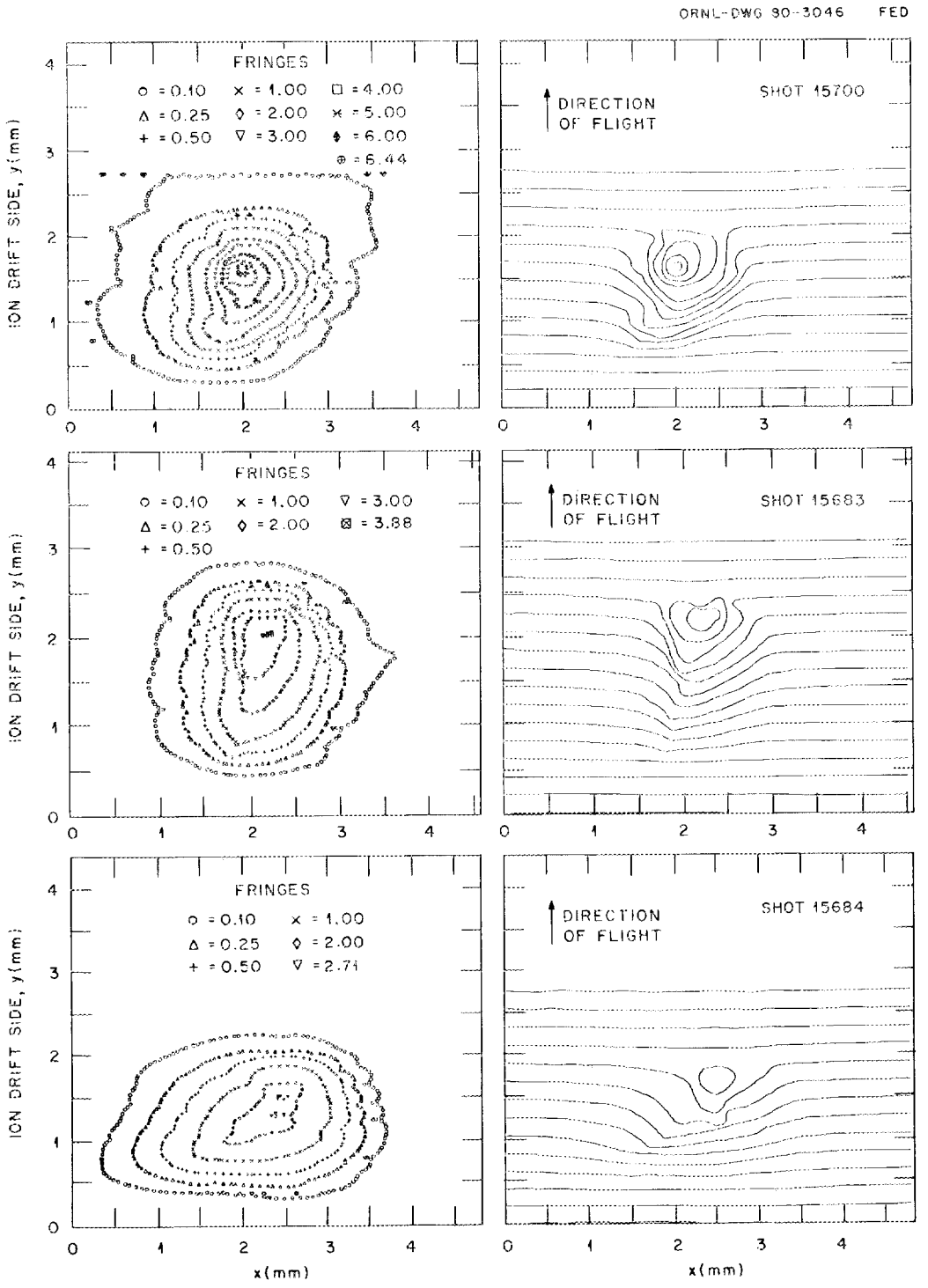

Fig. 5.11 Computer reconstruction of interferograms and plots of contours of constant $n_e \times \ell$ for shots 15700, 15683, and 15684.

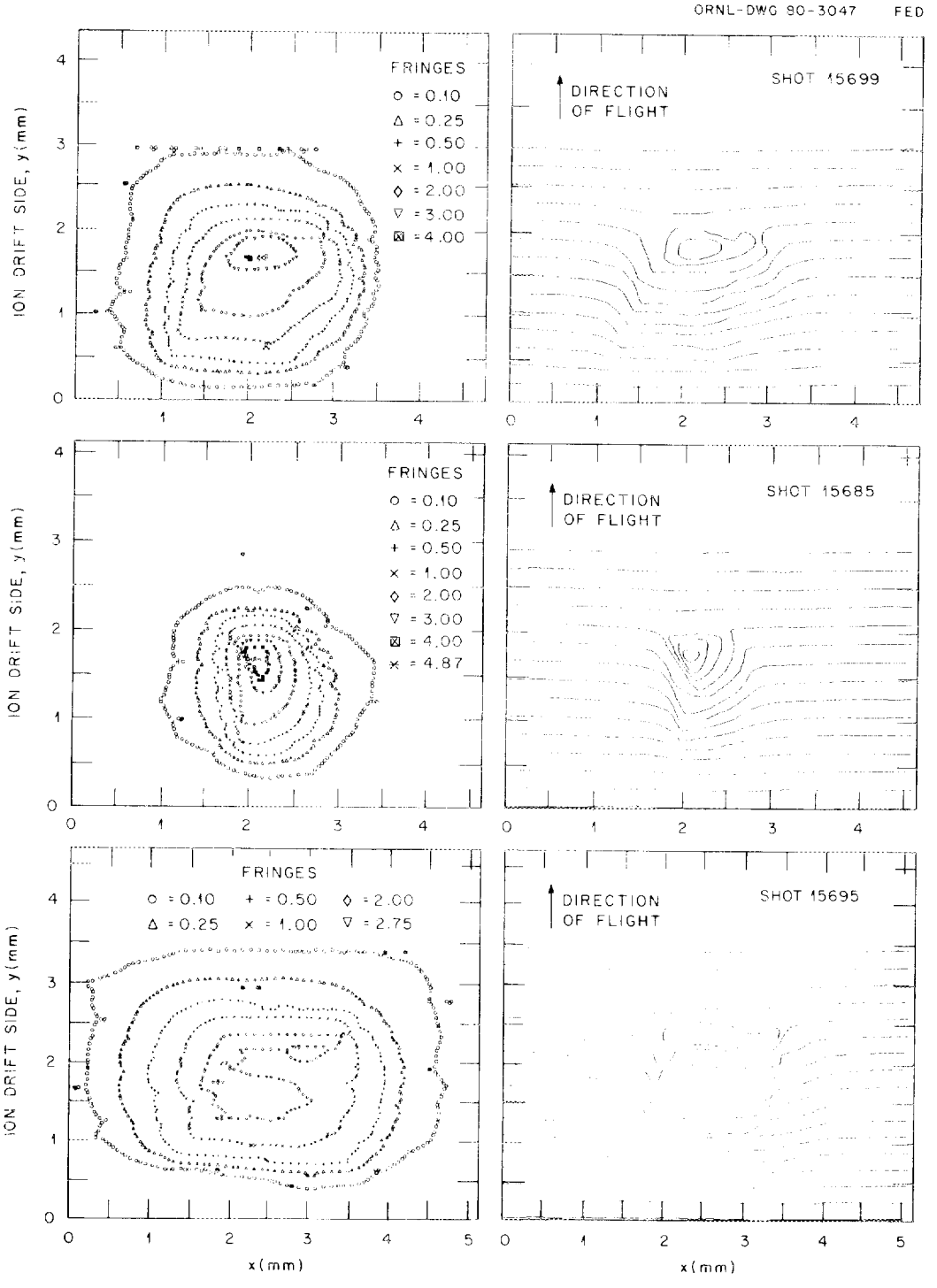

Fig. 5.12 Computer reconstruction of interferograms and plots of contours of constant $n_e \times \ell$ for shots 15699, 15685, and 15695.

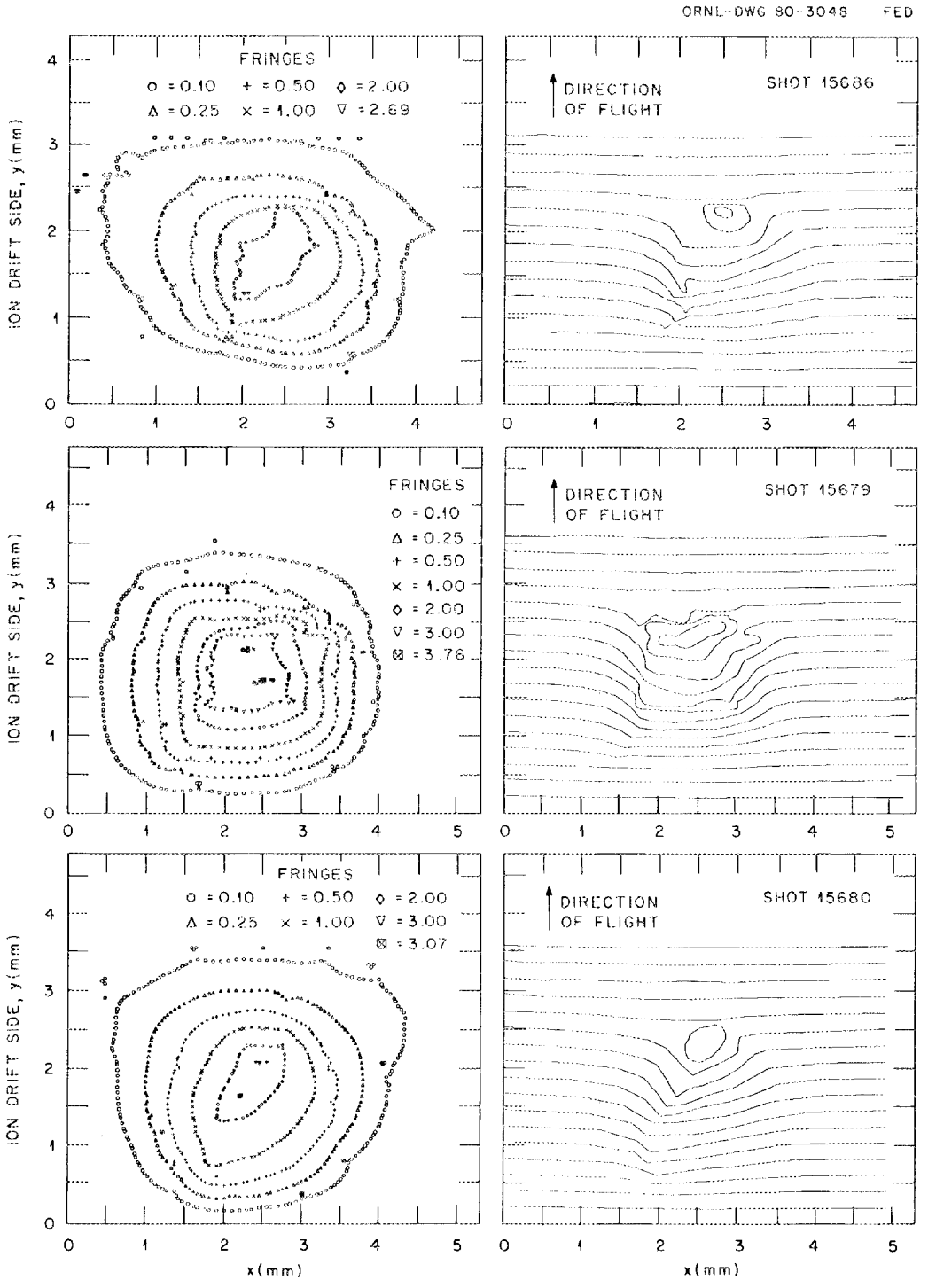

Fig. 5.13 Computer reconstruction of interferograms and plots of contours of constant $n_e \times \ell$ for shots 15686, 15679, and 15680.

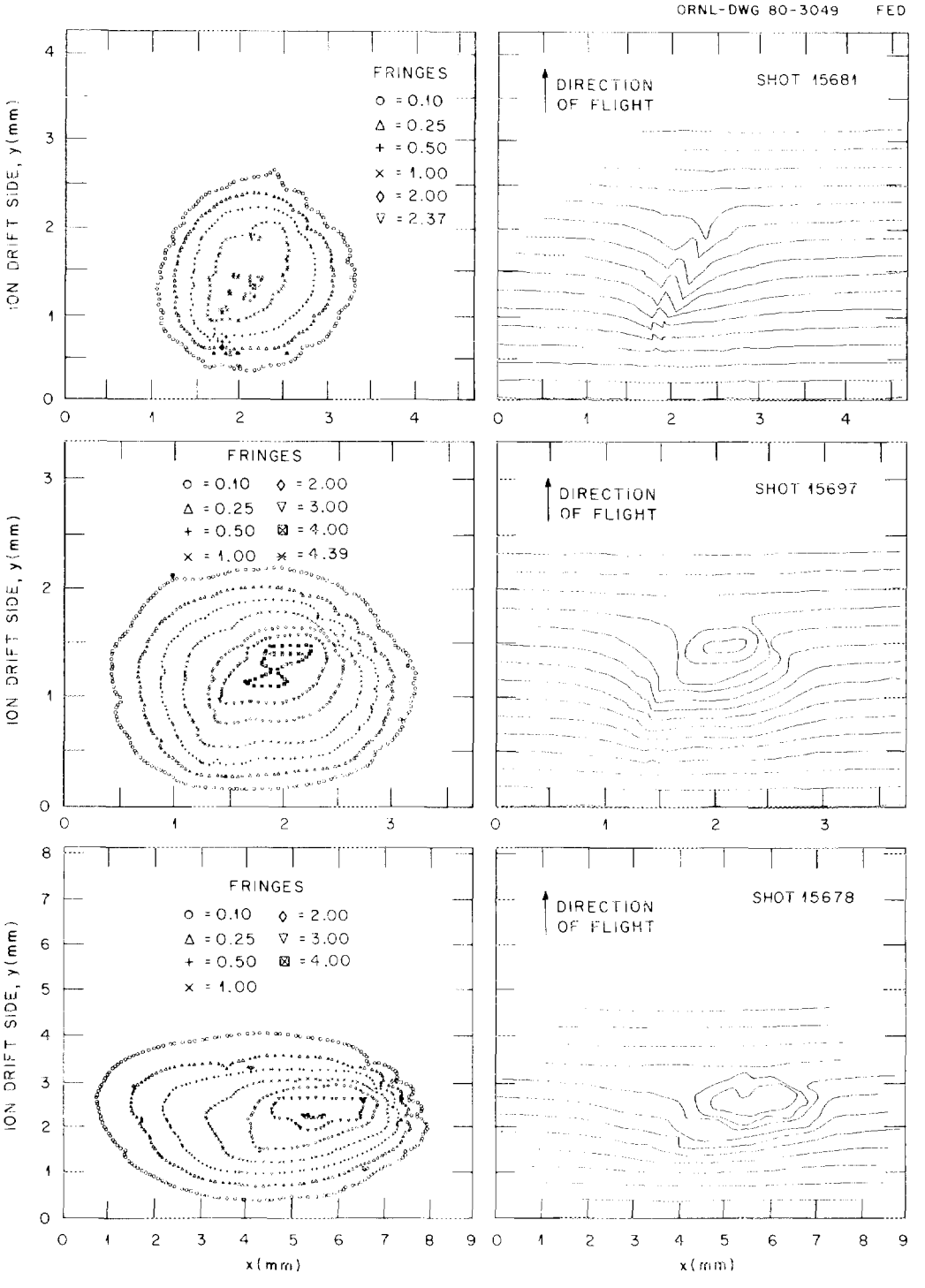

Fig. 5.14 Computer reconstruction of interferograms and plots of contours of constant $n_e \times \ell$ for shots 15681, 15697, and 15678.

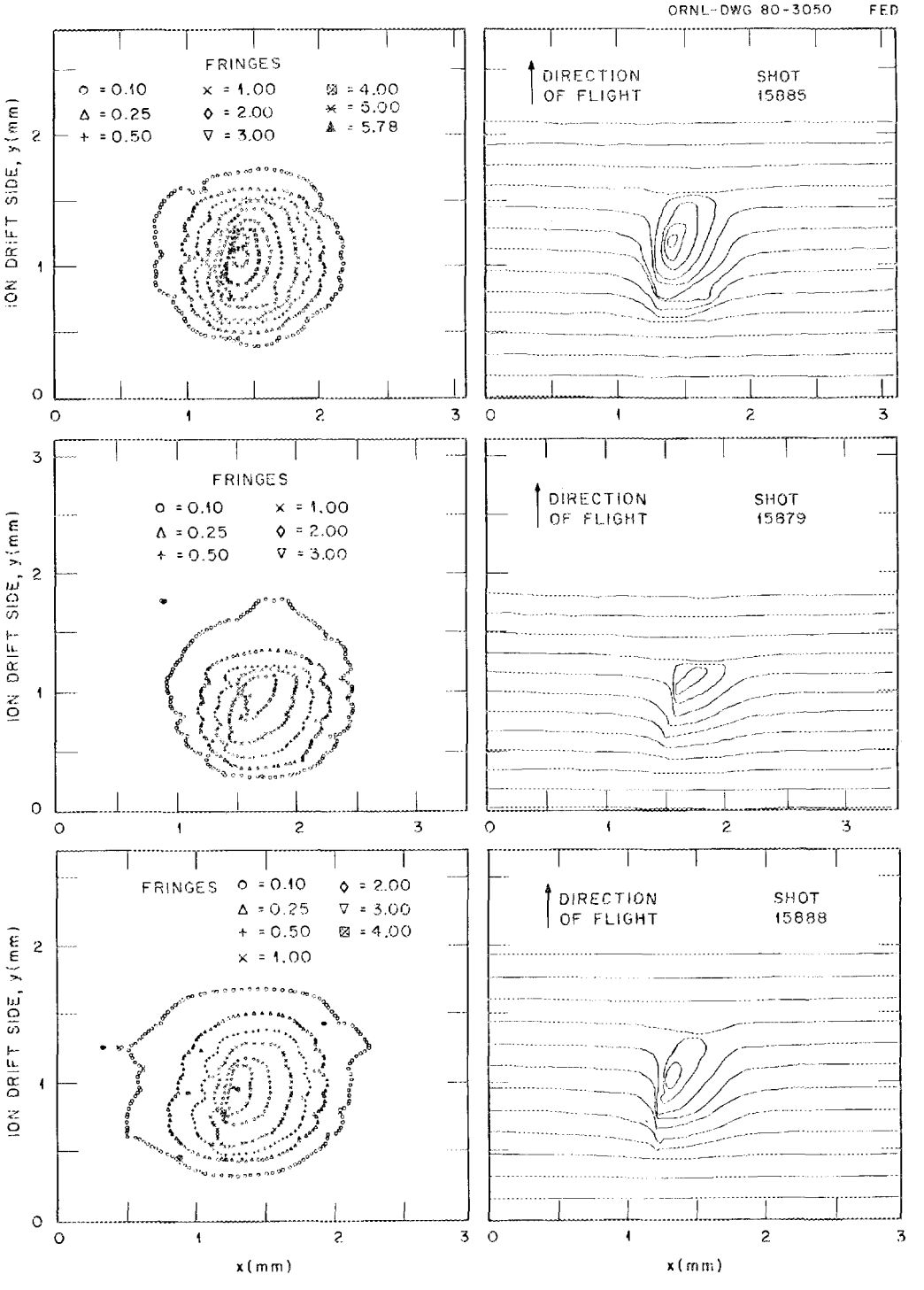

Fig. 5.15 Computer reconstruction of interferograms and plots of contours of constant $n_e \times \ell$ for shots 15885, 15879, and 15888.

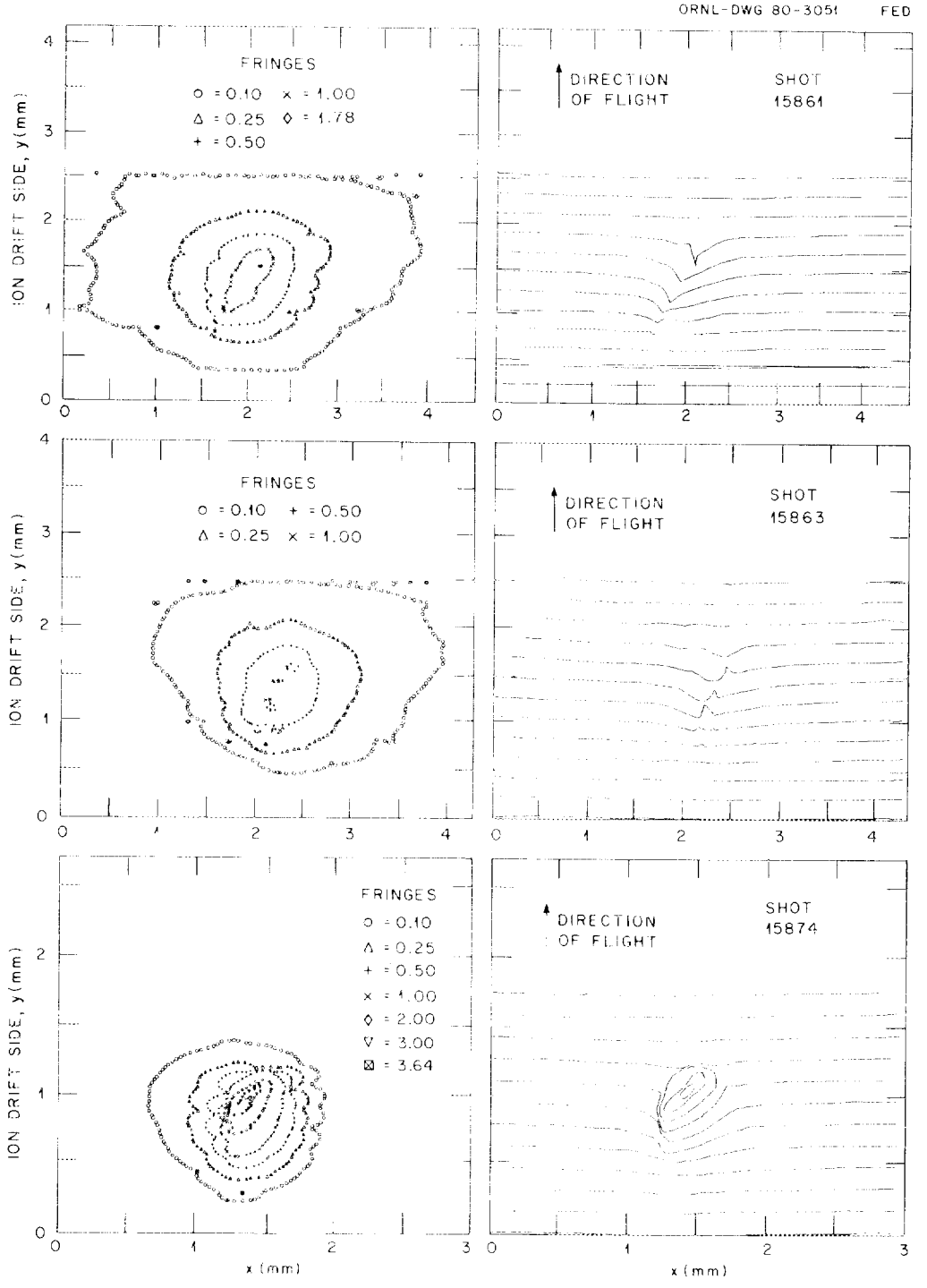

Fig. 5.16 Computer reconstruction of interferograms and plots of contours of constant $n_e \times \ell$ for shots 15874, 15861, and 15863.

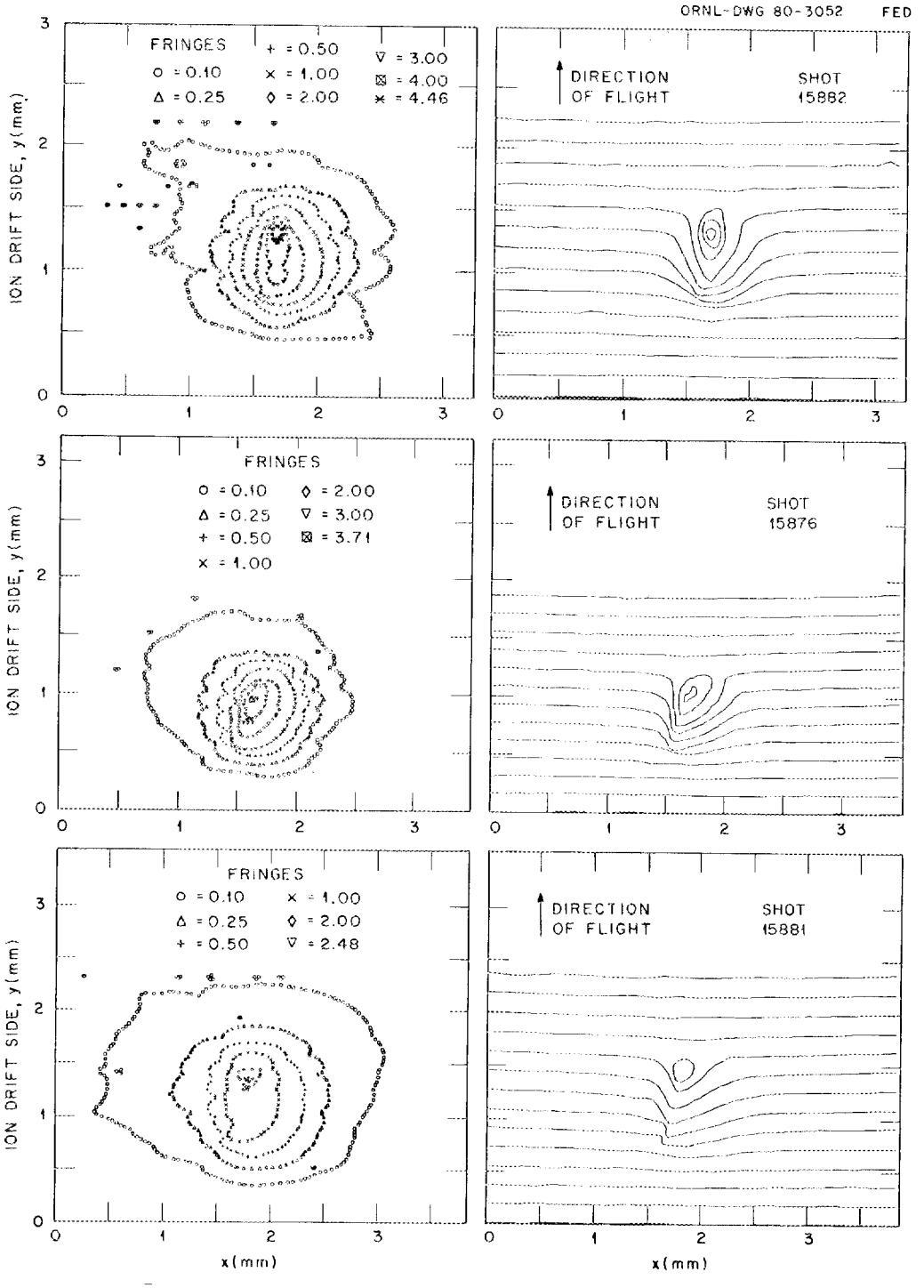

Fig. 5.17 Computer reconstruction of interferograms and plots of contours of constant $n_e \times \ell$ for shots 15882, 15876, and 15881.

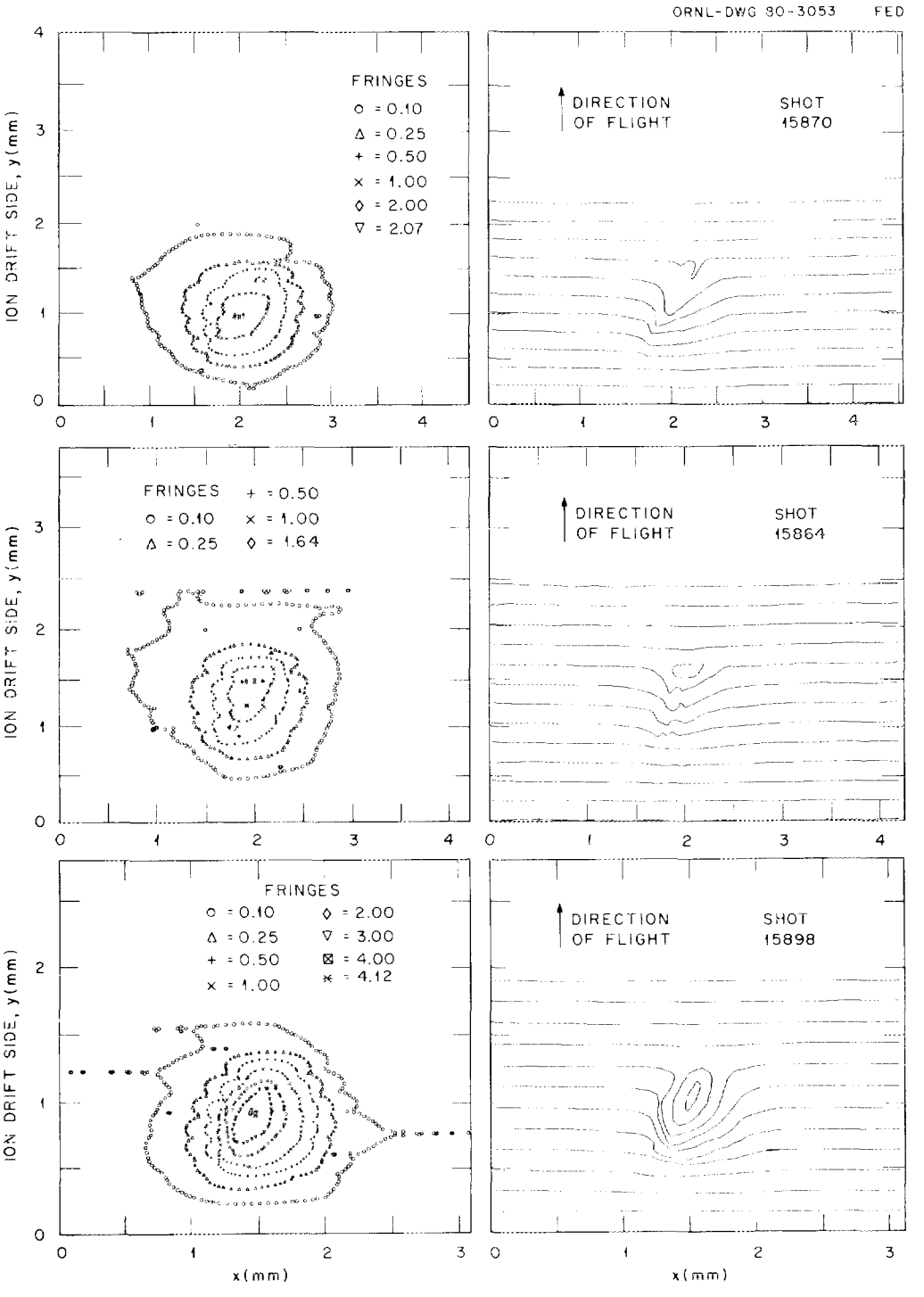

Fig. 5.18 Computer reconstruction of interferograms and plots of contours of constant $n_e \times \ell$ for shots 15870, 15864, and 15898.

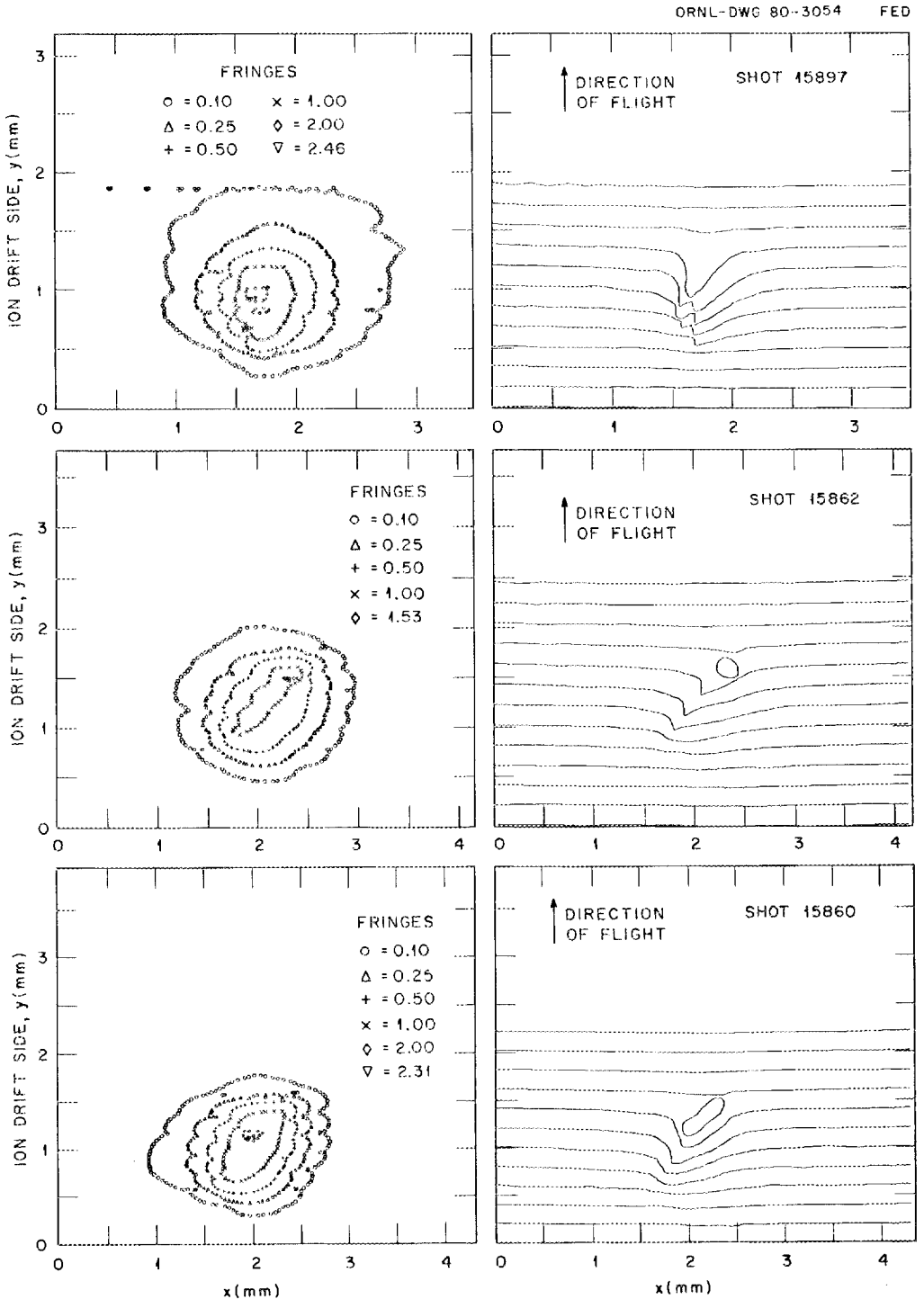

Fig. 5.19 Computer reconstruction of interferograms and plots of contours of constant $n_e \times \ell$ for shots 15897, 15862, and 15860.

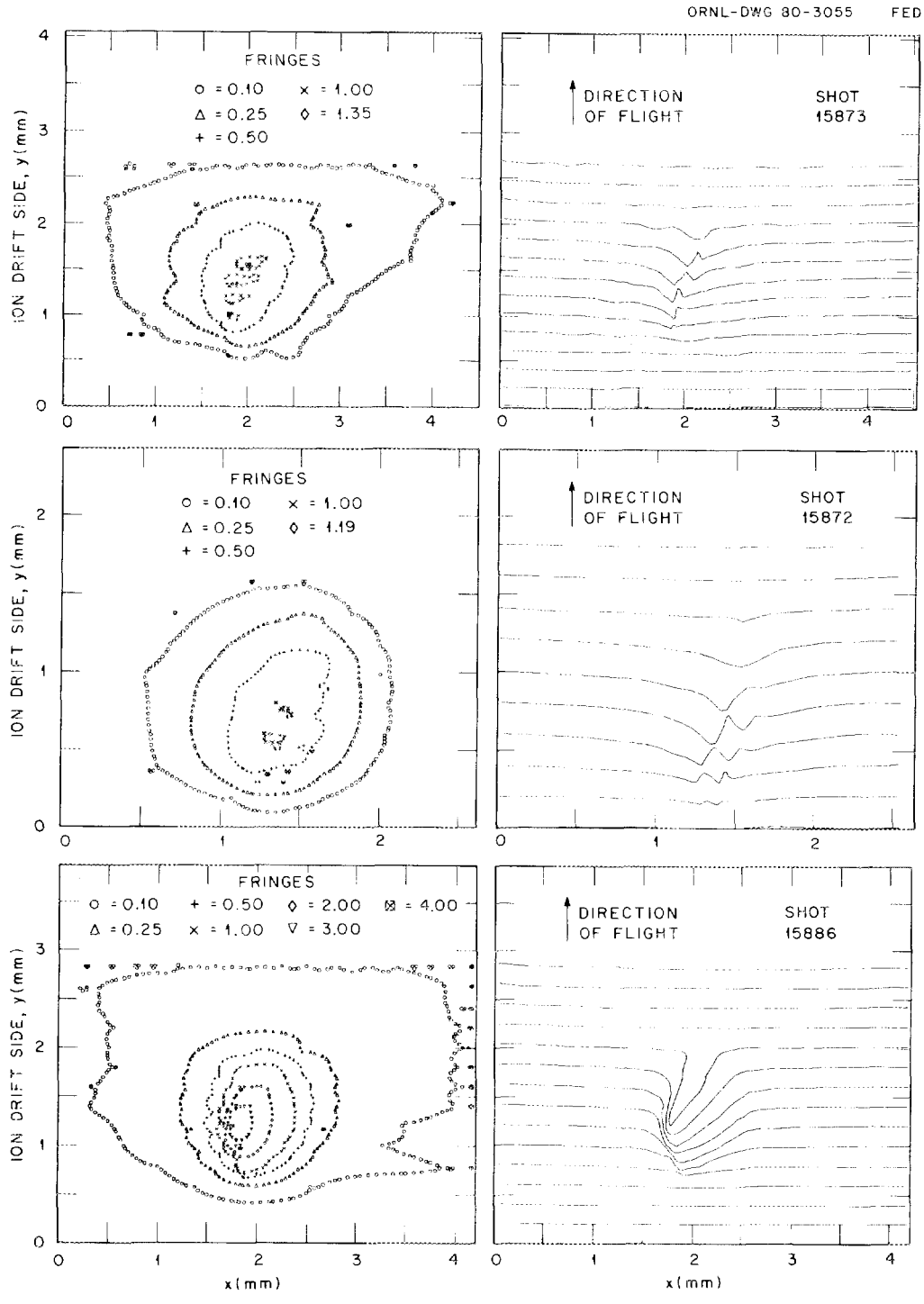

Fig. 5.20 Computer reconstruction of interferograms and plots of contours of constant $n_e \times \ell$ for shots 15873, 15872, and 15886.

Laplace's equation using the actual data points as boundary conditions. Both the idea of interpolating in this manner and the computer program to do it are the result of work at LASL.[8] The help of P. Forman and B. Woodworth at LASL, who provided the program, and of the people at LASL who wrote the program is gratefully acknowledged.

Solving Laplace's equation using the digitized fringe data points as boundary conditions guarantees an interpolation that introduces no extrema; however, it does not prevent saddle points, and where values are changing rapidly and the distance between fringes is relatively large, this effect can occur. The "scalloping" of the countours of $n_e \times \ell$ evident in the plots at some places is due to this effect and represents a numerical error in analysis of the data. The error is not particularly significant because it introduces a relatively small change in the position of the $n_e \times \ell$ contour.

Inside the first closed contour on an interferogram the direction of phase change is ambiguous. In some physical situations it is clear that closed fringes inside of closed fringes represent decreasing phase and increasing $n_e \times \ell$. In the experiments presented here, however, it is possible that closed fringes inside of closed fringes represent additional neutral density and therefore increasing phase. However, examining the interferograms where closed contours are not present, it is seen that as one penetrates the high-density region, the fringes are always shifted in the direction of decreasing phase; therefore, all closed fringes inside of closed fringes are interpreted as being in the direction of decreasing phase and representing additional $n_e \times \ell$.

The problem of correcting for neutral density has not been solved. The approximate number of neutrals remaining when the interferograms was made is known, but their distribution over the interferogram is not known. The $n_e \times \ell$ calculated and plotted is, therefore, a lower limit on the actual $n_e \times \ell$.

The computer-analyzed interferograms from September 6 are presented in order of increasing ablation rate. The interferograms from September 11 are presented in order of decreasing remaining pellet mass.

5.5.2 Curve fitting -- calculation of electron density from $n_e \times \ell$ data

If symmetry of some form is assumed then it is possible to calculate electron densities from the $n_e \times \ell$ data. Suppose that one assumes $n_e(r)$ has the following functional form:

$$n_e(r) = \frac{A}{2r_p} \frac{\mathrm{Exp}[-(r/r_p)^2/r_2^2]}{[1 + B(r^2/r_p^2)^y]}, \tag{5.5}$$

where A, r_2, B, and y are undetermined constants, r is the radial distance from the pellet center, and r_p is the actual instantaneous radius of the pellet, assuming solid density and spherical structure. Then $n_e \times \ell(r)$ can be calculated for any ray, where r is now the distance of the closest approach of the ray to the pellet center:

$$n_e \times \ell(r) = \frac{2A}{2r_p} \int_0^\infty \frac{\mathrm{Exp}[-(r^2 + p^2)/(r_p^2 r_2^2)]\, dp}{\left\{1 + B[(r^2 + p^2)/r_p^2]^y\right\}}. \tag{5.6}$$

Equation (5.6) is just the integral of electron density along the path of the ray. Making the substitutions

$$r' \equiv (r/r_p),$$

$$\mu \equiv p/r_p,$$

the integral becomes

$$n_e \times \ell(r') = A \int_0^{\infty} \frac{\mathrm{Exp}[-(r'^2 + \mu^2)/r_2^2]\, d\mu}{[1 + B(r'^2 + \mu^2)^y]} . \qquad (5.7)$$

Using the above function for $n_e \times \ell$, curves have been fitted to the $n_e \times \ell(r)$ data from the interferograms. For each interferogram $n_e \times \ell(r)$ is plotted in four different directions away from the point of maximum $n_e \times \ell$, which is arbitrarily taken to be the pellet center. Then a nonlinear least-squares curve-fitting program is used to fit Eq. (5.7) to the data in each direction. The fitting is done iteratively using a Taylor series analytic expansion for chi-square, the weighted sum of the squares of the error between the fitted curve and the data.[9] The computer program used to do the curve fitting and solve for the parameters A, B, r_2, and y was written by E. A. Lazarus of ORNL.

The four directions chosen to fit curves were the directions parallel and perpendicular to the toroidal magnetic field. The direction called forward is the direction of the pellet's flight toward the center of the tokamak. The direction called backward is opposite to forward. The direction called electron side is antiparallel to the toroidal magnetic field on the side of the pellet that would see the electron drift velocity. The direction called ion side is opposite to electron side. Equation (5.7) was evaluated at each fitted data point on each iteration by performing the indicated integral numerically. It took approximately two hours of CPU time on the ORNL Fusion Energy Division DEC-10 to fit four curves to an interferogram.

Figures 5.21-5.26 are the $n_e \times \ell$ data, fitted curves, and calculated $n_e(r)$ for three typical interferograms from the September 6 data. Note that the y-scales have been made dimensionless by dividing through by their maximum value, which is noted on the plot. The curve fitting was actually done in this nondimensional form, so the A parameter value listed must be multiplied by the maximum value listed on the plot (listed as "MAX"). There are five data points between symbols on the plotted curves. The x-scale has also been made dimensionless by dividing by the listed value of r_p (the pellet radius assuming solid density). The parameter listed as χ^2 on the plots is the reduced chi-square, the sum of the squares of the errors between the data and the fitted curve divided by the estimated error at each data point and divided by the degrees of freedom (number of data points minus number of fitting parameters).

The shots picked for analysis are typical stages in the pellet's life for the September 6 data. Shot 14455 is early in the pellet's life, shot 15685 is toward the middle of its life, and shot 15678 has caught the pellet just before complete evaporation.

What can be noticed in examining the fitted data and calculated electron densities is that they are distinctly asymmetric. The plotted $n_e \times \ell$ tends to fall off much faster in the forward direction than in any other direction, and the falloff in the directions parallel to the magnetic field is not as sharp as the falloff perpendicular to the

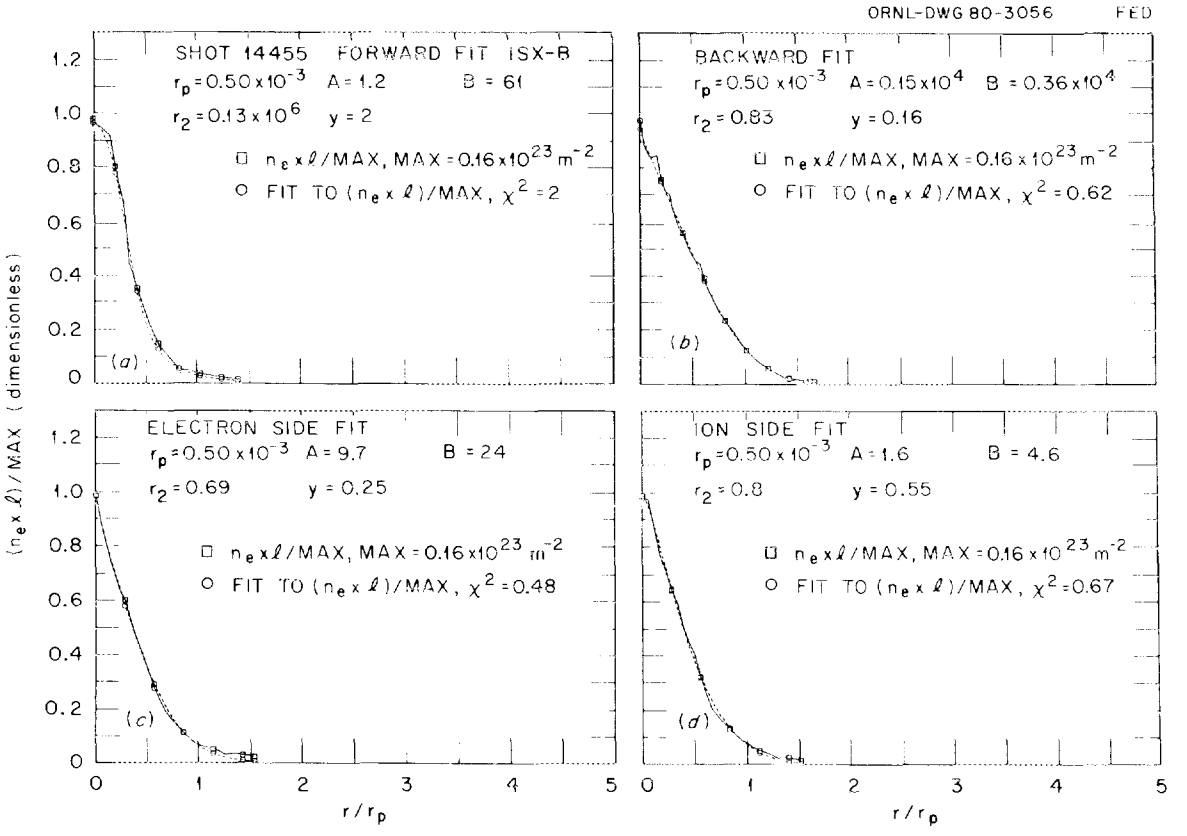

Fig. 5.21 Curves fitted to $n_e \times \ell$ data in four directions for shot 14455.

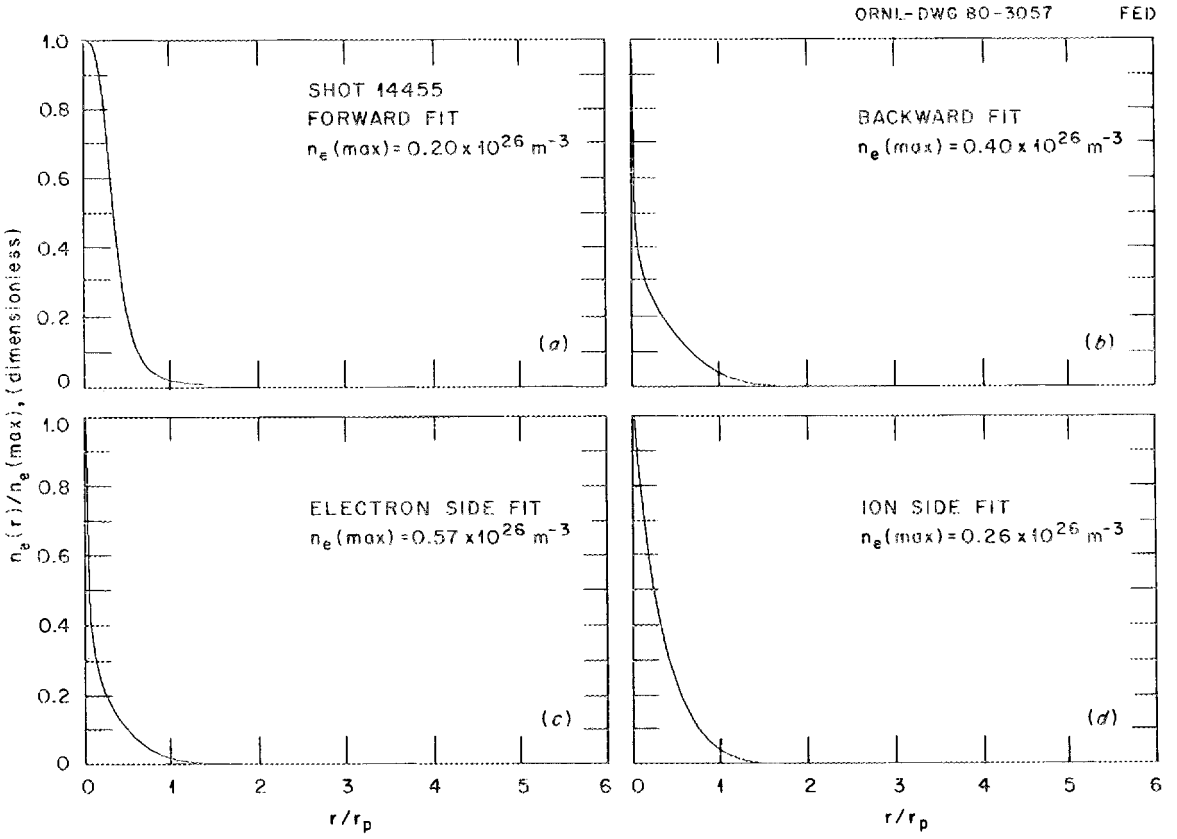

Fig. 5.22 Calculated $n_e(r)$ in four directions from pellet center, shot 14455.

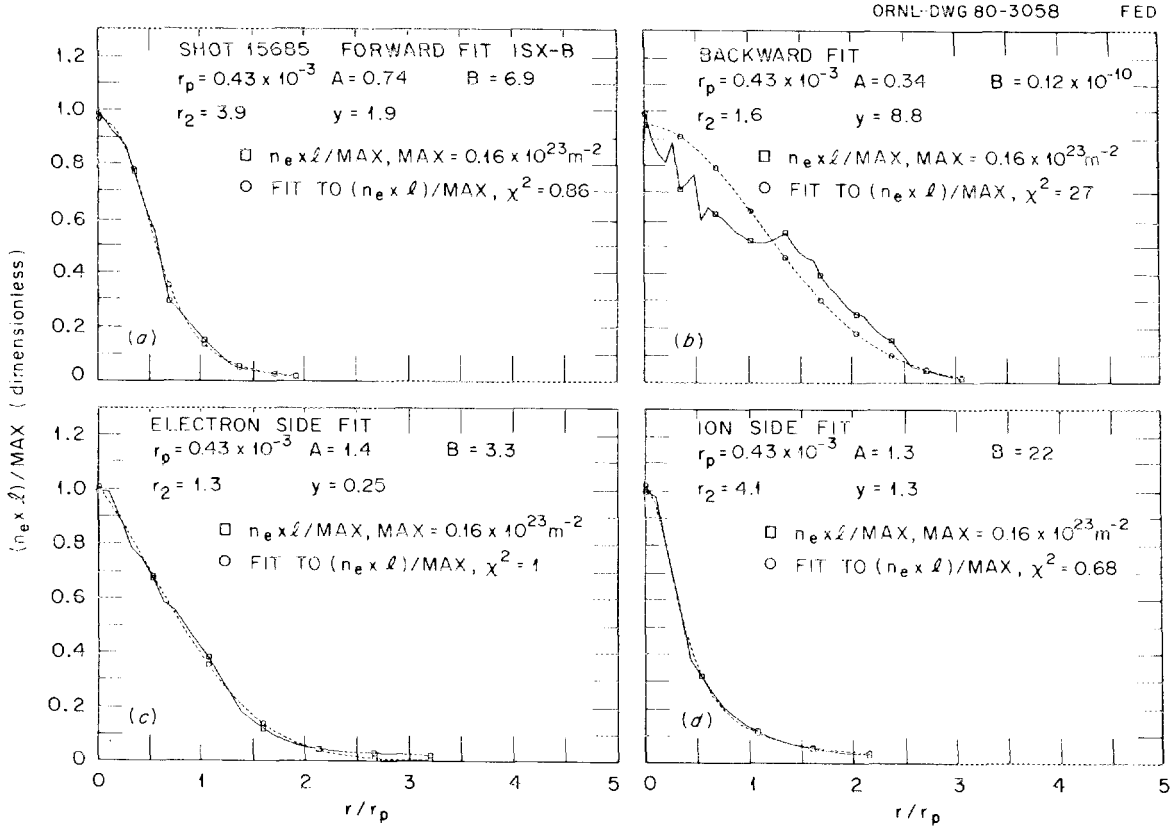

Fig. 5.23 Curves fitted to $n_e \times \ell$ data in four directions for shot 15685.

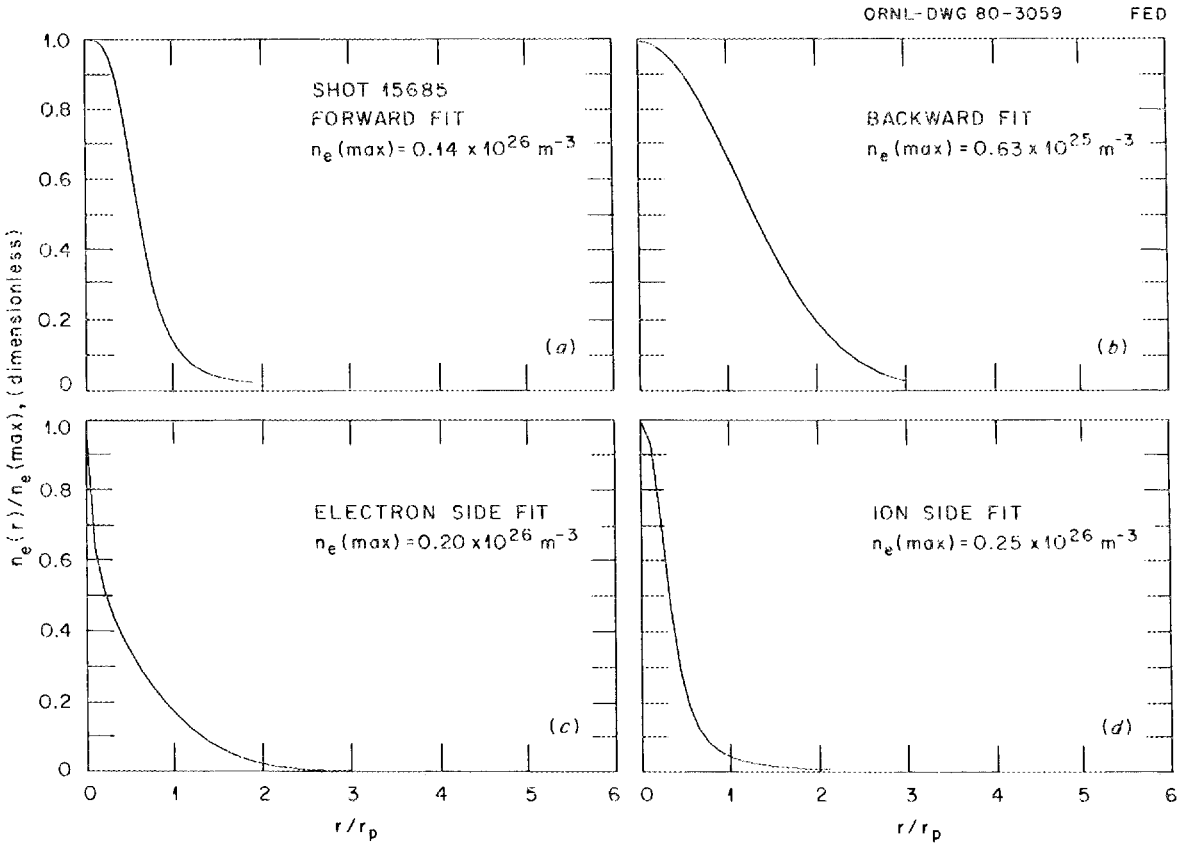

Fig. 5.24 Calculated $n_e(r)$ in four directions from pellet center, shot 15685.

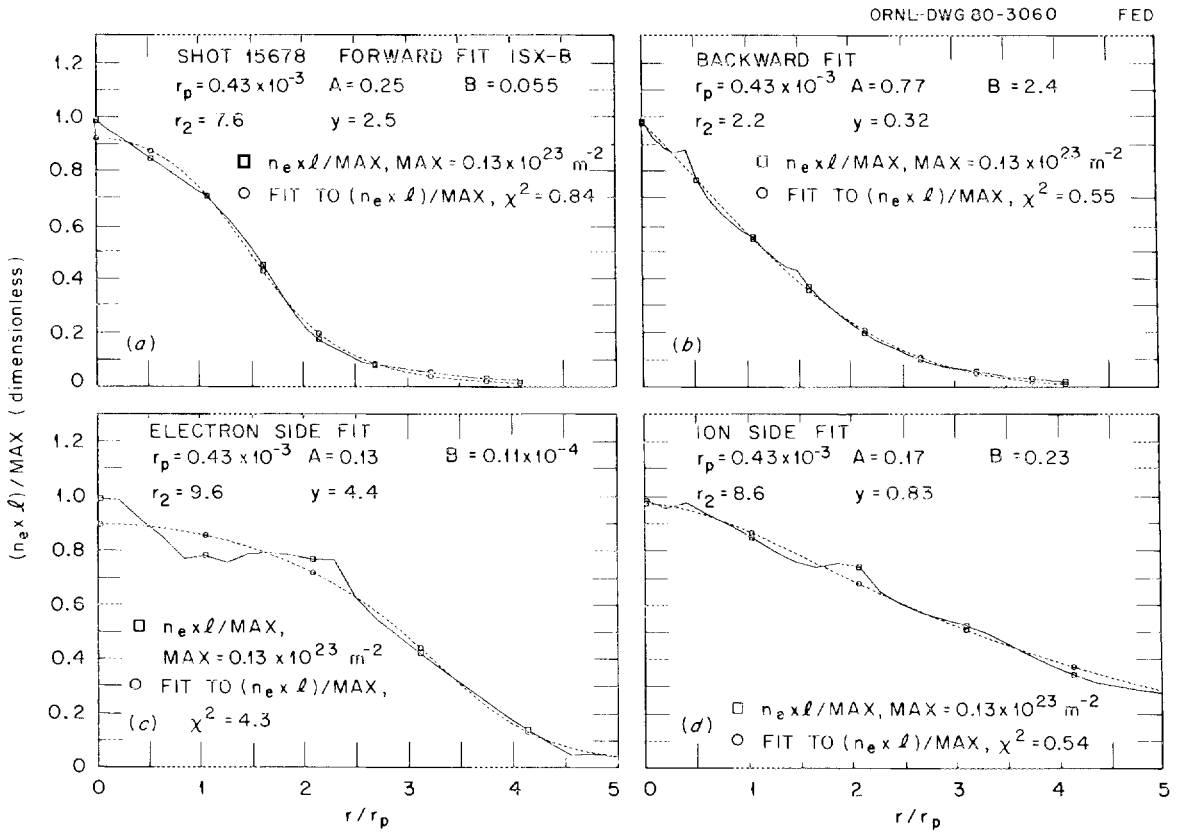

Fig. 5.25 Curves fitted to $n_e \times \ell$ data in four directions for shot 15678.

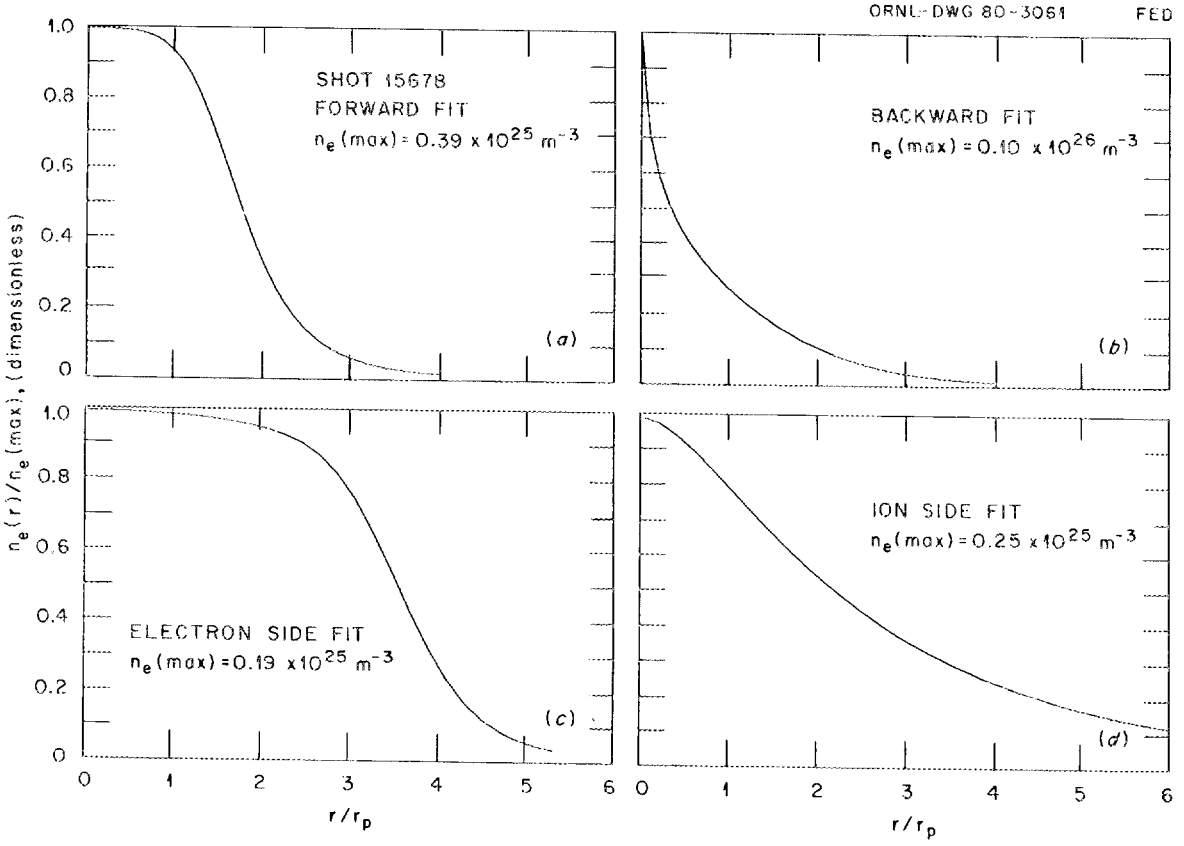

Fig. 5.26 Calculated $n_e(r)$ in four directions from pellet center, shot 15678.

magnetic field. Because symmetry was assumed in calculating $n_e(r)$, the actual asymmetry is probably larger than calculated. The assumption of symmetry tends to mask asymmetry.

Figures 5.27-5.32 are the $n_e \times \ell$ data, fitted curves, and calculated $n_e(r)$ for three typical interferograms from the September 11, 1979, data.

A general comment is in order before discussing the September 11 fitted curves. In examining all of the interferograms and shadowgraphs from September 11, the area of solid pellet mass appears to be elongated perpendicular to the magnetic field. That is, it appears that the pellet is ablated faster from the sides than the ends. With this observation in mind, the same general comments made concerning the September 6 data are still applicable. The more rapid falloff of the electron density perpendicular as opposed to parallel to the magnetic field can still be seen in the original interferograms, but it tends to be masked in the $n_e \times \ell$ plots by the elongation of the solid pellet material perpendicular to the magnetic field.

Again the data presented are typical of earlier in the ablation and toward the middle and close to the end of the pellet's life (shots 15888, 15876, and 15872).

It should be kept in mind that no attempt has been made to correct the data for neutral hydrogen density. Close to and inside the $r = r_p$ surface, these corrections could be large and might make the inferred $n_e \times \ell$ and $n_e(r)$ up to an order of magnitude larger. The correction is not

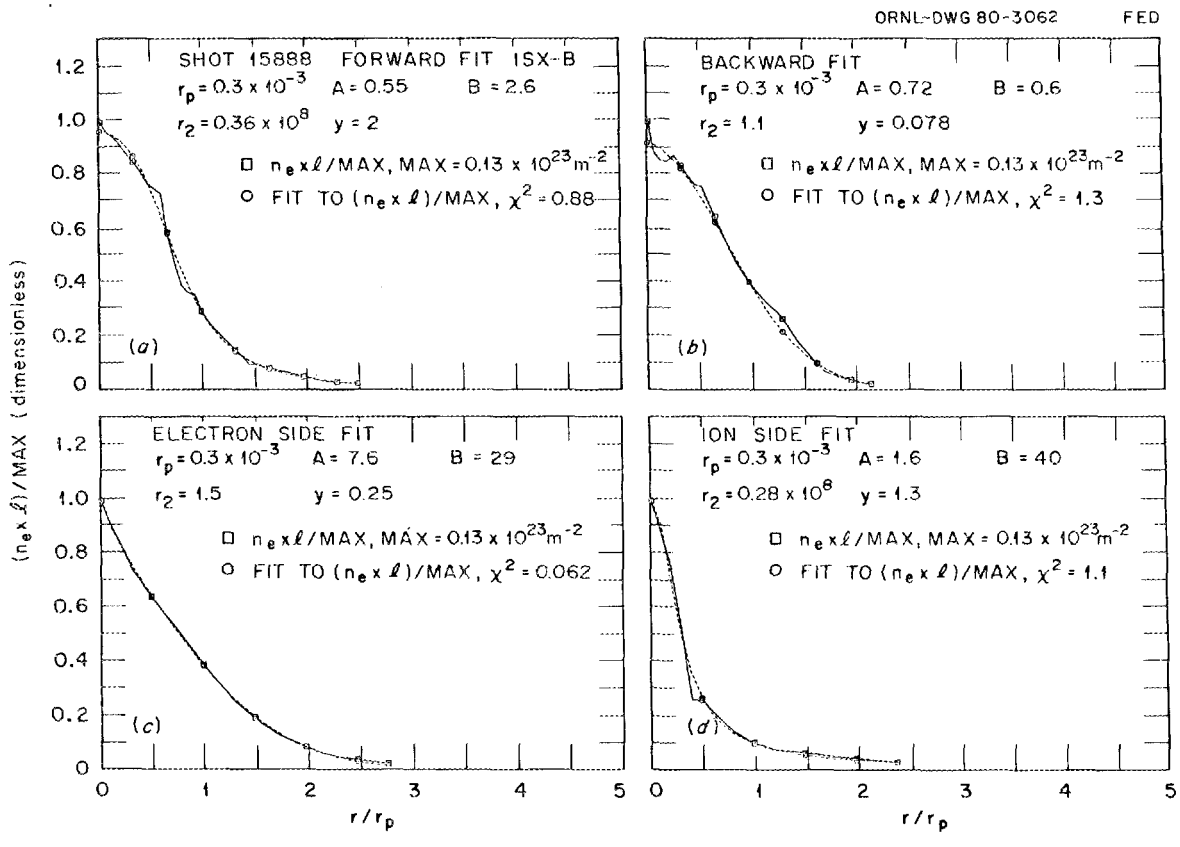

Fig. 5.27 Curves fitted to $n_e \times \ell$ data in four directions for shot 15888.

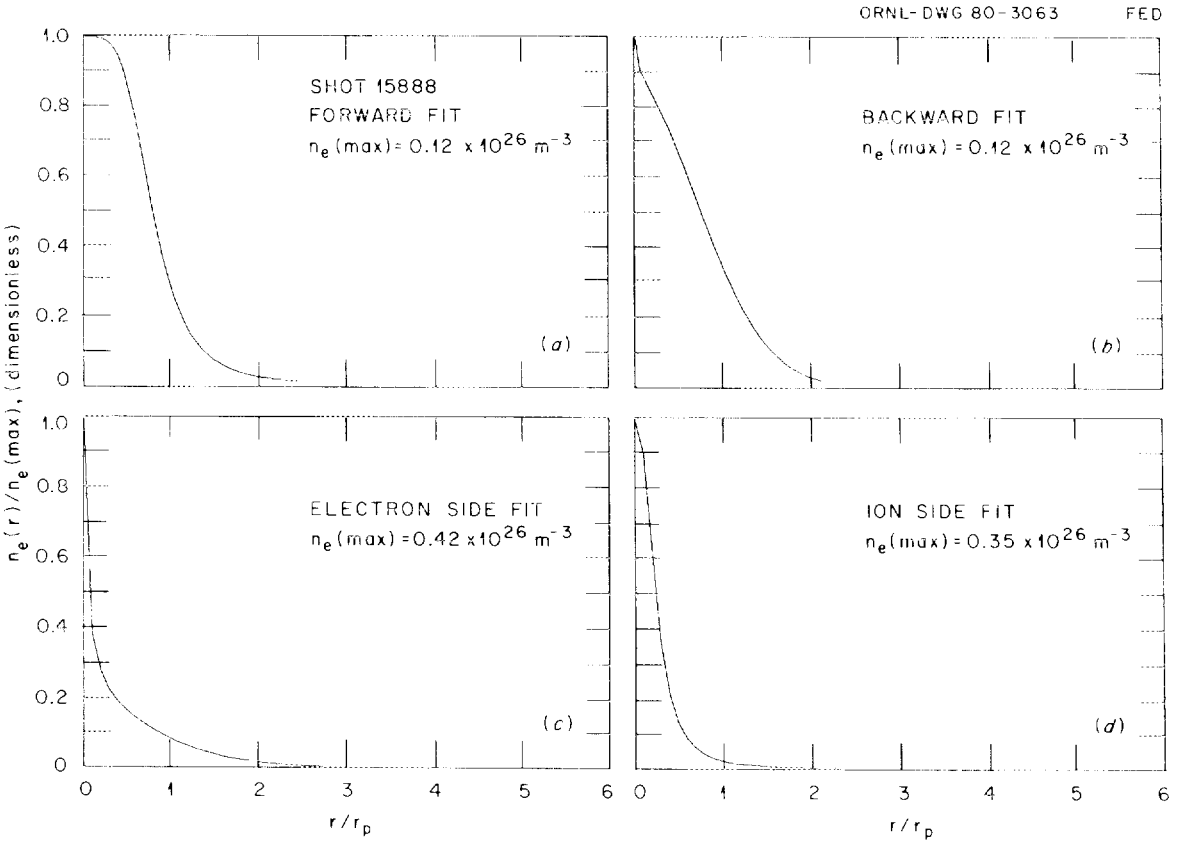

Fig. 5.28 Calculated $n_e(r)$ in four directions from pellet center, shot 15888.

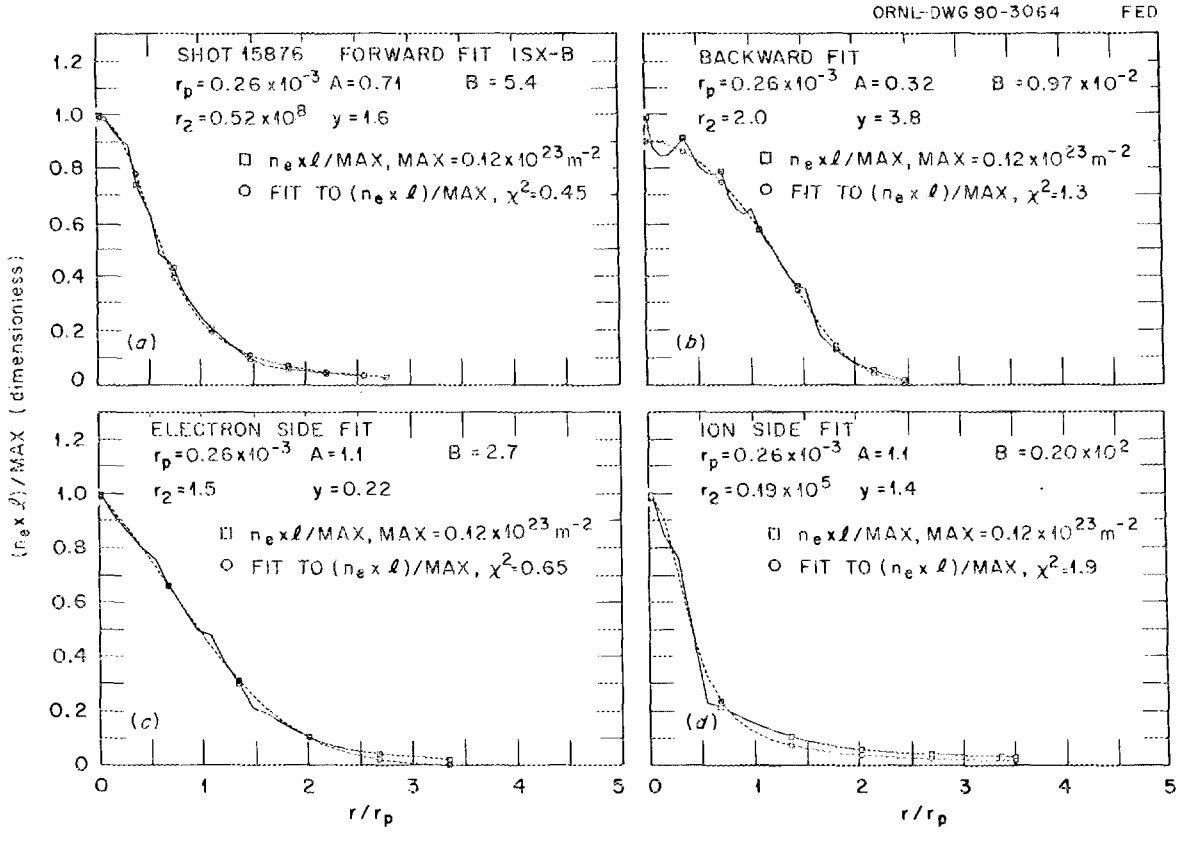

Fig. 5.29 Curves fitted to $n_e \times \ell$ data in four directions for shot 15876.

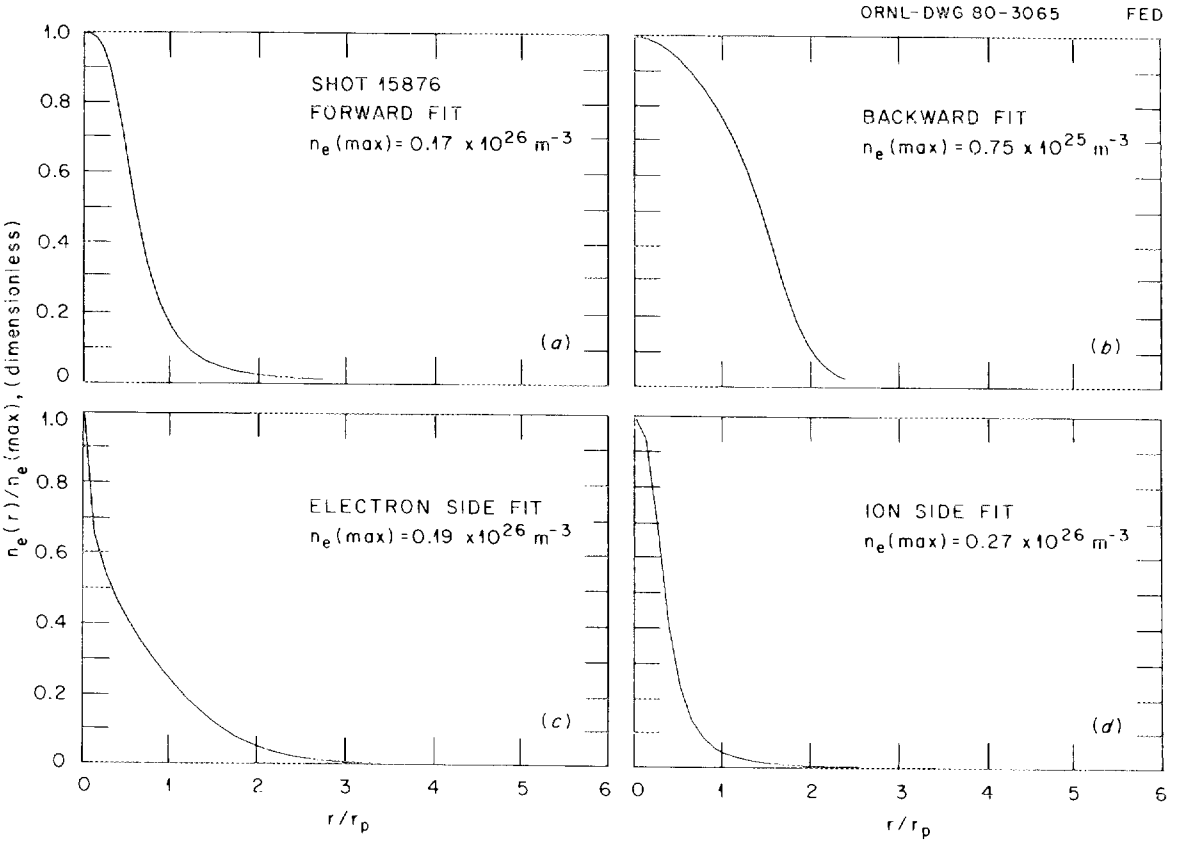

Fig. 5.30 Calculated $n_e(r)$ in four directions from pellet center, shot 15876.

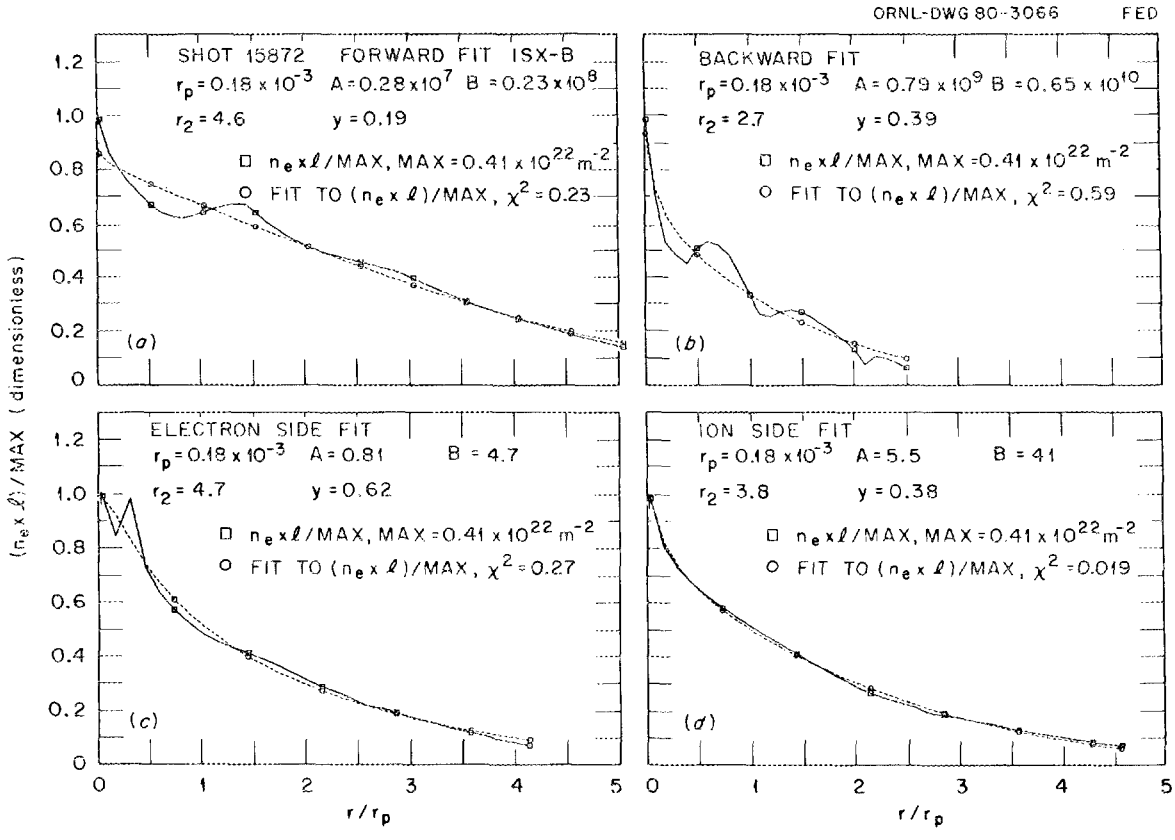

Fig. 5.31 Curves fitted to $n_e \times \ell$ data in four directions for shot 15872.

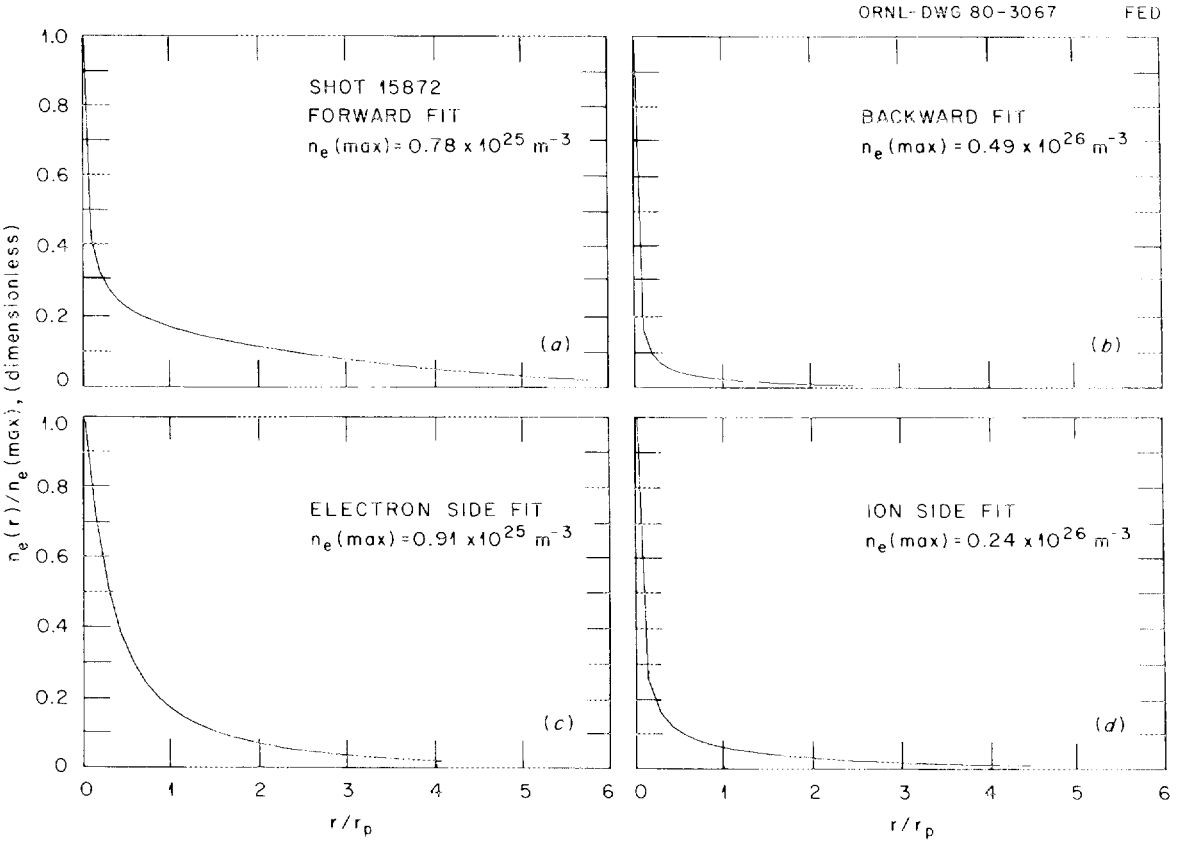

Fig. 5.32 Calculated $n_e(r)$ in four directions from pellet center, shot 15872.

so large outside the region of "solid" pellet and is larger inside the "solid" region.

5.5.3 Discussion of asymmetries

The observed asymmetry perpendicular and parallel to the magnetic field can probably be explained in terms of the $\vec{J} \times \vec{B}$ force on the expanding ablatant. If the ablatant is partially ionized, a current is induced as it tries to expand across the magnetic field,

$$\vec{J} = \sigma(\vec{V} \times \vec{B}), \tag{5.8}$$

where $\vec{V}$ is the ablatant velocity, σ is its conductivity, and $\vec{B}$ is the magnetic field. Taking $\sigma = 6.4 \times 10^3$ $(\Omega \cdot m)^{-1}$ as in Sect. 5.1, v = 1500 m/s (pellet velocity + ablation velocity), B = 1.5 T, and

$$\vec{F}\ell = \vec{J} \times \vec{B}\ell = \sigma v B^2 \ell \simeq 2 \times 10^4 \text{ Pa}. \tag{5.9}$$

This should be compared with the ablatant pressure. Assuming the neutral ablatant temperature to be about 20 K, and its density an order of magnitude larger than the electron density, which (Sect. 5.2) is $\sim 0.5 \times 10^{25}$ m^{-3}, and taking the electron temperature to be 1 eV, the total ablatant pressure is

$$P = (n_e q T_e + n_o k T_o) = 8 \times 10^5 \text{ Pa}. \tag{5.10}$$

Very close to the pellet surface the ablatant pressure dominates; however, a factor of 2 increase in temperature, decrease in density, and increase in velocity will make them the same order of magnitude. It

takes relatively little heating and expansion for the $\vec{J} \times \vec{B}$ force to significantly impede flow perpendicular to the magnetic field. The experimental data show strong discontinuities in electron density (see Sect. 5.5.4) preceding and following the pellet. These discontinuities are on the order of a third of a pellet radius from the pellet surface. Evidently the $\vec{J} \times \vec{B}$ force rapidly becomes important.

There are also significant asymmetries in $n_e \times \ell$ along the two dimensions parallel to the magnetic field. On the side of the pellet facing the electron drift velocity, $n_e \times \ell$ seems to increase smoothly and continuously into the pellet surface; on the side facing the ion drift velocity, there is generally a sharp discontinuity at the presumptive boundary of the pellet. Also, once outside the solid boundary $n_e \times \ell$ seems to fall off more rapidly on the electron side than on the ion side. This asymmetry parallel to the magnetic field can be explained only in terms of some asymmetry of the electron distribution function or perhaps by a rotation of the plasma as a whole. Whatever the cause, it appears that the ablatant is a fluid above the critical pressure on the side of electron drift velocity impact, where there are generally not discontinuities, but that it does not exceed the critical pressure on the ion side, where the discontinuity is obvious. The more rapid falloff of $n_e \times \ell$ outside the solid boundary on the electron side could be caused by more rapid heating and therefore acceleration of flow on the electron side.

5.5.4 Discussion of discontinuities in $n_e \times \ell$ preceding and following the pellet

Returning to the original interferograms and shadowgraphs of Chap. 4, discontinuities are observable preceding the pellet on the electron side and following the pellet on the ion side. The interferograms/shadowgraphs of shots 15679, 15683, 15685, and 15699 are good examples of these discontinuities. The discontinuities take the form of a dark line in a bright region on the shadowgraph and of a faint dark "hitch" in the fringes on the interferograms. Considering that we are looking at the integral of $n_e \cdot d\ell$, the fact that the discontinuity is visible at all means that it is a strong discontinuity. The discontinuity might be explained in terms of the $\vec{J} \times \vec{B}$ force of the previous section. One possibility is that the back pressure from the $\vec{J} \times \vec{B}$ force is causing the ablatant velocity to go from supersonic to subsonic (i.e., a shock). The other possibility is that it is a magnetic discontinuity where the ablatant pressure is being taken up by a thin current sheet; i.e., $\nabla p = \vec{J} \times \vec{B}$ and $\vec{J}$ exists in a thin sheet.

5.5.5 Discussion of apparent large electron densities in the regions of dense neutral hydrogen

Perhaps the most surprising and puzzling feature of the interferograms is that they show apparent large free-electron densities in the region of high-density neutral hydrogen material. Knowing that the

electron and neutral hydrogen indices of refraction are about equal when $(n_e/n_{H_2}) = 0.024$, the electron density in the region of solid hydrogen can be estimated as ∿3% of the solid hydrogen density, or $n_e \sim 8 \times 10^{26}$ m^{-3}. The energy necessary to produce this amount of ionization is trivial, assuming ∿16 eV per electron and a 1 mm diameter sphere:

$$E = 6.7 \times 10^{-2} \text{ J}$$

compared with stored energy in the plasma of $\sim 3 \times 10^3$ J. The problem is that typical recombination times are on the order of picoseconds. For instance, the dissociative recombination coefficient[3] for $e^- + H_2^+ \rightarrow 2H°$ is $\alpha \stackrel{\sim}{=} 4 \times 10^{-14}$ m^3/s at $T_e = 0.01$ eV. Then the recombination time would be

$$\tau \stackrel{\sim}{=} 1/n_e\alpha = 0.03 \times 10^{-12} \text{ s.}$$

There is an obvious problem. No good explanation for the apparent high density of free electrons in the neutral hydrogen has been advanced. It will simply be described as anomalous.

5.5.6 An estimate of the fractional ionization of the ablated material

An estimate can be made of the ionization fraction of the material ablated from the pellet. An energy loss equation, the incident-electron temperature, and the observed value of $n_e \times \ell$ at the pellet surface are sufficient for this estimate.

The energy loss equation for electrons incident on partially ionized hydrogen can be found from the work of Felber, Miller, Parks, Prater, and Vaslow[10] to be

$$dE/d\ell = 2L_o(E)n_{H_2} + 2L_e(E)n_e, \tag{5.11}$$

where

$$L_o(E)(eV \cdot m^2) = 8.62 \times 10^{19}[(E/100)^{0.823} + (E/60)^{-0.125} + (E/48)^{-1.94}]^{-1}, \tag{5.12}$$

$$L_e(E)(eV \cdot m^2) = 2.23 \times 10^{-16}\ E^{-0.94}\ n_e^{-0.03}, \tag{5.13}$$

and where

$E \equiv 2T_e(eV)$ = twice plasma electron temperature,

$n_e \equiv$ ablated electron density (m^{-3}), and

$n_{H_2} \equiv$ ablated neutral hydrogen density (m^{-3}).

Letting $dE/d\ell = E/\ell$ and defining

$$f_i \equiv n_e/(n_{H_2} + n_e), \tag{5.14}$$

Eq. (5.11) becomes

$$E = (n_e \cdot \ell)\left[\frac{1 - f_i}{f_i}(2L_o) + 2L_e\right]. \tag{5.15}$$

Solving Eq. (5.15) for f_i gives

$$f_i = [E/(2L_o n_e \ell) + 1 - L_e/L_o]^{-1}. \tag{5.16}$$

Using parameters typical of the data from September 6 and September 11, 1979,

$$E_e = 2000 \text{ eV},$$

$$n_e = 1 \times 10^{24} \text{ m}^{-3},$$

$$n_e \times \ell = 3.2 \times 10^{21} \text{ m}^{-2},$$

one finds that

$$f_i \tilde{=} 0.23.$$

The above calculation can only be described as an estimate of the ionization fraction of the ablation material, but it does indicate that the ablated material is significantly ionized.

This calculation is based on the premise that approximately 100% of the incoming plasma energy is absorbed by the ablated material. This assumption is experimentally justified.

5.6 Summary of Chapter 5

Section 5.1 discussed the downward curvature of the pellet trajectory and showed that it could be explained by a front-to-back current in the ablated material.

Section 5.2 discussed the effects of runaway electrons on a solid hydrogen pellet and showed that a relatively small runaway current could cause a rapid increase in the pellet radius (decrease in density of the pellet material). This process is important because it can greatly increase the ablation rate of the pellet.

In Sect. 5.3 it was shown that charge exchange losses due to pellet injection were too small to measure with the available diagnostics.

Pellet ablation rates inferred from H_α photon emission were discussed in Sect. 5.4. In the first two parts of Sect. 5.4 it was shown that the inferred ablation rates were consistent with the measurements of other diagnostics. In the remainder of Sect. 5.4 the experimental ablation rate was compared with the neutral shielding theoretical model, and it was shown that at high T_e the experimental ablation rates were a factor of 2-8 lower than the theoretical model would predict.

Section 5.5 was devoted to the analysis of interferograms. The interferograms were digitized and analyzed with the computer to produce plots of $n_e \times \ell$. Curves were then fitted to the $n_e \times \ell$ data, and electron density was inferred assuming spherical symmetry. It was found that the actual data were rather asymmetric, with slower falloff of electron density parallel to magnetic field lines. The more rapid falloff of $n_e \times \ell$ perpendicular to the magnetic field was explained in terms of the $\vec{J} \times \vec{B}$ force on the ablated material. The fact that discontinuities in $n_e \times \ell$ are observed was discussed, and it was suggested that these discontinuities represented either shocks or magnetic discontinuities. The apparent large number of free electrons in the high-density neutral hydrogen was discussed and described as anomalous. An energy loss equation and experimental data were used to estimate the ionization fraction of the ablated material. It was found that $f_i \sim 0.23$.

References

1. C. A. Foster, R. J. Colchin, S. L. Milora, K. Kim, and R. J. Turnbull, Nucl. Fusion 17, 1067 (1977).

2. N. A. Krall and A. W. Trivelpiece, Principles of Plasma Physics, McGraw-Hill, New York, 1973.

3. C. F. Barnett et al., Atomic Data for Controlled Fusion Research, ORNL-5207, Oak Ridge National Laboratory, Oak Ridge, Tennessee (1977).

4. R. D. Evans, The Atomic Nucleus, p. 625, McGraw-Hill, New York, 1972.

5. R. D. McCarty, Hydrogen Technological Survey -- Thermophysical Properties, NASA SP-3089, National Technical Information Center, Springfield, Virginia (1975).

6. S. L. Milora and C. A. Foster, IEEE Trans. Plasma Science PS-6, 578 (1978).

7. S. L. Milora, C. A. Foster, P. H. Edmonds, and G. L. Schmidt, Phys. Rev. Lett. 42, 97 (1979).

8. P. R. Forman (Los Angeles Scientific Laboratory), private communication, 1980.

9. P. R. Bevington, Data Reduction and Error Analysis for the Physical Sciences, McGraw-Hill, New York, 1969.

10. F. S. Felber, P. H. Miller, P. B. Parks, R. Prater, and D. F. Vaslow, Nucl. Fusion 19, 1061 (1979).

Chapter 6

Conclusions, Summary, and Recommendations

6.1 Conclusions

1) Holographic interferometry has been shown to be a useful and relatively inexpensive and easy to use diagnostic for the study of pellet ablation in high-temperature plasmas.

2) Instantaneous pellet ablation rates inferred from the emission of H_α photons have been shown to be in reasonable agreement with the results of other experimental diagnostics (microwave/FIR interferometry and Thomson scattering).

3) Comparison of experimentally observed ablation rates with the predictions of neutral shielding theory indicates that some additional mechanism is enhancing the shielding of hydrogen pellets from the high-temperature background plasma. The trend of the data indicates that at reactor temperatures shielding of the pellet could be an order of magnitude greater than predicted by neutral shielding theory.

4) The interferograms and shadowgraphs presented from the September 11 experiment show that when the pellet is not "blown up" by non-thermal electrons, it is preferentially ablated from the "sides" (surfaces perpendicular to the magnetic field).

5) The time-exposure photographs (Sect. 4.4), the low level of charge exchange energy loss, the interpretation of the downward curvature of the pellet trajectory, and the $n_e \times \ell$ data from the interferograms all add up to indicate that at higher ablation rates the material ablated from the pellet is significantly ionized, even very close to the pellet surface.

6) Analysis of the interferograms indicates that at higher ablation rates the flow of ablatant away from the pellet surface perpendicular to the magnetic field is impeded. This is a possible explanation for the observed enhanced shielding of the pellet.

7) The presence of high-energy electrons has been seen to cause the pellet to blow up and greatly increase the ablation rate. However, this should not cause difficulty for a device that is continuously fueled by pellet injection. The hard x-ray data show that the injection of a pellet removes high-energy electrons. Unless some mechanism is present that continuously produces a significant high-energy tail, only the first pellet or two injected should see any nonthermal electrons.

8) It has been shown that local charge exchange losses due to pellet injection are very small, on the order of 0.1% or less. These losses were too small to be measured within the accuracy of the available diagnostics.

9) The pellet ablation rate was observed to have very fast ($\sim$3 μs) large amplitude oscillations. These oscillations could be due either to short scale length fluctuations in the plasma temperature

and density, or to oscillations in the shielding cloud around the pellet.

10) The inferred presence of large numbers of free electrons in the high-density neutral hydrogen region remains a puzzling and unsolved mystery.

11) The high fractional ionization of the ablatant calculated from the $n_e \times \ell$ data shows that theoretical modeling which assumes Saha equilibrium at a single temperature is not appropriate. Instead, the ionization fraction of the ablatant should be calculated by extending the theoretical model to allow for a separate electron temperature or by balancing the rates of recombination and ionization.

12) The experimental results and conclusions presented here should be taken for what they are: a preliminary investigation of the use and usefulness of refueling plasmas with solid hydrogen pellets. A great deal of work remains to be done before pellet injection becomes an everyday tool for continuous refueling, and the results presented must stand the test of additional experimental investigation. However, what has been seen is very encouraging for the future of pellet refueling. The observations of enhanced shielding presented here, taken with the work of others on transport after pellet injection,[1,2] indicate that the refueling of fusion reactors can be accomplished by refining the existing technology — no new technological breakthroughs will be required.

6.2 Summary

Chap. 1 introduces the problem of pellet fueling of fusion devices. Prior to 1974 there was no experimental data concerning the interaction of plasmas with solid hydrogen. Since 1974 there have been experiments reported at RISO, Garching, and ORNL. The experimental work presented here uses new and existing diagnostic techniques for an experimental study of the ablation of ∿1 mm solid hydrogen pellets injected into the ISX-B tokamak at velocities of 1000 m/s. The new diagnostic techniques used are holographic interferometry and shadowgraphy of the pellet as it ablates. These techniques measure the local electron density around the pellet and the remaining area of solid hydrogen. The pellet ablation is also diagnosed by observing H_α photon emission, and by using conventional tokamak diagnostics (microwave/FIR interferometry, Thomson scattering, radiometry).

The experimental apparatus is described in Chap. 2. Design of the holographic interferometer is based on work done at TRW and at LASL. Holographic interferograms are normally focussed at the plane of the photographic plate, however, if they are out of focus due to displacement of the object, the replayed wave can be refocussed. This is a tremendous advantage of holographic interferometry over other forms of interferometry. The downward curvature of the pellet trajectory would have otherwise made the experiment impossible. An analysis is presented of the corrections to be made in magnification of the pellet, due to displacement of the

pellet from the focus of the interferometer optics. A precision velocity dependent digital diagnostic timer was designed to trigger the holographic laser, and other diagnostics, when the pellet was at the desired point in the field of view of the interferometer. Timing jitter was ∿5 μs.

Existing theoretical models of pellet ablation are briefly reviewed in Chap. 3. The existing models are discussed in light of experimental work. The conclusion is that it will be necessary to extend existing theories in order to explain experimental results.

The data from the experiments on ISX-B are presented in Chap. 4. The data are given with as little manipulation as is reasonable. Experimental results from two days are presented. On September 6, 1979, an experiment was performed at low $\bar{\bar{n}}_e$ and high $T_e(r = 0)$. The results of the experiment were dominated by the presence of runaway electrons in the discharge. On September 11, 1979, an experiment was performed at higher $\bar{\bar{n}}_e$ and lower $T_e(r = 0)$. The data from both days include: Thomson scattering density and temperature profiles immediately before and after pellet injection, microwave/FIR line average density immediately before and after pellet injection, local energy loss measured by a radiometer below the pellet injection port, hard x-ray measurements (from September 6 only), instantaneous pellet ablation rates inferred from H_α data for a number of shots, and interferograms and shadowgraphs made of the pellet ablating at various positions in the plasma. In addition to the above, time exposure photographs of the light emitted

by the ablating pellet are presented. These photographs were made using the shadowgraph optics of the interferometer, with the ruby laser line filter removed. These photographs exhibit bright streaks along the magnetic field lines which correlate with the observed oscillations in pellet ablation rate (discussed in Chap. 5).

Data analysis is done in Chap. 5. The experimental evidence of downward curvature of the pellet trajectory is discussed. It is shown that a front to back voltage potential in the ablation cloud approximately equal to the temperature gradient could drive enough current to cause the observed curvature of trajectory. Postpellet line-average density and density and temperature profiles are calculated from the experimentally inferred instantaneous ablation rates. These calculated quantities are compared with the microwave/FIR interferometer and Thomson scattering measurements and found to be in good agreement. The experimentally inferred average pellet ablation rates and shielding factors are compared with the predictions of the neutral shielding theoretical model. It is found that at higher electron temperatures the ablation rate is two to eight times less than predicted by the theoretical model. The observed large amplitude fast time scale oscillations of the pellet ablation rate are discussed. It is suggested that they are due either to plasma density and temperature fluctuations on a $\sim$3 mm spatial scale, or to oscillations in the shielding cloud around the pellet. Computer analysis of the interferograms is presented. Plots of contours

of constant $n_e \times \ell$ are given for each interferogram. The $n_e \times \ell$ data is used to calculate electron density profiles in four directions from the center of the pellet. The profiles are found to be asymmetric. Examination of the original interferograms and shadowgraphs shows that the flow of ablated material away from the pellet is impeded perpendicular to the magnetic field. Discontinuities in the refractive index are observed and these are interpreted as either shocks or magnetic discontinuities due to the $\vec{J} \times \vec{B}$ force. An energy loss equation is used to show that the ionization fraction of the ablated material close to the pellet is $\sim$20%. This is a low estimate, since it uses the perpendicular $n_e \times \ell$ (rather than parallel, which would be larger), and does not account for elastic scattering energy losses. These corrections would make the ionization fraction higher. Also, only an average, not the maximum, value of $n_e \times \ell$ is used in the calculation. The apparent large free electron densities in the remaining high density neutral hydrogen are discussed and described as anomalous.

Conclusions immediately precede this summary.

6.3 Recommendations for Further Work

1) The study of continuous fueling with pellets should be given high priority. The effects of both the pellet on the plasma and the plasma on the pellet need to be thoroughly studied. In order to accomplish this, reliable pellet injection devices capable of continuous refueling must be developed. This work is under way at ORNL and should be pursued vigorously.

2) The interaction of pellets with neutral beams and neutral-beam-heated plasmas should be examined. Some preliminary work has already been done at ORNL.

3) An advanced holographic interferometer should be designed and used for ablation studies on one of the latest generation of experimental devices (ISX-C, PDX, Doublet-III, ...). Some of the features of this interferometer would be production of multiple interferograms for each pellet, spaced in time, and two-frequency holographic interferometry (suggested by C. T. Chang, private communication, 1979) which would unambiguously give simultaneous electron and neutral density profiles.

4) A fast time scale Thomson scattering experiment should be performed. Electron density should be measured at each plasma radius in $\sim$100 μs intervals following pellet injection. This would give experimental data on fast transport processes and also allow a better experimental verification of the H_α inferred pellet ablation rate.

5) Pellet ablation experiments at near reactor conditions need to be performed. These experiments should give experimental scaling laws applicable to reactor conditions and demonstrate continuous fueling at reactor parameters.

6) The observed asymmetry of pellet ablation parallel to the magnetic field deserves more attention. Measurements of parallel electron temperature and plasma rotation immediately before and after pellet injection would be very interesting.

7) If the local electron temperature in the immediate vicinity of the pellet could be measured it would be a great help in calculating current flows and magnetic shielding effects in pellet ablation.

8) The inferred large free electron densities in the high density hydrogen should be studied. Perhaps these densities could be explained by a conduction band, or some local trapping of the electrons in the high density hydrogen.

9) Experiments using impurity doped pellets were proposed in 1977.[3] These experiments would give valuable information on impurity transport with pellet injection.

10) Finally an extended theoretical model of pellet ablation needs to be developed. This model should take account of the experimentally observed asymmetries and high ionization fraction of the ablated pellet material. It may be necessary to develop a two-dimensional, two-temperature model to properly account for the interactions of the ablated material with the magnetic field.

References

1. W. A. Houlberg, A. T. Mense, S. E. Attenberger, and S. L. Milora, p. 61, Proc. Fusion Fueling Workshop, NTIS USDC CONF-771129, Princeton, New Jersey (1977).

2. A. T. Mense, W. A. Houlberg, S. E. Attenberger, and S. L. Milora, Nucl. Fusion 19, 1473 (1979).

3. C. E. Thomas and P. A. Politzer, "Proposal for Diagnostics on Pellet-Plasma Interaction Experiments at ORNL," Nuclear Engineering Department, Massachusetts Institute of Technology, Cambridge, Massachusetts (August, 1977), unpublished.

APPENDIX

Index of Refraction — Interaction of 6943 Å (Ruby Laser) Light with Neutral Hydrogen and Plasma

A.1 Index of Refraction of H_2 and Calculations of H_2 Density Necessary for a Shift of One Fringe

Souers[1] gives an equation for the index of refraction of all phases of hydrogen at $\lambda = 5462$ Å:

$$N = 1 + (3.15 \times 10^{-6})\rho, \tag{A.1}$$

where N is the refractive index and ρ is the density in mole/m^3. Converting to molecular hydrogen density gives

$$N = 1 + 5.198 \times 10^{-30} n_{H_2}, \tag{A.2}$$

where n_{H_2} is the number of molecules of hydrogen per cubic meter.

This should be corrected to $\lambda = 6943$ Å. The Lorentz-Lorenz function is defined as

$$r_\lambda = \frac{(N_\lambda^2 - 1)}{\rho(N_\lambda^2 + 2)} \ (m^3 \cdot kg^{-1}), \tag{A.3}$$

where N_λ is the index of refraction of wavelength λ and ρ is the density in kg m^{-3}. Solving for N_λ [drop terms in $(\rho r_\lambda)^2$],

$$(N_\lambda - 1) \simeq \frac{3}{2} \rho r_\lambda. \tag{A.4}$$

Then for wavelengths λ_1 and λ_2,

$$\frac{(N_{\lambda_1} - 1)}{(N_{\lambda_2} - 1)} \simeq \frac{r_{\lambda_1}}{r_{\lambda_2}} . \tag{A.5}$$

Corruccini[2] gives corrected experimental values of r_λ for liquid normal hydrogen,

$$r_\lambda(5460\ \mathring{A}) = 1.032\ (cm^3/g),$$

$$r_\lambda(6939\ \mathring{A}) = 1.018\ (cm^3/g),$$

so that for 6943 $\mathring{A}$

$$(N - 1)_{H_2} = 5.13 \times 10^{-30} n_{H_2}. \tag{A.6}$$

Then for a shift of one wavelength path difference from vaccum,

$$(N - 1)_{H_2} \ell = (5.13 \times 10^{-30}) n_{H_2} \ell = \lambda, \tag{A.7}$$

or for λ = 6943 $\mathring{A}$

$$n_{H_2} \ell = 1.35 \times 10^{23}\ (m^{-2}). \tag{A.8}$$

In words, a molecular hydrogen density times path length of 1.35×10^{23} m^{-2} will cause an interferometer to detect a phase change of 2π or a fringe shift of one fringe when the wavelength used to make the measurement is 6943 $\mathring{A}$.

A.2 Index of Refraction of a Plasma and Calculation of n_e Density for a Shift of One Fringe

It is well known that for frequencies much greater than the plasma frequency ω_p, the index of refraction of a plasma is given by

$$(N - 1) \simeq -\frac{1}{2}\frac{\omega_p^2}{\omega^2}, \tag{A.9}$$

where

ω = frequency of interest,

$\omega_p^2 = n_e q^2/m\varepsilon_o$ = plasma frequency, and

n_e = electron density (m^{-3}).

Putting in the constants gives ($\lambda = 6943$ Å)

$$(N - 1) = -2.15 \times 10^{-28}\, n_e. \tag{A.10}$$

Then for a change of minus one wavelength path difference from vacuum,

$$(N - 1)\ell = -2.15 \times 10^{-28}\, n_e\, \ell = -\lambda. \tag{A.11}$$

Or for $\lambda = 6943$ Å

$$n_e\, \ell = 3.2 \times 10^{21}\ (m^{-2}). \tag{A.12}$$

That is, an electron density times path length of $3.2 \times 10^{21}\ m^{-2}$ will cause an interferometer to detect a phase change of -2π or a fringe shift of minus one fringe.

References

1. P. C. Souers, Cryogenic Hydrogen Data Pertinent to Magnetic Fusion Energy, UCRL-52628, Lawrence Livermore Laboratory, Livermore, California (1979).

2. R. J. Corrucini, Refractive Index and Dispersion of Liquid Hydrogen, National Bureau of Standards Technical Note 323 (1965).

ORNL/TM-7486
Dist. Category UC-20 a,f

INTERNAL DISTRIBUTION

1. L. Bighel
2. J. A. Cobble
3. R. J. Colchin
4. R. A. Dory
5. P. H. Edmonds
6. W. A. Houlberg
7. E. A. Lazarus
8. M. Murakami
9. J. A. Rome
10. M. J. Saltmarsh
11. S. D. Scott
12. J. Sheffield
13-17. C. E. Thomas
18-19. Laboratory Records Department
20-21. Central Research Library
22. Document Reference Section
23. Laboratory Records, ORNL-RC
24. ORNL Patent Office
25-26. Fusion Energy Division Library
27. Fusion Energy Division Reports Office

EXTERNAL DISTRIBUTION

28. D. J. Anthony, Manager, Advanced Energy Systems, Energy Systems Programs Department, Building 23, Room 290, General Electric Company, Schenectady, NY 12345
29. S. H. Be, Institute of Physical and Chemical Research, Wako-shi, Saitama 351, Japan
30. F. Bottiglioni, Association EURATOM-CEA sur la Fusion, DPh-PFC/SCP, B.P. No. 6, 92260 Fontenay-aux-Roses, France
31. K. Büchl, Max-Planck-Institut für Plasmaphysik, 8046 Garching bei München, Federal Republic of Germany
32. J. D. Callen, Department of Nuclear Engineering, University of Wisconsin, Madison, WI 53706
33. C. T. Chang, Association EURATOM, AEK Danish Atomic Energy Commission Research Establishment, Risø, DK-4000 Roskilde, Denmark
34. R. W. Conn, Department of Chemical, Nuclear, and Thermal Engineering, University of California, Los Angeles, CA 90024
35. R. J. Corrucini, Cryogenics Division, Institute for Materials Research, National Bureau of Standards, Boulder, CO 80303
36. N. A. Davies, Office of Fusion Energy, Office of Energy Research, Mail Station G-256, Department of Energy, Washington, DC 20545
37. S. O. Dean, Director, Fusion Energy Development, Science Applications, Inc., 2 Professional Drive, Suite 249, Gaithersburg, MD 20760
38. D. E. Diller, Cryogenics Division, Institute for Materials Research, National Bureau of Standards, Boulder, CO 80303
39. G. A. Emmert, Department of Nuclear Engineering, University of Wisconsin, Madison, WI 53706
40. H. P. Eubank, Princeton Plasma Physics Laboratory, P.O. Box 451, Princeton, NJ 08540
41. F. Felber, General Atomic Company, P.O. Box 81608, San Diego, CA 92138
42. P. R. Forman, Los Alamos Scientific Laboratory, P.O. Box 1663, CTR-8, MS-639, Los Alamos, NM 87545

43. H. K. Forsen, Exxon Nuclear Company, Inc., 777 106th Avenue, NE, Bellevue, WA 98004
44. T. K. Fowler, Associate Director for MFE, Lawrence Livermore Laboratory, P.O. Box 808, L-436, Livermore, CA 94550
45. H. P. Furth, Princeton Plasma Physics Laboratory, P.O. Box 451, Princeton, NJ 08540
46. S. L. Gralnick, Grumman Aerospace Corporation, Bethpage, NY 11714
47. R. Hancox, Culham Laboratory, UKAEA Research Group, Abingdon, Oxon OX14 3DB, United Kingdom
48. T. Hiraoka, Japan Atomic Energy Research Institute, Tokai, Ibaraki, Japan
49. R. L. Hirsch, Exxon Research and Engineering Company, P.O. Box 101, Florham Park, NJ 07932
50. A. L. Hunt, Lawrence Livermore Laboratory, P.O. Box 808, L-437, Livermore, CA 94550
51. D. W. Ignat, Princeton Plasma Physics Laboratory, P.O. Box 451, Princeton, NJ 08540
52. H. Ikegami, Plasma Physics Division, Institute of Plasma Physics, Nagoya University, Nagoya 464, Japan
53. F. C. Jahoda, Los Alamos Scientific Laboratory, P.O. Box 1663, Los Alamos, NM 87545
54. D. L. Jassby, Princeton Plasma Physics Laboratory, P.O. Box 451, Princeton, NJ 08540
55. L. W. Jorgensen, Association EURATOM, AEK Danish Atomic Energy Commission Research Establishment, Risø, DK-4000 Roskilde, Denmark
56. F. Kaufman, Office of Fusion Energy, Office of Energy Research, Mail Station G-256, Department of Energy, Washington, DC 20545
57. K. K. Kim, Department of Electrical Engineering, University of Illinois, Urbana, IL 61801
58. L. L. Lengyel, Max-Planck-Institut für Plasmaphysik, 8046 Garching bei München, Federal Republic of Germany
59. L. M. Lidsky, Department of Nuclear Engineering, Room 38-160, Massachusetts Institute of Technology, Cambridge, MA 02139
60. R. M. Marlay, Department of Energy, 1115 North Inglewood, Arlington, VA 22205
61. J. Marshall, Los Alamos Scientific Laboratory, P.O. Box 1663, MS 640, Los Alamos, NM 87545
62. D. M. Meade, Princeton Plasma Physics Laboratory, P.O. Box 451, Princeton, NJ 08540
63. G. H. Miley, University of Illinois, 214 Nuclear Engineering Laboratory, Urbana, IL 61801
64. R. G. Mills, Princeton Plasma Physics Laboratory, P.O. Box 451, Princeton, NJ 08540
65. M. R. Murphy, Office of Fusion Energy, Office of Energy Research, Mail Station G-256, Department of Energy, Washington, DC 20545
66. P. Nielsen, Association EURATOM, AEK Danish Atomic Energy Commission Research Establishment, Risø, DK-4000 Roskilde, Denmark
67. J. H. Norem, Fusion Power Program, Argonne National Laboratory, 9700 South Cass Avenue, Argonne, IL 60439
68. T. Ohkawa, General Atomic Company, P.O. Box 81608, San Diego, CA 92138

69. D. E. Ohlsson, Royal Institute of Technology, Division of Plasma Physics and Fusion Research, S-100 44 Stockholm, Sweden
70. E. Oktay, Office of Fusion Energy, Office of Energy Research, Mail Station G-256, Department of Energy, Washington, DC 20545
71. F. Oster, Association EURATOM, AEK Danish Atomic Energy Commission Research Establishment, Risø, DK-4000 Roskilde, Denmark
72. D. Overskei, Massachusetts Institute of Technology, Plasma Fusion Center, Building NW 14, Cambridge, MA 02139
73. R. R. Parker, Massachusetts Institute of Technology, Plasma Fusion Center, Building NW 14, Cambridge, MA 02139
74. P. E. Parks, General Atomic Company, P.O. Box 81608, San Diego, CA 92138
75. P. A. Politzer, Department of Nuclear Engineering, Massachusetts Institute of Technology, Cambridge, MA 02139
76. R. Prater, General Atomic Company, P.O. Box 81608, San Diego, CA 92138
77. B. A. Prichard, Princeton Plasma Physics Laboratory, P.O. Box 451, Princeton, NJ 08540
78. D. J. Rose, Department of Nuclear Engineering, Room 38-180, Massachusetts Institute of Technology, Cambridge, MA 02139
79. L. Ruby, Lawrence Berkeley Laboratory, Magnetic Fusion Energy Program, Berkeley, CA 94720
80. P. Rutherford, Princeton Plasma Physics Laboratory, P.O. Box 451, Princeton, NJ 08540
81. M. Salvat, Max-Planck-Institut für Plasmaphysik, 8046 Garching bei München, Federal Republic of Germany
82. G. Schilling, Princeton Plasma Physics Laboratory, P.O. Box 451, Princeton, NJ 08540
83. G. L. Schmidt, Princeton Plasma Physics Laboratory, P.O. Box 451, Princeton, NJ 08540
84. J. Schmidt, Princeton Plasma Physics Laboratory, P.O. Box 451, Princeton, NJ 08540
85. F. C. Schüller, Fom-Instituut voor Plasmafysica, Rijnhuizen, Jutphaas, Netherlands
86. F. R. Scott, Electric Power Research Institute, P.O. Box 10412, Palo Alto, CA 94304
87. T. Sekiguchi, University of Tokyo and IPP Nagoya, Tokyo, Japan
88. R. M. Siemons, Los Alamos Scientific Laboratory, P.O. Box 1663, Los Alamos, NM 87545
89. P. C. Souers, Lawrence Livermore Laboratory, P.O. Box 808, L-358, Livermore, CA 94550
90. L. D. Stewart, Princeton Plasma Physics Laboratory, P.O. Box 451, Princeton, NJ 08540
91. A. H. Sillesen, Association EURATOM, AEK Danish Atomic Energy Commission Research Establishment, Risø, DK-4000 Roskilde, Denmark
92. R. J. Taylor, Center for Plasma Physics and Fusion Engineering, University of California, Los Angeles, CA 90024
93. R. J. Turnbull, Department of Electrical Engineering, University of Illinois, Urbana, IL 61801
94. D. F. Vaslow, General Atomic Company, P.O. Box 81608, San Diego, CA 92138

95. C. M. Vest, Department of Mechanical Engineering, University of Michigan, Ann Arbor, MI 48109
96. G. H. Wolf, Institut für Plasmaphysik, KFA – Jülich, Postfach 1913 D-5170, Jülich 1, Germany
97. H. H. Woodson, Chairman, Department of Electrical Engineering, University of Texas, Austin, TX 78712
98. Office of Assistant Manager for Energy Research and Development, Department of Energy, Oak Ridge Operations Office, Oak Ridge, TN 37830

99–316. Given distribution as shown in TID-4500, Magnetic Fusion Energy (Distribution Category UC-20 a and f: Plasma Systems and Experimental Plasma Physics)

☆U.S. GOVERNMENT PRINTING OFFICE: 1981 740-062/512